THESE

présentée pour obtenir le grade de

DOCTEUR DE L'UNIVERSITE LOUIS PASTEUR

DE STRASBOURG

par

Sylvestre BONNET

Ru(terpy)(phen)(L)$^{2+}$ complexes as a new tool towards light-controlled molecular machines.

Photoinduced ligand substitution reactions, photoisomerisation and inclusion in a molecular ring.

Soutenue le 27 septembre 2005 devant la Commission d'examen

Prof. Mir Wais HOSSEINI	Président du jury
Prof. Dr. Gerard van KOTEN	Rapporteur
Dr. Bruno CHAUDRET	Rapporteur
Dr. Jean-Paul COLLIN	Co-Directeur de Thèse
Dr. Jean-Pierre SAUVAGE	Co-Directeur de Thèse

Thèse de S. Bonnet

présentée pour obtenir le grade de

DOCTEUR DE L'UNIVERSITE LOUIS PASTEUR

DE STRASBOURG

Les complexes Ru(terpy)(phen)$(L)^{2+}$: un nouvel outil pour la construction de machines moléculaires activées par la lumière.

Photosubstitution de ligands, photoisomérisation, inclusion dans un anneau.

Soutenue le 27 septembre 2005 devant la Commission d'examen

Prof. Mir Wais HOSSEINI	Président du jury
Prof. Dr. Gerard van KOTEN	Rapporteur
Dr. Bruno CHAUDRET	Rapporteur
Dr. Jean-Paul COLLIN	Co-Directeur de Thèse
Dr. Jean-Pierre SAUVAGE	Co-Directeur de Thèse

SOMMAIRE

REMERCIEMENTS

Je tiens à remercier tout particulièrement Jean-Pierre Sauvage pour m'avoir accepté comme doctorant dans son laboratoire. Il m'a donné l'opportunité de travailler dans un environnement particulièrement privilégié, tant par les moyens mis à ma disposition que par le dynamisme scientifique de l'équipe et l'attention particulière apportée au développement de relations cordiales, voire amicales, au sein de l'équipe. Son engagement dans la formation des doctorants et son respect de *tous* les aspects d'une thèse doivent ici être particulièrement soulignés.

Je remercie chaleureusement Jean-Paul Collin pour sa disponibilité sans faille, son suivi au jour le jour, son enthousiasme à déchiffrer les spectres de RMN et de masse les plus ardus, et sa bonne humeur quotidienne. Son encadrement a été très complémentaire de celui de Jean-Pierre ; mes deux encadrants m'ont permis d'avancer dans les directions dans lesquelles je souhaitais aller.

A toute l'équipe du laboratoire : Titi, Pierre, Elisa, Masatoshi, Fabio, Bryce, Benoît, Chröest, Jack, Fabien, Julie, Ulla, Oliver, Grande Valérie, Petite Valérie, Jean-Marc, Christiane, et tous les autres, merci d'avoir partagé avec bonne humeur mon quotidien pendant mes quatre années au LCOM. Je souhaite également remercier deux ex-thésard dont la présence m'a particulièrement importé : Damien pour ses discussions, ses idées brillantes, son physique d'athlète, sa nature bordellique et son mauvais comportement ; Benoist pour sa philosophie, son ouverture d'esprit, sa révolte, sa chevelure changeante et son goût des bonnes choses. Merci à la bière qui m'a permis de partager de bons moments avec tous ces gens.

Je remercie mes collègues qui m'ont permis de découvrir l'univers merveilleux du Macintosh. Merci à Apple d'avoir enfin produit un système informatique puissant, convivial et sur lequel on peut compter.

Roland Graff, Patrick Wehrung et Richard Welter, secondés de leurs équipes des services communs de RMN, de spectrométrie de masse et de cristallographie de l'Université Louis Pasteur, ont par leur grand professionnalisme grandement contribué à la réussite de mon travail. Qu'ils en soient particulièrement remerciés.

Ma femme Wiebke a vu naître et mûrir cette thèse. L'enrichissement qu'elle m'apporte au quotidien depuis cinq ans reste peu visible dans les pages qui suivent, mais il a fortement contribué à la réussite de ce travail. Merci à mon fils Max, son aide dans la rédaction des chapitres 2, 3 et 4 a été décisive ! Merci à mes parents : par leur éducation et leur amour, ils m'ont permis de réaliser mon rêve d'enfant : devenir chercheur... Cela n'a pas de prix.

Parce que devenir scientifique demande du temps et de la passion, je dédicace ce travail à tous mes professeurs de Sciences Physiques et de Chimie, notamment : Gérard Ganivet, Eric Brottier, Luc Martel, André Collet, Jean-François Le Maréchal, Daniel Simon et Lutz Gade.

GENERAL INTRODUCTION

I. Natural molecular machines

I.1. Motion in living systems

Nature is the most beautiful source of inspiration for chemists. The symmetry of natural structures, the complexity of biological pathways or the efficiency of natural photochemical processes are reasons to wonder. Although researchers sometimes succeeded in the mimicking of biological systems, there is a field where artificial molecules have stayed far behind in terms of beauty, complexity and efficiency: the field of molecules displaying motion.

Motion is one of the most important features of monocellular and pluricellular living organism: it enables them to move, to develop, to feel and to reproduce. All these macroscopic effects are often due to the motion of molecules at the nanoscale. The motion of myosin heads on actin filaments enable our muscles to contract; the gliding of ribosomes along ARN filaments enables polypeptides to be synthesised; the photoinduced isomerisation of retinal is responsible for our ability to see; the vibrations of their flagellae gives to spermatozoids the possibility to move towards the ovum.

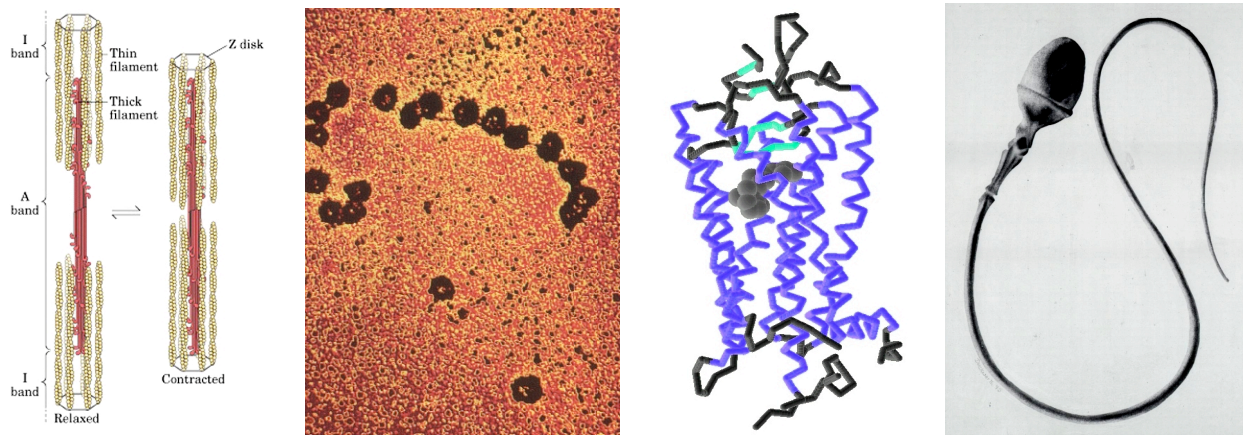

Figure 1: from left to right: contraction of a muscle due to the gliding of the thin and thick filaments;[1] ribosomes along an ARN_m filament;[2] retinal (in grey CPK model) inside bovine rhodopsin;[3] the flagellum of a spermatozoid.[4]

All these motions are based on protein architectures immobilised in biologic membranes. Most of these proteins are far too complex to be synthesised or modified by chemical means. For this reason, chemists have tried for decades to reproduce similar motions using artificial systems that can be synthesised. In this mimicking process, aromatic rings and saturated flexible chains are covalently linked like mechanical elements are soldered or attached to ropes, chains and bands.

Unsaturated bonds and metal centres are used as reactive sites to induce motion at the nanoscopic level like motors, switches and pipes enable macroscopic mechanical elements to be set in motion.[5]

I.2. A rotating molecular motor: ATPase

One of the most fascinating families of natural molecules displaying motion is ATPases. These quaternary assemblies of proteins (550 to 650 kDa) are very efficient rotating molecular machines common to bacteria, plants, animals and humans.[6] They transform H^+, Na^+ or K^+ ion gradients across a lipidic membrane into new ATP molecules. ATPases can thus be regarded as energy transductors:[7] the difference in chemical potential across the membrane is transformed into chemical energy that can be directly used by other proteins. In ATP synthase for example, the proton gradient may be the result of respiration (in mitochondria) or photosynthesis (in chloroplasts).[6] ATP synthase is thus one of the key elements of the bioenergetic conversion scheme turning solar energy into cellulose.

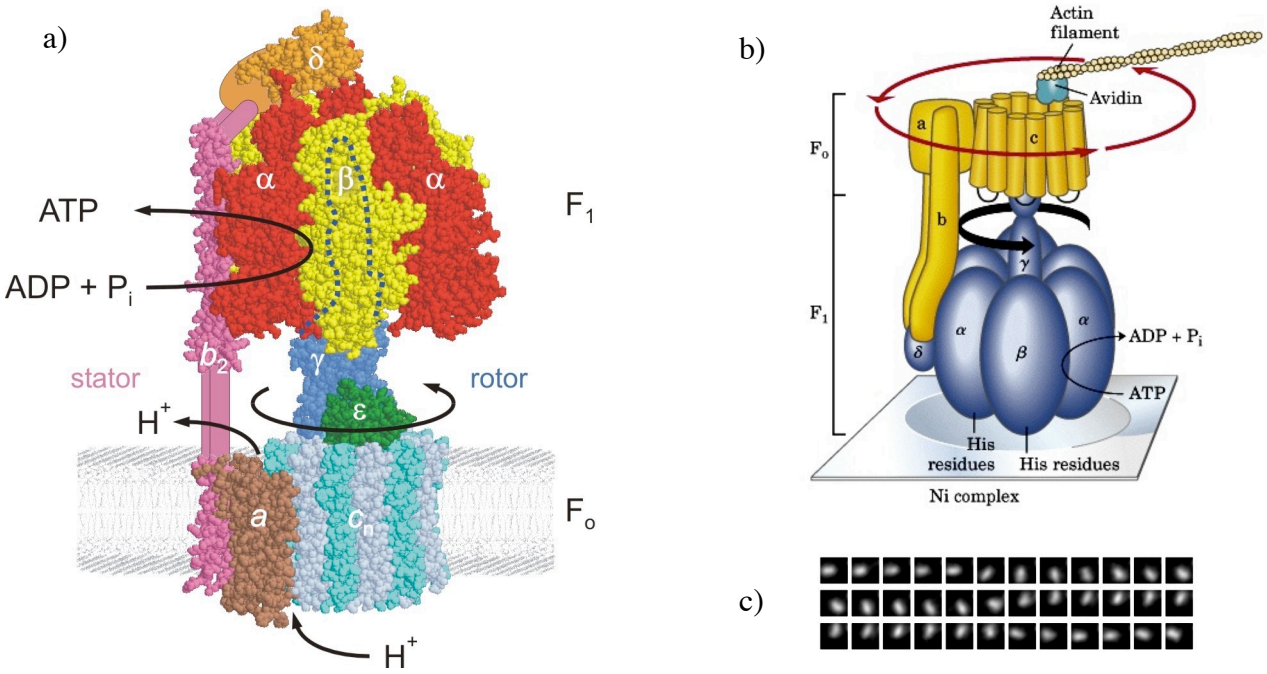

Figure 2: a) structure of ATP synthase bound to a lipidic membrane. The F_1 stator is composed of $\alpha_3\beta_3\delta ab_2$ subunits; the F_0 rotor is composed of $c_{12}\varepsilon\gamma$ subunits; (b) experimental evidence of the rotation consecutive to ATP hydrolysis. The $\alpha_3\beta_3$ subunit is linked to a surface; a fluorescent filament attached to the c_{12} rotor rotates continuously and can be filmed; c) selected pictures of the film.

On the mechanical point of view, ATP synthase is a rotating molecular machine coupled to a catalytic site for hydrolysis / synthesis of ATP.[8] It consists into a stator ($ab_2\delta\alpha_3\beta_3$ subunits) and a rotor ($c_{12}\gamma\varepsilon$ subunits, see Figure 2a). The stator is bound to the membrane and incorporates three catalytic sites (each $\alpha\beta$ subunit). The rotor is mechanically coupled to the proton flux across the membrane, so that when protons go through the ac_{12} "channel" they cause the rotation of the

system. When the rotor rotates, its dissymmetric γ shaft actions successively the three α or β units like a lever would open doors or let them closed. Depending on the position of the doors, ATP or ADP and inorganic phosphate can either enter the catalytic site or be released. Fascination comes not only from this auto-optimised design, but also from the fact that the whole system is fully reversible: if a proton gradient across the membrane is present, it drives the rotation of the rotor in one direction and doing so synthesises ATP from ADP and P_i. On the contrary if ATP is present on the side of the $\alpha_3\beta_3$ stator, it is hydrolysed, which induces rotation of the rotor in the other direction and creates a proton flux across the membrane. The rotation consecutive to ATP hydrolysis was clearly demonstrated by extraordinary experiments of Noji *et al.*[9] They attached the $\alpha_3\beta_3$ stator to a surface, a fluorescently labelled actin microrod to the rotor (γ shaft) and plunged the surface into a solution containing ATP (Figure 2b). They directly observed the rotational motion by fluorescence microscopy (Figure 2c), which showed unambiguously the nature of ATPase: it is a rotary molecular motor.

I.3. Brownian motion in natural molecular machines

Common sense tends to lead us to a bad representation of what mechanics may be at the nanoscale. In the macroscopic sense indeed, machines are plunged into a vertical gravitational field that drives all motions towards the bottom; in addition, we all feel inertia as a basic mechanical rule, and motors are designed in order to cope with it.[10] At the nanoscopic scale, gravitation is always negligible with respect to electromagnetic forces and inertia is usually very small compared to thermal agitation.[11,12] As a consequence, natural molecular machines were optimised during biological evolution in order to cope with Brownian motion.[13] In ATP synthase for example, rotation of the rotor do not always occur in the same direction: whenever an ion or a particle gives an impulse backwards, the machine will rotate in the "wrong" direction for a while until the driving force leads the system in the forward direction again. The resulting rotation is on average unidirectional, but single elementary motion units may occur either in one or in the other direction. Such a forward rotation with backwards "errors" have been both experimentally observed and modelled (see Figure 3).[14,7] The ability to perform a directed motion in a Brownian world is one of the highest achievements of Nature.

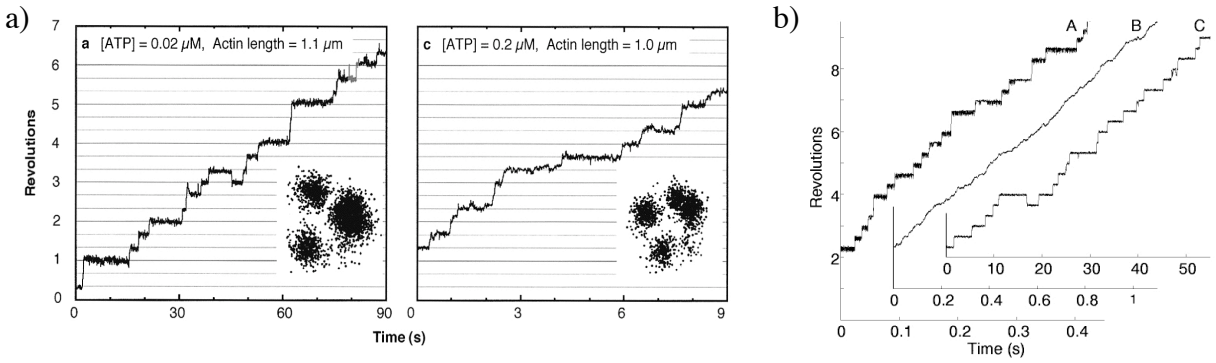

Figure 3: a) experimental curves[14] for the rotation of F_1-ATPase attached to a surface in contact with an ATP solution. Black dots represent the positions of the fluorescent actin filament on the CCD captor and show that each step is a 120° rotation; b) theoretical curves[7] for the rotation of the γ-shaft of ATP synthase with respect to $\alpha_3\beta_3$; A : ATP concentration is 2mM ; B and C : a drag coefficient equivalent to a 1μm long actin filament is added on the γ-shaft ; ATP concentration is 2mM for B and 20nM for C.

The understanding of such an achievement is still a challenge, but great progress has been made due to the last single-molecule techniques of visualisation[15,16]. Proteins are chiral so that their interaction energy profiles are intrinsically asymmetric: in spatially periodic systems like microtubules, actin filaments or the c_{12} subunit of ATP synthase, the steepness of the slope in one direction of the motion is different from the steepness in the other direction. However, it is impossible to obtain a directed motion with a dissymmetric potential only. According to the 2nd law of thermodynamics, the potential energy profile of a system may be symmetric or not, diffusion cannot produce work.[17]

A theoretical model called "the Brownian ratchet model" has been developed[12] and is more precisely developed in Annex A. It explains how a dissymmetric potential may lead to a directed motion in case it is coupled with random diffusion. In order to achieve this coupling, the dissymmetric potential needs to be cut off or modified regularly.[18] The direction and speed of the overall motion does not depend only on the energetic profile; it also depends on the diffusion constants of the species and the time interval between two modifications of the potential.[19, 20, 21]

In Nature such a modification often comes from chemical reactions: the binding of ATP to a catalytic site or the release of ADP+P_i modifies the energetic profile of the system.[11, 13] This modification takes place regularly, for each single ATP hydrolysis reaction. Such periodical change of the potential energy of the system, combined to the chirality of proteins enables an overall directed rotation of ATP synthase despite the intrinsic undirected nature of Brownian motion.

I.4. The role of organisation in the use of mechanical energy

Natural molecular machines are complex, beautiful and efficient. However, they would be as useful as cars inside the see if they were not organised inside biological systems. ATP synthase, for

example, is anchored inside a membrane. The membrane has an inside (cytoplasm) and an outside (periplasm): it is a directed medium. Differences in concentrations may occur across the membrane, which fuel the rotation of the molecule. When ATP synthase is dissolved in solution, it hydrolyses ATP[22] but the consequent rotational motion cannot be used: its internal nature only dissipates the chemical energy of the ADP-P_i bond. The organisation of the rotary motor inside the membrane enables Nature to use this chemical energy to induce a concentration difference; or to use a concentration difference in order to store chemical energy.[8]

In our muscles, a similar analysis can be done: one single myosin head can be released from the active site of an actin filament by coordination of ATP; hydrolysis, binding to another site, release of P_i and power stroke will occur (see Figure 4a).[23] During the power stroke, a 5 to 10nm lever arm is actioned,[24, 25] which is the elementary unit of motion (Figure 4b). However, this mechanism will *not* induce translational motion of *one* single myosin molecule along the actin filament because the next binding of ATP will detach the myosin head from the actin active site. Such a translation is the result of a population of myosin molecules assembled in corn ears-like fibres (thick filaments) parallel to actin polymeric chains (thin filament, see Figure 4c). In such a myosin fibre, each myosin molecule transforms the chemical energy of ATP into a power stroke of the head.[26] These power strokes do not occur in a coordinated manner, but the overall result is a translational gliding of the myosin assembly along the actin fibre. Here again, organisation of myosin molecules enables Nature to 1) transform the chemical energy of ATP into usable mechanical energy 2) take advantage of thermal diffusion to induce directed motion in an asymmetric system according to the Brownian ratchet model (see Annex A).[27, 28]

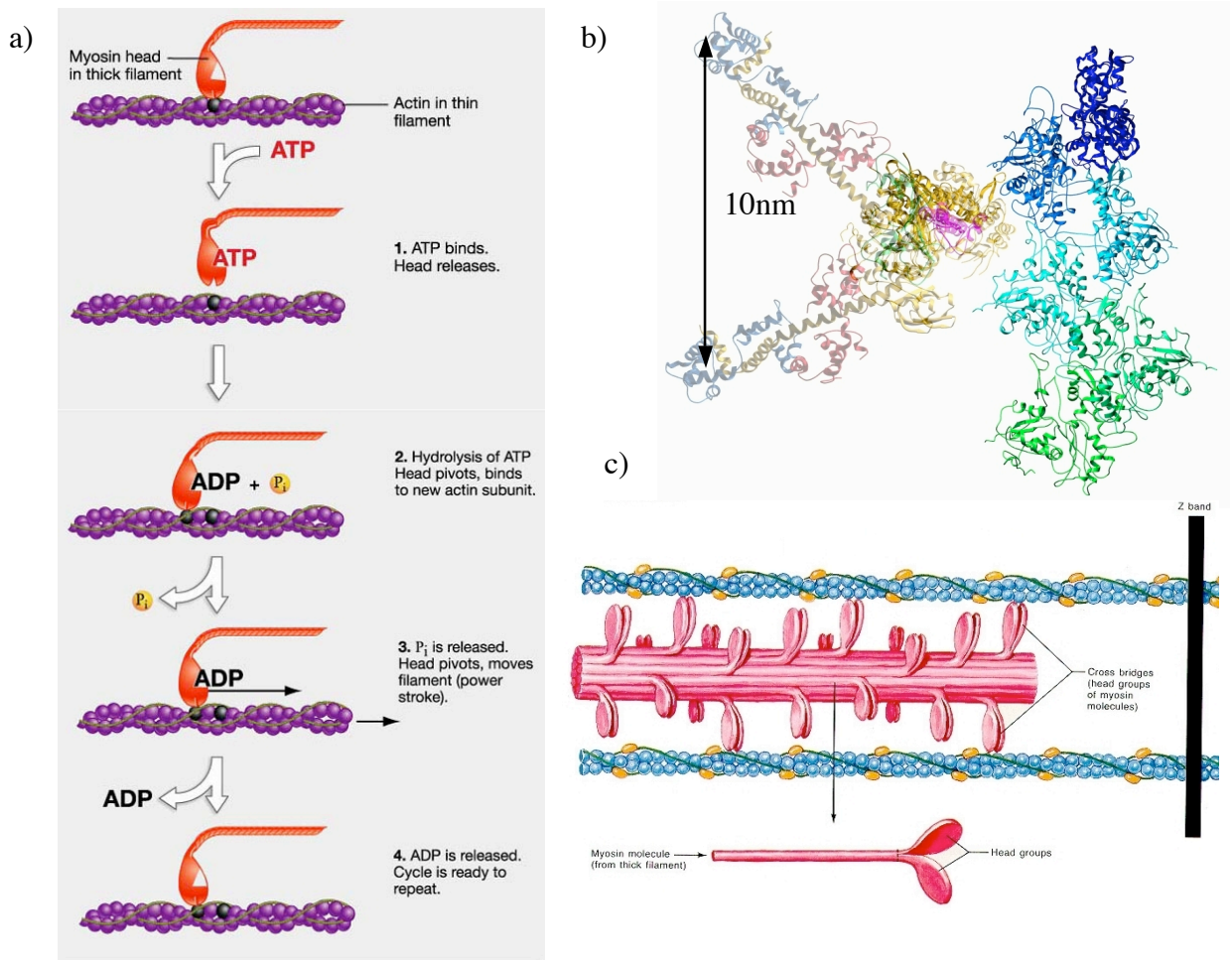

Figure 4: a) one single myosin head is in interaction with ATP and an actin filament. The molecular motion is a bending of the head with respect to the tail during the power stroke;[29] b) during the power stroke a ≈ 10 nm lever arm is rotated with a 5 to 10 nm stroke;[30] c) a collection of myosin molecules assembled in a corn ears fashion (thick filament) parallel to actin fibres (thin filaments) display a global translation motion as each myosin head move independently from one another.[31]

As will be discussed in Part II, artificial molecular machines have been achieved in solution by molecular chemists. The relative motion of one part of a molecule with respect to another part has been realised, but it always led to dissipation of energy. The direct *use* of mechanical energy or its transformation into another type of energy is still a great challenge, as it requires expertise both in molecular and supramolecular chemistry, polymer sciences and surface sciences. To our knowledge, the organisation of individual artificial molecular machines in arrays, surfaces or chains has not been realised yet.

II. Artificial molecular machinery

II.1. Definitions

A molecular machine is a molecule made of two distinct parts, one of which can display a large amplitude motion with respect to the other one under the action of an external stimulus.[5] As a

first consequence, a molecular machine is an energy transductor: the energy introduced in the system as the "external stimulus" is transformed into a motion at the molecular level.

When dealing with molecular machines, one has to keep in mind that:

1) Thermal diffusion leads to motion at the nanoscale but not in a directed way; it is not considered as an external stimulus;

2) The statistical distribution of a molecular system between several states of similar energies is not considered as a "controlled" motion;

3) The motion at the nanoscale has to lead to changes at the macroscopic level in order to be experimentally proven. For example, the rotation of a methyl group or a dynamic conformational equilibrium between conformers cannot be considered as a molecular machine.

In a molecular machine, the motion can be either a translation or a rotation. In the case of a translation, when one atom only is concerned the motion is called "translocation".[32] The rotational oscillation of a molecular ring between two positions A and B is generally named as a "flip-flop" motion: one cannot say whether the motion takes place in one or the other direction, but the system goes from one state to a different state. A minimum of three positions A, B and C are needed in order to say that a motion is a rotation.[33, 34] A molecular motor is generally defined as a molecular machine where the motion is a unidirectional rotation; some also required that the rotation produce useful work.[35]

II.2. How to control motion at the molecular level

As molecules are very small objects, they do not feel gravitation and are prone to Brownian motion.[10] These two properties make it difficult to precisely control the motion at the molecular level (there are no "twisters" for molecules). In order to induce the motion, macroscopic signals like light or electricity need to be used that selectively action one part of the molecule.[5] This action is a change in the stability of the reactive centre. The presence of other states lower in energy induces a motion, so that the system minimises its free energy.

Four main types of macroscopic signals have been used:

- An electrochemical signal: the oxidation or reduction at an electrode provokes the motion;[36]

- A chemical signal: a pH change,[37, 38] the addition of a metal ion[39] or the introduction of oxidising or reducing molecules[40] provokes the motion;

- A photochemical signal: light triggers the motion but a sacrificial agent is used to drive the system;[36, 41]
- A photonic signal: light is the only signal that provokes the motion. Thermal energy may be needed for the completion of the motion after light triggering.[42-45]

Starting from a pure sample of the molecule in state A, two cases can be generally distinguished:

- the signal definitively alters the environment of the molecular machine, leading to a change of the relative stability of state A in the new conditions (pH change for example). Evolution towards the more stable state B occurs;
- the signal triggers a transformation of the molecule from state A to state *A without changing the environment (in photochemical systems for example).[42, 45, 46] This high-energy state leads spontaneously to more stable states like A or B. The final A/B ratio is controlled by the external signal; it is not a thermodynamic equilibrium but a stationary state. All macroscopic parameters are independent of time, but the external signal continuously provides free energy to the system.

III. Rotaxanes and catenanes as central building blocks of artificial molecular machines

III.1. Definitions

A rotaxane is a ring threaded around an axle, the ends of which are terminated by two groups larger than the ring (Figure 5a).[47] These "stoppers" prevent the ring to de-thread in case the link between ring and axis is broken. A catenane is the shortest possible chain made of two interlocked rings (Figure 5b). These two rings can be separated from each other only by breaking one of them.

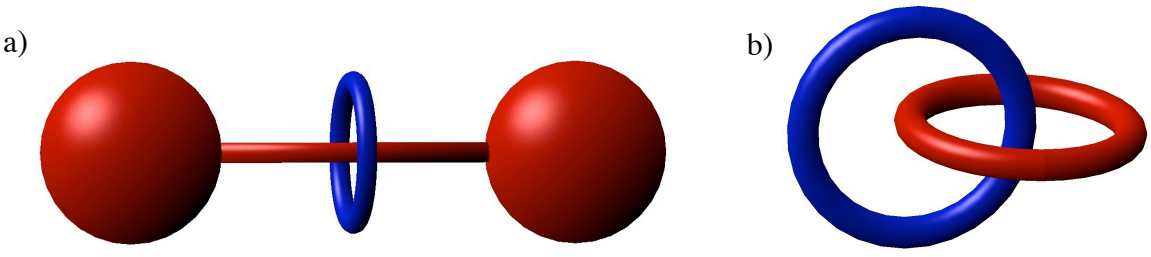

Figure 5: a) a rotaxane; b) a catenane.

The topology of a catenane is not trivial, as it cannot be drawn on a plane without crossings. Although a rotaxane has, strictly speaking, a trivial topology, its geometry is similar to that of a catenane, as the stoppered thread can be compared, by its effects, to an infinitely large ring in a catenane. Considering the fact that such topologies / geometries are not easy to obtain at the

nanoscale, catenanes and rotaxanes used to be challenging target molecules for synthetic chemists. Since the first templated synthesis in 1983 however,[48] their constitutive building blocks have been pre-organised in order to achieve good to almost quantitative yields. Such a pre-organisation has been based on different types of interactions:

- coordination on metals;[48, 49]
- hydrophobic effects;[49, 50]
- hydrogen-bond formation;[51-53]
- charge-transfer interactions;[53-55]
- covalent bonds;[56, 57]

III.2. Application of catenanes and rotaxanes to molecular machines

Although they were initially purely aesthetic molecules, rotaxanes and catenanes found years later unexpected applications, first in the field of electron transfer,[58] secondly in the field of molecular machines.[59, 60] In such objects indeed, two molecular objects may *both* be held close to each other *and* perform a relative motion, even if the chemical link between them is broken. In a "free" catenane or rotaxane, neither covalent bonding nor weaker interactions like hydrogen-bonding, π–π stacking or coordination bonds are responsible for the link between the two parts. However, it is necessary to break one covalent or coordination bond in order to release one ring from the rest of the molecule. This type of link is called a "mechanical" link and is reminiscent of mechanical joints in the macroscopic world.

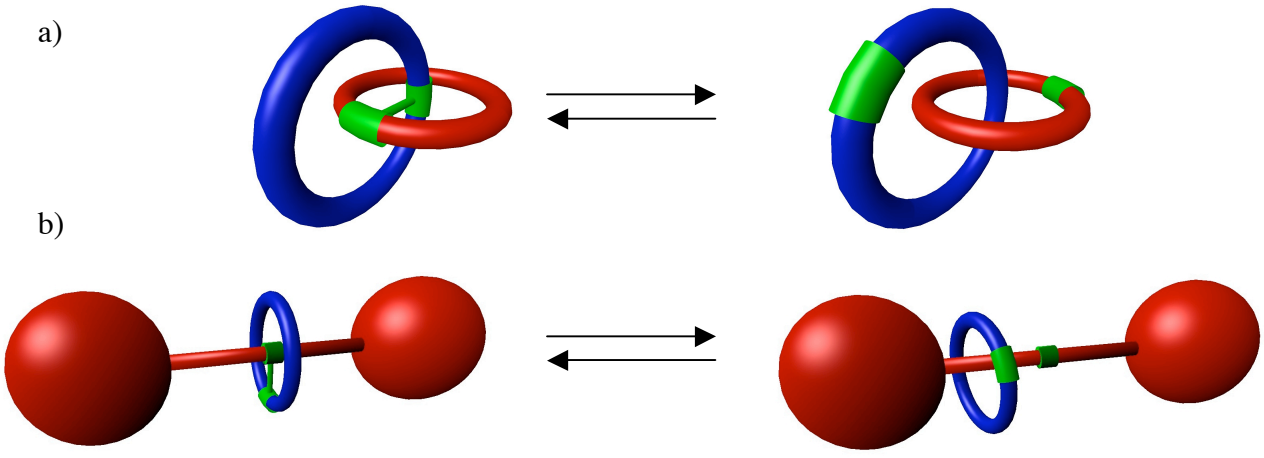

Figure 6: motion inside a molecular catenane (a) or rotaxane (b). The « free » blue ring does not fall apart or leave the proximity of the red part due to the mechanical link inherent to such interlocked systems.

In free catenanes and rotaxanes, internal reactions between the ring and the rest of the molecule are more likely to happen, as both parts remain close from each other (see Figure 6).

Some interpreted this high probability as a high "local concentration".[61] Moreover, each part is hindered towards intermolecular reactions due to the presence of the other part. As a consequence, intramolecular reactions, hence relative motion inside a single molecule, are more likely to occur than bimolecular processes. That is why rotaxane and catenane structures have been particularly used in the design of molecular machines.

III.3. An alternative: scorpionate molecules

Another way to keep a reactive group of atoms close to a complementary reactive centre is to attach the former to the latter by covalent bonds. The resulting geometry is a big size "body" with a "tail" attached to its periphery. This tail may, or may not, be linked by one single chemical bond to the body of the molecule, like the tail of a scorpion lays close to the head of the animal, or far behind it (see Figure 7). Since the first use of this name by Swiatoslsw Trofimenko for poly(pyrazolyl)borate metal complexes,[62] molecules of this kind have been called "scorpionates".

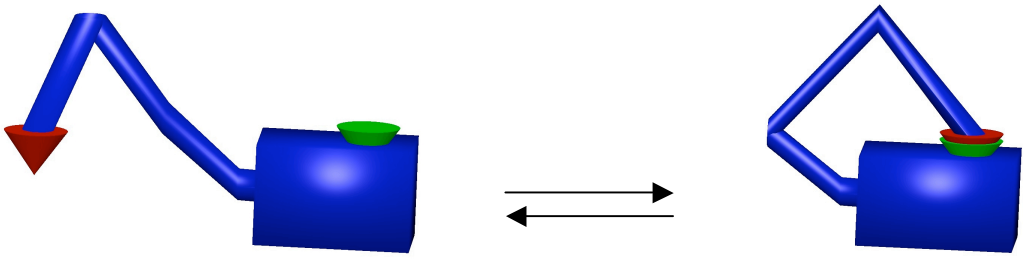

Figure 7: in a scorpionate, whether the head is, or is not, bound to the head, it does not leave its proximity.

IV. Examples of artificial molecular machines

IV.1. Machines based on donor-acceptor interactions

IV.1.a. Hydrogen-bond interactions

Supramolecular chemistry has been developed due to the discovery of crown ethers, cryptands and spherands and their ability to bind alkali and ammonium ions.[63] In the particular case of ammonium, the interactions responsible for the binding to the polyether cycle were shown to be hydrogen bonding. The complementarity between dialkylammonium ions and crown ethers is a logical development that led to the synthesis of rotaxane structures.[51] If a base is added to such an assembly, the ammonium is deprotonated and the resulting secondary amine is only weakly interacting with the crown ether. Based on this principle, Stoddart *et al* developed a pH-driven molecular shuttle with a rotaxane geometry.[37] The ring of the rotaxane is composed of dibenzo-24-crown-8 and the axle is composed of two different positions: a dibenzylammonium group

interacting strongly with the ring and a bipyridinium station ($Bpym^{2+}$) interacting only weakly. The addition of a base leads to deprotonation of the ammonium ion, which results in the displacement of the ring towards the $Bpym^{2+}$ moiety. Addition of triflic acid reprotonates the secondary amine, leading to the reverse motion of the ring and recovery of the initial state (see Scheme 1).

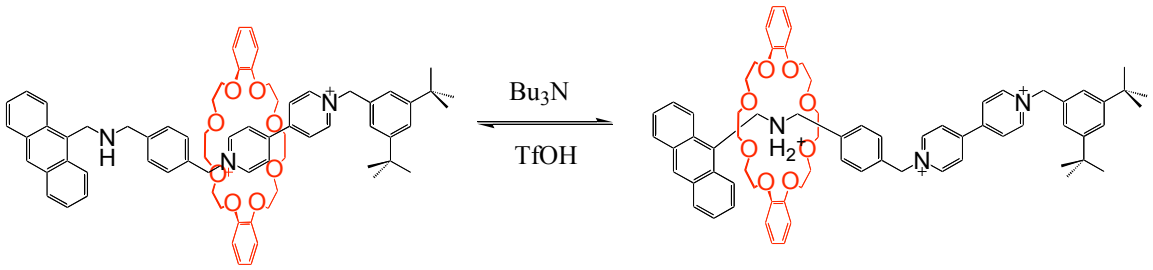

Scheme 1: pH-driven molecular shuttle based on hydrogen bonding.

IV.1.b. Charge transfer interactions

The group of Fraser Stoddart has also used charge transfer donor-acceptor interaction in order to realise a controlled motion at the molecular level.[40, 64, 65] The interaction between the tetrathiafulvalene unit (TTF) and cyclobis(paraquat-p-phenylene) ring ($CBPQT^{4+}$) is high because of the electron-richness of TTF and electron-deficiency of $CBPQT^{4+}$. Upon oxidation, TTF becomes a +2 species, which drastically reduces its affinity towards the positively charged ring. The affinity of the 1,5-dioxynaphtalene unit (DNP) towards the ring is weaker than TTF but higher than TTF^{2+}. As a result, motion of the ring along the axle of the rotaxane quantitatively occurs, which can be unambiguously demonstrated by NMR analysis. The reverse motion is obtained by reduction of the TTF^{2+} moiety into TTF (see Scheme 2).

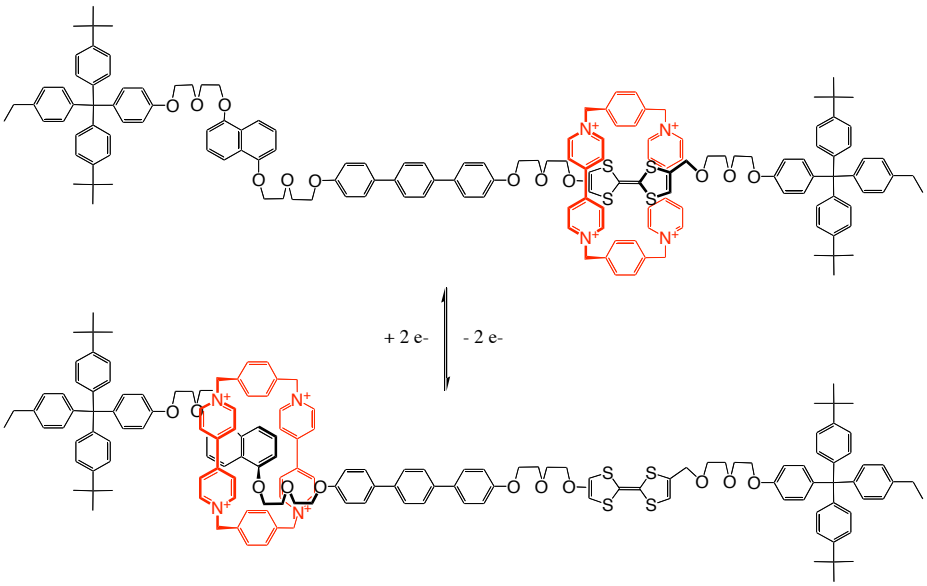

Scheme 2: a rotaxane structure built on charge transfer interactions acts like a molecular shuttle: the position of the $CBPQT^{4+}$ ring on the axle is controlled via oxidation of the TTF unit by tris(p-bromophenyl)aminium hexachloroantimonate or reduction of TTF^{2+} by zinc powder. In the most extended conformation, the distance between the two stations is 3.7 nm.

IV.2. Machines based on photoinduced geometrical rearrangements

IV.2.a. Cis-trans isomerisation of azobenzene

The photoreactivity of azobenzene derivatives has been used for decades to change the shape of crown ether-containing molecules. During the trans / cis UV-promoted isomerisation, the nature of the ligand (crown ether / cryptand, see Scheme 3a)[66] or the size of the cavity (Scheme 3b)[67] can be changed, which alters the affinity of the molecule for alkali metal ions. In such a process, light induces a controlled motion at the molecular level that results in a change of the macroscopic properties. Since the first publications of Shinkai *et al,* many variations on this principle have been published so far.[68, 69]

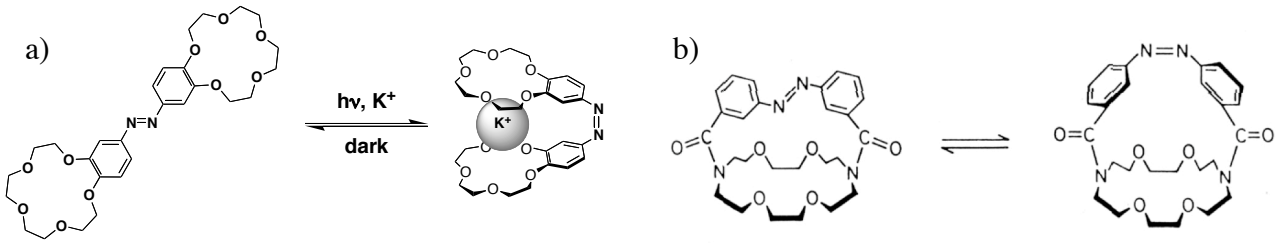

Scheme 3: photoinduced trans→cis isomerisation of a N=N double bond a) inducing a change in the affinity of the molecule for potassium ions b) changing the size of a cavity for supramolecular recognition.

IV.2.b. Cis-trans isomerisation of C=C double bonds

The isomerisation of a C=C double bond is the pendent of azobenzene photochemistry; it is also the basic mechanism responsible for the generation of a nerve impulse in vision cells when a photon is absorbed by retinal.[70]

Based on the trans-cis photoinduced geometrical change, Leigh *et al* developed a family of molecular machines relying on hydrogen bonding (see Scheme 4).[33, 71, 72] In the trans configuration, the fumaramide (E) moiety can form 4 hydrogen bonds with the H-bond donor ring, whereas the cis maleamide (Z) analogue can form only 1 H-bond. As a result, interaction with the latter is very weak and in case the double bond is isomerised by UV light absorption the ring moves towards the succinic amide ester analogue. [72] This approach was generalised by Leigh's group in the synthesis of [2]catenanes showing reversible rotation[71] and [3]catenanes showing unidirectional rotation.[33]

The group of Feringa developed a different approach. They combined highly sterically hindered alkenes and chiral information to realise a continuous, unidirectional rotation triggered by light (see Scheme 5). Three generations were designed with different temperatures and types of light.[45, 73, 74] However, they all rely on the photoinduced isomerisation of a C=C double bond, followed by thermal rearrangement of the helical molecular structure to achieve the most stable species. A complete rotation can be achieved by repeating twice the irradiation+heating reaction

scheme. The chiral nature of two sp^3 carbon atoms makes the rotation unidirectional. The last generation is the only unidirectional artificial molecular machine that continuously moves at room temperature under light irradiation.

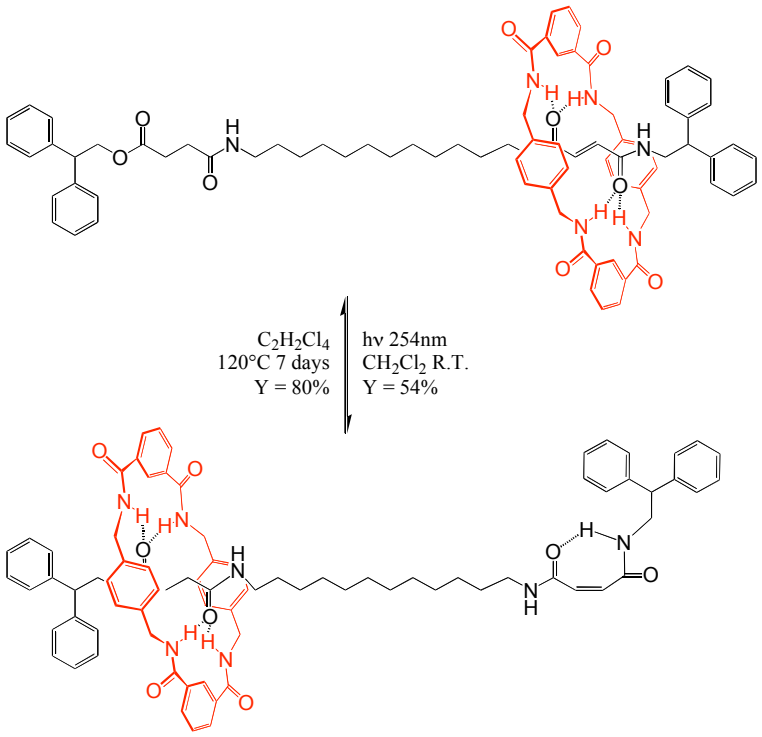

Scheme 4: Leigh's molecular shuttle based on configurational rearrangement of a C=C double bond. The photoinduced trans → cis isomerisation weakens the interaction between the ring and the double-bond containing hydrogen-bond acceptor of the axle. Heating at 120°C re-establishes the most stable trans configuration and the ring moves back to the initial position.

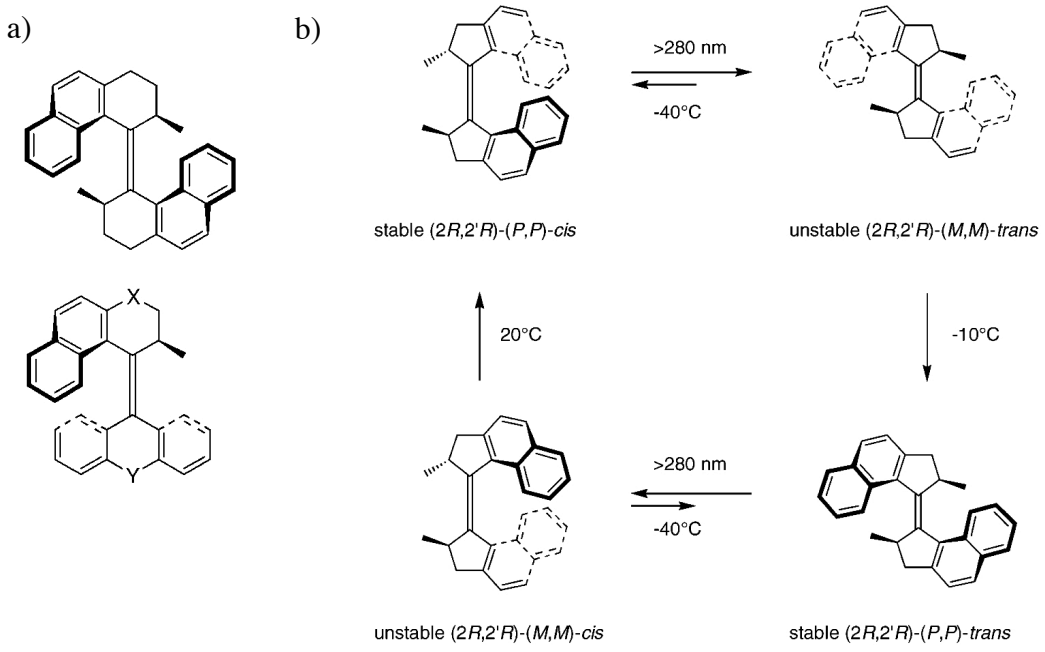

Scheme 5: a) Feringa's 1st and 2nd generation molecular rotor based on sterically hindered alkanes; b) 3rd generation is working at very low temperatures compared to the older systems, but the light used is in the UV region.

IV.3. Machines based on preferred coordination modes

IV.3.a. Cu(I) / Cu(II) redox systems

One of the pioneering works on molecular machines has developed on rotaxanes and catenanes constructed around copper. Whereas one ring of the molecule includes a single bidentate chelate, the other part (ring or axle) is composed of two different chelates linked together by flexible chains. One of these chelate is bidentate and the other terdentate, so that in combination with the ligand of the first ring the coordination number of the copper ion may be either 4 or 5. The motion comes from different preferred coordination numbers for Cu(I) and Cu(II): Cu(I) likes to be tetra-coordinated, whereas Cu(II) prefers to be pentacoordinated. As a consequence, a tetracoordinated Cu(II) complex will spontaneously rearrange to achieve a pentacoordinated environment, whereas a pentacoordinated Cu(I) complex will rearrange to achieve a tetracoordinated environment. A catenane and different rotaxanes have been synthesised with such ligands; they display reversible motion by changing the oxidation state of the copper ion (see Scheme 6). The redox transformation can be achieved by chemical, electrochemical or photochemical means.[36, 59] These systems have been optimised in term of motion speed, so that the minutes that were initially necessary for the motion to occur have turned to milliseconds.[75]

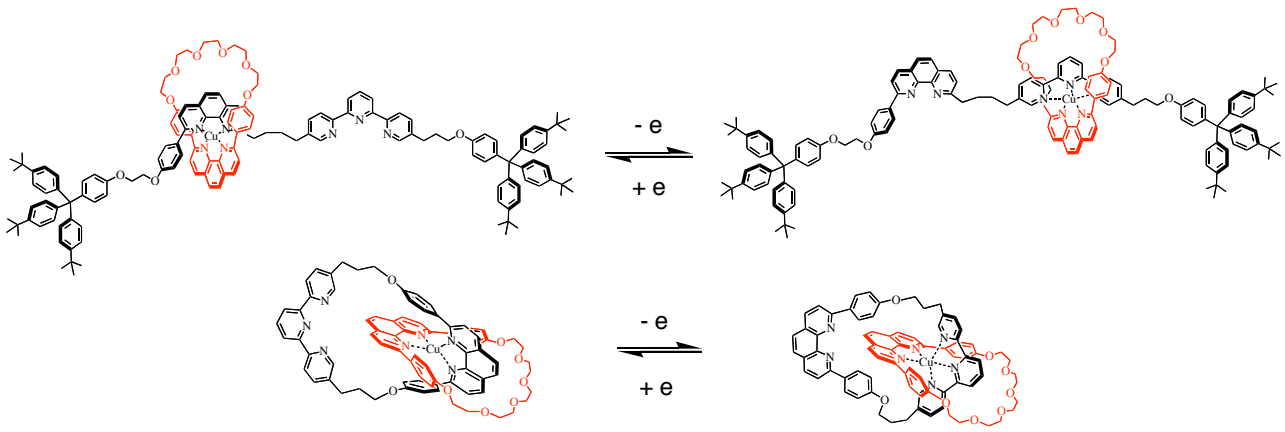

Scheme 6: a rotaxane and a catenane as molecular machines driven by electrochemical signals : in the rotaxane the ring shuttles along the axis, whereas in the catenane the mt33 ring has a flip-flop motion.

IV.3.b. An artificial molecular muscle set in motion by ion exchange

A similar approach was developed using a rotaxane dimer. A molecular axle bearing a bidentate chelate and terminated on one side by a ring bearing another bidentate chelate was synthesised. Such a molecule was dimerised by coordination to two Cu(I) ions; reaction with a stoppered terpyridine on each side of the molecule afforded a doubly interlocked rotaxane dimer.[39]

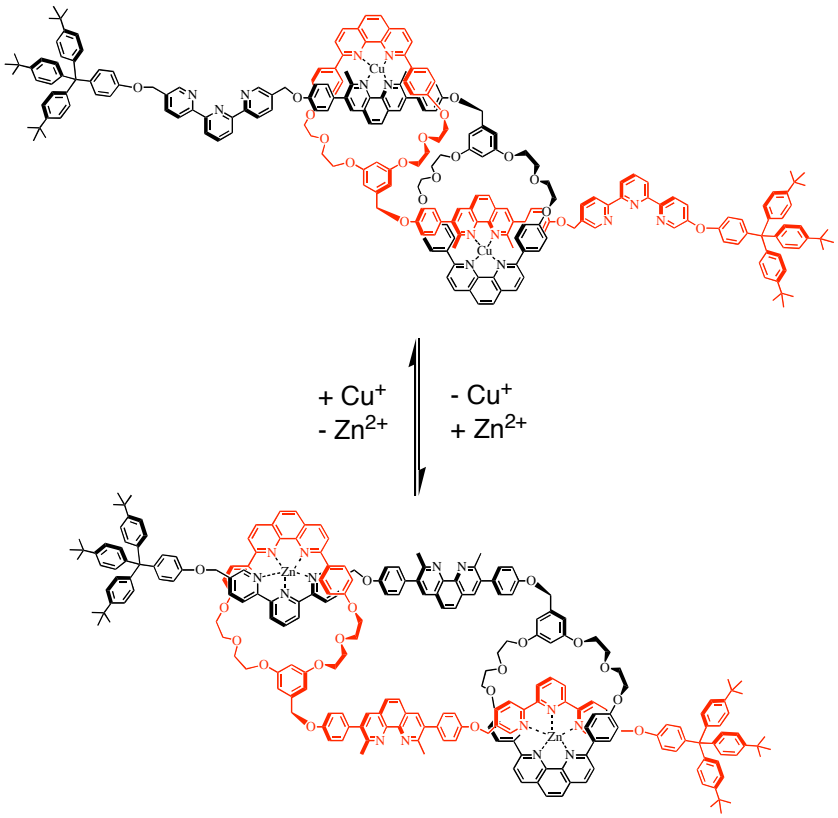

Scheme 7: an artificial molecular muscle. The motion is performed by changing the nature of the coordinated ions : Cu(I) prefers a tetrahedral environment whereas Zn(II) prefers a pentacoordinated environment. In the stretching process, the length of the molecule changes from 8.3 nm to 6.5 nm.

For mechanical and chemical reasons, oxidation of the two Cu(I) did not lead to the stretching of the molecule; however, total removing of copper and addition of zinc(II) ions led to the stretched molecule as zinc (II) prefers a pentacoordinated environment. Further addition of Cu(I) in excess led to the expulsion of zinc and coordination of copper in the initial "released" configuration where the two metal ions are tetracoordinated (see Scheme 7). This stretching-contraction motion is reminiscent of the relative translation of thin and thick filaments in myofibrils. For this reason, this system has been presented as an "artificial molecular muscle".

V. Ruthenium (II) polypyridyl complexes

V.1. Photoreactivity

Ruthenium (II) polypyridyl complexes have been known for years for their interesting photochemical properties. They generally absorb visible light due to their metal-to-ligand charge transfer bands (MLCT). The photoinduced singlet excited states (^{1}MLCT) lead through intersystem crossing to their corresponding triplet states (^{3}MLCT, see Figure 8).

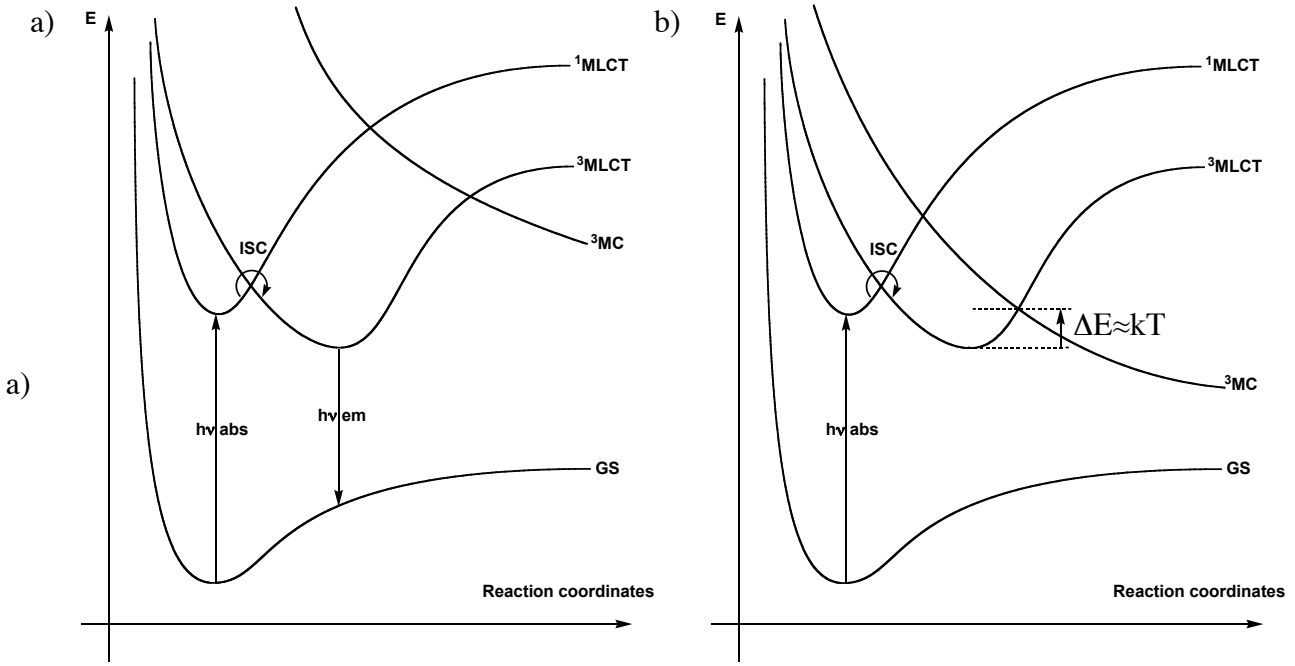

Figure 8: energy diagram for ruthenium (II) polypyridyl complexes: a) high-lying ^{3}MC states only : photoinduced ^{3}MLCT lead to fluorescence ; b) low-lying ^{3}MC state : photoinduced ^{3}MLCT lead to ligand photoexpulsion (right).

If the metal-centred triplet states (^{3}MC) are high in energy or the temperature too low (Figure 8a), this ^{3}MLCT states lead to fluorescence; this is the case in complex $Ru(phen)_3^{2+}$ for example.[76] However a ^{3}MC state may be sufficiently low in energy at a given temperature to allow its thermal population from the ^{3}MLCT states (Figure 8b). Given the antibonding character of such metal-centred excited states, expulsion of one ligand may occur. The resulting unsaturated complex reacts quickly with incoming solvent molecules in order to saturate the coordination sphere of the metal atom. The neat result of this process is a ligand photosubstitution.

The photoexpulsion step is all the more efficient, as the ^{3}MC states are low in energy. As hindered ligands decrease the ligand field and hence diminish the energy difference between e_g and π* orbitals, they have been used particularly in our group in the design of molecular machine prototypes. In the case of $Ru(phen)_2(L)^{2+}$ compelxes, L = 6,6'-dimethyl-2,2'-bipyridine (dmbp) has been successfully used (see Scheme 8):[77] the photosubstitution quantum yield in acetonitrile is relatively high (ϕ = 0.020).[42]

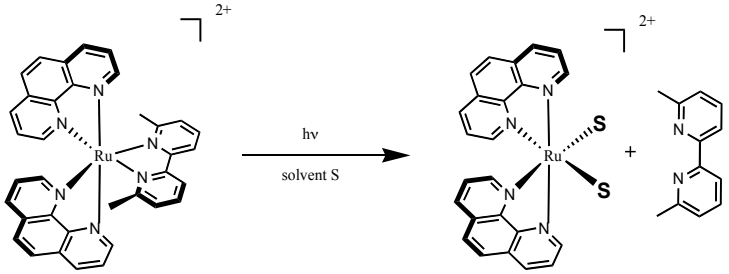

Scheme 8: photoreactivity of $Ru(phen)_2(dmbp)^{2+}$.

V.2. Template syntheses

In order to synthesise catenanes and rotaxanes including ruthenium (II) polypyridyl cores, it is necessary to use the template approach. In the case of second-row transition metals indeed, thermal and photochemical coordination chemistry are mainly governed by kinetics. The template approach enabled P. Mobian *et al* to synthesise catenanes[78, 79] and D. Jouvenot *et al* to synthesise rotaxanes.[46] In these syntheses, the $Ru(phen)_2(L)^{2+}$ moiety was included into a ring or a thread, respectively. The two phenanthrolines were covalently linked by a para-phenylene bridge in order to avoid isomerisation of the complex during photoexpulsion of the chelate.[80] The bridged phenanthrolines were then coordinated to ruthenium. For example, Scheme 9 shows one of the two ruthena-macrocycles including a complex of the $Ru(phen)_2(L)^{2+}$ family: as can be seen, the two remaining coordination sites point towards the inside of the macrocyclic cavity. This position enables the threading processes leading to catenane or rotaxane precursors.

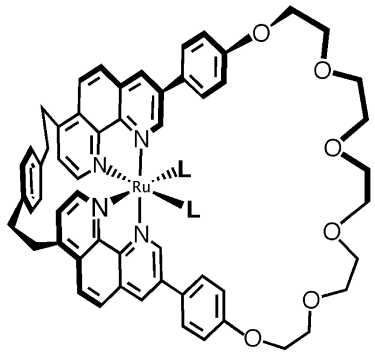

Scheme 9: ruthena-macrocycle including a $Ru(phen)_2$ core. The two monodentate sites are located inside the ring cavity.

In the case of catenanes, a modified dmbp chelate bearing terminal olefins was threaded into the ruthena-macrocycle; subsequent macrocyclisation by Grubbs catalysed olefin metathesis led to the final molecule (Scheme 10a). In the case of rotaxanes, the ring was synthesised independently of the metal, then coordinated to the ruthenium in a threading reaction before attaching the stoppers by a standard Williamson reaction (Scheme 10b). The threading and macrocyclisation steps are key points for both syntheses.

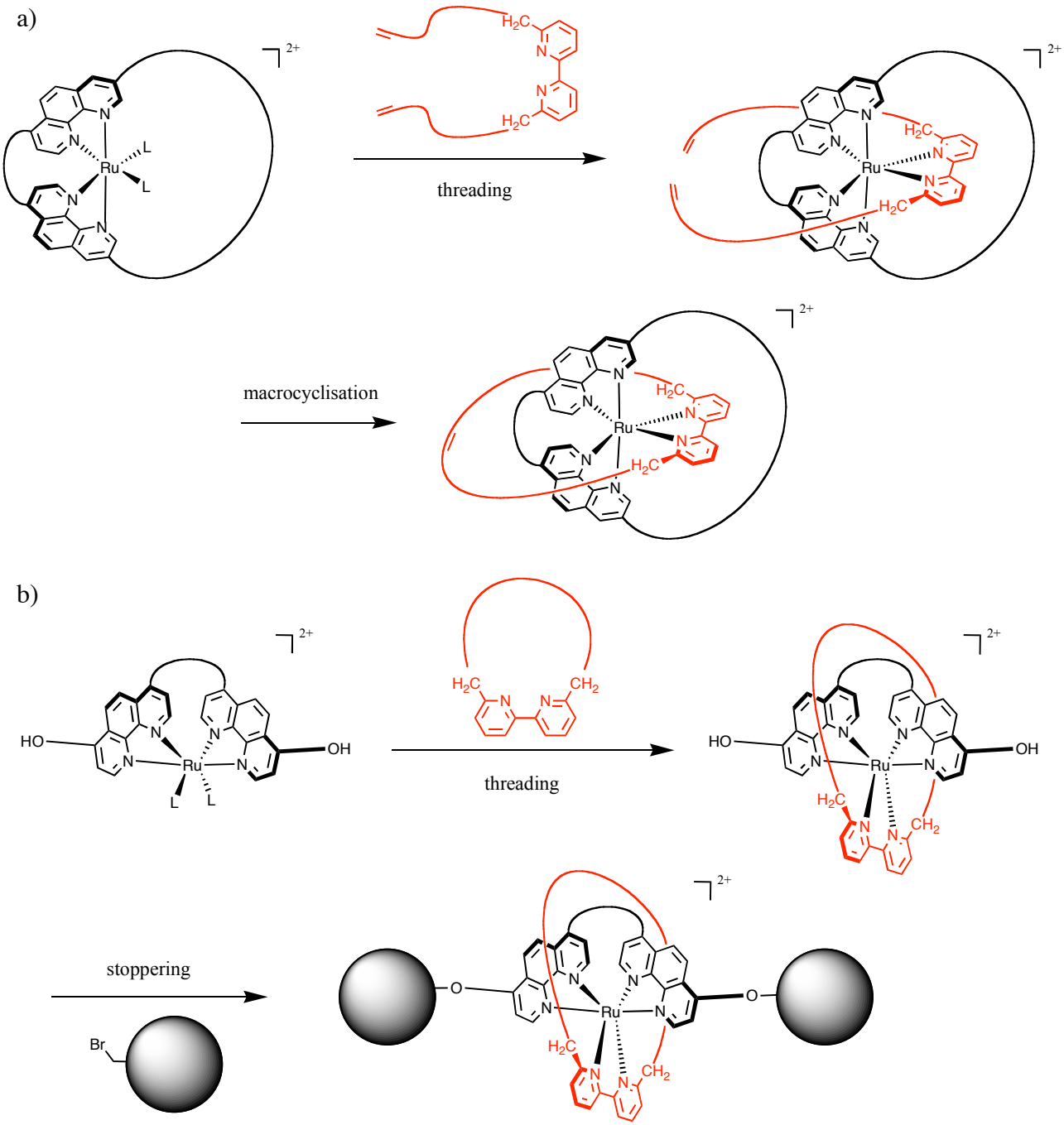

Scheme 10: synthetic strategies for the templated synthesis of catenanes (a) and rotaxanes (b) using a $Ru(phen)_2(L)^{2+}$ complex.

V.3. Molecular machine prototypes based on ruthenium (II) photochemistry

The catenane and rotaxane described above act as prototypes of molecular machines.[81] Upon irradiation of a solution of such complexes, photoexpulsion of the hindered bidentate chelate occurred, leading to the "free" species where two solvent molecules were coordinated to the two monodentate sites of the $Ru(phen)_2$ core and the chelate was uncoordinated (Scheme 11).

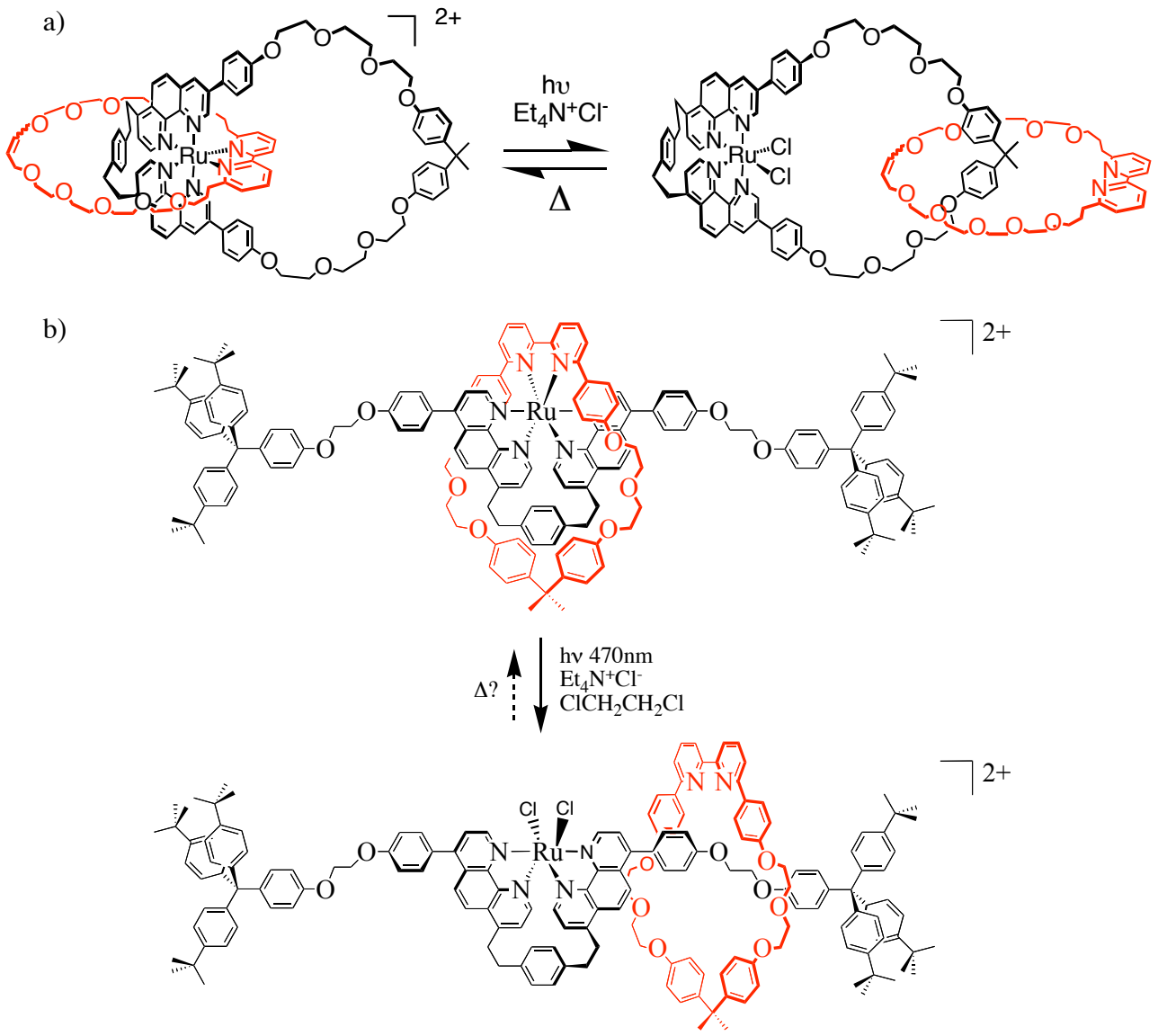

Scheme 11: molecular machines based on $Ru(phen)_2(L)^{2+}$ complexes a) catenane structure: both irradiation and thermal back-coordination are quantitative b) rotaxane structure: the back coordination step was not achieved yet for unknown reasons.

In the case of the catenane, back-coordination of the ring occurred efficiently in relatively mild thermal conditions due to the intramolecular nature of the reaction. This molecule acts thus as a prototype of molecular machine:

- a large amplitude motion at the molecular level occurs; it consists in the rotation of a ring inside another ring;
- this motion is triggered by light; thermal energy is needed both in the irradiation step (room temperature) and in the back-coordination step (higher temperature);
- the motion can be proven by UV-visible and NMR spectroscopic changes.

In the case of the rotaxane, the thermal back-coordination step was more difficult; the group is still working to enhance the efficiency of this step and explain the difference in reactivity with the

catenane. Such mechanically interlocked systems were shown to be very sensitive to steric factors.[82] The phenylene bridge used in order to block the isomerisation of the two phenanthrolines is maybe too much hindering towards the ring of the rotaxane and prevents back-coordination.

VI. Design of the project

VI.1. Drawbacks of $Ru(phen)_2(L)^{2+}$ complexes

As explained above, $Ru(phen)_2(L)^{2+}$ complexes were successfully used in the design of photocontrolled molecular machines based on catenane and, to a lesser extent, rotaxane architectures. However a few problems could not be solved in order to improve these photochemical systems:

- the back coordination step is sometimes difficult: in the case of the rotaxane it could not be realised. More generally, due to its hindering nature the dmbp chelate requires high temperatures in order to be coordinated to the ruthenium;
- it was difficult to find other bidentate chelates that would 1) be able to coordinate to the $Ru(phen)_2$ moiety 2) be photoexpelled upon visible light irradiation 3) be able to be inscribed in a molecular ring. Bis-thioether,[82] 6,6'-dianisyl-2,2'-bipyridine[82] and bis-benzonitrile[77] chelates were developed but they did not lead to significant improvements of the system.

Due to their high photochemical stability and linear geometry, $Ru(terpy)_2^{2+}$ complexes are not suitable building blocks for the design of molecular machines.[83] By contrast, $Ru(terpy)(N\text{-}N)(L)^{n+}$ complexes where L is a monodentate ligand and N-N a bidentate chelate were shown:

- to display photochemical ligand substitution reactions;[84-86]
- to have a bent geometry;[84, 87]
- to accept a wide variety of monodentate ligands with different light absorption properties.[84, 88, 89]

In our group, Anne-Chantal Laemmel proved that even with a hindered bidentate chelate like N-N = dmbp, the photoinduced ligand expulsion was selective on the monodentate ligand.[80] For these reasons, and also because of the expertise of the group in the synthesis of 1,10-phenanthroline derivatives, we began to study complexes of the $Ru(terpy)(phen)(L)^{2+}$ family (Scheme 12).

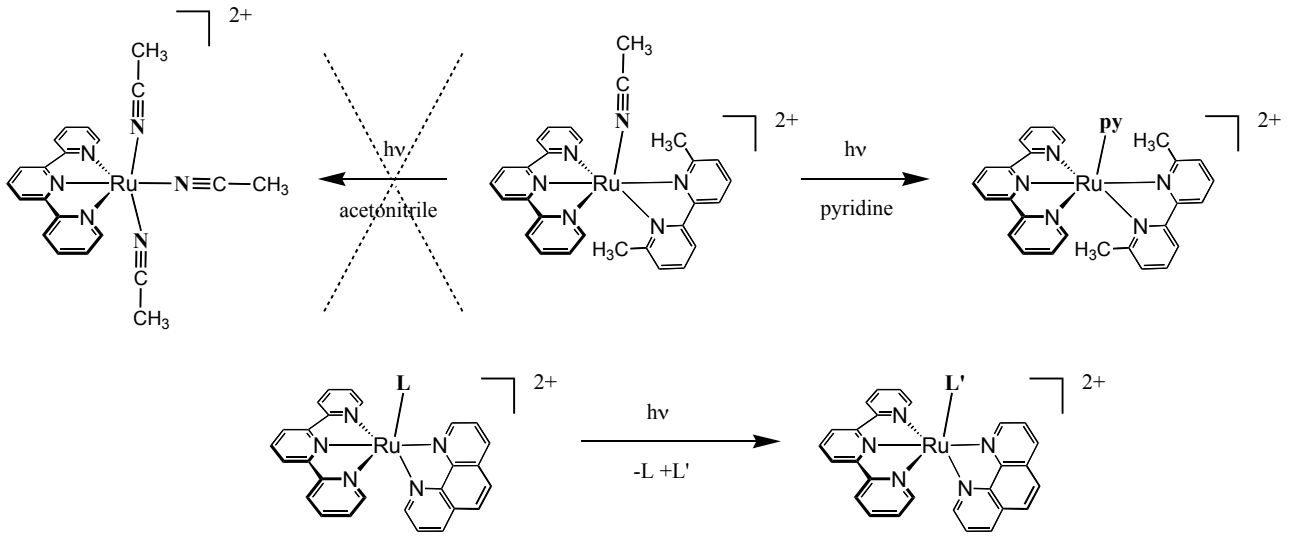

Scheme 12: a) in complex Ru(terpy)(dmbp)$(CH_3CN)^{2+}$, despite the hindered nature of the dmbp chelate irradiation leads to selective photosubstitution of the monodentate ligand, *not* to the decoordination of the bidentate dmbp; b) in the Ru(terpy)(phen)$(L)^{2+}$ family, the monodentate ligand is selectively photosubstituted.

VI.2. The work of Emma Schofield

Emma Schofield started to work with Ru(terpy)(phen)$(L)^{n+}$ complexes. She synthesised and characterised many complexes with substituted pyridine derivatives and showed the generality of the photosubstitution reaction of the monodentate ligand.[90] She showed that preparative scale photochemical reactions were a good alternative to conventional thermal syntheses. She also synthesised a scorpionate complex as the first model of a molecular machine based on a Ru(terpy)(phen)$(L)^{2+}$ reactive centre.[91] In this complex, the terpyridine was covalently linked to a benzonitrile monodentate ligand by a flexible polyether chain. An X-ray structure (Scheme 13a) showed that the benzonitrile moiety occupied the sixth coordination site on the ruthenium atom. Upon visible light irradiation in an acetone / water mixture, benzonitrile was photoexpelled and substituted by an aquo ligand (Scheme 13b). When the "open" complex was dissolved in neat acetone, the benzonitrile tail slowly replaced the aquo ligand at room temperature; two hours of reflux led to complete back-formation of the ruthena-macrocycle. These thermal conditions were very smooth, which confirmed the hypothesis that monodentate ligands were easier to coordinate than hindered bidentate chelates like dmbp.

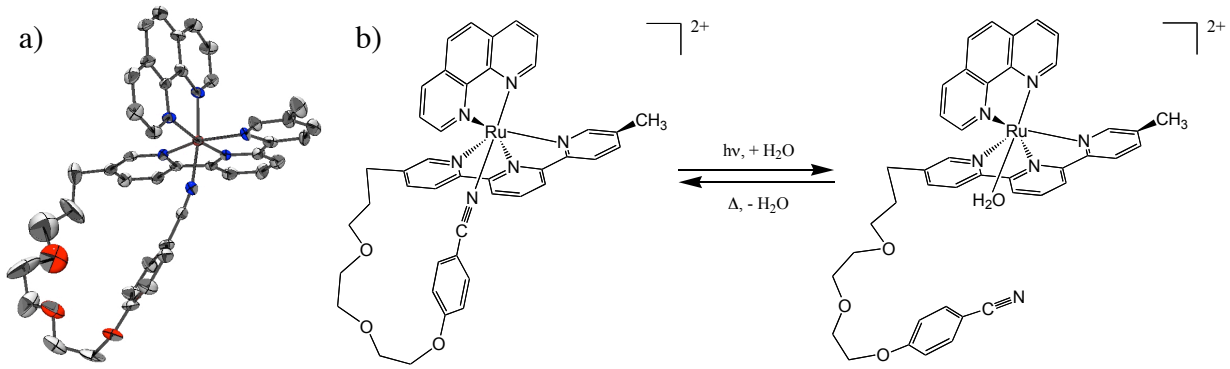

Scheme 13: a) X-ray structure of the scorpionate complex; b) photoinduced decoordination of the benzonitrile tail and thermal coordination are quantitative.

VI.3. General overview of this PhD-thesis

In Chapter 1, we extended the synthetic work of Emma Schofield by synthesising Ru(terpy*)(phen)(L)$^{n+}$ complexes with a wide variety of monodentate ligands including thioethers, sulfoxides, substituted pyridines and benzonitriles. We confirmed that all these complexes led to selective photoexpulsion of the monodentate ligand by white light irradiation. We also showed that hindering the spectator phenanthroline moiety by adding methyl groups in α position to the nitrogen atoms increased the photoreactivity of the corresponding Ru(terpy)(dmp)(L)$^{n+}$ complexes (dmp = 2,9-dimethyl-1,10-phenanthroline). We qualitatively correlated this enhanced photoreactivity to the distortion of the solid-state structures of some complexes. We also gathered experimental arguments consistent with the hypothesis of a dissociative mechanism for the photosubstitution reaction. These experimental arguments were theoretically confirmed by TD-DFT calculations made by Julien Bossert in his PhD thesis.

In Chapter 2, we extended the work of Emma Schofield on scorpionate molecules by the addition of a second monodentate ligand to the complex. By contrast however, the two monodentate ligands were attached to the phenanthroline instead of the terpyridine. As a result isomerisation of the phenanthroline became a key issue in the coordination of either one or the other ligands. We synthesised and characterised the two corresponding coordination isomers and studied the isomerisation process during irradiation at room temperature and during thermal closing of the tails.

In Chapter 3, we made the substitution pattern of the bidentate chelate dissymmetric in order to modify the isomerisation properties of the complex. Using 8-anisyl-2-mesityl-1,10-phenanthroline as the bidentate chelate, we showed that photoinduced isomerisation was quantitative and led to the isomer where the mesityl group was on the same side as the monodentate ligand. We found thermal conditions where the reverse motion was achieved and afforded the isomer where the anisyl group was on the side of the monodentate ligand.

In Chapter 4, we used this result to include the Ru(terpy)(phen)$(L)^{2+}$ moiety in a molecular ring with the monodentate ligand inside the ring cavity. The synthesis was realised on the ruthenium complex with a key cyclisation step done by olefin metathesis. Depending on the geometry of the aromatic part of the ruthenium complex, the conformation of the flexible chain was shown to vary. In this sense we realised the photoinduced control of the conformation of a flexible alkane or polyethylene glycol chain.

CHAPTER 1: SYNTHESIS OF RU(TERPY)(PHEN)(L)$^{N+}$ MODEL COMPLEXES AND LIGAND SUBSTITUTION REACTIONS

I. Introduction

In the context of photocontrolled molecular machines, ruthenium (II) polypyridyl complexes have proved to be interesting building blocks as they display clean ligand photoexpulsion reactions, provided that the triplet metal-centred dissociative state be not too high in energy. This property enabled the group of Jean-Pierre Sauvage to synthesise prototypes of molecular machines based on $Ru(phen)_2L^{2+}$ complexes where L was the hindered bidentate chelate 6,6'-dimethylbypyridine (dmbp, see General Introduction).[81] However, despite their efficient behaviour in the photoexpulsion step, these systems suffered from difficult to impossible thermal back-coordination reactions. It was also difficult to design a chelate different from dmbp that would give to its ruthenium (II) bis-phenanthroline complex the same photoexpulsion properties *but* different absorption spectra and/or thermal coordination conditions.[77]

The possibility to drive a molecular motion by selective irradiation of one or the other component would maybe lead to molecular machines purely driven by light. In order to achieve that, two main issues have to be considered 1) one needs different complexes based on the same ruthenium core but with different types of leaving ligands leading to different light absorption properties 2) the different ligands have to be able to be inscribed in one single molecular object built around the ruthenium complex. Within this frame, the monodentate nature of L in $Ru(terpy)(N\text{-}N)(L)^{n+}$ complexes (where N-N was a bidentate chelate) enabled 1) a wide diversity of available ligands L 2) an easier thermal coordination step.

In the present work, we synthesised a wide series of complexes $Ru(terpy)(phen)(L)^{n+}$ where L was a monodentate ligands. For L = unhindered pyridines, benzonitriles, acetonitrile, thioethers and sulfoxides, we verified that the monodentate ligand was selectively and quantitatively photoexpelled by visible light irradiation in their ^{1}MLCT absorption band.[90] We studied this photoexpulsion reaction and gathered experimental indications consistent with the hypothesis of a dissociative mechanism. We also showed that the quantum yield for the photosubstitution reaction was dramatically enhanced when steric hindrance of the spectator bidentate chelate was increased.[92] This enhanced photoreactivity was qualitatively correlated to the solid-state structures of some complexes. As many of the monodentate ligands we studied would easily be inscribed in more

complex molecular structures, we demonstrated the high potential of the Ru(terpy)(phen)$(L)^{2+}$ moiety as a photosensitive building block in the design of molecular machines.

II. Synthesis and characterisation of Ru(terpy*)(phen)$(L)^{n+}$ complexes

The series of complexes Ru(terpy*)(phen)$(L)^{n+}$, where L = Cl^-, H_2O, acetonitrile (AN), pyridine (PY), 3,5-lutidine (LUT), 2,6-dimethylbenzonitrile (MeBN), 2,6-dimethoxybenzonitrile (MeOBN), dimethylsulfide (DMS), dimethylsulfoxide (DMSO) and phenothiazine (PTZ, see Scheme 14 for the formulae of the ligands) has been synthesised and characterised by electrospray mass spectrometry, nuclear magnetic resonance and UV-vis spectroscopy.

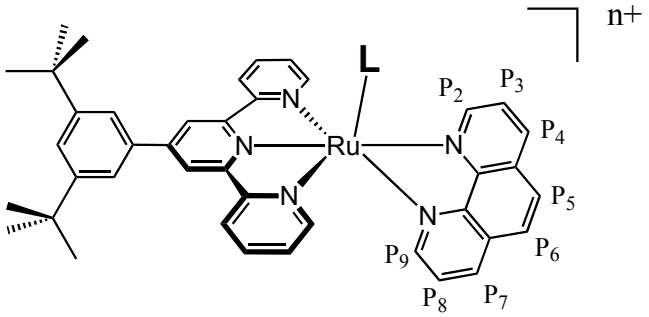

$\mathbf{1}^+$: L = Cl^- (Cl)
$\mathbf{2}^{2+}$: L = H_2O (H_2O)
$\mathbf{3}^{2+}$: L = CH_3CN (AN)
$\mathbf{4}^{2+}$: L = C_5H_5N (PY)

$\mathbf{5}^{2+}$: L = 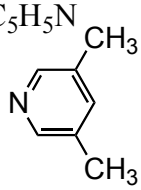 (LUT)

$\mathbf{6}^{2+}$: L = 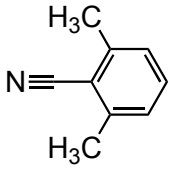 (MeBN)

$\mathbf{7}^{2+}$: L = 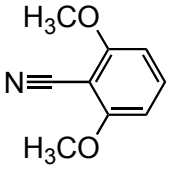 (MeOBN)

$\mathbf{8}^{2+}$: L = CH_3SCH_3 (DMS)
$\mathbf{9}^{2+}$: L = CH_3SOCH_3 (DMSO)

$\mathbf{10}^{2+}$: L = 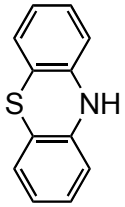 (PTZ)

Scheme 14: formulae and notations for the ligands L of the Ru(terpy*)(phen)$(L)^{n+}$ series of complexes.

II.1. Synthesis of precursors

In order to improve the solubility of the ruthenium complexes in organic solvents and hence increase the yields of all the syntheses, terpy* = 4'-(3,5-ditertiobutylphenyl)-2,2';6',2"-terpyridine[93] was used as the terdentate ligand instead of terpyridine. The classical route described in the literature[94] with 2,2';6',2"-terpyridine and 2,2'-bypyridine was used to coordinate terpy* to ruthenium trichloride, and 1,10-phenanthroline to Ru(terpy*)Cl_3. This afforded the main precursor

of the series, complex $\mathbf{1}^{+}$ Ru(terpy*)(phen)(Cl)$^{+}$. Reaction of $\mathbf{1}^{+}$ with silver tetrafluoroborate enabled the trapping of the chloride ion to yield, depending on the solvent, complexes $\mathbf{2}^{2+}$ Ru(terpy*)(phen)(OH_2)$^{2+}$ or $\mathbf{3}^{2+}$ Ru(terpy*)(phen)(CH_3CN)$^{2+}$. Scheme 15 gives the overall synthesis pattern for these precursor complexes.

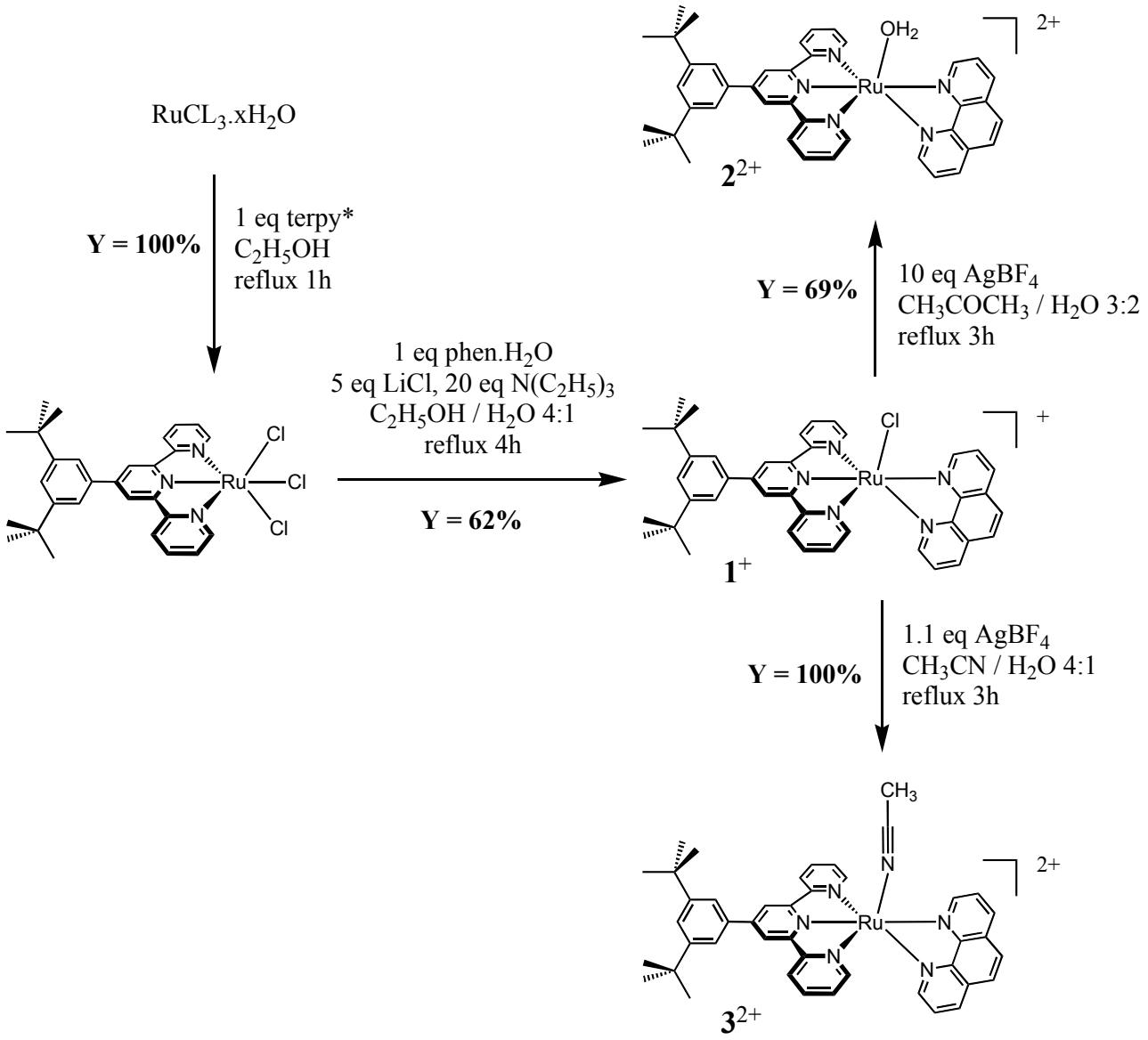

Scheme 15 : synthesis of precursor complexes $\mathbf{1}^{+}$, $\mathbf{2}^{2+}$ and $\mathbf{3}^{2+}$.

Due to the good coordination properties of acetonitrile, $\mathbf{3}^{2+}$ was also prepared in absence of silver salt but with much longer reflux duration. $\mathbf{1}^{+}$, $\mathbf{2}^{2+}$ and $\mathbf{3}^{2+}$ displayed different properties as starting materials:

- in $\mathbf{1}^{+}$ the chloride ligand can be trapped with silver, leading to the acetonate complex. As acetone is very weakly coordinated to the ruthenium, this method was efficient for the further coordination of weak or sensitive ligands at relatively low temperatures;

- water is poorly coordinated in complex Ru(terpy)(phen)$(H_2O)^{2+}$ and also very labile; however, $\mathbf{2}^{2+}$ can be purified by chromatography and well characterised, unlike the acetonate complex. As a result $\mathbf{2}^{2+}$ was the most useful starting material for the coordination of sensitive and / or weakly coordinating ligands; however, as ruthenium withdrew electron density from the oxygen atom, complex $\mathbf{2}^{2+}$ was quite acidic so that it was a bad starting material for the coordination of basic ligands like pyridines;
- in $\mathbf{3}^{2+}$ acetonitrile is relatively strongly coordinated to the ruthenium, so that this complex was not suitable for the coordination of weak ligands or ligands in low concentrations. However $\mathbf{3}^{2+}$ was not sensitive to the action of bases, so that it was the preferred starting material for the coordination of pyridines.

II.2. Thermal ligand exchange reactions

II.2.a. Reactivity

In Ru(terpy*)(phen)$(L)^{n+}$ complexes, the monodentate ligand L was thermally substituted by heating the starting material in presence of the entering ligand L'. This method afforded complexes $\mathbf{4}^{2+}$, $\mathbf{5}^{2+}$ and $\mathbf{6}^{2+}$ from starting material $\mathbf{3}^{2+}$. $\mathbf{7}^{2+}$ was synthesised by the addition of 2,6-dimethoxybenzonitrile on the acetonate solution derived from $\mathbf{1}^{+}$; $\mathbf{8}^{2+}$ and $\mathbf{9}^{2+}$, having respectively dimethylsulfide and dimethylsulfoxide as the monodentate ligand, were directly obtained from $\mathbf{2}^{2+}$. The yields of these thermal syntheses were good to quantitative (see Table 1).

Precursor	Complex	Conditions	Coordinated ligand L'	Yield
$\mathbf{3}^{2+}$	$\mathbf{4}^{2+}$	neat pyridine, reflux 2h	PY	100%
$\mathbf{3}^{2+}$	$\mathbf{5}^{2+}$	neat 3,5-lutidine, reflux 2h	LUT	88%
$\mathbf{3}^{2+}$	$\mathbf{6}^{2+}$	10 eq of L' in acetone, reflux 15h	MeBN	68%
$\mathbf{1}^{+}$	$\mathbf{7}^{2+}$	1) $AgBF_4$ excess in acetone, reflux 1h 2) 100 eq of L' in butanol, reflux 4h	MeOBN	67%
$\mathbf{2}^{2+}$	$\mathbf{8}^{2+}$	dimethylsulfide / ethanol 1:5, reflux 2h	DMS	100%
$\mathbf{2}^{2+}$	$\mathbf{9}^{2+}$	dimethylsulfoxide / ethanol 1:10, reflux 2h	DMSO	100%

Table 1: ligand substitution reactions in thermal conditions.

II.2.b. X-ray structures

The X-ray structures of four Ru(terpy*)(phen)$(L)^{2+}$ complexes were obtained (see Annex D for crystal data). Their ORTEP representations are given on Figure 9. The crystal structure of $\mathbf{2}^{2+}$ unambiguously proved the nature of the sixth coordinated ligand, as the water molecule was seen

neither by NMR spectroscopy nor by electrospray mass spectrometry. In the cases of $\mathbf{2}^{2+}$ and $\mathbf{6}^{2+}$, the terpyridine moiety was distorted from its ideal planar geometry. As revealed by careful analysis of the cell packing, these distortions may be due to intermolecular interactions within the crystal cell and not to intramolecular steric hindrance between the ligands. This phenomenon was already noted by Rasmussen *et al*[95] and will be more carefully discussed in Part III.

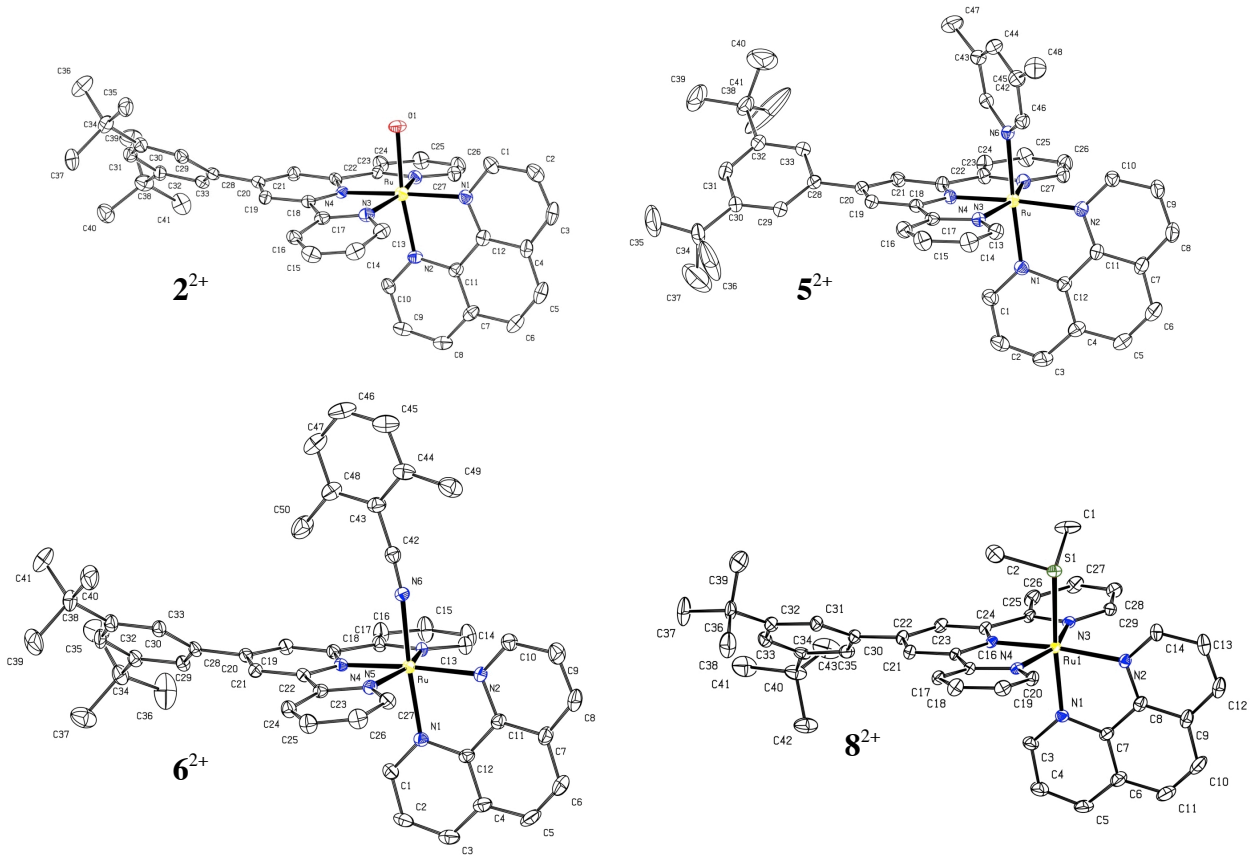

Figure 9: X-ray structures of complexes $\mathbf{2}^{2+}$, $\mathbf{5}^{2+}$, $\mathbf{6}^{2+}$ and $\mathbf{8}^{2+}$. See Annex D for crystal data.

II.2.c. Steric hindrance in Ru(terpy)(phen)(L)$^{n+}$ where L is a substituted pyridine*

L = pyridine was very efficiently coordinated in Ru(terpy*)(phen)(py)$^{2+}$, and although no crystal structure with a terpy* was obtained, the structure of Ru(terpy)(phen)(py)$^{2+}$ was already published by our group[90] and showed no distortion of the coordination sphere of the metal. As proven by the high yield and undistorted crystal structure of complex $\mathbf{5}^{2+}$, L = 3,5-dimethylpyridine did not induce any steric compression by coordination to a Ru(terpy)(phen)(L)$^{2+}$ moiety. The methyl groups in β position to the nitrogen of the pyridine point towards the outside of the complex and do not interfere with the other ligands.

By contrast, Meyer *et al* underlined the difficulty to isolate complex Ru(terpy)(bpy)(2-pic)$^{2+}$ (with bpy = 2,2'-bipyridine and 2-pic = 2-methylpyridine).[84] It seemed that the structure with one methyl group in α-position to the nitrogen of the pyridine monodentate ligand was only poorly

stable as it pointed directly into the terpyridine moiety. We confirmed this fact using 1,10-phenanthroline as the bidentate chelate: the synthesis became highly inefficient using L = 2-methylpyridine or 2,5-dimethylpyridine, and the corresponding complexes could not be isolated. Similarly, L = 2,6-dimethylpyridine was unable to coordinate and make a stable, or even detectable, Ru(terpy)(phen)(2,6-lut)$^{2+}$ complex.

This phenomenon was not observed with benzonitrile ligands, as proven by the undistorted structure of complex **6**$^{2+}$. The linearity of the nitrile group introduced additional distance that enabled methyl or methoxy groups to be present in α-position to the CN function without destabilisation of the complex.

II.3. Photochemical ligand exchange reactions

II.3.a. Absorption spectroscopy of Ru(terpy)(phen)(L)$^{n+}$ complexes*

The photoreactivity of Ru(terpy*)(phen)(L)$^{n+}$ complexes relies on their absorption bands located in the visible region between 400 and 450 nm. According to the literature,[96, 97] these bands correspond to singlet metal-to-ligand charge transfert excited states (^{1}MLCT) mainly centred on the terpyridine ligand. TD-DFT calculations done by Julien Bossert and Chantal Daniel confirmed[98] the ^{1}MLCT nature of the excited states, but they showed that the electron density moved from the metal to *both* the phen *and* the terpy ligands (see also Annex F). Table 2 gives the ^{1}MLCT absorption maxima for selected complexes.

Complexes	**Ligand L**	**λ_{MLCT} (nm) / ε_{MLCT} (x10^3 L.mol^{-1}.cm^{-1})**
1^{+}	Cl^-	516 / 13.6
2^{2+}	H_2O	487 / 12.1
3^{2+}	CH_3CN	466 / 16.0
4^{2+}	PY	487 / 13.2
7^{2+}	MeOBN	465 / 15.2
8^{2+}	DMS	473 / 11.5
9^{2+}	DMSO	431 / 14.0

Table 2: UV-vis spectroscopy data in neat pyridine (except **2**$^{2+}$ in acetone) for selected Ru(terpy*)(phen)(L)$^{n+}$ complexes.

As can be seen, the identity of the ligand at the sixth coordination site in the complex strongly influenced the position of its ^{1}MLCT absorption maximum. The corresponding wavelength experimentally increased in the order DMSO < MeOBN < DMS < PY ≈ H_2O < Cl^-. As the σ-donor properties of the monodentate ligands increased, the energy of the t_{2g} orbital centred on the

ruthenium atom increased and hence the energy needed to promote an electron from these orbitals to the π* orbitals centred on the polypyridyl ligands decreased. In addition, the π acceptor character of the ligands diminished in the series, which leads to the same consequences. Thus the DMSO ligand is the weakest σ-donor / strongest π-acceptor ligand in opposition to the chloride ion who is strongly σ-donating and even slightly π-donating.

II.3.b. Preparative scale reactions

In order to increase some of the yields obtained in thermal conditions *and* to verify the versatility of the photosubstitution ligand reaction on Ru(terpy)(phen)(L)$^{n+}$ complexes, we realised preparative syntheses of some complexes in photochemical conditions. One representative example was the white light irradiation of precursor **1**$^{+}$ in an acetonitrile / water mixture: it quickly and quantitatively yielded **3**$^{2+}$ without the need of silver (I). **3**$^{2+}$ was the basis for a great variety of photochemical preparations. Table 3 give representative examples.

Complex	Precursor	Conditions	Coordinated ligand L'	Yield
3^{2+}	**1**$^{+}$	acetonitrile / water 2:1	CH_3CN	100%
4^{2+}	**3**$^{2+}$	neat pyridine	PY	100%
10^{2+}	**3**$^{2+}$	10 eq L' in acetone	PTZ [(a)]	92%

Table 3: selected examples of preparative photosubstitution experiments. PTZ stands for phenothiazine. (*a*) Schofield[90] and Deutsch[99] showed that PTZ coordinates by its sulfur atom.

One has to note that for a given photon flux the irradiation time needed for completion of the photosubstitution experiment depended on the scale of the reaction, so that the durations of the irradiations are not given in Table 3. A typical value with a 250W slide projector and 20 mg of starting complex was 1 to 3 hours.

II.3.c. Kinetic studies by UV-vis absorption spectroscopy

In order to compare the photosubstitution reaction rates, we worked in reproducible white light irradiation conditions with a given number of moles of the starting compound (0.15 μmol). The entering ligand L' was also the solvent. The kinetics of the reactions was followed by UV-vis spectroscopy. In each case, a neat isosbestic point was observed, which showed that the ligand photosubstitution reaction was selective (see Figure 10a). As the entering ligand was in large excess, all reactions led to quantitative conversions. The plots of ln $[(A_0-A_\infty) / (A_t-A_\infty)]$ versus time were linear (Figure 10b) and the pseudo-first order rate constants k_{obs} reported in Table 4 were calculated using least-squares treatment.

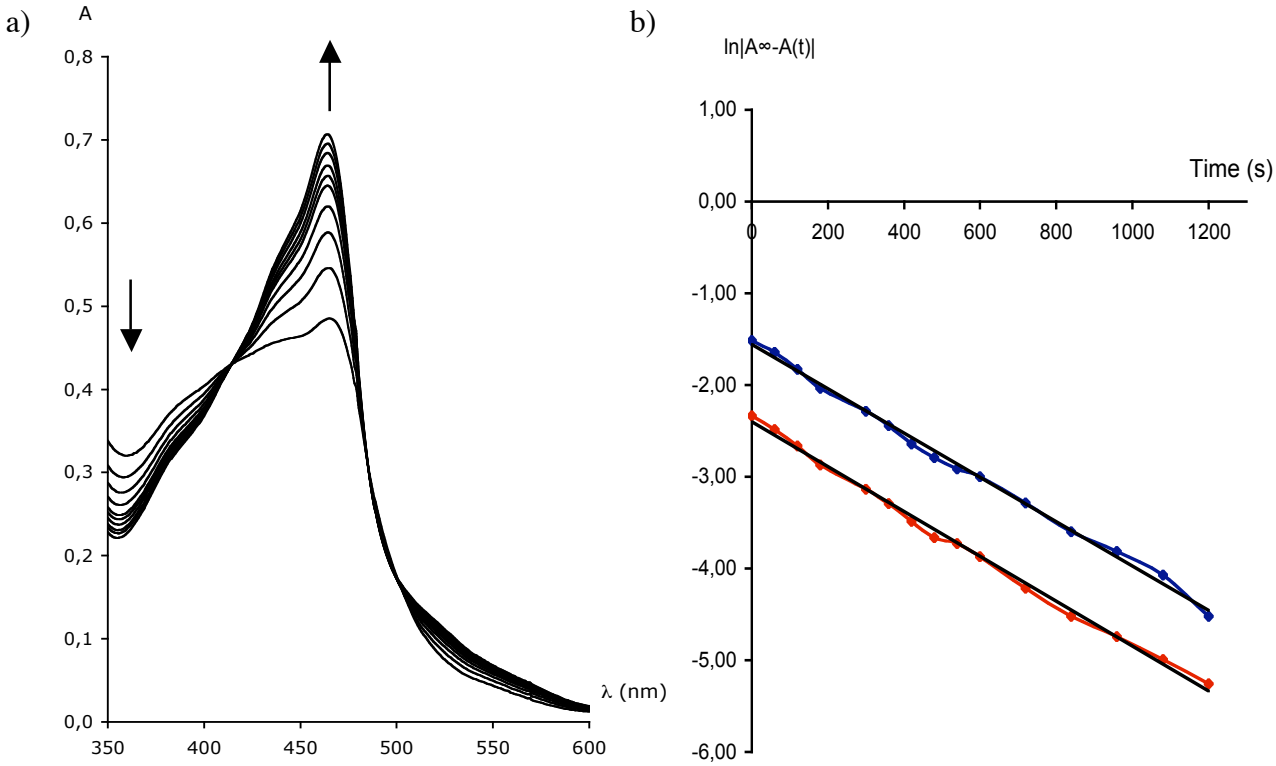

Figure 10: (a) time evolution of the UV-vis spectrum of a solution of **10**$^{2+}$ irradiated in CH_3CN (t = 0, 2, 4, 6, 8, 10, 12, 16, 20 and 32 minutes); (b) pseudo-first order treatment at the wavelengths of the disappearing (red; 359 nm) and appearing (blue; 464 nm) compounds. Both slopes were 0.0024 s^{-1} ± 0.0001 s^{-1}.

Irradiated compound	**Leaving ligand L**	**Solvent L'**	**Half-reaction time (in seconds)**	**Rate constant k_{obs} (in s^{-1})**
5^{2+}	LUT	BN	7700	0.000090
5^{2+}	LUT	DMSO	13000	0.000051
7^{2+}	MeOBN	PY	310	0.0022
7^{2+}	MeOBN	DMS	230	0.0030
7^{2+}	MeOBN	DMSO	200	0.0035
8^{2+}	DMS	BN	120	0.0059
8^{2+}	DMS	PY	210	0.0033
9^{2+}	DMSO^{i}	BN	120	0.0059
9^{2+}	DMSO^{i}	PY	120	0.0059
10^{2+}	PTZ	BN	360	0.0019
10^{2+}	PTZ	CH_3CN	290	0.0024
10^{2+}	PTZ	PY	140	0.0048

Table 4: selected ligand photosubstitution experiments followed by UV-vis spectroscopy. See Scheme 14 for the notations of the ligands. In all experiments, the concentration and irradiation conditions were kept constant (C = 5.10^{-5} M).

Two main tendencies appeared in our kinetic data:

- the photosubstitution of 3,5-lutidine by benzonitrile or DMSO were characterised by very low rate constants compared to all the other leaving ligands. The ligand field induced by coordination of a unhindered pyridine was probably very high so that in this case the ^{3}MC excited state leading to the photoexpulsion of the monodentate ligand was too far from the ^{3}MLCT state; this led to very low photoexpulsion rates;
- for other leaving ligands like thioethers, sulfoxides[100-107, *] and nitriles, the rate constant variations were small compared to the variation of the coordinating properties of the entering ligands L'. For example, complex $\mathbf{9}^{2+}$ irradiated in pyridine or benzonitrile led almost to the same photosubstitution rate constants (0.0059 s^{-1}) although pyridine was a better σ-donor than benzonitrile. This fact was consistent with the hypothesis of a dissociative mechanism in which the ligand photoexpulsion step would be rate determining. In this hypothesis, the nature of the entering ligand had only little importance as its coordination was very fast.

II.3.d. NMR studies

In some cases, the deuterated solvent was available and the ligand photosubstitution reaction was followed by NMR. The reaction was monitored due to the P_2 peak corresponding to the proton α to the nitrogen of the phen that was on the same side as the monodentate ligand L (see Scheme 1). This signal was indeed very sensitive to the nature of the coordinated monodentate ligand. To each Ru(terpy*)(phen)$(L)^{n+}$ species in solution corresponded one particular position for the P_2 signal in a region free from any other peaks (≈ 11.0 to 9.5 ppm). Table 5 give characteristic chemical shifts for representative complexes.

As L = pyridine was coordinated perpendicularly to the plane of the terpyridine, the P_2 proton was pointing directly towards the shielding cone of the monodentate ligand, leading to an upfield-shifted signal. By contrast, the phenothiazine was shown to be almost parallel to the terpyridine unit:[90] in consequence, the P_2 proton was located perpendicularly to the shielding cone of the ligand, leading to very high chemical shifts.

Figure 11 shows the evolution of the P_2 signal when complex $\mathbf{10}^{2+}$ was irradiated in CD_3CN. As can be seen, the monitoring of the photochemical reaction was easy due to the absence of any

[*] DMSO has been shown to thermally bind tu ruthenium(II) by its sulfur atom. S / O linkage isomerizations have been observed in the solid state, in polymer films and in DMSO solutions. All our irradiation experiments in solvents other than DMSO showed ligand substitution processes where the DMSO ligand was photoexpelled and replaced by a solvent molecule. See references 100-107 for informations about linkage isomerization of ruthenium (II) dimethylsulfoxide complexes.

other peak in the P_2 region. In this particular case, NMR confirmed that the phenothiazine ligand was quantitatively and selectively photosubtituted by deuterated acetonitrile.

Complex	L	δ (P2)
$\mathbf{1}^{+}$	Cl^-	10.57
$\mathbf{2}^{2+}$	H_2O	10.19
$\mathbf{3}^{2+}$	CH_3CN	10.27
$\mathbf{4}^{2+}$	PY	9.41
$\mathbf{7}^{2+}$	MeOBN	10.26
$\mathbf{8}^{2+}$	DMS	10.30
$\mathbf{9}^{2+}$	DMSO	10.67
$\mathbf{10}^{2+}$	PTZ	11.06

Table 5: chemical shifts of the P2 proton for complexes $Ru(terpy^*)(phen)(L)^{n+}$ with typical ligands L. Values are given in ppm in CD_3COCD_3.

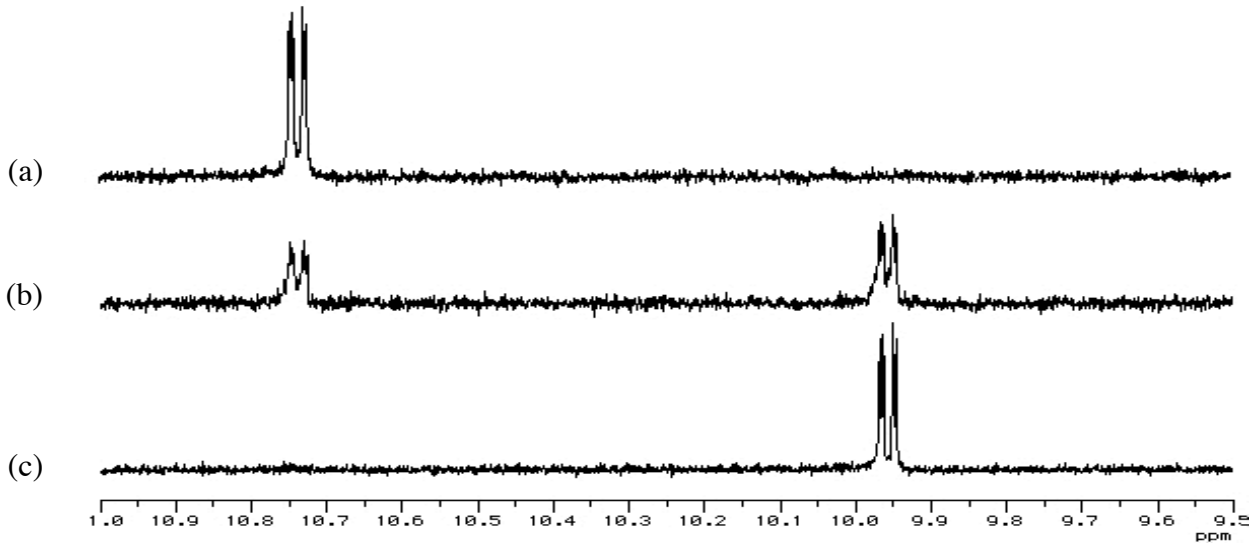

Figure 11: time evolution of the NMR spectrum of 10^{2+} in CD_3CN (a) before, (b) during and (c) after irradiation. Scale is 11.0 to 9.5 ppm (P_2 region). The final peak was characteristic for complex $\mathbf{3}^{2+}$ in CD_3CN.

III. Enhancement of the photosubstitution efficiency in $Ru(terpy^*)(N\text{-}N)(L)^{2+}$ where N-N is a diimine bidentate chelate

As already noted in Part II-1, hindered monodentate ligand like 2,5- or 2,6-dimethylpyridine did not coordinate to the $Ru(terpy)(phen)(L)^{2+}$ moiety. However, the general idea that increased steric hindrance would decrease the energy level of the ^3MC excited state and increase the photoexpulsion efficiency already led to good results with $Ru(phen)_2(L)^{2+}$ complexes (see General Introduction). In order to combine these facts, we considered putting steric hindrance on the bidentate spectator chelate of the $Ru(terpy)(phen)(L)^{2+}$ moiety. As will be demonstrated below,

substitution of hydrogen atoms by methyl groups in 2,9 position of the phenanthroline led to the expected ligand field destabilisation and quantum yield enhancement.

III.1. Synthesis of complexes with a crowded coordination sphere

The synthesis of Ru(terpy*)(dmp)(L)$^{n+}$ complexes where dmp is 2,9-dimethyl-1,10-phenanthroline followed the same route than the unhindered phen series. However, all the complexes were much more sensitive to light so that the syntheses had to be run in the dark and with lower yields. Notably complex Ru(terpy*)(dmp)(Cl)$^{+}$ could not be purified and its derivative **11**$^{2+}$ Ru(terpy*)(dmp)(CH_3CN)$^{2+}$ was used as main starting material. The complexes with L = DMSO and PTZ could not be isolated either; we suspect these ligands to be too hindering for the dmp chelate. Scheme 16 describes our synthetic results.

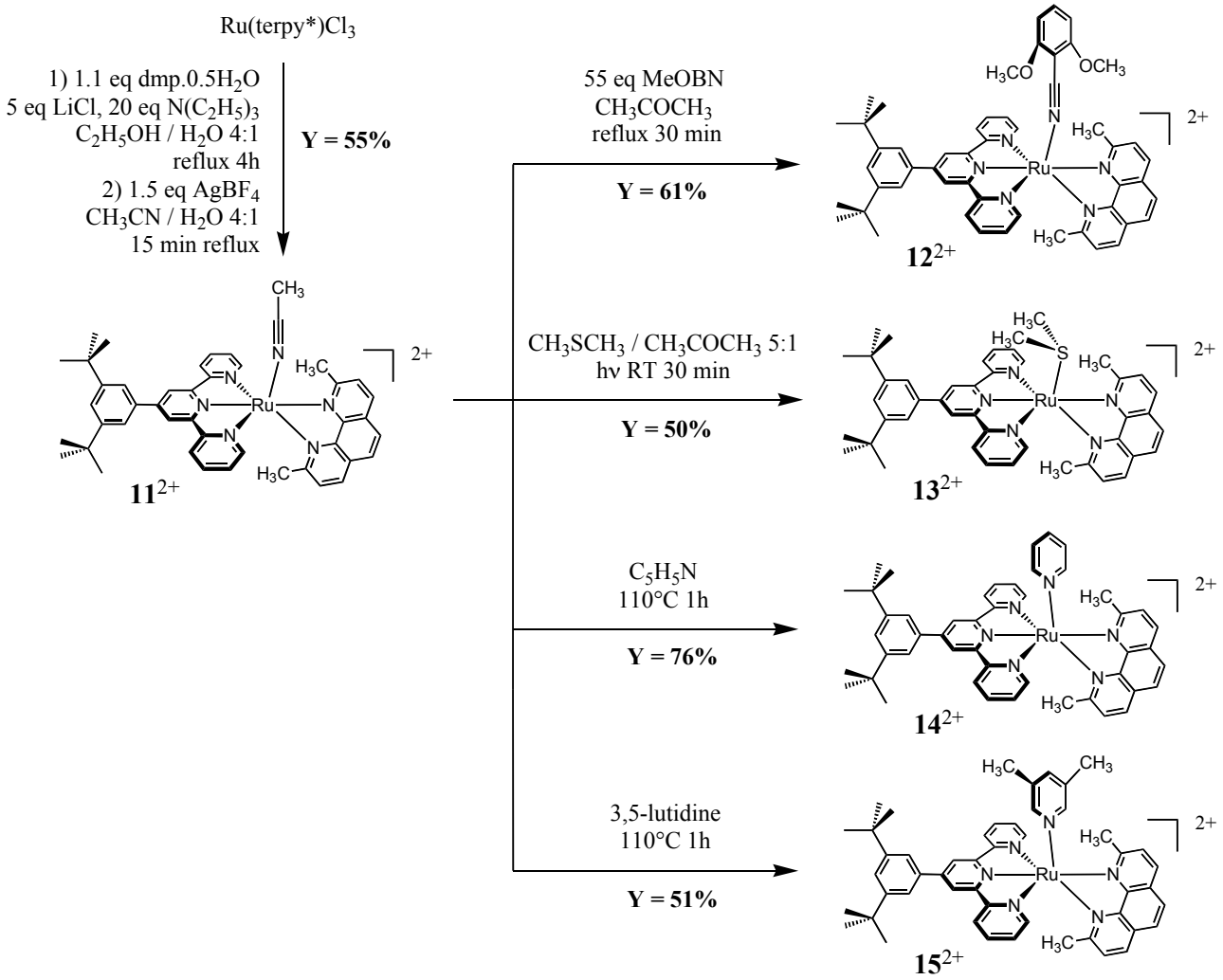

Scheme 16: synthesis of Ru(terpy*)(dmp)(L)$^{2+}$ complexes using thermal or photochemical conditions. MeOBN is 2,6-dimethoxybenzonitrile.

The crystal structures of two of these complexes were obtained and are depicted on Figure 12.

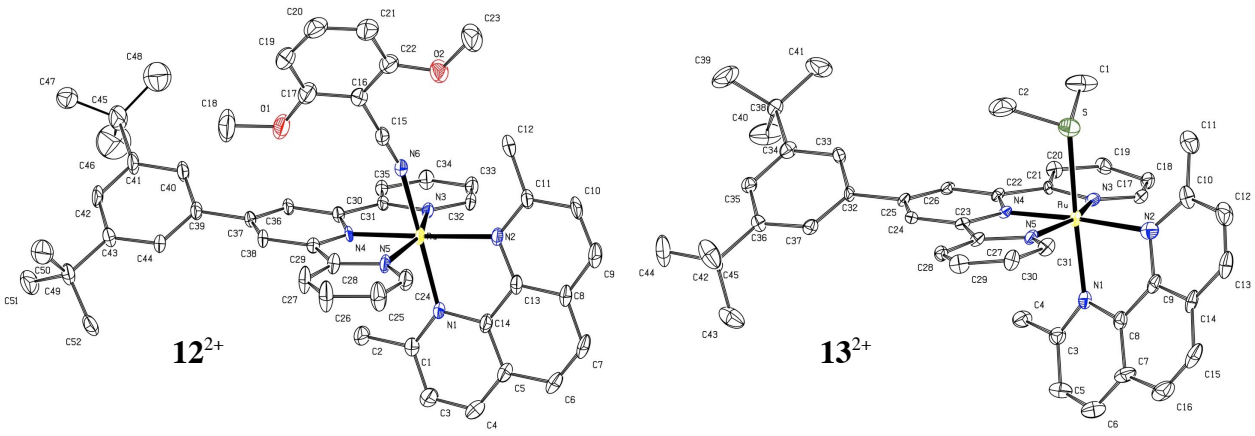

Figure 12: solid-state structures of complexes $\mathbf{12}^{2+}$ and $\mathbf{13}^{2+}$. See Annex D for crystal data.

They clearly demonstrated the nature of the coordinated monodentate ligand. They also showed that the coordination sphere was highly distorted due to the hindering methyl substituents on the dmp that bumped into the monodentate ligand L (see Part III-3).

III.2. Enhanced photoreactivity with a hindered bidentate chelate

III.2.a. Absorption spectroscopy

The dmp series of complexes Ru(terpy*)(dmp)(L)$^{2+}$ followed the same order MeOBN < DMS < PY as the phen series. A general bathochromic shift was observed for the ^{1}MLCT band of the dmp series compared to the phen series (see Table 6). The two methyl groups of the dmp increased indeed the σ-donor properties of the bidentate chelate, which reduced the energy difference between t_{2g} and π* orbitals of the polyimine chelates and hence the energy of the singlet excited state.

Complexes	**Ligand L**	**λ_{MLCT} (nm) / ε_{MLCT} (x10^3 L.mol^{-1}.cm^{-1})**
11^{2+}	CH_3CN	469 / 15.7
12^{2+}	MeOBN	467 / 12.4
13^{2+}	DMS	492 / 9.84
14^{2+}	PY	495 / 11.9
15^{2+}	LUT	496 / 12.4

Table 6: UV-vis spectroscopic data for Ru(terpy*)(dmp)(L)$^{n+}$ complexes in neat pyridine. See Scheme 14 for the notation of the monodentate ligands.

III.2.b. Kinetic studies in white light irradiation experiments

Like in the case of the phen series we investigated ligand photoinduced substitution reactions using the white light of a slide projector and the entering ligand as the solvent. In each case, a clear isosbestic point was observed and the conversion was quantitative. The first-order rate constants

were measured by the same treatment than for the phen series. The resulting rate constants k_{obs} are given Table 7.

Comparison of Table 7 and Table 4 immediately demonstrated that the photoreactivity of dmp complexes was highly enhanced compared to their phen equivalents: the first-order rate constants were multiplied by one to two orders of magnitude. We interpreted this increased reactivity as a consequence of a faster photoexpulsion step as the influence of the incoming ligand L' was small As will be discussed in Part III-3, this faster photoexpulsion step was a consequence of the destabilised coordination sphere of the ruthenium due to steric hindrance between the methyl groups of the dmp and the monodentate ligand L.

White light irradiation experiments were simple to perform and very useful for preparative purposes; however, they only led to indicative data, as far as kinetic properties were concerned. By contrast, quantitative data concerning photoreactivity required precise determination of quantum yields using a monochromator (see Annexe C).

Irradiated compound	**Leaving ligand L**	**Solvent L'**	**Half-reaction time (in seconds)**	**Rate constant k_{obs} (in s^{-1})**
11^{2+}	CH_3CN	DMS	10	0.068
11^{2+}	CH_3CN	DMSO	7.0	0.099
12^{2+}	MeOBN	PY	35	0.019
12^{2+}	MeOBN	DMSO	32	0.022
13^{2+}	DMS	BN	6.4	0.11
13^{2+}	DMS	PY	5.0	0.14
13^{2+}	DMS	DMSO	49	0.014
15^{2+}	LUT	BN	37	0.019
15^{2+}	LUT	DMSO	49	0.014

Table 7: selected ligand photosubstitution experiments followed by UV-vis spectroscopy. See Scheme 14 for the notations of the monodentate ligands. In all experiments, the concentration and irradiation conditions were kept constant ($C = 5.10^{-5}$ M).

III.3. Compared photosubstitution quantum yields and X-ray structures of selected complexes

III.3.a. Photosubstitution quantum yields

In order to better characterize the photoreactivity of complexes of the type Ru(terpy*)(N-N)(L)$^{2+}$, where N-N is a unhindered (phen) or hindered (dmp) bidentate chelate, the quantum yields of the photosubstitution reactions of L by pyridine were measured for complexes **7**$^{2+}$, **12**$^{2+}$ and **13**$^{2+}$

in neat pyridine (see Annexes B and C). McMillin *et al* published the quantum yield for the same reaction performed on the complex $Ru(terpy)(bpy)(CH_3CN)^{2+}$ but using a 1M solution of pyridine in acetonitrile as the solvent.[84] To compare our own results to this previous work, we also measured the quantum yield of the photosubstitution reaction of acetonitrile by pyridine in the analogous complex $Ru(terpy)(phen)(CH_3CN)^{2+}$ using the same solvent. Table 8 gives the quantum yields for the five complexes.

Complexes	**L**	**Solvent**	**Excitation wavelength**	**Quantum yields**
$Ru(terpy)(bpy)(CH_3CN)^{2+}$ (b)	CH_3CN	pyridine 1M in acetonitrile	464	0.0013 ±0.0001
$Ru(terpy)(phen)(CH_3CN)^{2+}$ (c)	CH_3CN	pyridine 1M in acetonitrile	464	0.0016 ±0.0002
$Ru(terpy^*)(phen)(MeOBN)^{2+}$ (**7**$^{2+}$)	MeOBN	neat pyridine	476	0.0035 ±0.0009
$Ru(terpy^*)(dmp)(MeOBN)^{2+}$ (**12**$^{2+}$)	MeOBN	neat pyridine	476	0.079 ±0.015
$Ru(terpy^*)(dmp)(DMS)^{2+}$ (**13**$^{2+}$)	DMS	neat pyridine	513	0.36 ±0.11

Table 8: Quantum yield for the photosubstitution reactions of L by pyridine. (a) all measurements were done at 25°C on PF_6^- salts ; (b) see Meyer *et al*[84] (c) prepared according to Schofield *et al*[90]

As expected, the photosubsitution quantum yield for complex $Ru(terpy)(phen)(CH_3CN)^{2+}$ was found to be very close ($\phi = 0.0016$) to the value previously reported in the case of its bipyridine analogue ($\phi = 0.0013$). Changing simultaneously acetonitrile for benzonitrile (MeOBN), terpy for terpy* and the solvent did not change significantly the order of magnitude of the photosubsitution quantum yield ($\phi = 0.0035$). However, a dramatic change was observed when, leaving all other conditions unchanged, the bidentate phen was replaced by its hindered derivative dmp. Although steric hindrance was introduced on a spectator ligand and not on the leaving monodentate ligand, once the complex was formed it was redistributed in an overall fashion within the coordination sphere of the ruthenium atom. As a result, the photosubstitution quantum yield became 22 times higher for **12**$^{2+}$ ($\phi = 0.079$) than for **7**$^{2+}$ and was even significantly higher than the photosubstitution quantum yield of the hindered chelate 6,6'-dimethyl-2,2'-bipyridine (dmbp) by two acetonitrile molecules in the complex $Ru(phen)_2(dmbp)^{2+}$ ($\phi = 0.020$). Keeping dmp as the bidentate ligand but changing L to dimethylsulfide, the quantum yield was multiplied still further by a factor of 4.5 to reach the value $\phi = 0.36$ for complex **13**$^{2+}$. This value is rather unusual for a ruthenium (II) polypyridyl complex.

Although the irradiation conditions, hence the quantitative quantum yields and first-order rate constant were different in both measurement methods, qualitative comparison led to the same reactivity order. Table 9 recalls the first order rate constants obtained in white light irradiation experiments.

Complex	**Relative rate constants k** [(a)]	**$t_{1/2}$** (s)
7^{2+}	1	310
8^{2+}	1.5	210
12^{2+}	8.9	35
13^{2+}	62	5.0

Table 9: Kinetic data of white light irradiation experiments in neat pyridine. (a) Value for complex **7**$^{2+}$: k_{obs} = 0.0022 s^{-1}

In compounds **12**$^{2+}$ and **13**$^{2+}$ the presence of methyl groups in P_2 and P_9 positions of the phenanthroline chelate (see proton assignment on Scheme 14) increased the photosubstitution rates as compared to compounds **7**$^{2+}$ and **8**$^{2+}$ by a factor 9 and 60 respectively. The more hindered situation in **13**$^{2+}$ led to the fastest reaction (k = 0.14 s^{-1}). The reaction was also performed for complex **8**$^{2+}$ and showed a moderate photochemical efficiency, between the values found for complexes **7**$^{2+}$ and **12**$^{2+}$.

III.3.b. Compared X-ray structures

We were unfortunately not able to crystallise complex **7**$^{2+}$. However the X-ray structures of complexes **6**$^{2+}$, **8** $^{2+}$, **1 2**$^{2+}$ and **1 3**$^{2+}$ were determined. Although dimethylbenzonitrile and dimethoxybenzonitrile are slightly different, they share the same coordinating group PhCN, and their complexes of the phen series did not show very different properties. As a consequence, we believe that the structure of **6**$^{2+}$ was a good model for the structure of **7**$^{2+}$.

Precise torsion angle measurements were undertaken in order to quantify steric hindrance in the four complexes. These angles are given Table 10. The "idealised values" correspond to the hypothetic non-distorted structure of a Ru(terpy*)(N-N)(L)$^{2+}$ complex where 1) the phenanthroline would be perfectly perpendicular to the terpyridine 2) both chelates would be planar 3) the Ru-L axis would be perpendicular to the plane of the terpyridine. The distortions in the real molecules can be obviously depicted by a simple look in the Ru → N4 direction (N4 is the nitrogen atom of the central pyridine ring of the terpy*).

Entry	Idealized values [a]	Experimental values			
		$\mathbf{6}^{2+}$	$\mathbf{8}^{2+}$ [b]	$\mathbf{12}^{2+}$	$\mathbf{13}^{2+}$
I	0°	*RU-N1-C5-C9* **0.75**	*RU1-N1-C11-C13 / RU2-N6-C53-C47* **2.70 / 7.07**	*RU-N1-C6-C10* **13.61**	*RU-N1-C16-C12* **23.30**
II	180°	*RU-N1-N2-C5* **179.91**	*RU1-N1-N2-C11 / RU2-N6-N7-C53* **175.72 / 174.48**	*RU-N1-N2-C6* **169.46**	*RU-N1-N2-C16* **158.14**
III	0°	*C20-N4-N5-C25* **12.37**	*C22-N4-N5-C18 / C65-N9-N10-C70* **7.93 / 0.78**	*C37-N4-N5-C26* **6.76**	*C25-N4-N5-C29* **4.95**
IV	0°	*C20-N4-N3-C15* **6.97**	*C22-N4-N3-C27 / C65-N9-N8-C60* **5.38 / 3.16**	*C37-N4-N3-C34* **10.61**	*C25-N4-N3-C19* **2.38**
V	0°	*C27-C24-C16-C13* **4.73**	*C20-C17-C26-C29 / C72-C69-C61-C58* **1.85 / 7.64**	*C24-C27-C35-C32* **1.21**	*C31-C28-C20-C17* **11.22**
VI	180°	*N6-RU-N2-N1* **179.60**	*S1-RU1-N2-N1 / S2-RU2-N7-N6* **177.24 / 178.57**	*N6-RU-N2-N1* **172.20**	*S-RU-N2-N1* **173.68**
VII	0°	*N6-RU-N2-C10* **1.34**	*S1-RU1-N2-C14 / S2-RU2-N7-C46* **4.92 / 5.95**	*N6-RU-N2-C11* **16.46**	*S-RU-N2-C10* **16.33**

Table 10: torsion angles in complexes $\mathbf{6}^{2+}$, $\mathbf{8}^{2+}$, $\mathbf{12}^{2+}$ and $\mathbf{13}^{2+}$. (a) see text ; (b) two distinct molecules in the unit cell.

Figure 13 shows four front views of the complexes: the distortion of the bidentate chelate (phen or dmp) obviously increased in the series $\mathbf{6}^{2+} < \mathbf{12}^{2+} < \mathbf{8}^{2+} < \mathbf{13}^{2+}$. We interpreted these distortions as the result of steric hindrance between the monodentate ligand and the methyl group of the dmp. This increased hindrance was higher with L = DMS than with L = MeBN / MeOBN as with the latter the bulkiness of the monodentate ligand was rejected further from the coordination sphere due to the linearity of the nitrile function.

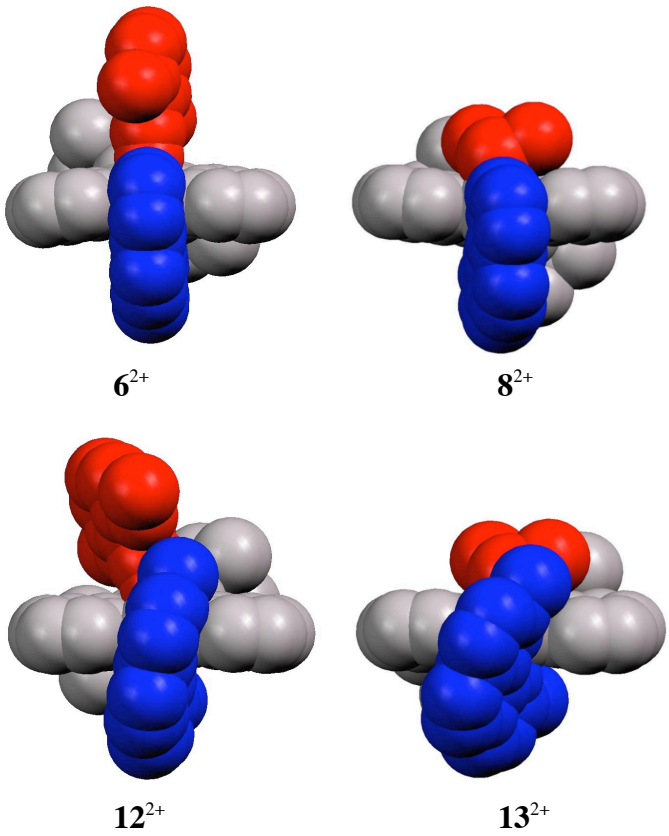

$\mathbf{6}^{2+}$ $\mathbf{8}^{2+}$

$\mathbf{12}^{2+}$ $\mathbf{13}^{2+}$

Figure 13: front view of four complexes showing the distortion of the phenanthroline moiety (in blue) due to the steric hindrance with the monodentate ligand (in red).

III.3.c. Correlations between solid-state distortions and photochemical reactivity

Within the hypothesis that the structure of $\mathbf{6}^{2+}$ modelled that of $\mathbf{7}^{2+}$, we were able to qualitatively correlate the evolution of the photosubsitution quantum yields in the series $\mathbf{7}^{2+} < \mathbf{12}^{2+} < \mathbf{9}^{2+}$ to the evolution of the torsion angles between the plane of the phenanthroline and the ideal plane perpendicular to the terpyridine in the X-ray structures. Entries I and II of Table 10 gave increasing values of 0.75 °< 13.61° < 23.30° and decreasing values of 179.91° > 169.46° > 158.14°, respectively. By replacing phen by dmp and MeOBN by DMS, the steric demand around the ruthenium centre increased because of the increasing interaction with the methyl group borne by the P2 carbon atom of the phenanthroline moiety. Doing so, the ligand field of the complex was decreased, which reduced the energy gap between the antibonding metal-centred e_g and ligand-centred π* orbitals. It cannot be excluded that ^{3}MLCT state be also affected by distortion. Overall, the photogenerated ^{3}MLCT state approached the dissociative ^{3}d-d metal-centred excited state, leading to a higher photoexpulsion efficiency.

The qualitative correlation between quantum yield values and distortion angles in the X-ray structures was generalised to the whole series of complexes $\mathbf{7}^{2+}$, $\mathbf{8}^{2+}$, $\mathbf{12}^{2+}$ and $\mathbf{13}^{2+}$ using the first-order rate constants k_{obs} obtained in white light irradiation experiments. The distortion in $\mathbf{8}^{2+}$ was indeed between the distortions observed in $\mathbf{12}^{2+}$ and $\mathbf{7}^{2+}$, which correlated the reactivity order of these three complexes (see rate constants in Table 9).

IV. **Conclusion**

In a series of four complexes of the type Ru(terpy*)(N-N)(L)$^{2+}$, substitution of hydrogen atoms by methyl groups in 2,9 positions of the bidentate chelate dramatically increased both the distortions seen in the solid-state structures *and* the photoexpulsion efficiency of the monodentate ligand. Such an increase of the reactivity was previously reported for the thermal substitution of the aqua ligand by acetonitrile in a series of Ru(terpy)(bidentate ligand)(H_2O)$^{2+}$ complexes and allowed to give a quantitative estimation of steric ligand effects for bidentate bipyridyl ligands.[108] In another work, the same group described a similar effect on *fac*-Ru(tpmm)(bidentate)(H_2O)$^{2+}$ complexes (tpmm = tris(2-pyridyl)methoxymethane).[109] For some tris chelate complexes of ruthenium(II) it was demonstrated that the photosubstitution quantum yields were closely related to the energy gap law.[110] In other cases the photoreactivity depends also on steric factors.[111] In the present study, it has been possible to correlate the photoreactivity of the complexes in solution with some characteristic dihedral angles found in the solid-state structures. The possibility of controlling the rate of photosubstitution reactions by steric adjustment could be of particular interest in the design of molecular machines based on photochemical processes.

V. Mechanistic investigations

V.1. Influence of the concentration of the entering ligand L'

In order to test the classical assumption that the photosubsitution mechanism is dissociative, it was necessary to find a poorly coordinating solvent in which the effect of the concentration of the entering ligand L' on the reaction rate could be measured. The best candidate was nitromethane: the visible spectrum of a solution of **12**$^{2+}$ in degassed $MeNO_2$ did not show any modification after 10 minutes of irradiation. De-aerated nitromethane solutions of **11**$^{2+}$ were irradiated in presence of 3,5-lutidine in excess to maintain pseudo-first order conditions. As shown by spectrophotometric monitoring, clear isosbestic points were observed in each case and the calculated rate constants were found independent of the concentration (see Figure 14).

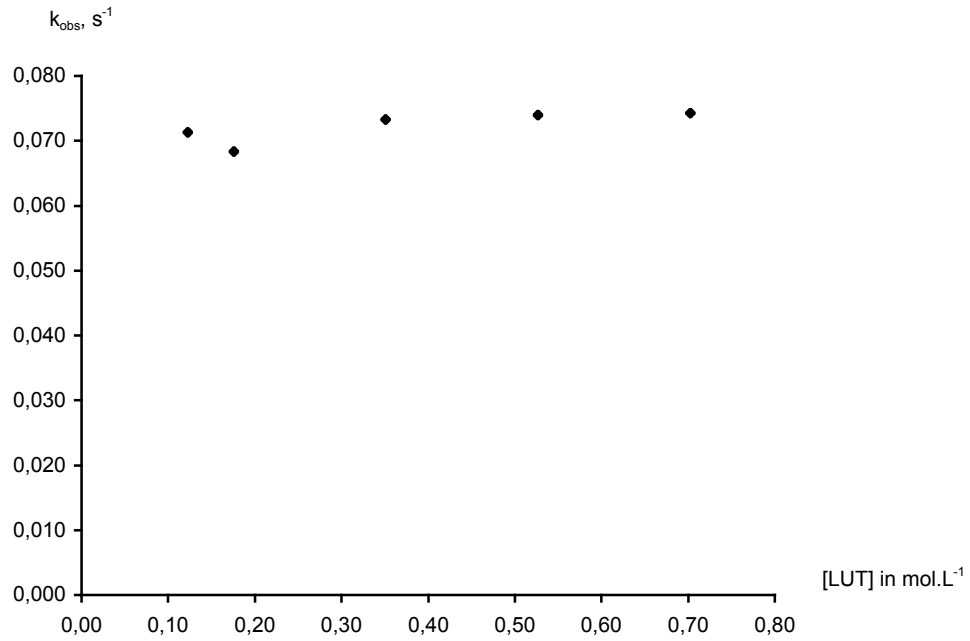

Figure 14: evolution of the pseudo-first order photosubstitution rate constant with the concentration of the incoming ligand LUT = 3,5-lutidine. Complex **11**$^{2+}$ was irradiated with white light in CH_3NO_2 at room temperature.

These results were in good agreement with the hypothesis of a dissociative mechanism for ligand photosubstitution in ruthenium (II) polypyridyl complexes with a rate-determining photoexpulsion step and a fast bimolecular coordination of the entering ligand L'.[86]

V.2. Isomerisation of the phenanthroline moiety during ligand photosubstitution

The average plane of the bidentate chelate is a symmetry element in Ru(terpy)(phen)$(L)^{n+}$ complexes. Rotation of the phenanthroline in this plane is theoretically possible, but it leads to a complex that cannot be differentiated provided that the phenanthroline be symmetric. With a dissymmetric bidentate chelate however, the two coordination isomers are different. As a consequence, the phenanthroline is theoretically able to be involved in a swinging process consisting in a 90° rotation (see Figure 15). In order to experimentally study this isomerisation process, we used as the dissymmetric bidentate chelate 4-anisyl-7-methyl-1,10-phenanthroline (aphen) synthesised by Didier Pomeranc.[112] This phenanthroline was substituted in the back of the chelate so that once coordinated no steric interactions were possible with the terpyridine or the monodentate ligand.

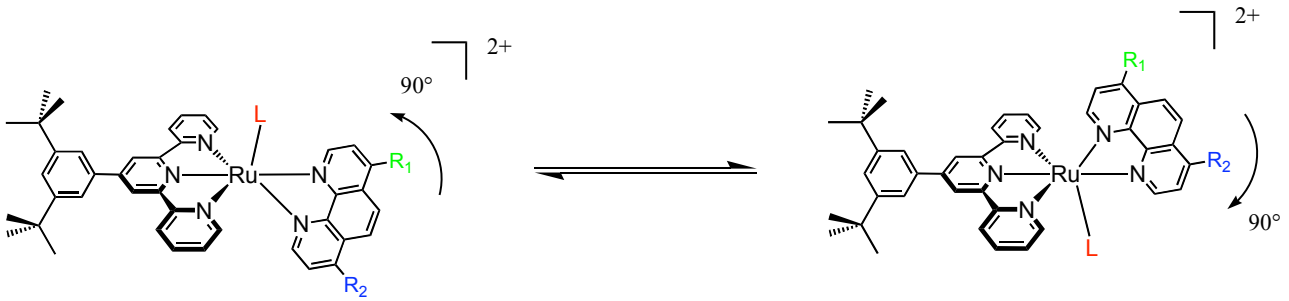

Figure 15: 90° rotation of a dissymmetric phenanthroline ($R_1 \neq R_2$) around a Ru(terpy) knee-joint.

We synthesised and purified by chromatography the two isomers **16**$^{+}$ and **16'**$^{+}$ of the complex Ru(terpy*)(aphen)(Cl)$^{+}$. Compound **16**$^{+}$ refluxed in acetonitrile / water in the dark and in presence of silver (I) gave one single compound **17**$^{2+}$ characterised as Ru(terpy*)(aphen)(CH_3CN)$^{2+}$. Isomer **16'**$^{+}$ gave in the same conditions the second isomer **17'**$^{2+}$, which proved that the isomerisation did not take place during this thermal ligand exchange reaction. However, irradiation at room temperature of a pure sample of **17**$^{2+}$ *or* **17'**$^{2+}$ in acetonitrile gave a 50:50 mixture of **17**$^{2+}$ *and* **17'**$^{2+}$ (see Scheme 17 and Figure 16). This showed that the isomerisation took place during the photochemical ligand exchange.

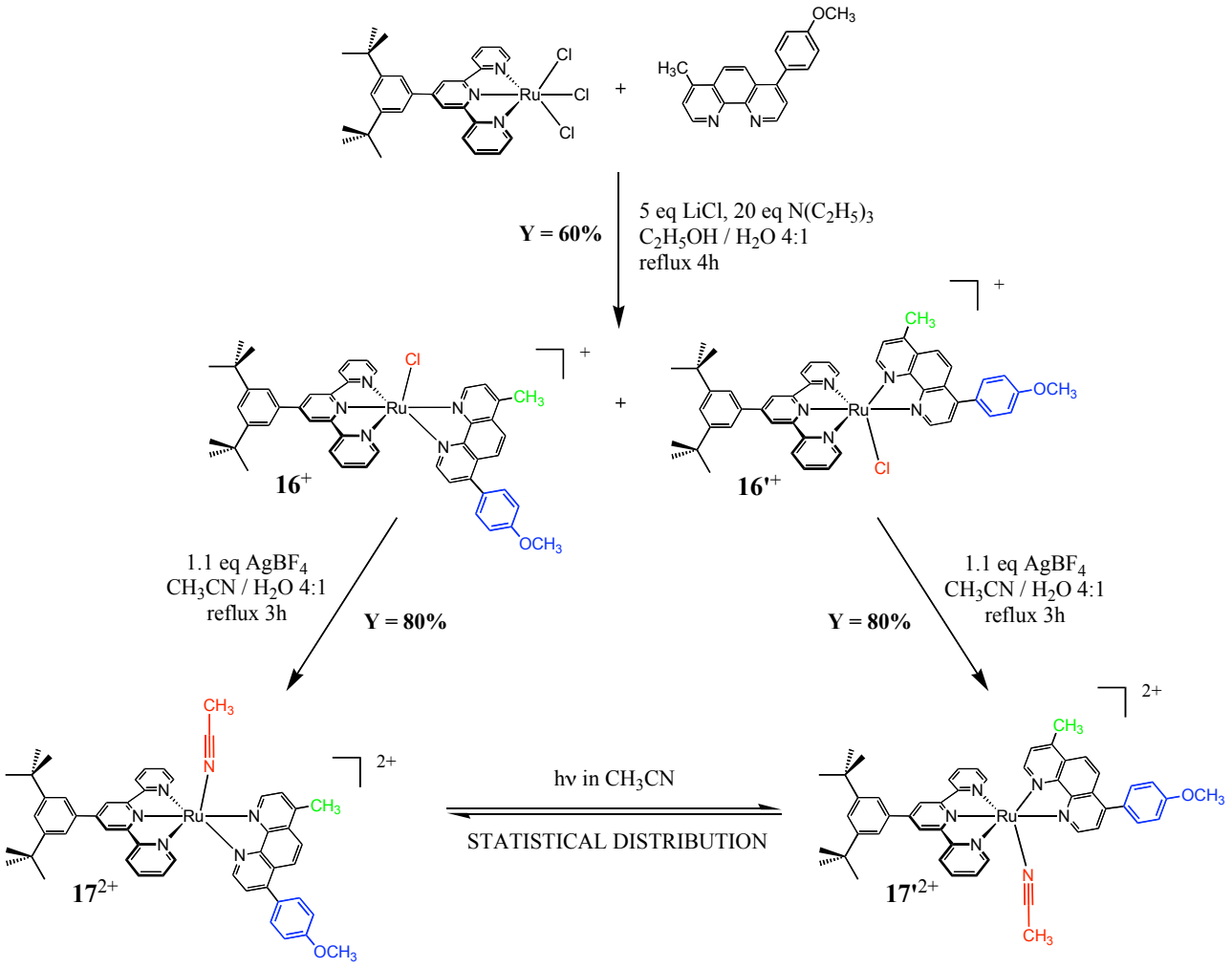

Scheme 17: thermal preparation and photochemical interconvertion of coordination isomers **17**$^{2+}$ and **17'**$^{2+}$.

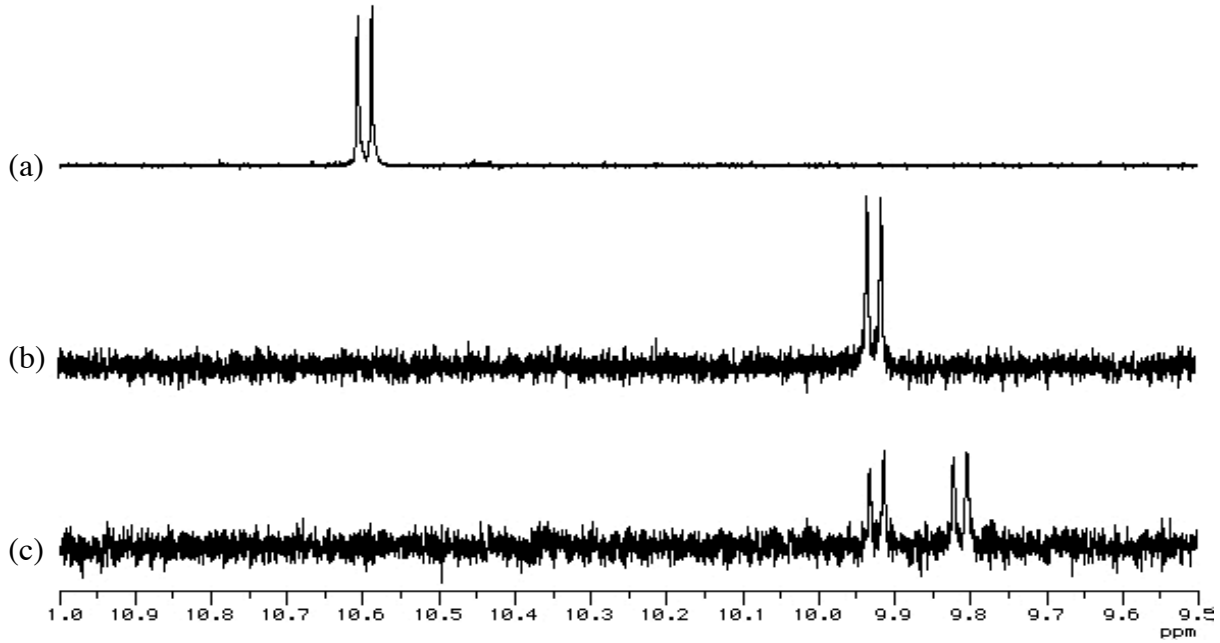

Figure 16 : (a) purified isomer $\mathbf{16}^{+}$ with L = chloride ; (b) $\mathbf{17}^{2+}$ single isomer with L = acetonitrile obtained from $\mathbf{16}^{+}$ by thermal ligand exchange reaction ; (c) statistical mixture of $\mathbf{17}^{2+}$ and $\mathbf{17'}^{2+}$ obtained by irradiation of $\mathbf{17}^{2+}$ in CD_3CN.

Such an isomerisation process was already observed by Laemmel and co-workers with other dissymmetric bidentate chelates.[80, 86] It is a strong argument that favours a dissociative mechanism for the photoinduced ligand exchange reaction. In this hypothesis, the isomerisation would take place on the transient pentacoordinated species derived from the starting complex by the ligand photoexpulsion step. The absence of dissymmetry close to the ruthenium atom on the phen would explain the final statistical distribution between the two rotational positions.

V.3. Theoretical calculations

In his PhD thesis,[98] Julien Bossert worked in collaboration with our group on $Ru(terpy)(dmp)(CH_3CN)^{2+}$ and $Ru(terpy)(dmp)^{2+}$ fragments. Both fragment were minimised using Time-Dependent Density Functional Theory.[113] The binding energy of the CH_3CN monodentate ligand was evaluated to 173 $kJ.mol^{-1}$. Minimisation of the pentacoordinated fragment $Ru(terpy)(dmp)^{2+}$ led to two different geometries:

- a dissymmetric C_s geometry directly derived from the $Ru(terpy)(dmp)(CH_3CN)^{2+}$ fragment by simple abstraction of the acetonitrile ligand, without rotation of the dmp chelate. This geometry was a local minimum and its relative stability was consistent with the hypothesis of a dissociative mechanism;
- a symmetric C_{2v} geometry where the dmp chelate had rotated of a 45° angle around the ruthenium atom. This geometry corresponded to a transition state. This transition state was much higher in energy than the C_s geometry, with an energy difference of 42 $kJ.mol^{-1}$. The

normal mode corresponding to the saddle point was consistent with the rotation of the phenanthroline with respect to the Ru(terpy) fragment.

Both C_s and C_{2v} geometries are represented on Figure 17 along with the proposed isomerisation scheme. In the case of dmp, both C_s geometries were equivalent, but such a mechanism could also explain our experimental results obtained with a dissymmetric phenanthroline (see also Chapter 2). It has to be noted that 42 kJ/mol is a very high-energy difference, which seemed to predict a slow isomerisation process.

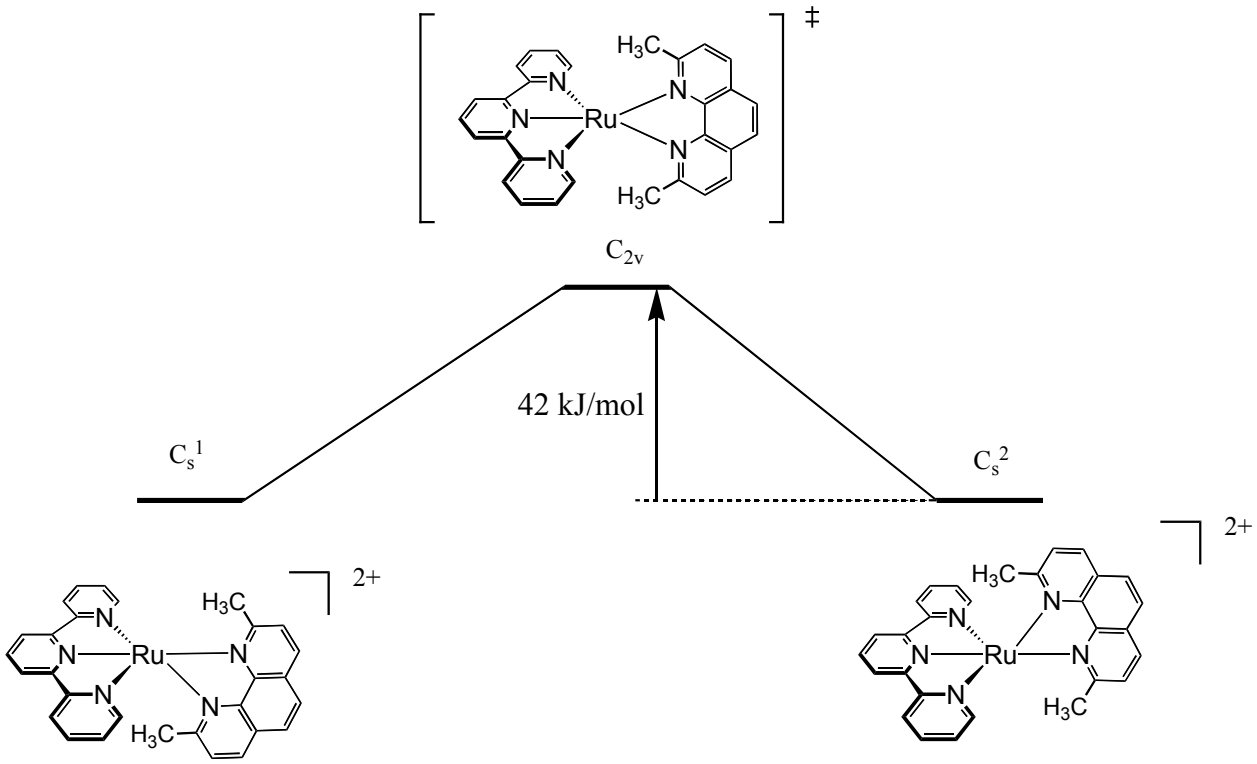

Figure 17: TD-DFT calculations on the pentacoordinated species Ru(terpy)(dmp)$^{2+}$.

V.4. Conclusion : proposed mechanism for the thermal and photochemical ligand substitution reactions

Although it is generally impossible to prove the reality of a chemical mechanism, we have gathered several experimental and theoretical results consistent with the hypothesis of a dissociative mechanism for the photochemically induced ligand substitution reaction of the monodentate ligand in Ru(terpy)(phen)(L)$^{n+}$ complexes:

- the first order reaction rates were poorly dependent on the nature of the incoming ligand used as the solvent (parts II-3 and III-2);
- the photosubstitution quantum yields were qualitatively correlated to the distortions of the solid-state structures (part III-3): the most distorted structures (hence least stable)

corresponded to the highest reactivity. As it is generally admitted that such structures are good models for the ground-state structures of the molecules in solution, it was consistent with the hypothesis of the photoexpulsion step being rate-determining;

- the apparent first order reaction rates did not depend on the concentration of 3,5-lutidine in the irradiation of $\mathbf{11}^{2+}$ in nitromethane (part IV-1);
- we observed the isomerisation of a non-hindered, dissymmetric phenanthroline chelate consistent with the existence in solution of a pentacoordinated species (part IV-2);
- theoretical calculations confirmed the local stability of this pentacoordinated species and the existence of a transition state consistent with the isomerisation process experimentally observed (part IV-3).

In such a dissociative mechanism, the first elementary step is the selective photoexpulsion of the monodentate ligand, leading to an unsaturated pentacoordinated species. This step would be rate determining. If the unsaturated species lived long enough, a rotation of the phenanthroline moiety might occur, leading to the second pentacoordinated isomer. The last step is the fast thermal bimolecular reaction between the highly reactive pentacoordinated species and an incoming monodentate ligand. This mechanism is represented Scheme 18.

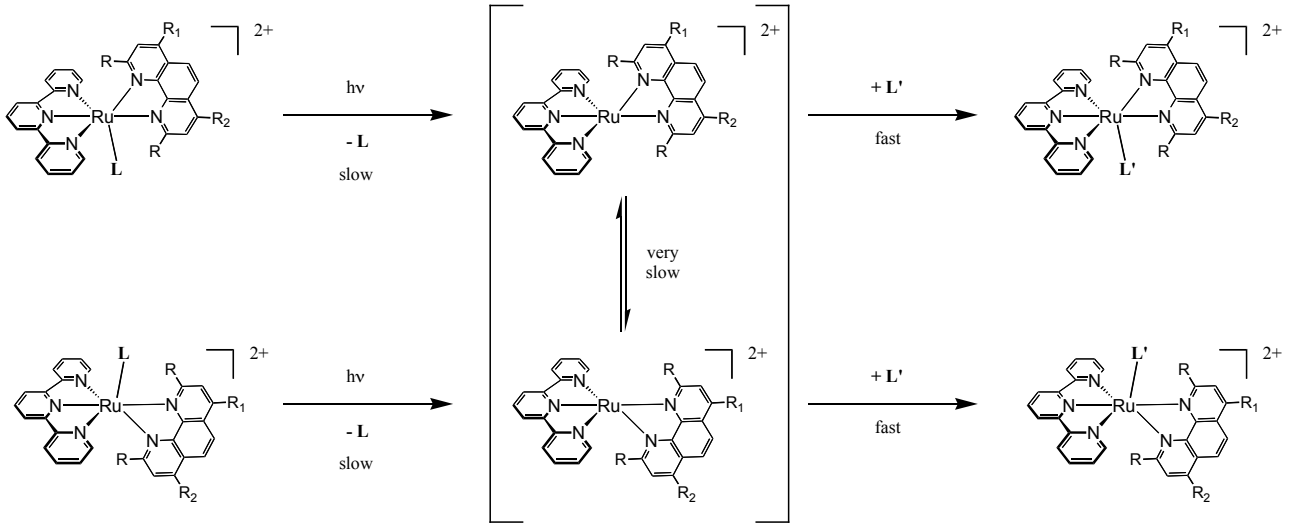

Scheme 18: postulated mechanism for the photochemically induced ligand substitution reaction. R = H or CH_3 ; R_1 and R_2 may, or may not, be different.

Considering that the isomerisation process takes place on the photoinduced pentacoordinated species at room temperature and that thermal ligand substitution performed in the dark was not followed by isomerisation, we exclude the possibility that the mechanism in thermal conditions would imply a pentacoordinated species. As a consequence, we predict an associative mechanism in thermal conditions, which consists of a single bimolecular elementary step with a heptacoordinated

transition state (see Scheme 19). Further studies need to be done in order to confirm this preliminary hypothesis.

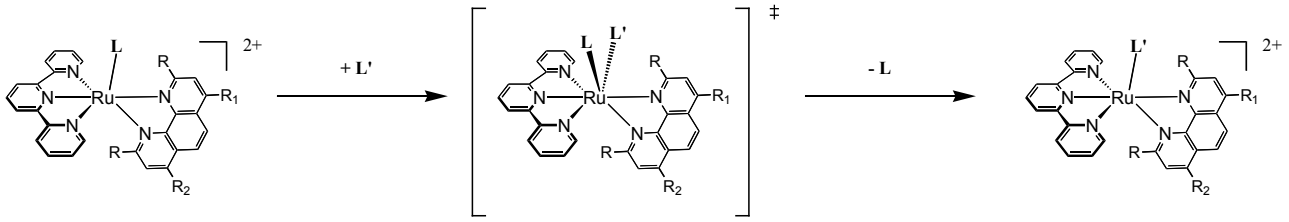

Scheme 19: postulated mechanism for the thermally induced ligand substitution reaction. R = H or CH_3 ; R_1 and R_2 may, or may not, be different.

CHAPTER 2: SYNTHESIS AND PHOTOCHEMISTRY OF A TWO-POSITION RU(TERPY)(PHEN)(L)$^{2+}$ SCORPIONATE COMPLEX.

I. Introduction

In 2001 Emma Schofield synthesised the first prototype of molecular machine based on a Ru(terpy)(phen)(L)$^{2+}$ complex.[91] It was a scorpionate molecule where an arm covalently attached to the terpyridine moiety bore a monodentate ligand L_1 at its end. The ligand L_1, a benzonitrile moiety, was shown by X-ray diffraction to be coordinated to the ruthenium atom. White light irradiation of the complex led to selective and quantitative photoexpulsion of L_1, with a consecutive opening of the ruthena-macrocycle and replacement of the benzonitrile by a solvent molecule (see General Introduction). The presence of the covalent arm enabled the monodentate ligand to stay close to the complex, which resulted in an easy back-coordination of the benzonitrile ligand to the ruthenium centre. In acetone, the thermal reaction was quantitative within one day at room temperature or two hours of reflux.

In the quest of purely light-driven molecular switches based on transition metal complexes, this work could have been continued by the addition of a second different monodentate ligand on the terpyridine moiety (Figure 18a). However, preliminary work detailed in Chapter 1, Part IV.2 led us to consider attaching these two arms on the phenanthroline moiety (Figure 18b). In this position, each monodentate ligand plays the role of a wedge that keeps the phenanthroline in one or the other position by coordination to the last site available on the Ru(terpy)(phen) core.

In this chapter we describe the synthesis and the photoreactivity of a double scorpionate complex of the type drawn on Figure 18b. The two monodentate ligands were chosen to be L_1 = benzonitrile and L_2 = dimethylsulfoxide. The model complexes **7**$^{2+}$ Ru(terpy*)(phen)(MeOBN)$^{2+}$ and **9**$^{2+}$ Ru(terpy*)(phen)(DMSO)$^{2+}$ showed indeed ^{1}MLCT absorption bands far enough from each other in the visible region (465 and 431 nm, respectively, see Chapter 1) to envisage selective irradiation experiments. These two ligands were attached by flexible “tails” made of polyether chains linked in 3,8 position of the phenanthroline by rigid phenyl linkers. The length of the polyether chains was determined on CPK models of the two isomers of the ruthenium scorpionate. Scheme 20 shows the exact chemical structures of the two forms **18**$^{2+}$ and **19**$^{2+}$ of the target molecule.

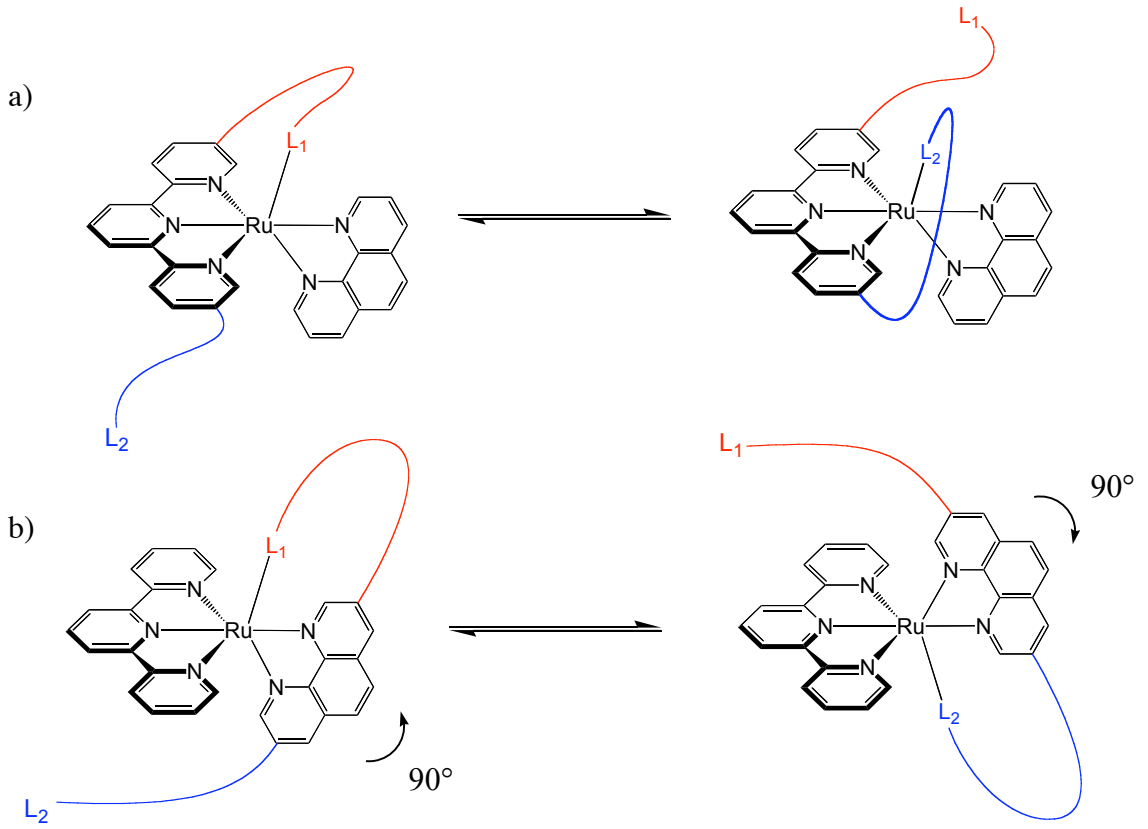

Figure 18: design of a two-position molecular switch based on linkage isomerism in a Ru(terpy)(phen)(L)$^{2+}$ complex.

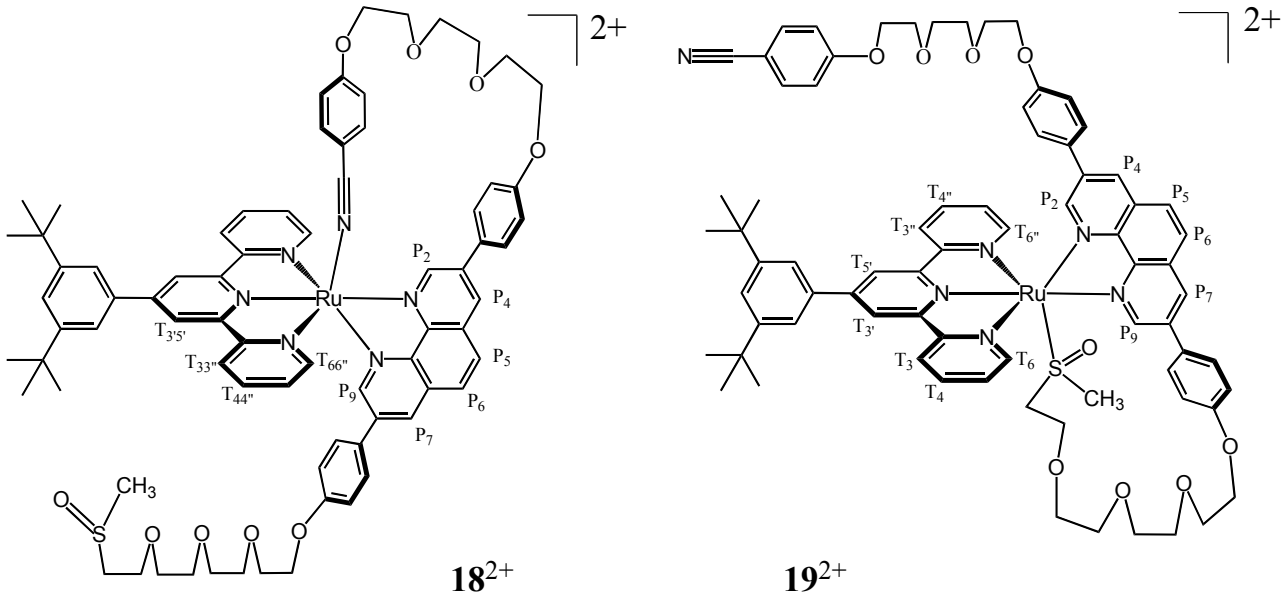

Scheme 20: the target double scorpionate molecule has two coordination isomers.

We studied the possibility to control the 90° rotation of the phenanthroline moiety around the ruthenium knee-joint by light and, hence, the conversion of one form of this complex into the other one.

II. Synthesis of the 3,8-dissymmetrically substituted phenanthroline 20

The syntheses of the two alkylbromides **20** and **21** are depicted on Scheme 21 and Scheme 22. In the synthesis of **20**, the first reaction led to an inseparable mixture of the desired benzonitrile and of the starting (2-(2-chloroethoxy)-ethoxy)ethanol. This mixture was used in the mesylation and bromination steps and 3,6-dioxa-1-bromo-8-chlorooctane could be removed by chromatography as a side-product to yield pure **20** in a 3 g scale. In the synthesis of **21**, alcohol **24** was tosylated instead of mesylated as the latter option led to a compound soluble in water, hence difficult to extract. The moderate hydrophilicity of tosylate **25** probably explains the low yield of this step. This sulfoxide chain **21** was prepared on a 700 mg scale.

The main starting material towards 3,8-disubstituted 1,10-phenanthroline is the symmetric 3,8-dibromo-1,10-phenanthroline (see Scheme 23).[114] This symmetric molecule was turned into 3,8-di(hydroxyphenyl)-1,10-phenanthroline by common literature procedures.[115]

The di(hydroxyphenyl)-phenanthroline was further reacted in a dissymmetric Williamson reaction using a statistical approach. This last key step involved an equimolar mixture of the two alkylbromides **20** and **21** bearing at their ends the two ligands L_1 (benzonitrile) and L_2 (dimethylsulfoxide). The dissymmetric Williamson reaction yielded a mixture of three phenanthrolines: the dissymmetric one **26** bearing two different ligands (L_1-phen-L_2) and two symmetric ones bearing two monodentate ligands of the same kind (**26'** = L_1-phen-L_1 and **26"** = L_2-phen-L_2). The separation of this mixture by chromatography was possible due to the higher polarity of the sulfoxide chain compared to the benzonitrile chain. The 40% isolated yield in **26** was close to the maximum value (50%). **26** was prepared on a 200 mg scale. It was characterised by ^{1}H 1D NMR, 2D COSY and ROESY and FAB mass spectrometry. ^{1}H-^{13}C HSQC and HMBC heteronuclear correlation experiments enabled complete peak attribution of the ^{13}C NMR spectrum.

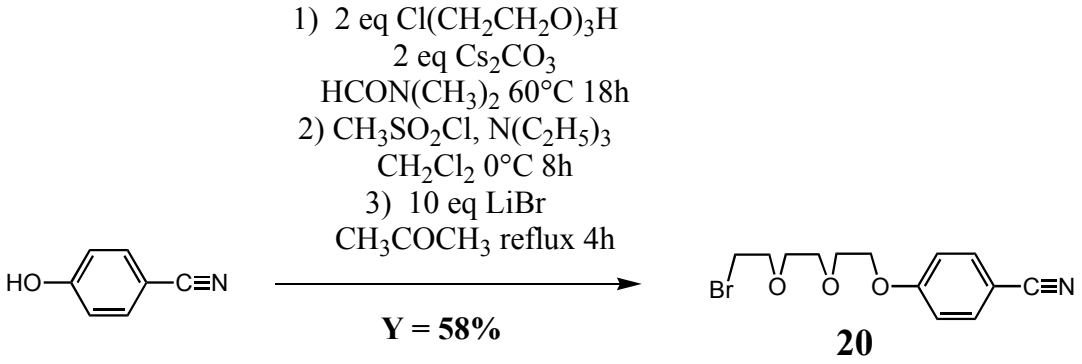

Scheme 21: synthesis of the alkylbromide chain **20** bearing a benzonitrile ligand L_1.

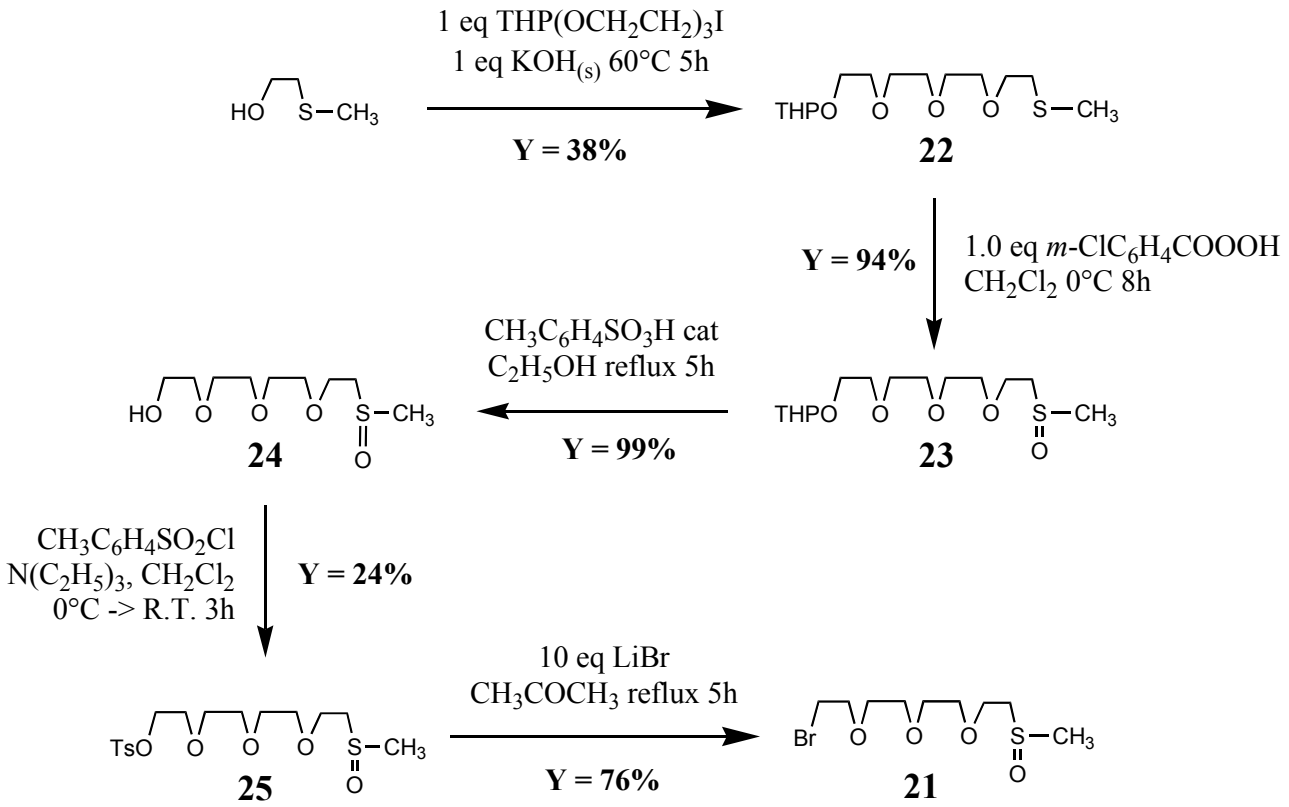

Scheme 22: synthesis of the alkylbromide chain **21** bearing a dimethylsulfoxide ligand L_2.

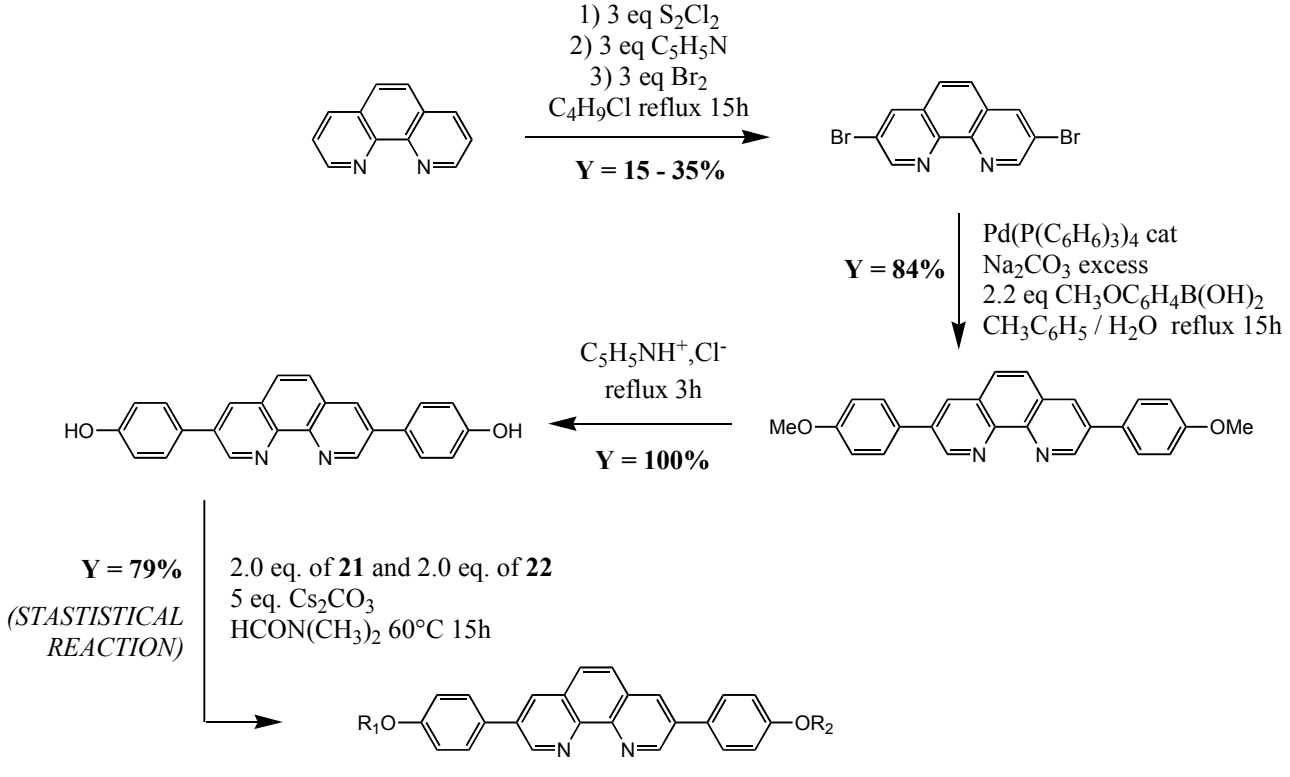

26 R_1 = -$(CH_2CH_2O)_3$-C_6H_4-CN, R_2 = -$(CH_2CH_2O)_3$-$CH_2CH_2SOCH_3$: 40%

26' $R_1 = R_2$ = -$(CH_2CH_2O)_3$-C_6H_4-CN : 19%

26" $R_1 = R_2$ = -$(CH_2CH_2O)_3$-$CH_2CH_2SOCH_3$: 20%

Scheme 23: synthesis of the dissymmetric phenanthroline **26** by a statistical approach.

III. Coordination of phenanthroline 26 to the ruthenium

As the asymmetry elements of the bidentate chelate **26** is located far from the coordinating nitrogen atoms, its coordination to Ru(terpy*)Cl_3 yielded a statistical mixture of the two chloro isomers Ru(terpy*)(**26**)$(Cl)^+$ noted $\mathbf{27}^+$ and $\mathbf{27'}^+$ (see Scheme 24). These two coordination isomers could not be separated at this stage. After removal of the chloride ion by silver (I) in acetone, we were able to isolate by chromatography two complexes noted $\mathbf{18}^{2+}$ and $\mathbf{19}^{2+}$.

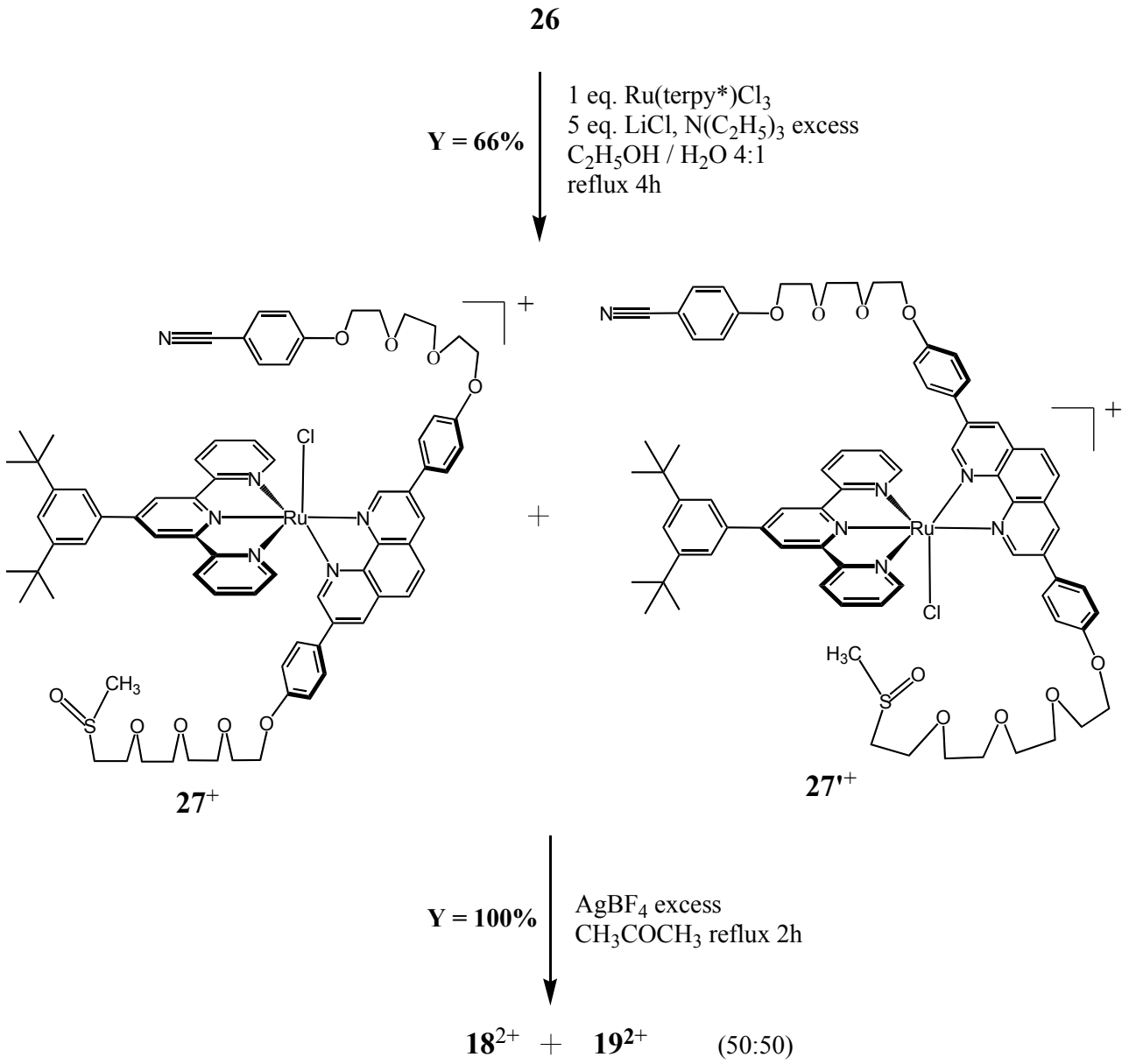

Scheme 24: synthesis of the two coordination isomers $\mathbf{18}^{2+}$ and $\mathbf{19}^{2+}$.

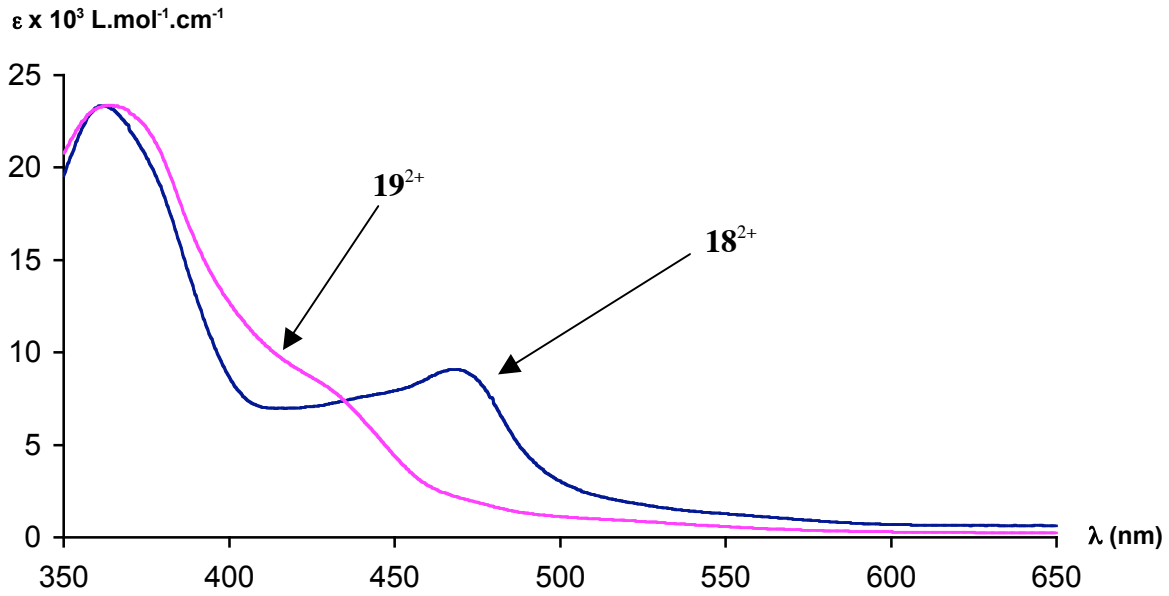

Figure 19: UV-visible spectra of $\mathbf{18}^{2+}$ (blue) and $\mathbf{19}^{2+}$ (violet) in acetone.

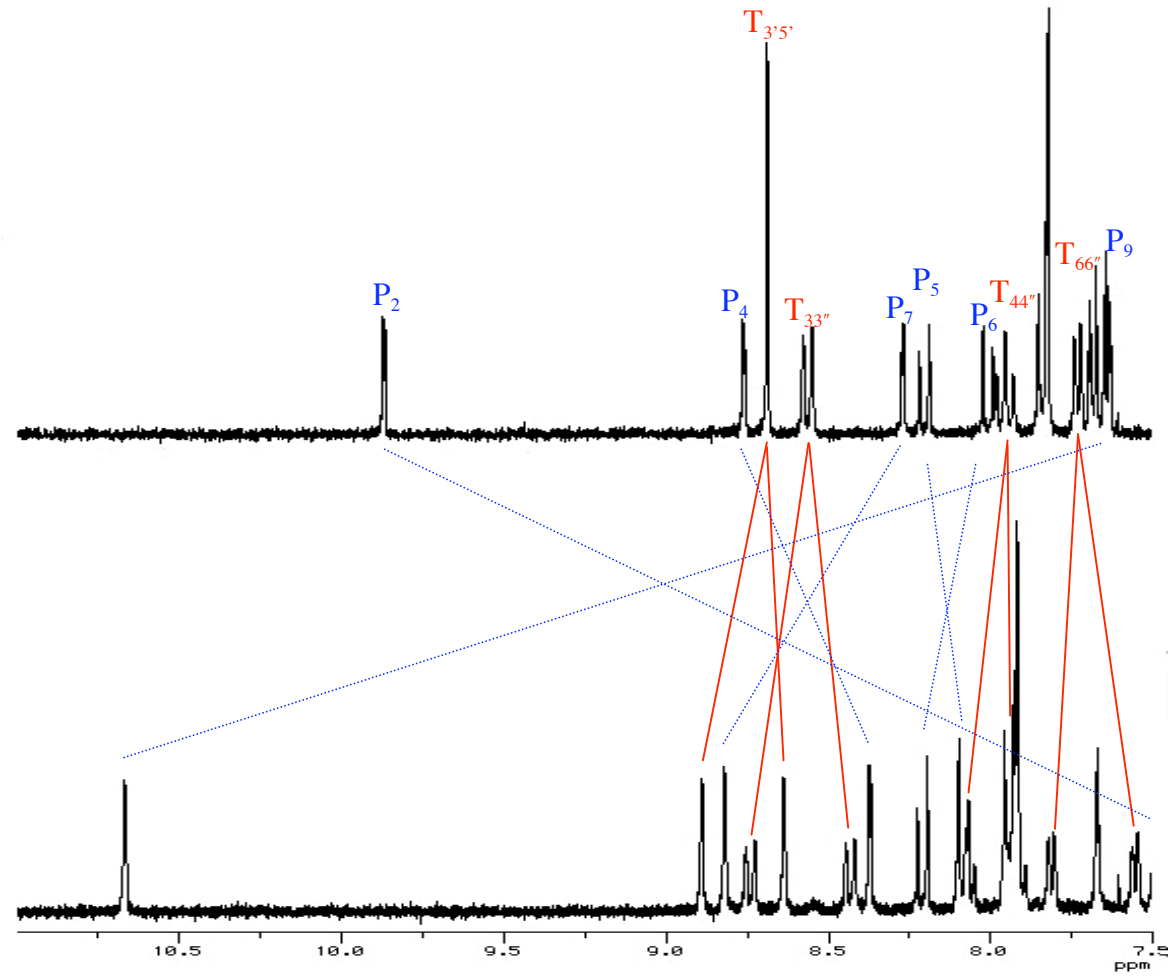

Figure 20: ^{1}H NMR spectra of $\mathbf{18}^{2+}$ and $\mathbf{19}^{2+}$ in $CDCl_3$; scale is 11-7.5 ppm; in red (full line) : signals of the terpyridine; in blue (dashed line) : signals of the phenanthroline. See Scheme 20 for proton assignment.

The two complexes **18**$^{2+}$ and **19**$^{2+}$ displayed the same mass spectra but very different proton NMR and UV-vis spectra:

- the UV-vis spectra in acetone of the two complexes showed a ^{1}MLCT absorption maximum at 468 nm for **18**$^{2+}$ and a shoulder around 430 nm for **19**$^{2+}$ (see Figure 19). These values were consistent with, respectively, a benzonitrile and a sulfoxide ligand coordinated to a Ru^{II}(terpy)(phen) core (see Chapter 1);
- in the proton NMR spectrum of **18**$^{2+}$ the terpy* moiety showed symmetric signals, which was consistent with the diastereogenic sulfoxide ligand being far from the coordination sphere of the ruthenium; on the contrary, both sides of the terpy* moiety in **19**$^{2+}$ were very distinctly different; this was consistent with the sulfoxide ligand being close to the coordination sphere of the ruthenium (see Figure 20);
- ROESY correlation experiments unambiguously showed the close proximity of the protons near the ruthenium atom on the terpy* and phen chelates and, respectively, the benzonitrile ligand in **18**$^{2+}$ and the sulfoxide ligand in **19**$^{2+}$.

These three experimental pieces of evidence demonstrated that **18**$^{2+}$ and **19**$^{2+}$ were coordination isomers with, respectively, the benzonitrile and the sulfoxide ligands coordinated to the ruthenium. These two complexes are depicted on Scheme 20.

IV. Reactivity of complexes 18^{2+} and 19^{2+}

We studied the two reactions depicted on Scheme 25:

- the photoinduced expulsion of the monodentate ligand, resulting in the opening of the ruthena-macrocycle and coordination of a solvent molecule S; the resulting "open species" Ru(terpy*)(**26**)(S)$^{n+}$ is schematised on Scheme 25b;
- the thermal back-coordination of the scorpion's tail, resulting in the closing of the ruthena-macrocycle and release of the solvent molecule S; the resulting product is a mixture of the starting product (Scheme 25a) and its isomer (Scheme 25c);

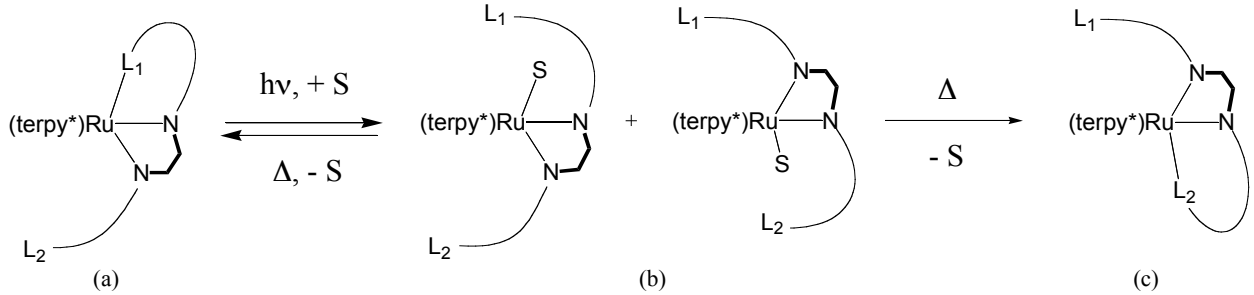

Scheme 25: photoinduced opening and thermal closing of the scorpion's tail.

IV.1. Experimental results for the irradiation step

In order to study the photochemical isomerisation process we used a source of white light filtered by interference filters centred either at 470 nm or at 430 nm, which corresponded to the ^{1}MLCT absorption bands of complexes **18**$^{2+}$ and **19**$^{2+}$, respectively. During photoexpulsion of the tail, a five-coordinate species was produced, on which isomerisation was possible. Coordination of a solvent molecule S froze the 90° rotation of the phenanthroline, leading to one or the other stable isomer of complex Ru(terpy*)(**26**)(S)$^{n+}$.

Two NMR probes enabled us to distinguish the species in solution:

- the proton ortho to the nitrogen atom of **26** that is on the side of the monodentate coordination site. It enabled us to determine the nature of the monodentate ligand (see Chapter 1);
- the methyl group borne by the sulfoxide ligand. It enabled us to determine the rotational position of phenanthroline **26**.

We were able to determine by peak integration the number and exact nature of the species in solution. Notably, the percentage of isomerisation could be measured on complex Ru(terpy*)(**26**)(S)$^{n+}$. Our results after irradiation at room temperature of scorpionates **18**$^{2+}$ and **19**$^{2+}$ are given Table 11.

Entry	Starting complex	Solvent system	S	Irradiation time / wavelength	Yield [(a)] (%)	Percentage of isomerisation
I	**18**$^{2+}$	CD_3CN	CD_3CN	0.5h / 470 nm	***100***	***40***
II	**18**$^{2+}$	CD_3COCD_3 / 20% D_2O	D_2O	1h / 470 nm	***100***	***27***
III	**18**$^{2+}$	CD_3COCD_3 / 4% D_2O + Cl^-,$N(C_2H_5)_4^+$	Cl^-	3h / 470 nm	***100***	***14***
IV	**18**$^{2+}$	CD_2Cl_2 / Cl^-,$N(C_2H_5)_4^+$	Cl^-	3h / 470 nm	***100***	***5***
V	**19**$^{2+}$	C_4D_8O	C_4D_8O	3h / 430 nm	***95***	***46***
VI	**19**$^{2+}$	CD_3COCD_3 / 20% D_2O	D_2O	3h / 430 nm	***96***	***43***
VII	**19**$^{2+}$	CD_2Cl_2 / Cl^-,$N(C_2H_5)_4^+$	Cl^-	3h / 430 nm	***100***	***9***

Table 11: photoexpulsion of the tail and photoisomerisation of **18**$^{2+}$ and **19**$^{2+}$. *(a)* calculated as the number of mole of both isomers of the photoproduct Ru(terpy*)(**26**)(S)$^{n+}$, divided by the number of mole of irradiated complex.

Three main tendencies appeared from the NMR data:

- in acetonitrile, acetone/water and tetrahydrofuran solutions (entries I, II, V, VI), complexes **18**$^{2+}$ and **19**$^{2+}$ led to a statistical mixture of the two open isomers of Ru(terpy*)(**26**)(S)$^{2+}$. After total disappearance of the starting product, further irradiation led to an increase of the percentage of isomerisation until the statistical distribution 50:50 was reached;

- in chlorination conditions (entries III, IV, VII) the ring opening process took place with negligible isomerisation, leading to the open isomer Ru(terpy*)(**26**)(Cl)$^{+}$ where the chloride is on the same side than the original monodentate ligand. After total disappearance of the starting product, further irradiation did not lead to an increase of the percentage of isomerisation;
- in all cases, the photochemical product *without* isomerisation was produced faster than the photochemical product *with* isomerisation.

Unfortunately we never detected the direct production of **19**$^{2+}$ after irradiation of **18**$^{2+}$, or vice-versa.

It is noteworthy that the absence of isomerisation during the chlorination experiments enabled us to independently measure the NMR spectra of the two chloro isomers **27**$^{+}$ and **27'**$^{+}$.

IV.2. Back coordination of the scorpion tail

The back coordination of the scorpion tail was too slow at room temperature to take place during irradiation. We did not have better results performing the irradiation at 40°C. Alternatively, it is also possible that **19**$^{2+}$ absorbed too much light at 470 nm, so that it also reacted during irradiation of **18**$^{2+}$. As a consequence the lamp was switched off during the back-coordination experiments.

Scheme 26 describes the system: a X:Y mixture of the two isomers of Ru(terpy*)(**26**)(S)$^{n+}$ gave the corresponding mixture of the closed scorpionates **18**$^{2+}$:**19**$^{2+}$ in a X':Y' ratio with X'=X and Y'=Y (within experimental errors).

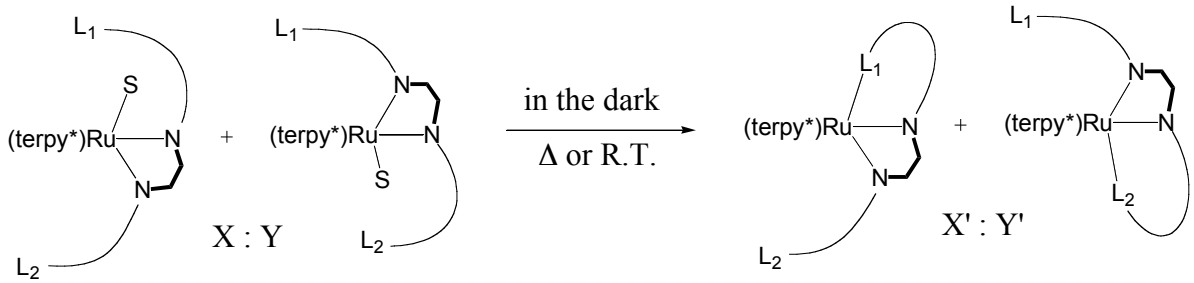

Scheme 26: thermal back-coordination of the tail.

Table 12 summarises our experimental results. When S was poorly coordinating like D_2O or C_4D_8O (entries II, V, VI), the tail spontaneously came back for coordination on ruthenium, with moderate yields however. When S was a chloride ion (entries IV and VII) the use of an excess of silver salt enabled to trap Cl^- and force coordination of the tail with quantitative yields. In all cases, we detected no significant changes in the isomer ratios during thermal processes. An associative mechanism cannot be totally excluded for such intramolecular thermal reactions.

Entry of Table 11 / irradiated complex	S in Ru(terpy*)(26)S^{n+}	Thermal conditions	Ratio 18^{2+} : 19^{2+}	Yield in scorpionate (%)
I / 18^{2+}	CD_3CN	Reflux in CH_3CN	-	0
IV / 18^{2+}	Cl^-	$AgBF_4$ excess Acetone 2h reflux	95 : 5	100
V / 19^{2+}	C_4D_8O	C_4D_8O 7 days at R.T.	46 : 54	60
VI / 19^{2+}	D_2O	Acetone 2 hours reflux	40 : 60	60
VII / 19^{2+}	Cl^-	$AgBF_4$ excess Acetone 2h reflux	8 : 92	100

Table 12: thermal back-coordination of the tail.

IV.3. Irradiation of a mixture of 18^{2+} and 19^{2+}

In order to check the selectivity of the irradiation process, we repeated the following photochemical sequence twice on the same sample initially composed of pure **18^{2+}**:

1) one hour of bandpass irradiation at 470 nm in an acetone:water mixture;
2) addition of NEt_4^+, Cl^- into the irradiation vessel and stirring 24h at R.T. in the dark; isolation of the complex was performed by a standard precipitation / filtration workup;
3) two hours of reflux in acetone with $AgBF_4$; removing AgCl by filtration, standard workup.

Starting with pure **18^{2+}**, the **18^{2+}**:**19^{2+}** ratios after step 3 were measured by NMR and gave the following results: 62:38 (after run 1) and 44:56 (after run 2).

V. Discussion

No thermal isomerisation of the phenanthroline has ever been noticed at room temperature on a saturated hexacoordinated species. In addition, we have gathered several pieces of information consistent with the common hypothesis[84, 86, 97] of a dissociative mechanism for the photosubstitution reaction of L in Ru(terpy*)(phen)L^{2+} complexes (see Chapter 1). Within this hypothesis we suppose that the isomerisation of **26** occurs on the photoinduced pentacoordinated species (see Scheme 27). The longer this pentacoordinated species lives, the higher the isomerisation percentage will be. Considering the symmetric nature of the phenanthroline near the ruthenium centre, a very long lifetime leads to a statistical 1:1 mixture of the two isomers of Ru(terpy*)(**26**)(S)$^{n+}$.

The kinetics of the coordination of a solvent molecule S to the pentacoordinated species may be of primary importance. If $k_S[S]$ is small compared to k_i, isomerisation takes place before the rotation is frozen by coordination of S. This was probably the case in weakly coordinating solvents like C_4D_8O or CD_3COCD_3/D_2O mixtures. On the contrary if $k_S[S]$ is high enough, as in the case of

chlorination reactions, the coordination sphere of the ruthenium is saturated before any isomerisation may occur.

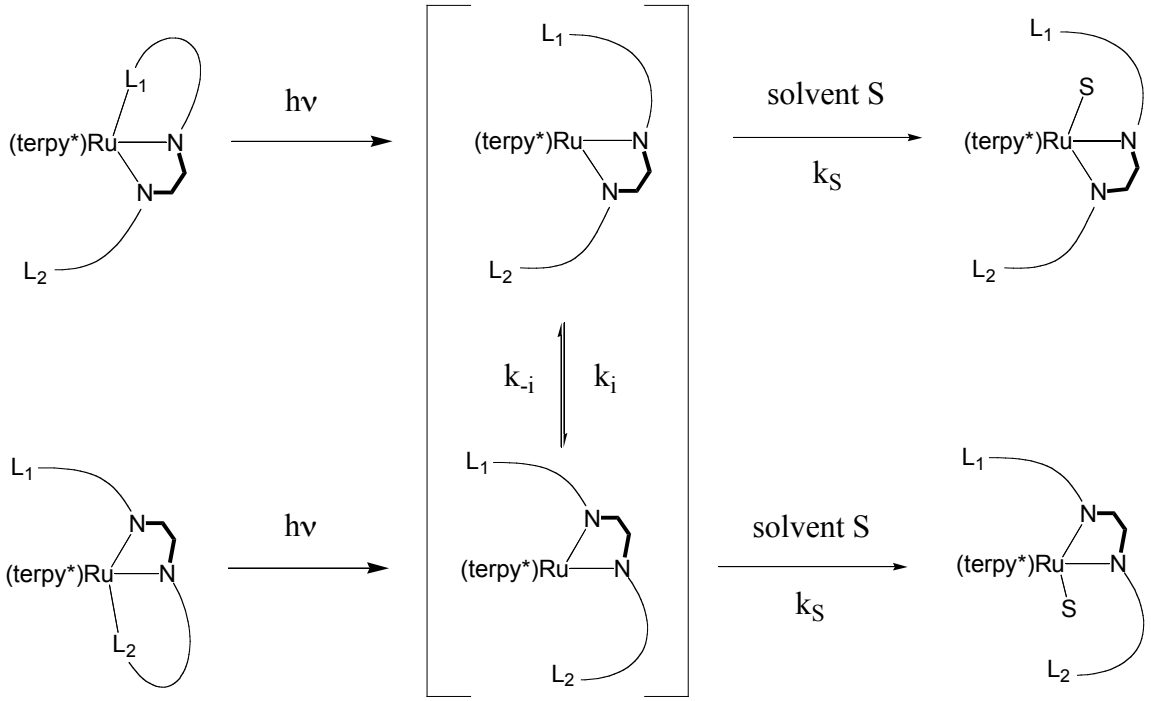

Scheme 27: proposed mechanism for the photoinduced isomerisation

The question of the photoreactivity of the photoproduct has also to be considered. The two interference filters were centred at the wavelength of the ^{1}MLCT absorption band of the starting complexes. However, after total disappearance of the starting complex in acetonitrile, acetone/water and tetrahydrofuran solution, the isomerisation ratio changed with irradiation time. This could be interpreted as a photochemical reactivity of the photochemical products. On the contrary, complex Ru(terpy*)(**26**)$(Cl)^+$ was not isomerised by further irradiation at 430 or 470 nm, so that in this case the ^{1}MLCT of the photoproduct was probably bathochromically shifted far enough to prevent light absorption of the photoproduct.

The thermal ring formation reaction was efficient only with S = Cl^-. In the cases of S = D_2O and C_4D_8O, back-coordination took place but the low yields of these reactions prevented recycling of the whole process in order to gradually convert $\mathbf{18}^{2+}$ into $\mathbf{19}^{2+}$. Acetone and tetrahydrofuran are wet solvents, and catalytic processes involving Ru(terpy)(**26**)$(H_2O)^{2+}$ are suspected to be responsible for the low yields obtained at reflux of these solvents.[87, 116-118]

In order to avoid heating, we designed a sequence where 1) the tail is photoexpelled and replaced by water *with* isomerisation 2) water is replaced by chloride at room temperature 3) chloride is trapped by silver(I) and the tail re-coordinates. Repeating several times these three steps

enabled us to gradually enrich in $\mathbf{19}^{2+}$ a pure sample of $\mathbf{18}^{2+}$. The 44:56 ratio after two repetitions is beyond the theoretical statistical limit of 50:50, which proves that the second irradiation with an interference filter centred at 470 nm was selective on isomer $\mathbf{18}^{2+}$ and left $\mathbf{19}^{2+}$ untouched.

However, the inherent experimental complexity of this sequence (3 precipitations!) obviously limits the potential of our scorpionate as a photochemically controlled molecular switch. The long and flexible nature of the polyether chain may be a limiting factor for the coordination at room temperature of the tail during the irradiation.

VI. Conclusion

Two ruthenium (II) polypyridyl complexes $\mathbf{18}^{2+}$ and $\mathbf{19}^{2+}$ were synthesized and fully characterized by absorption spectroscopy, mass spectrometry, ^{1}H and ^{13}C nuclear magnetic resonance. Their scorpionate nature was demonstrated and they were shown to be coordination isomers. Due to the different nature of their coordinated monodentate ligand, their ^{1}MLCT absorption bands were different enough to envisage selective irradiation by wavelength selection. The photoexpulsion of the coordinated tail led to two processes: 1) the ruthena-macrocycle opens and a solvent molecule S coordinate to the ruthenium; 2) isomerisation of the phenanthroline takes place on the transient pentacoordinated species, which consists in a 90° rotation of the bidentate chelate around the ruthenium knee-joint.

These processes were studied in different solvent systems showing either strong or poor coordinating properties. In our irradiation conditions, the tail of the scorpion does not coordinate to the ruthenium. The thermal back-coordination was investigated in the dark; it was not followed by rotation of the phenanthroline. Two major types of conditions were found, with either an efficient photochemical isomerisation step and a low-yielded thermal recoordination step, or a photoinduced ring opening with little isomerisation but a quantitative back-coordination step. We experimentally showed that it was possible to selectively irradiate one scorpionate in a mixture of $\mathbf{18}^{2+}$ and $\mathbf{19}^{2+}$ two by using an interference filter. The enrichment process enabled to interconvert more than 50% of the initial complex to its coordination isomer. This interconvertion can be described as the 90° rotation of a phenanthroline chelate around a ruthenium centre.

CHAPTER 3: RU(TERPY)(PHEN)(L)$^{2+}$ COMPLEXES WITH A DISSYMMETRICALLY 2,8-DISUBSTITUTED BIDENTATE CHELATE.

I. Introduction

In Chapter 2, the phenanthroline used was dissymmetric far from its coordinating nitrogen atoms. That is to say, in the pentacoordinated species the fact that the two monodentate ligands were different remained far from the coordination sphere of the ruthenium. As the rotation of the phenanthroline moiety took place supposedly on this pentacoordinated intermediate, the final composition of the mixture approached the statistical 50:50 distribution without being able to go further. It was difficult to build a photocontrolled molecular switch based on such a ratio.

In order to realise a simpler system, we considered using a phenanthroline that was dissymmetrically substituted *near* the ruthenium atom. We designed a 2,8-disubstituted chelate with a very bulky mesityl substituent in position 2. Our initial hope was that this group would block the rotation of the phen by preventing the monodentate ligand L to be on the same side (see Figure 21). As will be seen in this chapter, this hope was exaggerated. These complexes showed indeed a very unexpected and interesting reactivity, as their photoinduced isomerisation became quantitative.

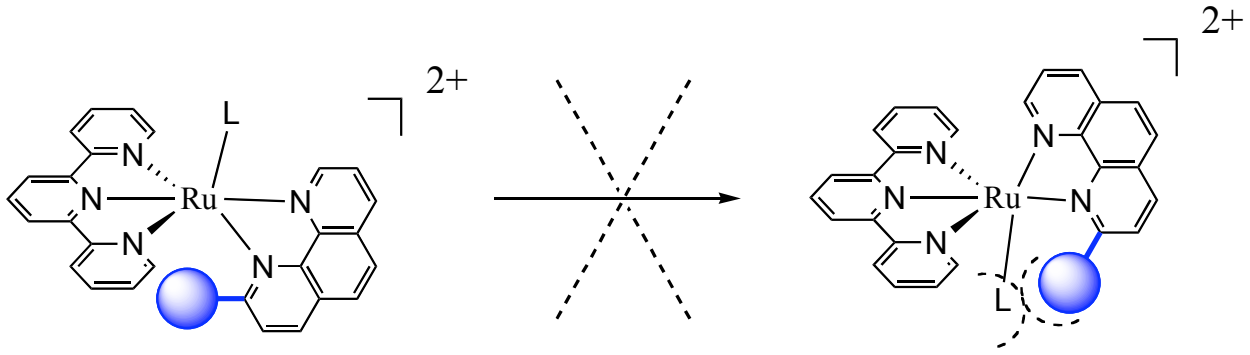

Figure 21: working hypothesis: is it possible to block the rotation of a dissymmetric phenanthroline, hence the formation of one of the two isomers, by introducing a hindering group α to one nitrogen atom of the bidentate chelate?

We describe in this chapter the synthesis of the two chelates: **28** = 4'-(3-anisylphenyl)-2,2';6',2"-terpyridine and **29** = 8-anisyl-2-mesityl-1,10-phenanthroline; their coordination to ruthenium; and the coordination- and photochemistry of their ruthenium complexes.

II. Ligand synthesis and coordination to ruthenium

II.1. Synthesis of terpyridine 28

Amongst the main synthetic methods towards terpyridines,[119, 120] Kröhnke reaction was preferred due to the absence of toxic or dangerous reagents like arsenic oxide or concentrated sulphuric acid. The condensation of chalcone **30** and pyridinium iodide **31** in presence of a source of nitrogen generates the central pyridine ring of terpyridine **32** with a very acceptable yield of 63%. It has to be noted that the reaction needed oxidation by air, so that it failed under argon. The Suzuki cross-coupling reaction[121] between 4'-(3-bromophenyl)-2,2';6',2"-terpyridine (**32**) and anisylboronic acid resulted in terpyridine **28**. The whole synthesis is depicted on Scheme 28.

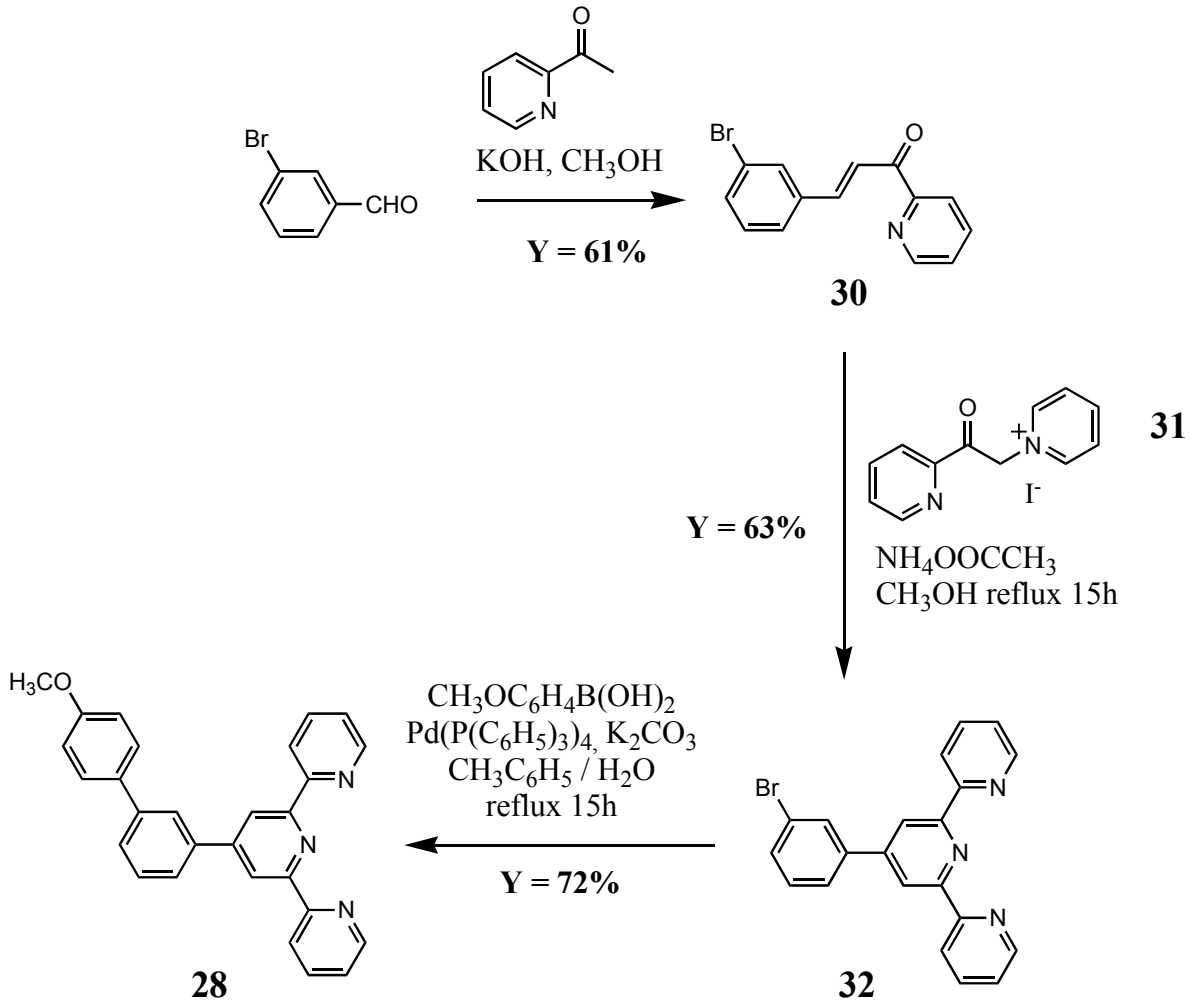

Scheme 28: synthesis of terpyridine **28.**

28 could be prepared in very large scale (10 g) and was characterised by high-resolution FAB mass spectrometry, elemental analysis, proton and carbon NMR. All carbon peaks could be attributed due to ^{1}H-^{13}C HSQC and HMBC correlation experiments.

II.2. Synthesis of phenanthroline 29

The bromination of 1,10-phenanthroline in 3 or 3,8 position needs harsh conditions and is generally performed as the first step (see Scheme 29).[122] On the other hand, addition of lithiated derivatives followed by re-aromatisation is a very efficient and selective method for the introduction of aryl substituents in α-position to the nitrogen atom of an aromatic polypyridine ligand,[123, 124] provided that no other halide is present on the conjugated system.[125] We used hence the following synthetic strategy:

- monobromination of phenanthroline hydrochloride;
- Suzuki cross-coupling of an anisyl group;
- monoaddition of mesityllithium on the other side of the anisyl group.

The first of these three step, although well described in the literature, was very sensitive to the reaction conditions and only poorly reproducible. Notably 3-bromophenanthroline was often polluted with 5 to 35% of 3,5 dibromophenanthroline that could not be removed by chromatography. We used a modified crystallisation procedure based on the difference in basicity between these two phenanthrolines in order to increase the purity of our samples.[126]

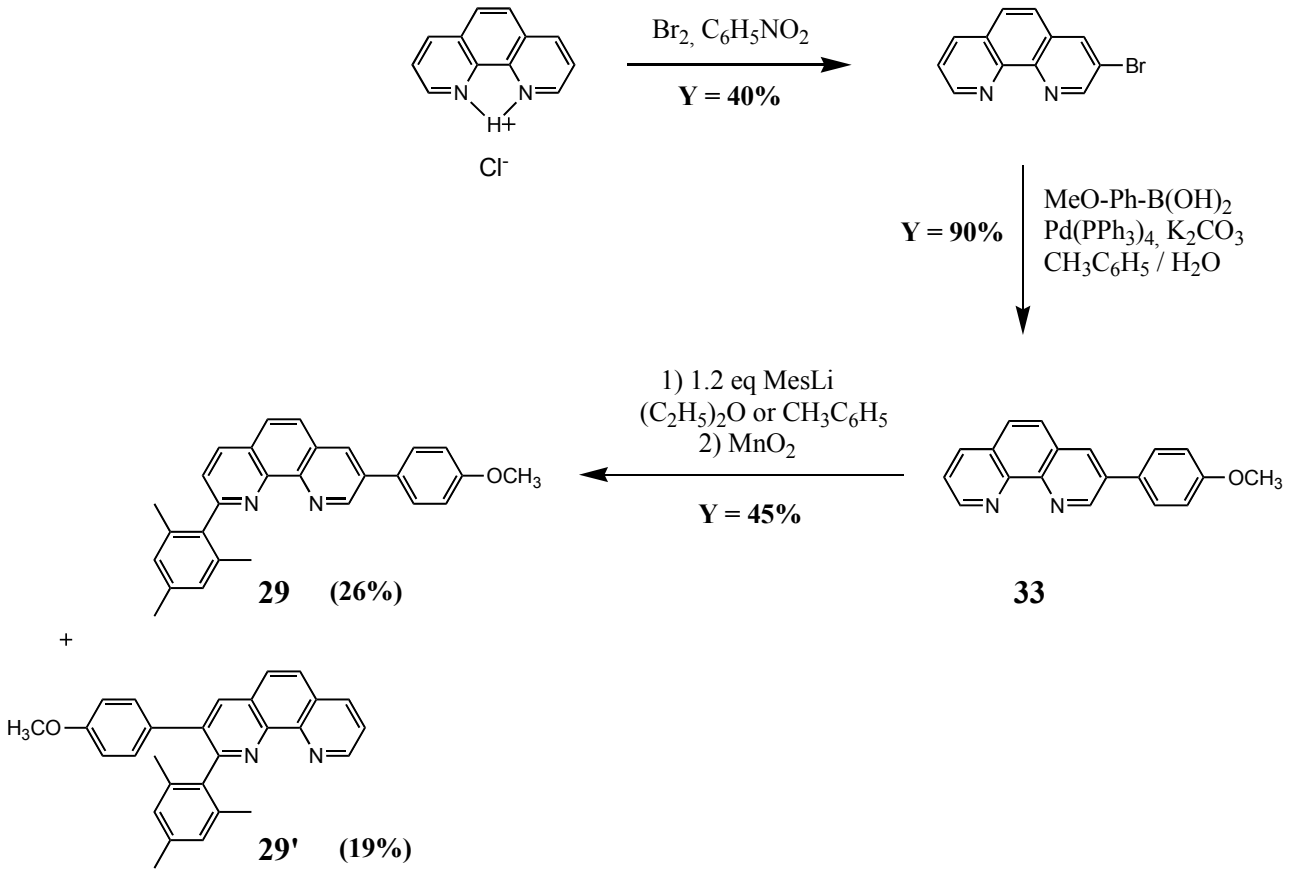

Scheme 29: synthesis of phenanthroline **29**

The last step combined two issues: 1) the hindered nature of the mesityl group 2) the low regioselectivity. They both led to a moderate yield in the right 2,8 substituted compound **29** and to the production of an appreciable amount of the 2,3 regioisomer **29'**: in ether or toluene, the yields for the two products were 26 and 19 percent, respectively. The whole synthesis is depicted on Scheme 29. **29** could be prepared on a 500 mg scale. It was characterised by high-resolution FAB mass spectrometry, elemental analysis, proton and carbon NMR. All the carbon peaks could be attributed due to ^{1}H-^{13}C HSQC and HMBC correlation experiments.

II.3. Coordination of terpyridine 28 and phenanthroline 29 to ruthenium

Coordination of terpyridine **28** on $RuCl_3.xH_2O$ was efficient and enabled the large-scale (5 g) preparation of Ru(**28**)Cl_3 (compound **34**) as a very insoluble material that was characterised by mass spectrometry and elemental analysis (see Scheme 30).

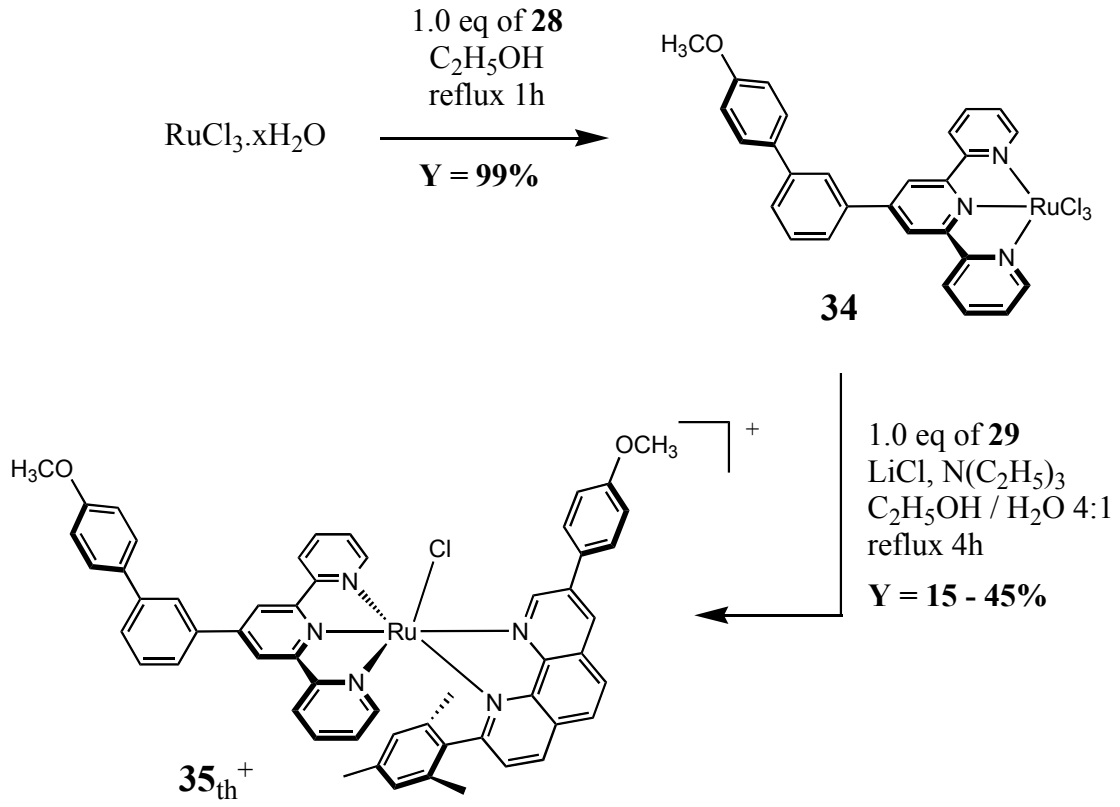

Scheme 30: coordination of terpyridine **28** and phenanthroline **29** on ruthenium.

The coordination of phenanthroline **29** to **34** turned up to be the limiting step of this work. With an unhindered bidentate chelate like 1,10-phenanthroline, the standard conditions[94] - LiCl and triethylamine in excess, ethanol/water as the solvent - give the Ru(terpy)(phen)$(Cl)^+$ complex with 60 to 70% yield (see Chapter 1). However, these "standard" reaction conditions always also produced ruthenium black and $Ru(terpy)_2^{2+}$ as side products. The reducing properties of ethanol and triethylamine were indeed needed for the production of ruthenium (II). However, as the reduction

always partially led to ruthenium (0) (even in absence of triethylamine), the terpyridine was released and reacted with the starting Ru(terpy)Cl_3 in solution to give the bis-terpyridine complex. In the case of phenanthroline **29**, these side-reactions limited the yield in Ru(**28**)(**29**)$(Cl)^+$ to irreproducible low values between 15 and 45%, depending on the scale of the reaction and the quantity of NEt_3. The electron-donating properties of the mesityl group in **29,** as long as its hindering nature could explain this limited yield. Free ligand **29** was always present at the end of the reaction, which made the purification process difficult.

As expected in the design of **29**, the coordination to Ru(**28**)Cl_3 was very stereoselective and afforded only isomer $\mathbf{35}_{th}^+$ where the chloride ion is on the side of the anisyl group (see Scheme 30). $\mathbf{35}_{th}^+$ could be prepared on a 150 mg scale and was analysed by high-resolution electrospray mass spectroscopy, proton and carbon NMR. All carbon peaks could be attributed due to ^1H-^{13}C HSQC and HMBC correlation experiments.

II.4. Coordination chemistry of Ru(28)(29)(L)$^{n+}$ complexes

II.5. Thermal ligand substitution reactions

The thermal coordination chemistry of this series of complexes followed the classical frame described in Chapter 1 (see Scheme 31). Complex $\mathbf{35}_{th}^+$ reacted slowly in an acetonitrile – water mixture to afford complex $\mathbf{36}_{th}^{2+}$ where the monodentate CH_3CN ligand was still on the side of the anisyl group. When this complex was refluxed in pyridine it quickly and quantitatively gave complex $\mathbf{37}_{th}^{2+}$ with a pyridine in place of acetonitrile. The three complexes $\mathbf{35}_{th}^+$, $\mathbf{36}_{th}^{2+}$ and $\mathbf{37}_{th}^{2+}$ were called “thermal isomers” and abbreviated as “th” as they were synthesized by *thermal* ligand substitution reactions.

A crystal structure of $\mathbf{37}_{th}^{2+}$ was obtained and is depicted Figure 22 (see Annex D for Crystal Data). The geometry in the solid-state structure was consistent with the ROESY interactions observed in solution. The mesityl group was located below the terpyridine moiety with a probable π-stacking between the central pyridine of the terpyridine and the mesityl aromatic cycle (mean distance between the two cycles is 3.4 Å). On the other side of the ruthenium atom, the pyridine monodentate ligand had no interaction with the mesityl group but was close from the anisyl group. The torsion angle O1-C20-C30-O2 was 45.71° and the two methoxy groups pointed both toward the top of the molecule, so that we could envisage the inclusion of this complex in a molecular ring (see Chapter 4). The O1-O2 distance was 17.89 Å in this isomer.

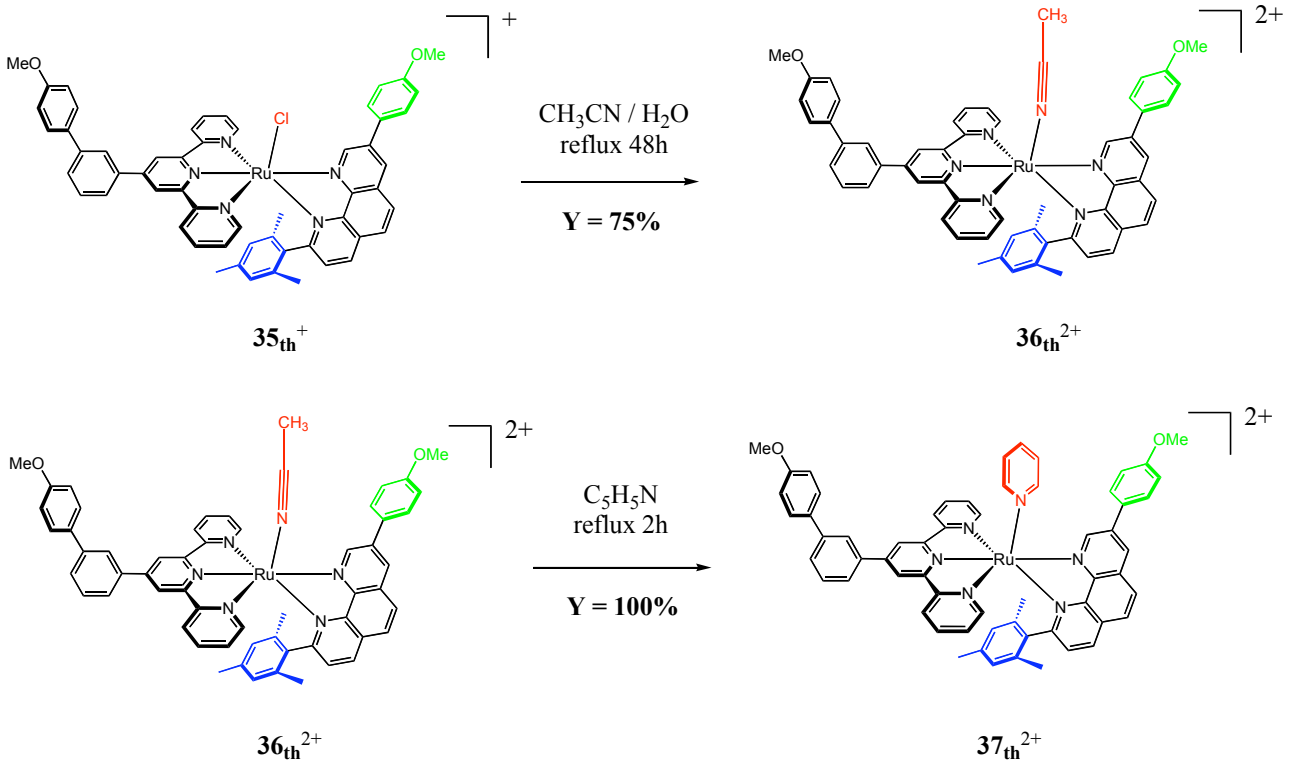

35$_{th}^{+}$ **36**$_{th}^{2+}$ **36**$_{th}^{2+}$ **37**$_{th}^{2+}$

Scheme 31: thermal ligand substitution pattern of Ru(**28**)(**29**)(L)$^{n+}$ complexes.

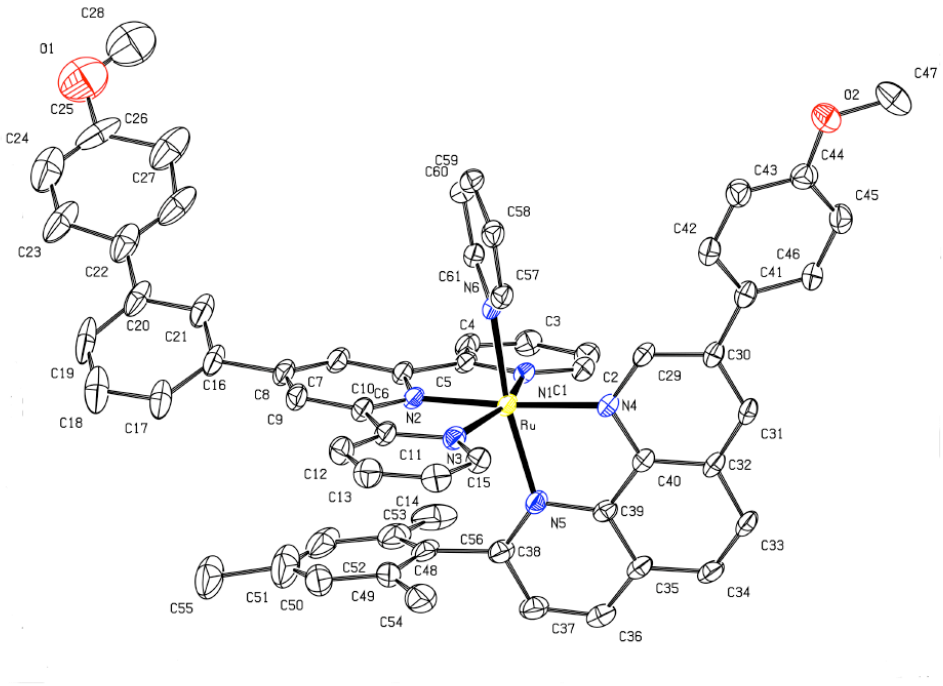

Figure 22: ORTEP diagram of the X-ray structure of **37**$_{th}^{2+}$. Atoms are drawn with 30% probability. H-atoms are omitted for clarity. See Annex D for Crystal Data.

All complexes **35**$_{th}^{+}$, **36**$_{th}^{2+}$ and **37**$_{th}^{2+}$ could be prepared on a 50 to 100 mg scale and were characterised by high-resolution electrospray spectrometry, proton and carbon NMR. All carbon peaks could be assigned due to ^{1}H-^{13}C HSQC and HMBC correlation experiments.

II.6. Photochemical substitution reactions

When $\mathbf{37}_{th}^{2+}$ was irradiated in pyridine, its proton NMR spectrum radically changed (see Figure 23): all the signals corresponding to the side of the anisyl (P_6, P_7, P_9, P_a and P_b) *and* the mesityl singlet P_m were upfield shifted, whereas the P_3, P_4 and P_5 protons were shifted downfield. ROESY correlation experiments proved that, whereas in $\mathbf{37}_{th}^{2+}$ the mesityl group was close to the terpyridine and far from the pyridine ligand, in the new product noted $\mathbf{37}_{photo}^{2+}$ it was close to the pyridine and far from the terpyridine (see Scheme 32). A correlation peak was also seen in $\mathbf{37}_{th}^{2+}$ between the P_9 proton of the phenanthroline and the meta proton of the pyridine, whereas this P_9 proton was alone in $\mathbf{37}_{photo}^{2+}$ (see Scheme 32).

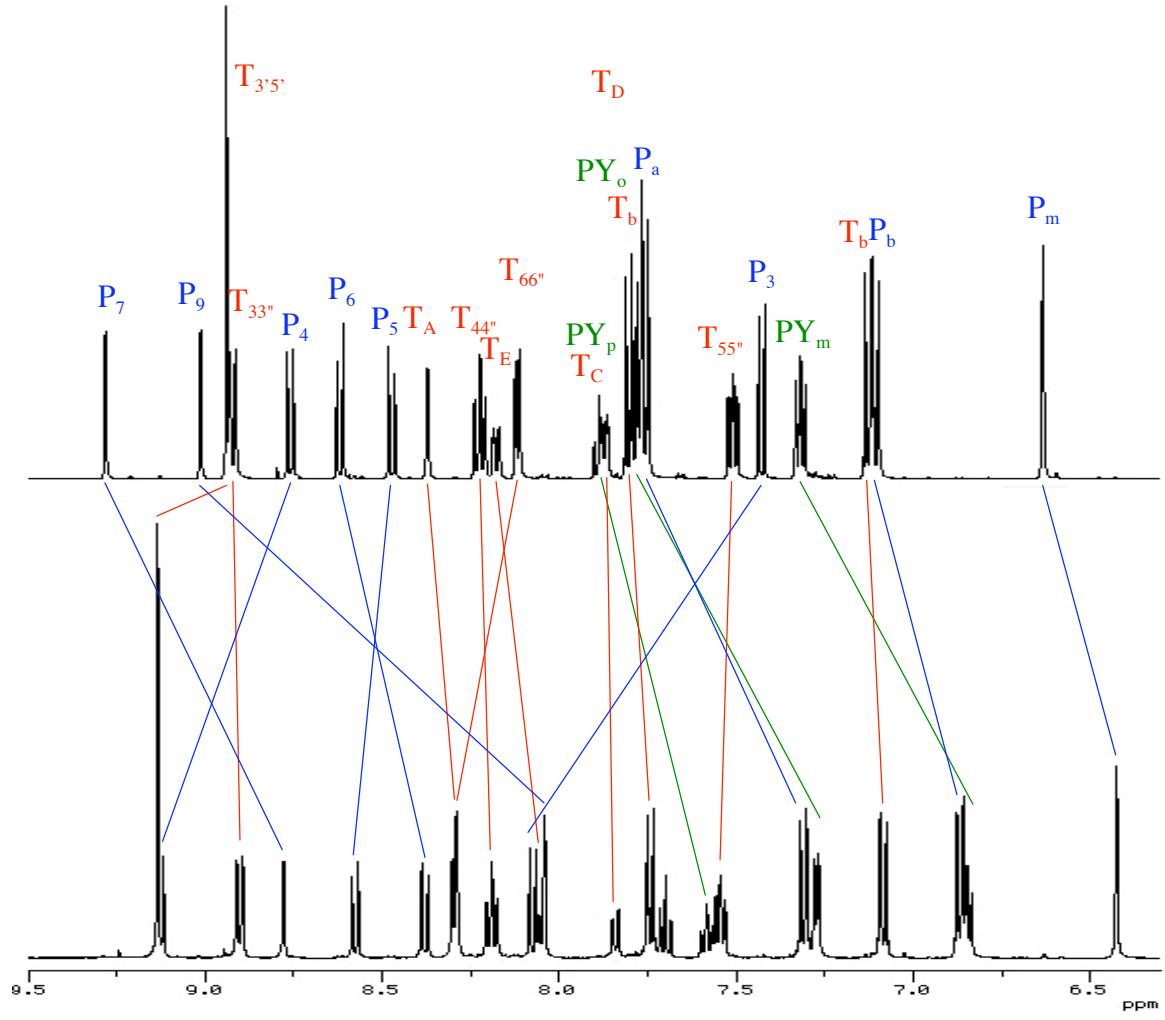

Figure 23: proton NMR spectra of $\mathbf{37}_{th}^{2+}$ and $\mathbf{37}_{photo}^{2+}$ (aromatic region). In blue: peaks of the phenanthroline ; in red: peaks of the terpyridine ; in green: peaks of the pyridine (noted PY). Scale is 9.5-6.3 ppm in acetone-d6. See Scheme 32 for complete notations of the protons.

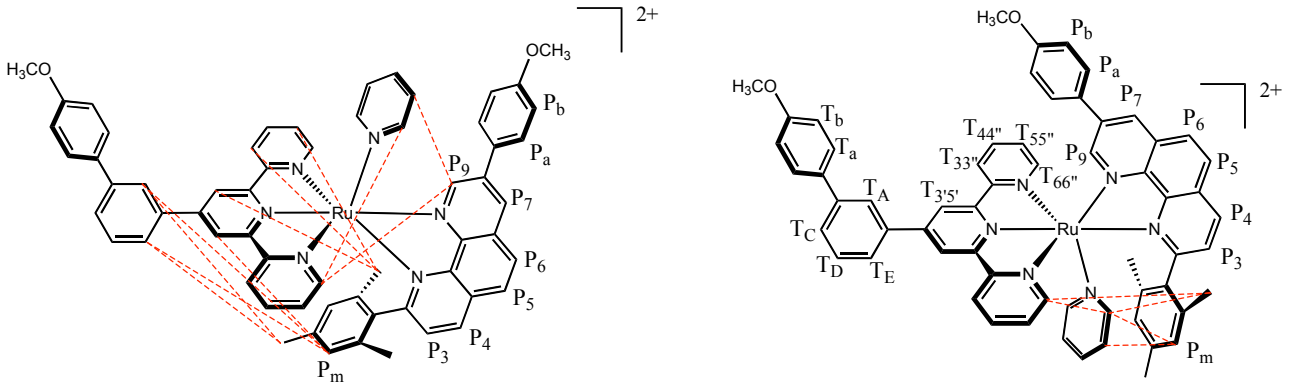

37$_{th}^{2+}$ **37**$_{photo}^{2+}$

Scheme 32: chemical structures of complexes **37**$_{th}^{2+}$ and **37**$_{photo}^{2+}$ and notations of the protons. Selected ROESY interactions appear in dashed lines.

The same photochemical isomerisation took place when **36**$_{th}^{2+}$ was irradiated in acetonitrile: the phenanthroline moiety quantitatively rotated of a 90° angle to yield complex **36**$_{photo}^{2+}$ where the acetonitrile ligand was on the side of the mesityl group. This new isomerisation reaction was also directly undertaken from complex **35**$_{th}^{+}$ in acetonitrile / water and afforded in one quantitative step **36**$_{photo}^{2+}$. In a similar manner, **36**$_{th}^{2+}$ irradiated in pyridine gave directly **37**$_{photo}^{2+}$ with 100% yield. Scheme 33 summarizes the photochemical ligand substitution pattern of Ru(**28**)(**29**)(L)$^{n+}$ complexes. The two new complexes **36**$_{photo}^{2+}$ and **37**$_{photo}^{2+}$ are called "photochemical isomers" and abbreviated "photo" as they were synthesized by photochemical ligand substitution reactions.

The two isomers of one particular complex had very similar UV-vis absorption spectra, with a bathochromically shifted shoulder for the photochemical isomer that induced a slight colour change during the isomerisation process. For example, **37**$_{th}^{2+}$ was bright orange whereas **37**$_{photo}^{2+}$ was brownish; Figure 24 gives the corresponding spectra in acetone.

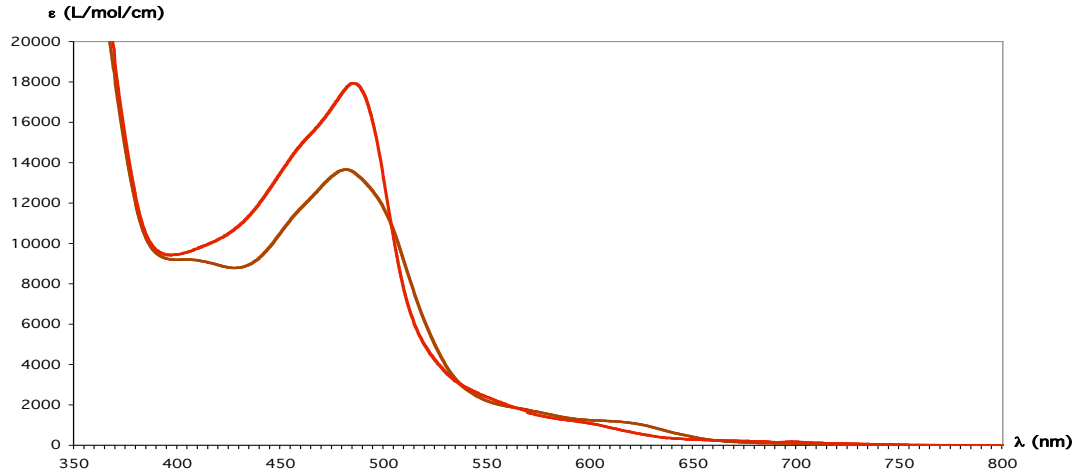

Figure 24 : compared UV-vis spectra of **37**$_{th}^{2+}$ (orange) and **37**$_{photo}^{2+}$ (brown) in acetone.

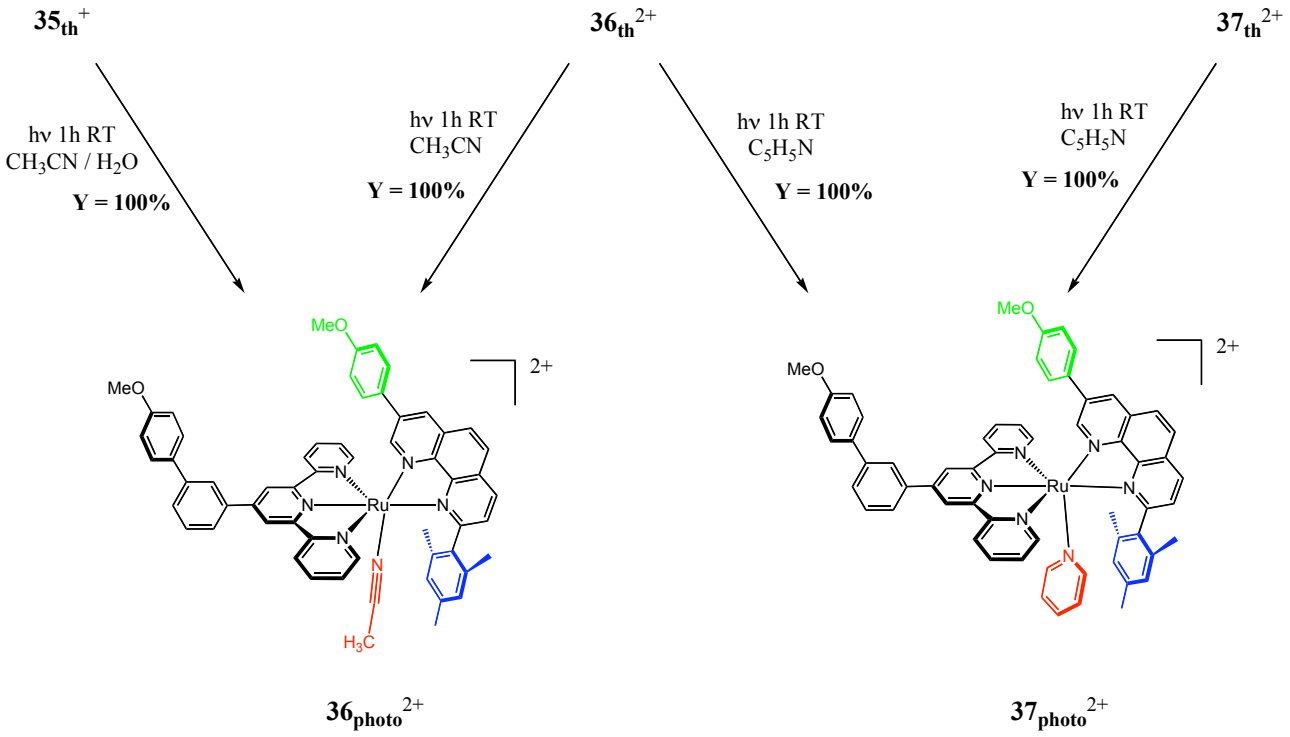

Scheme 33: photochemical ligand substitution pattern of Ru(**28**)(**29**)(L)$^{n+}$ complexes.

III. Thermal ligand substitution reactions on photochemical isomers

36$_{photo}^{2+}$ refluxed 2h in pyridine led quantitatively to **37**$_{photo}^{2+}$: the ligand substitution took place without coming back to the thermal isomer **37**$_{th}^{2+}$. Starting from complex **37**$_{photo}^{2+}$, several thermal ligand substitution reactions L → L' were realised using L' = chloride, 3,5-dimethylpyridine, benzonitrile and dimethylsulfoxide as the entering ligands. The conditions were kept equal for the four reaction: 140°C for two hours in the entering ligand as the solvent, except for the chloride anion that was used in large excess in dichloroethane. The results were very different, depending on L':

- in 3,5-lutidine and benzonitrile, pyridine was quantitatively exchanged *without isomerisation* to yield **38**$_{photo}^{2+}$ (Ru(**28**)(**29**)((CH$_3$)$_2$C$_5$H$_3$N)$^{2+}$) and **39**$_{photo}^{2+}$ (Ru(**28**)(**29**)(C$_6$H$_5$CN)$^{2+}$), respectively;
- in the chlorination conditions, pyridine was quantitatively substituted *with only 13% of back isomerisation* to the thermal isomer, yielding 87% of **35**$_{photo}^{+}$ (Ru(**28**)(**29**)(Cl)$^{+}$) as the main product;
- in DMSO the back-isomerisation to the thermal isomer was *quantitative*; in this process, pyridine was quantitatively removed, yielding 90% of the thermal isomer of complex Ru(**28**)(**29**)(CH$_3$SOCH$_3$)$^{2+}$ (noted **40**$_{th}^{2+}$) and 10% of a thermal isomer with an unknown

monodentate ligand L. As $\mathbf{40}_{th}^{2+}$ could not be purified on silica, it was directly converted to $\mathbf{35}_{th}^{+}$, $\mathbf{36}_{th}^{2+}$ or $\mathbf{37}_{th}^{2+}$ by refluxing 2h in CH_2Cl_2 / NEt_4^+, Cl^-, CH_3CN or C_5H_5N, respectively.

Complexes $\mathbf{38}^{2+}$ and $\mathbf{39}^{2+}$ were unambiguously analysed by NMR and mass spectrometry. The chlorination conditions enabled us to isolate complex $\mathbf{35}_{photo}^{+}$ which was never seen before. Scheme 34 gives the chemical shift differences in $CDCl_3$ between free chelates **28** and **29** and the two isomers $\mathbf{35}_{th}^{+}$ and $\mathbf{35}_{photo}^{+}$. This analysis was a proof for the geometry of the new complex $\mathbf{35}_{photo}^{+}$ despite the absence of ROESY interactions with the chloride ligand. As can be seen, the P_9 proton in $\mathbf{35}_{photo}^{+}$ was very much shielded because it laid just above the terpyridine aromatic cycle, whereas in $\mathbf{35}_{th}^{+}$ it was very much de-shielded because of the coordination to the ruthenium of the nitrogen in α position. This effect was also seen on proton P_7, although in smaller amplitude. In addition, the shielding effect of the terpyridine moved down the chemical shifts of all mesityl signals in $\mathbf{35}_{th}^{+}$ whereas in $\mathbf{35}_{photo}^{+}$ this effect was observed on the anisyl group.

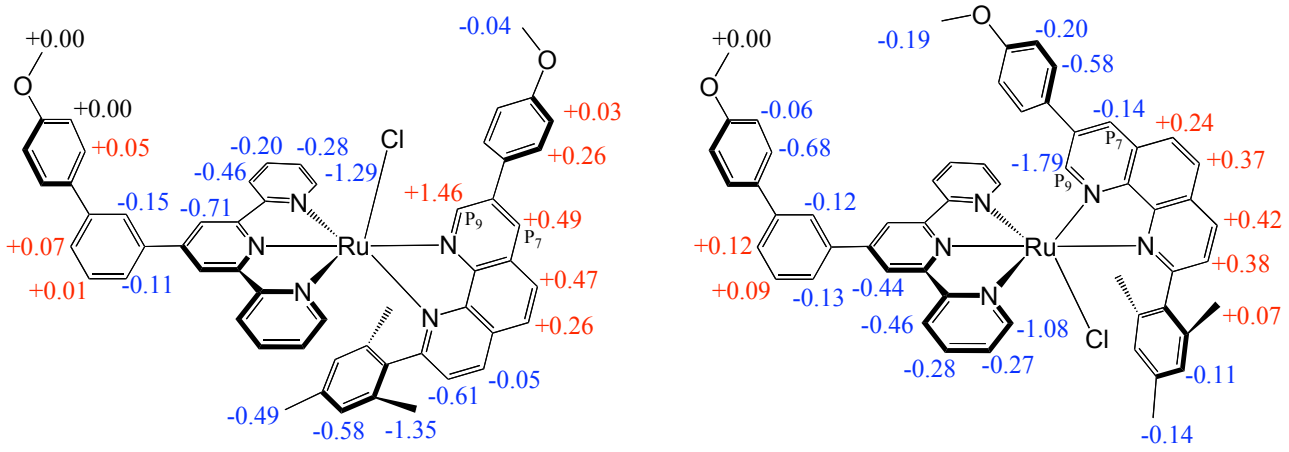

Scheme 34: chemical shift differences between free and coordinated ligands in $CDCl_3$ for the two isomers of Ru(**28**)(**29**)$(Cl)^+$ (left: thermal; right: photochemical).

Complex $\mathbf{40}_{th}^{2+}$ was impossible to purify as the DMSO ligand seemed to be very weakly coordinated to the ruthenium. It was indeed the only complex that was not stable on silica gel chromatography. However, crude samples were precipitated and analysed by NMR: they did not contain any free or coordinated pyridine. Both NMR spectrum and UV-vis absorption spectroscopy were characteristic for the thermal isomer of a Ru(terpy)(phen)$(L)^{2+}$ complex with coordinated CH_3SOCH_3: in acetone the P_9 proton at 11.0 ppm was typical for the geometry of the thermal isomer, and the wavelength maxima at 437 and 490 nm were consistent with S-bonded and O-bonded DMSO on a Ru(terpy)(phen)$(DMSO)^{2+}$ complex.[100] A mass spectrum of complex $\mathbf{40}_{th}^{2+}$ was obtained, showing clearly its precise nature (m/z = 499.642 compared to 499.638 for [Ru(**28**)(**29**)$(DMSO)]^{2+}$).

IV. Discussion

Ru(**28**)(**29**)(L)$^{n+}$ complexes generally exist in two forms that are coordination isomers:

- a "thermal" isomer obtained in thermal ligand exchange reactions;
- a "photochemical" isomer obtained in photochemical ligand exchange reactions at room temperature.

For a given L we have no real argument to say which isomer was the more stable thermodynamically. However we will consider as usual that ruthenium coordination chemistry and photochemistry are controlled by kinetics. In the following discussion, we will give to both isomers of a given hexacoordinated complex Ru(**28**)(**29**)(L)$^{n+}$ the same free enthalpy.

For any L → L' ligand substitution reaction, we call R_{th}^{n+} or R_{photo}^{n+} the two isomers of the starting product Ru(**28**)(**29**)(L)$^{n+}$ and $P_{th}^{n'+}$ or $P_{photo}^{n'+}$ the two isomers of the ligand exchange product Ru(**28**)(**29**)(L')$^{n'+}$. We saw that depending on the starting isomer and the photochemical or thermal reaction conditions, isomerisation of the phenanthroline may, or may not, occur. In each case, we could *a priori* consider either an associative or a dissociative mechanism. Considering the bulkiness of the mesityl group, the entering ligand L' is probably unable to coordinate to the ruthenium on the same side as the mesityl during rotation of the phenanthroline, so that we excluded the possibility of a thermal associative mechanism leading to isomerisation. We also excluded any photochemical associative mechanism as it would need an interaction between L' and the ruthenium complex before absorption of the photon. This hypothesis has been excluded for polypyridyl ruthenium (II) complexes years ago.[97]

Three possibilities remained: a) a thermal associative mechanism without isomerisation; b) a thermal dissociative mechanism leading, or not, to isomerisation; c) a photochemical dissociative mechanism leading, or not, to isomerisation. In the dissociative mechanisms, we considered that the expulsion of ligand L, either thermally or photochemically induced, was an elementary step that took place without rotation of the phenanthroline.

IV.1. The isomerisation process

We propose to consider the isomerisation of the phen as an elementary step occurring on the pentacoordinated species Ru(**28**)(**29**)$^{2+}$.[86] In his PhD-thesis indeed,[98] Julien Bossert realised TD-DFT calculation on a simpler pentacoordinated derivative Ru(terpy)(dmp)$^{2+}$. He showed that the C_s form directly derived from ligand abstraction from the starting complex (i.e. with the phen in one extreme rotational position) was a local minimum, and that the C_{2v} symmetric species where the

phen is symmetrically oriented between these two positions was a transition state with an energy 42 kcal/mol higher. Scheme 35 gives the notations of the isomerisation process with our system.

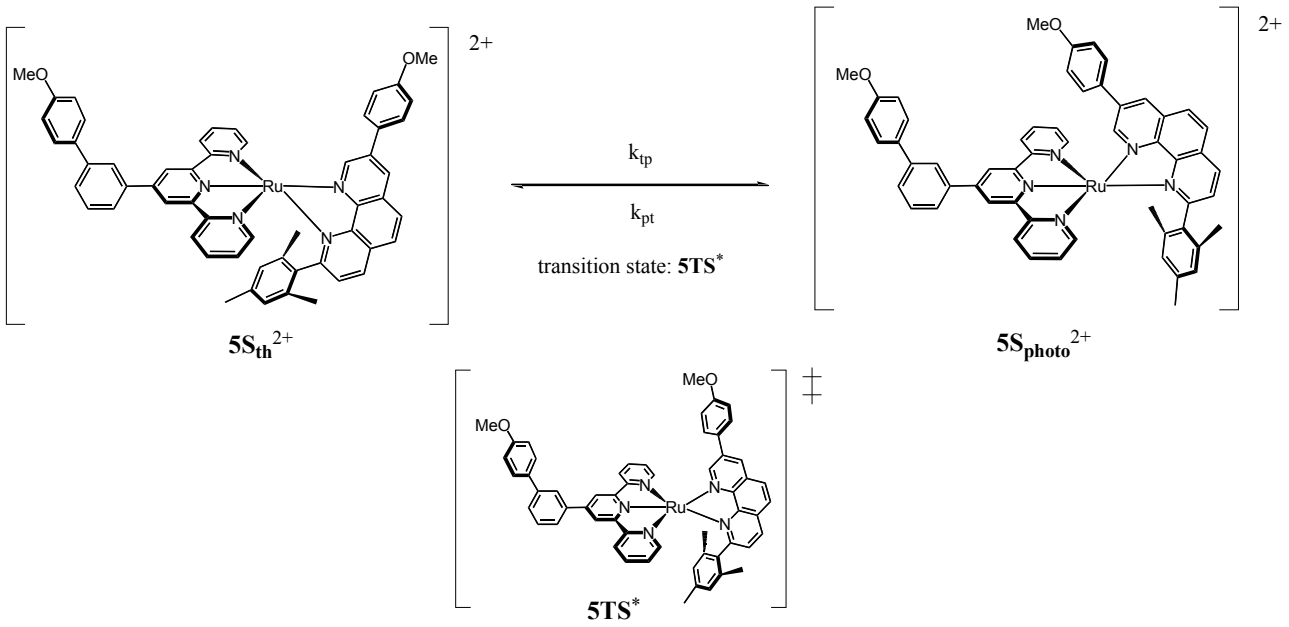

Scheme 35: notations for the isomerisation step in the dissociative mechanism.

In the calculations of Julien Bossert and coworkers,[98] the phenanthroline was symmetrical so that the two $5S^{2+}$ isomers were identical. In our case, the dissymmetry of the bidentate chelate obviously induced an energy difference between the two isomeric pentacoordinated species. We call them $5S_{th}^{2+}$ and $5S_{photo}^{2+}$ as they derive by ligand abstraction from the two starting isomers R_{th}^{n+} and R_{photo}^{n+}, respectively. We call $5TS^{2+}$ the pentacoordinated transition state of the isomerisation process.

Compared stabilities of the pentacoordinated species $5S_{th}^{2+}$ and $5S_{photo}^{2+}$: In absence of detailed theoretical calculations with ligand **29**, it was difficult to evaluate the electronic influence of the mesityl group on the relative stability of $5S_{th}^{2+}$ and $5S_{photo}^{2+}$. Its well-known electron-donor properties probably create a dissymmetry between the two nitrogen atoms of the chelate, but this effect was difficult to quantify. Steric factors were easier to evaluate. A side view of the X-ray structure of $\mathbf{36}_{th}^{2+}$ showed that the methyl group in para-position on the mesityl group was bumping into the 4'-phenyl substituted terpyridine ligand (see Figure 25).

The C38-C48 bond indeed is not parallel to the C51-C55 bond, with an angle of 9.15° between the two directions showing a distortion of the mesityl group. The C17-C55 distance of 3.66 Å is short and the hydrogens of the methyl group are very close to the protons T_A or T_F (see Experimental Part for proton assignment; the anisylphenyl group is free to rotate around bond C8-C16). In a saturated complex, this steric hindrance is not high enough to lead to spontaneous expulsion of the monodentate ligand L as the monodentate ligand acts like a "wedge" that prevents

the phenanthroline moiety to rotate. But in a pentacoordinated species where this wedge has gone, steric hindrance would be high enough to induce a destabilisation of $5S_{th}^{2+}$, which would cause in this transient species the rotation of the phenanthroline moiety like a set spring to give $5S_{photo}^{2+}$.

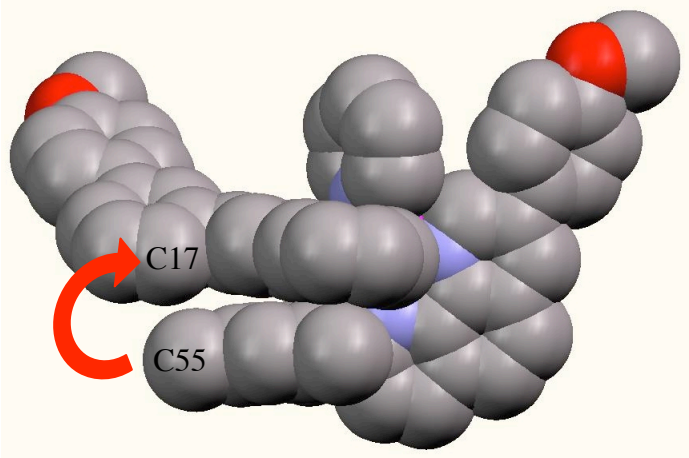

Figure 25: side view of complex $\mathbf{37}_{\mathbf{th}}^{2+}$ showing steric hindrance between C55 and C17.

As a conclusion, we propose that $5S_{th}^{2+}$ be higher in energy than $5S_{photo}^{2+}$. In terms of kinetics, $5S_{th}^{2+}$ would lie closer in energy to the isomerisation transition state $5TS^{2+}$ than $5S_{photo}^{2+}$, so that the first order rate constant k_{tp} would be higher than k_{pt}.

IV.2. Coordination of the entering ligand L'

When the entering ligand L' coordinates to the pentacoordinated species, it saturates the coordination sphere of the ruthenium and blocks the position of the phenanthroline like a new wedge. This step is probably a thermal bimolecular step occurring between L' and $5S_{th}^{2+}$ or $5S_{photo}^{2+}$, yielding respectively the two isomeric products P_{th}^{n+} or P_{photo}^{n+}. Scheme 36 gives the notations for these two processes.

Considering the experimental results, we make the hypothesis that the energy of TS_{th}^{*} is relatively independent from the hindering properties of L' and its ability to have donor-acceptor π-interactions, whereas for TS_{photo}^{*} the interactions between L' and the mesityl group are of primary importance:

- with large, spherical ligands, steric hindrance between L' and the mesityl group destabilises TS_{photo}^{*};
- with flat, π-acceptor ligands, acceptor-donor interactions between L' and the mesityl group stabilise TS_{photo}^{*}.

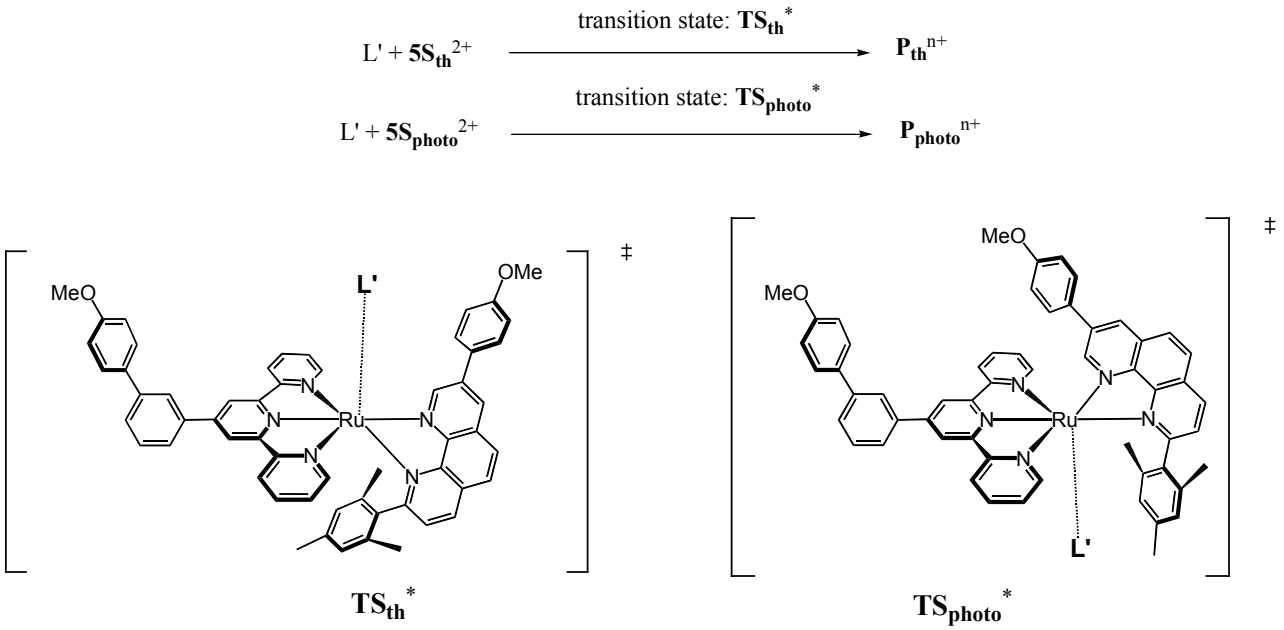

Scheme 36: notations for the bimolecular step of the dissociative mechanisms.

The last hypothesis can be reinforced by the fact that in the transition state the entering ligand L' has already begun to interact with the ruthenium ion, which probably reduces the electron density of the coordinating L' and enhances its interaction with the electron-rich mesityl group.

IV.3. The associative ligand substitution mechanism

In order to explain our experimental results, we needed to take into account an associative pathway for the thermal ligand substitution reaction. This process is composed of a single elementary step. Scheme 37 gives a representation of the associated transition states.

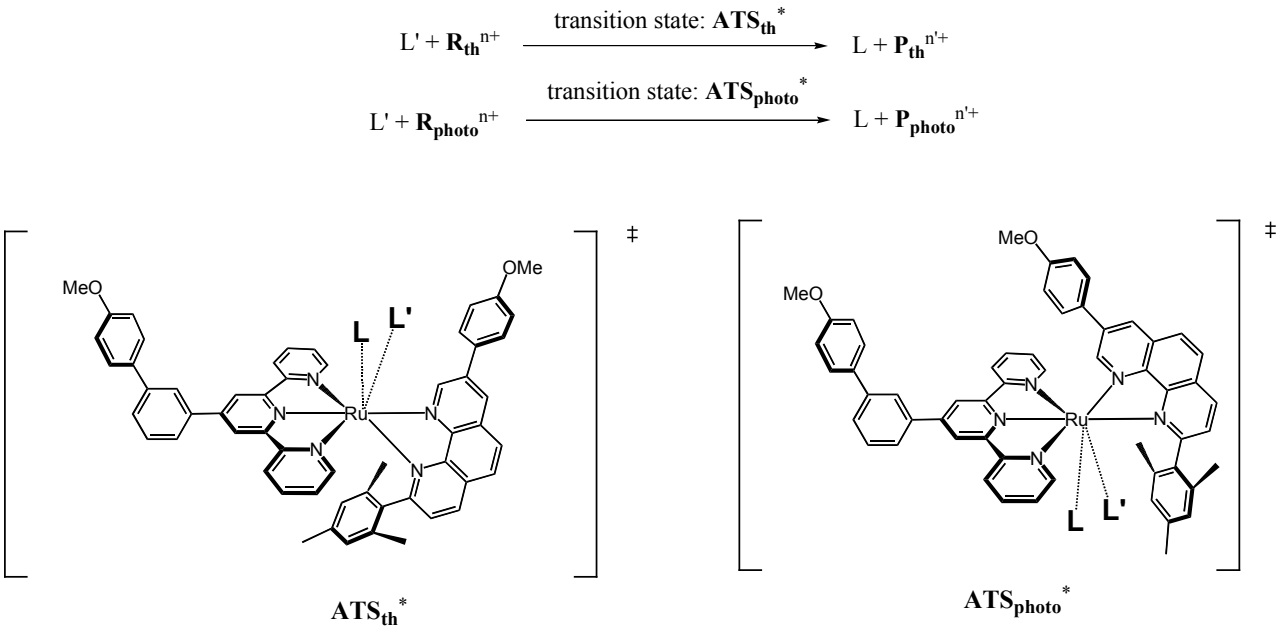

Scheme 37: notations for the associative pathway.

As depicted on these two representations, rotation of the phenanthroline is not possible during such a process as the entering ligand L' comes on the same side of the complex as the leaving ligand L. Both transition states ATS_{th}^{*} and ATS_{photo}^{*} have different free enthalpies depending on the isomer, L and L', and reaction conditions. However ATS_{photo}^{*} may be very sensitive to steric hindrance of ligand L' as the coordination sphere is very crowded.

IV.4. Interpretation of the experimental results

First experimental fact: whichever the starting isomer was, the photoinduced ligand substitution reaction always led to the photochemical isomer of the product.

This reaction being done at room temperature, we can admit that it was difficult to induce thermal decoordination of ligand L, so that in these "low temperature" conditions the dissociative thermal mechanism can be excluded (ligand exchange reactions at room temperature were never observed, except with L = H_2O). Depending solely on the nature of the starting product, the photoinduced pentacoordinated isomer may be either $5S_{th}^{2+}$ or $5S_{photo}^{2+}$. These two states are high in energy compared to the reagents and products. As they are coordinatively unsaturated they both react readily with L', which means that the free enthalpies of TS_{th}^{*} and TS_{photo}^{*} are relatively low. However at low temperature a bimolecular process is disfavoured compared to a monomolecular one as the former require the meeting of two chemical entities when the latter do not. $5S_{th}^{2+}$ being very close in energy to $5TS^{*}$, it isomerises to $5S_{photo}^{2+}$ quicker than it reacts with L' to produce $P_{th}^{n'+}$. On the contrary, the conversion of $5S_{photo}^{2+}$ into $5S_{th}^{2+}$ is slow because $5S_{photo}^{2+}$ is lower in energy, and the bimolecular reaction takes place preferentially, leading to $P_{photo}^{n'+}$. Hence starting either from R_{th}^{n+} or R_{photo}^{n+}, both photochemical processes performed at room temperature lead to the unique $5S_{photo}^{2+}$ species and, after coordination of L', to $P_{photo}^{n'+}$. The free enthalpy scheme consecutive to this analysis is given Figure 26.

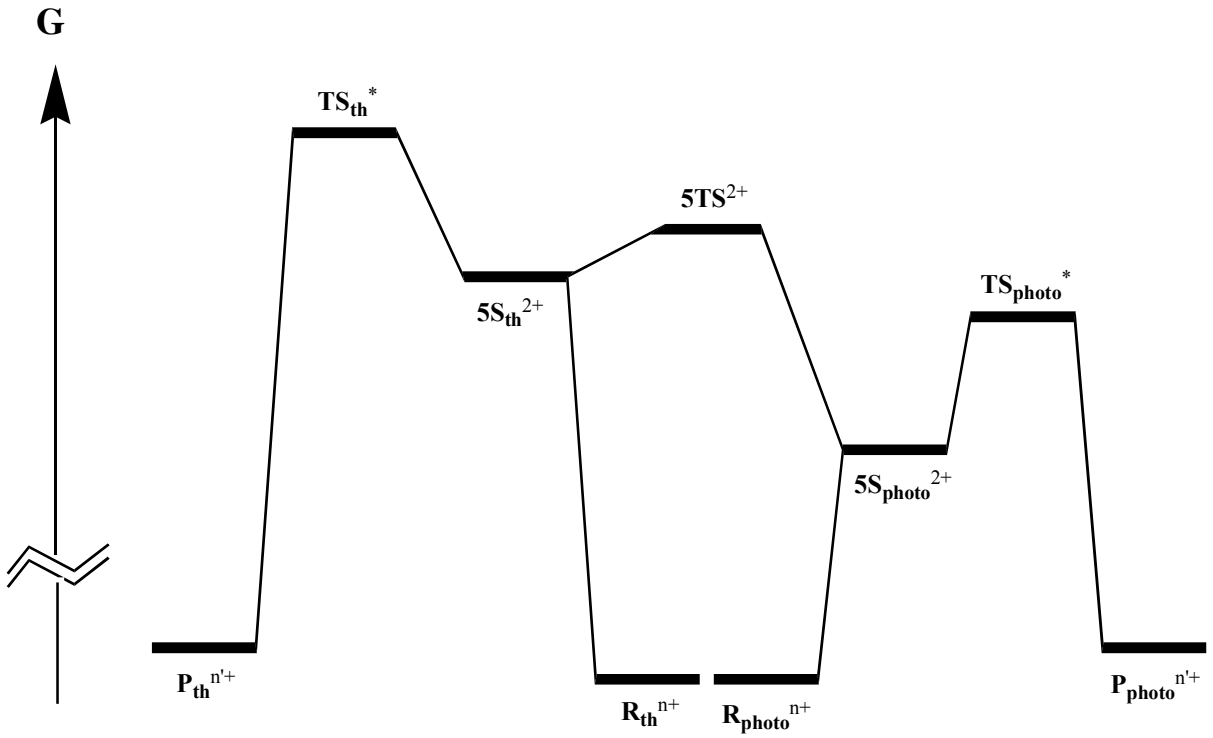

Figure 26: free enthalpy diagram for the photochemical dissociative pathway at RT.

Second experimental fact: the thermal ligand substitution reaction on R_{photo}^{n+} may, or may not, be followed by isomerisation, depending on the nature of the entering ligand L'.

In these "high temperature" conditions, both thermal associative and thermal dissociative mechanisms may take place. The associative mechanism is helped by the high concentration of the entering ligand used as the solvent. With sterically demanding ligands like DMSO, this mechanism will however not take place as the corresponding ATS_{photo}^{*} transition state lies too high in energy. With other flat ligands like pyridine, 3,5-lutidine, acetonitrile or benzonitrile, it explains the absence of isomerisation during the ligand exchange reaction.

The hypothesis of a dissociative mechanism needs to be considered in order to explain the isomerisation observed with L' = DMSO and Cl^-. Thermal expulsion of the monodentate ligand leading to the high-energy species $5S_{photo}^{2+}$ may happen as the temperature is high enough. At such temperatures, the energy difference between $5S_{th}^{2+}$ and $5S_{photo}^{2+}$ is not critical anymore, and isomerisation in both directions takes quickly place on the pentacoordinated species. The resulting thermal equilibrium between $5S_{th}^{2+}$ and $5S_{photo}^{2+}$ is in slight favour of $5S_{photo}^{2+}$, but the main parameter to take into account is the activation enthalpy of the bimolecular process.

As explained above, with big spherical ligands like DMSO (and to a lesser extend chloride ion) the interactions between the mesityl group and L' destabilise the TS_{photo}^{*} transition state (no π–π donor-acceptor interactions, high steric hindrance). These unfavourable interactions are not present on TS_{th}^{*}, so that in these conditions the pentacoordinated species lead preferentially to the

thermal isomer $P_{th}^{n'+}$. On the contrary, π–π donor-acceptor interactions between the mesityl group and flat entering ligands like benzonitrile or 3,5-lutidine may stabilise the corresponding TS_{photo}^{*} species compared to TS_{th}^{*} where they do not exist. In such solvents, the dissociative mechanisms would lead to the photochemical isomer $P_{photo}^{n'+}$. Figure 27 gives a free enthalpy diagram of the dissociative mechanism in thermal conditions.

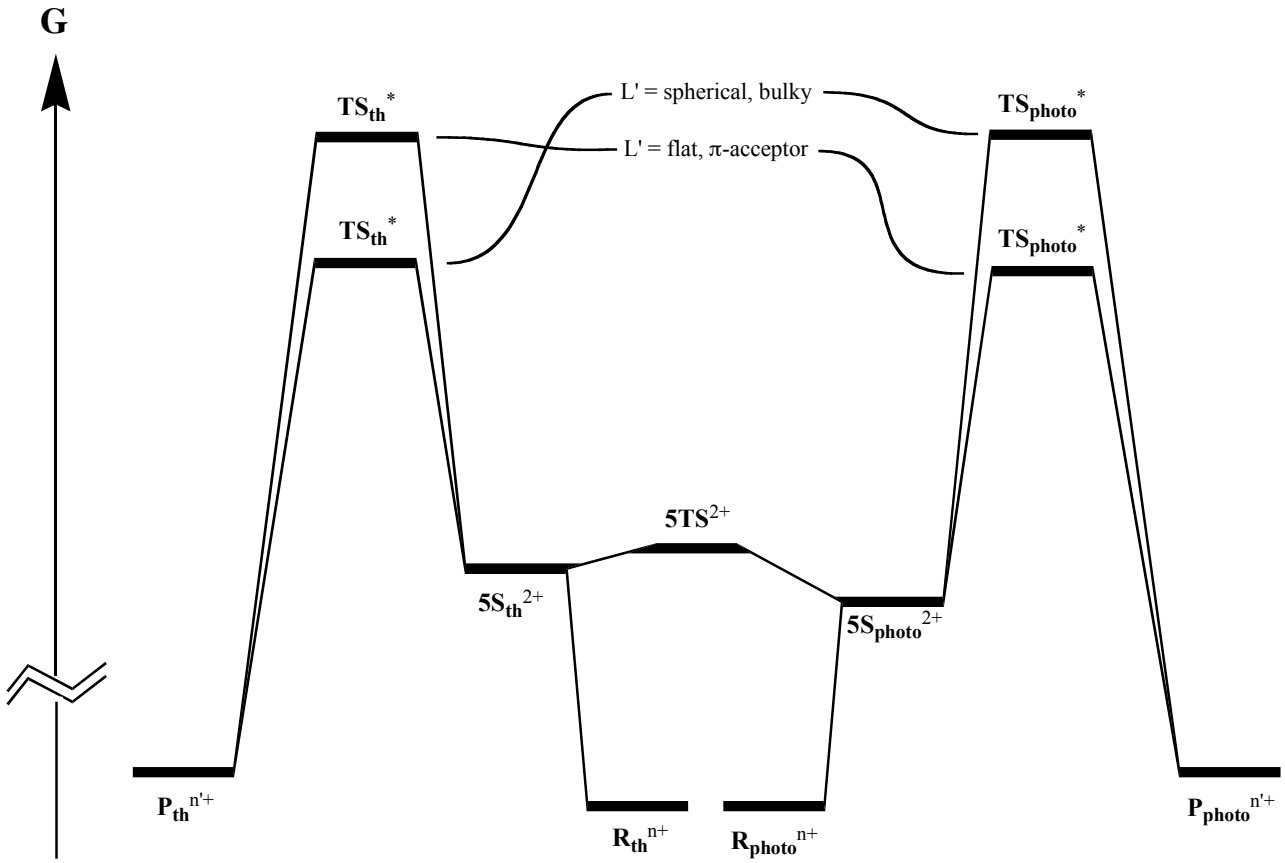

Figure 27: free enthalpy diagram for the thermal dissociative pathway at high temperatures.

In order to explain that the thermal substitution reaction done on R_{th}^{n+} with flat π-accepting ligands led exclusively to $P_{th}^{n'+}$, we have to admit that the associative mechanism is much faster than the dissociative mechanism. Therefore thermal reactions on thermal isomers lead to ligand substitution *without* isomerisation.

V. Conclusion

We synthesised and coordinated to ruthenium (II) two chelates **28** and **29** where **29** is a 2,8 dissymmetrically substituted phenanthroline. The series of ruthenium(II) complexes with the formula Ru(**28**)(**29**)$(L)^{n+}$ displays a classical reactivity in thermal conditions with L = Cl^{-}, CH_3CN or C_5H_5N. This classical reactivity was accompanied by an original isomerisation phenomenon: a quantitative 90° rotation of the phenanthroline moiety at room temperature under light irradiation, and the reverse motion heating in the dark at 140°C in dimethylsulfoxide. Although

photoisomerisation of double bonds is a classics in photochemistry, photoinduced isomerisation inside the coordination sphere of a metal has been reported only once by Durham *et al.*[127] In $Ru(bpy)_2(OH_2)_2^{2+}$ indeed, *trans* to *cis* and *cis* to *trans* isomerisation occurs via the pentacoordinated species derived from the starting complex by photoexpulsion of H_2O. This system was characterised by a trans/cis ratio of 3:2 at the photostationnary state. In our system, the photoinduced conversion to the photochemical isomer is quantitative so that we were unable to measure the ratio between isomers. Although quantitative calculation would be needed for a more complete comprehension of our system, we propose an analysis based on the interactions between the mesityl group of phenanthroline **29** and 1) the terpyridine **28** bearing a phenyl substituent in 4' position; 2) the monodentate ligand L' entering into the coordination sphere of the ruthenium during the substitution reaction. Our explanation relies on the role of the methyl in para position on the mesityl group, and our work should be continued by the replacement of the mesityl group in **29** by a 2,6-dimethylbenzene substituent.

Independently of the understanding of this isomerisation process, our system displayed a very efficient geometrical reorganisation that can be summed up in Scheme 38. It could be used in the design of molecular machines as a molecular knee-joint that can rotate of 90° in both directions.

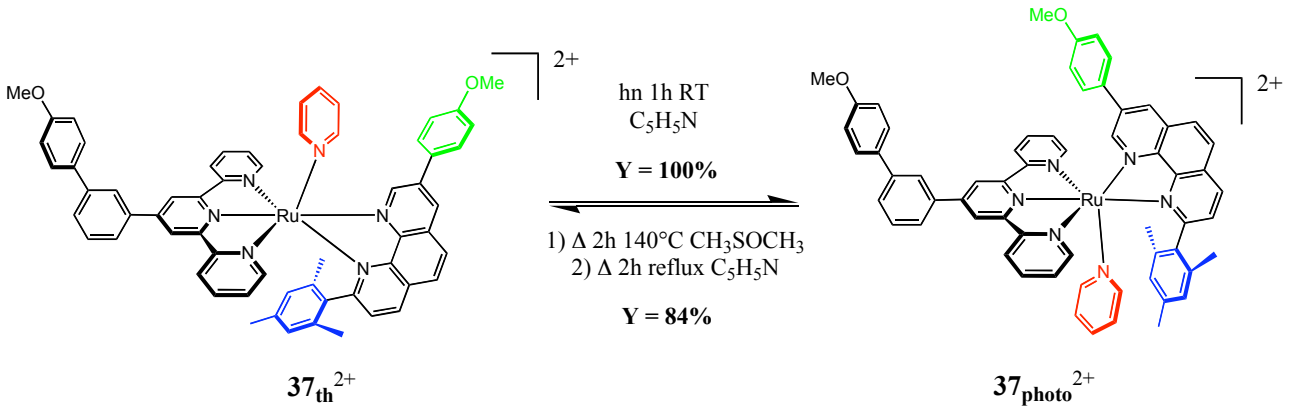

37$_{th}^{2+}$ **37**$_{photo}^{2+}$

Scheme 38: back and forth 90° rotation of a phenanthroline moiety in a $Ru(terpy)(phen)(L)^{2+}$ complex.

CHAPTER 4: INCLUSION OF A RU(TERPY)(PHEN)(L)$^{2+}$ COMPLEX IN A MOLECULAR MACROCYCLE WITH A PHOTOSWITCHABLE SHAPE

I. Introduction

In Chapter 3, we demonstrated that complex Ru(**28**)(**29**)(L)$^{2+}$, in which **28** was 4'-(3-anisylphenyl)-2,2';6',2"-terpyridine and **29** was the dissymmetric chelate 8-anisyl-2-mesityl-1,10-phenanthroline, existed as two isomers **37**$_{th}^{2+}$ and **37**$_{photo}^{2+}$. The rotational position of the phenanthroline moiety could be controlled either by irradiation at room temperature or by heating in dimethylsulfoxide. In our quest to macrocycles including a Ru(terpy)(phen)L^{2+} unit, we considered the use of **37**$_{th}^{2+}$ and / or **37**$_{photo}^{2+}$ as starting building blocks. Preliminary results showed indeed that coordination of terdentate, bidentate or monodentate ligands bearing terminal olefins on ruthenium could lead to substantial polymerisation and / or double bond migration. These processes prevented the isolation of an hypothetic Ru(terpy)(phen)(L)$^{2+}$ complex surrounded by terminal olefins as a precursor for macrocyclic species. We suspected that unsaturated Ru(terpy)(phen)$^{2+}$ transient species, notably with an aquo ligand, may be very reactive and lead to catalytic processes.[116, 117]

Another strategy towards macrocycles consisted in introducing the terminal olefins by performing organic chemistry on the periphery of ligands that were previously coordinated around ruthenium in a stable, saturated Ru(terpy)(phen)(py)$^{2+}$ complex. Pyridine being strongly coordinated in Ru(terpy)(phen)(py)$^{2+}$ complexes, it acted as a "protecting group" for the inorganic catalytic monodentate coordination site. We were able to develop an efficient synthesis of macrocycles on complexes of the type Ru(**28**)(**29**)(py)$^{2+}$. At the end of the synthesis the pyridine ligand could be replaced by a more labile acetonitrile, chloride or even water molecule for further use of these macrocycles in templated syntheses of catenanes and rotaxanes.

II. Synthesis of ruthena-macrocycles by a chemistry-on-the complex strategy

II.1. General frame

In the field of metal-templated macrocycle, catenane and molecular knot synthesis, one of the very successful approaches was the use of olefin metathesis as the cyclisation step.[47] As this

reaction is under thermodynamical control, it generates preferentially the smallest monomeric species so as to maximize the entropy of the system. Oligomers and polymers are slowly "repaired" into the monomeric macrocycle provided that the geometry of the precursor is favourable enough. The Grubbs' cyclisation reaction requires hence the synthesis of a precursor complex surrounded by flexible chains, each terminated by an olefin function. In the case of $Ru(phen)_2(L)^{2+}$ complexes, Mobian *et al* were able to synthesise a [2]-catenane by the introduction of a 6,6'-dimethylbipyridine chelate bearing olefin-terminated chains inside a macrocycle containing a $Ru(phen)_2Cl_2$ unit.[79, 128] A similar strategy gave disappointing results with $Ru(terpy)(phen)(L)^{2+}$ complexes (see Figure 28a). It led indeed mainly to polymerisation and, as a minor species, to a complex where the terminal double bond was isomerised into a $CH=CH-CH_3$ group. As we believed that the remaining monodentate coordination site on the $Ru^{II}(terpy)(phen)$ core was able to catalyse hydrogen migration reactions, the introduction of the olefins was performed on a saturated complex with a pyridine ligand as a monodentate protecting group. With this strongly coordinated ligand, we were able to perform a deprotection reaction of methoxy groups, a Williamson reaction at 60°C, an olefin metathesis reaction, a catalytic hydrogenation on the complex and a final ligand exchange reaction to give a macrocycle with the monodentate ligand inside the macrocyclic cavity (see Figure 28b).

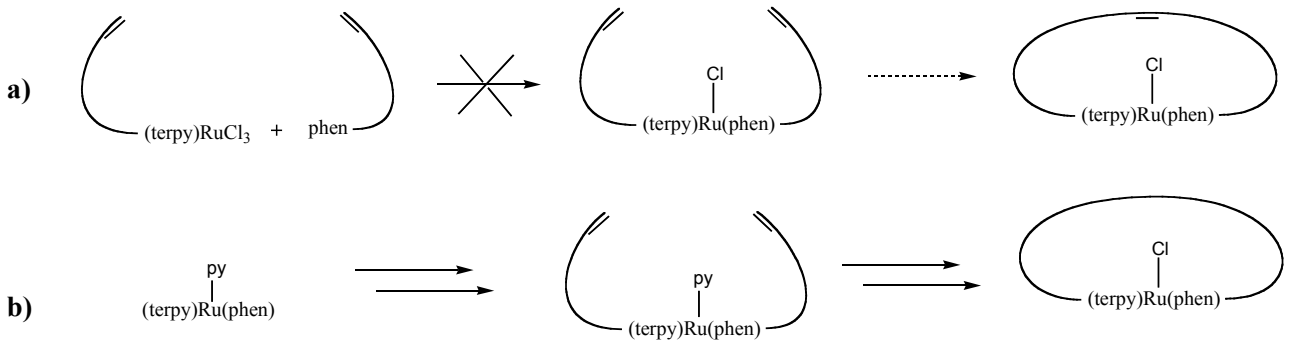

Figure 28: two strategies towards macrocycles including the $Ru(terpy)(phen)(Cl)^+$ unit

As already noted in Chapter 3, the X-ray structure of $\mathbf{37}_{th}^{2+}$ was obtained and showed that the two anisyl groups pointed towards the same side of the complex. The 54.0° angle between the two anisyl groups seemed acute enough for the synthesis of a macrocycle, although the torsional angle of 45.7° between the two groups was relatively higher than expected. The target molecule was a macrocycle where the monodentate ligand would be located inside the macrocyclic cavity. In terms of $Ru(\mathbf{28})(\mathbf{29})(py)^{2+}$, this situation fitted the geometry of the thermal isomer and not of the photochemical one. However, and despite complex $\mathbf{37}_{photo}^{2+}$ could not be crystallised, Chem3D models showed that the angle and torsional angle between the two anisyl groups were a lot smaller than in $\mathbf{37}_{th}^{2+}$, probably close to zero. As ring-closing metathesis is known to be very sensitive to the geometry of the precursor,[129] we considered to try both thermal and photochemical geometries of $Ru(\mathbf{28})(\mathbf{29})(py)^{2+}$.

The length of the flexible chains, another critical parameter in Grubbs cyclisation reactions, were determined on CPK and Chem3D models of the target thermal macrocycle: a total number of 18 methylene groups on the macrocyclic species seemed not too short for the macrocycle to be built. With such a length, a benzonitrile ligand was still able to fit in the inner monodentate coordination site of the Ru(terpy)(phen) complex without being too close from the alkane unit. We also used a longer polyethylene glycol chain made of a total of 22 atoms in order to vary the length and nature of the chain. As described below, the results were very dependent on the geometry of the inorganic complex and not so much on the length and nature of the chains.

II.2. Synthesis of the precursors

Both isomers $\mathbf{37}_{th}^{2+}$ and $\mathbf{37}_{photo}^{2+}$ were used as starting materials for the four precursor species $\mathbf{42}_{th}^{2+}$, $\mathbf{42}_{photo}^{2+}$, $\mathbf{43}_{th}^{2+}$ and $\mathbf{43}_{photo}^{2+}$. These precursor were synthesised by the two following steps:

- boron tribromide deprotection of the methoxy groups to give the phenol complexes $\mathbf{41}_{th}^{2+}$ and $\mathbf{41}_{photo}^{2+}$;
- Williamson reaction with either 10-bromo-dec-1-ene or 3,6-dioxa-8-bromooctyl allyl ether to give the precursors $\mathbf{42}^{2+}$ and $\mathbf{43}^{2+}$.

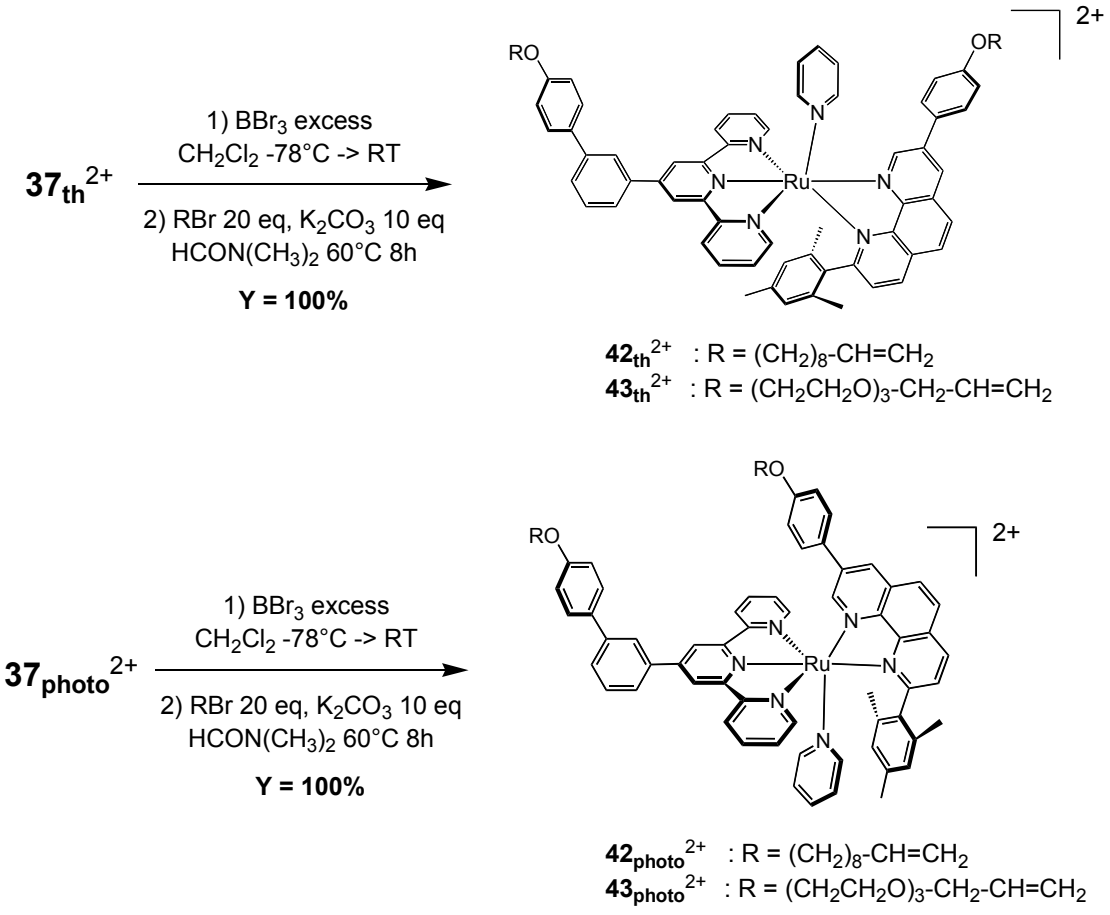

Scheme 39: synthesis of the precursors for the Grubbs cyclisation.

Both steps were quantitative with straightforward purification procedures. They showed that the Ru(terpy)(phen)(py)$^{2+}$ inorganic centre was stable to BBr_3 at room temperature and to basic conditions in dimethylformamide at 60°C. Scheme 39 describes the synthesis of the four precursors. They could be prepared on a 50 mg scale and were analysed by high-resolution electrospray mass spectroscopy, proton and carbon NMR. All carbon peaks could be assigned due to ^{1}H-^{13}C HSQC and HMBC correlation experiments.

II.3. Macrocyclisation of the precursors

We used Grubbs' 1st generation catalyst in order to realise the cyclisation by olefin metathesis. The two isomers of each precursor **42**$^{2+}$ and **43**$^{2+}$ reacted very differently:

- the thermal isomers needed 5 to 7 days to complete the reaction. Once the oligo- / polymeric species were removed, the crude product was still a mixture of two different complexes. The less polar fraction was shown by mass spectrometry to be the monomer, whereas the more polar fraction was a 4+ complex corresponding to the dimer. Careful NMR analysis revealed that this dimer was a 1:1 mixture of two inseparable products. We analysed this mixture as the statistical distribution between the terpy-phen-terpy-phen and the terpy-phen-phen-terpy regioisomer. With the alkane chain the monomer : dimer ratio was 21 : 25%; with the polyethylene glycol chain it was 26 : 28%.
- the photochemical isomer reacted in only 2 days yielding one major product. ESMS showed that this product was a +2 species, hence the monomeric macrocycle. The isolated yields were 78% with the alkane chain and 83% with the polyether chain.

As can be seen, the two geometries led to very different results relatively independently of the length of the chains (provided that they were long enough!): in the thermal isomer, the 60° angle between the directions of the anisyl groups was relatively high, whereas in the photochemical isomer both anisyl groups were almost parallel to each other, which put the olefin function very close to each other. This resulted in a unique monomeric macrocycle **44**$_{photo}^{2+}$ and **45**$_{photo}^{2+}$ in the latter case, whereas the former led to a bad yield in monomers **44**$_{th}^{2+}$ and **45**$_{th}^{2+}$ and formation of their dimers.

As we suspected that olefins were fragile during ligand substitution on Ru(terpy)(phen)(L)$^{2+}$ complexes, we reduced the macrocycles **44**$^{2+}$ and **45**$^{2+}$ before any ligand exchange reaction was undertaken. This last step was catalytically realised using hydrogen in presence of Pd/C. It quantitatively afforded the four corresponding macrocycles with $(CH_2)_{18}$ alkane (**46**$_{th}^{2+}$ and **46**$_{photo}^{2+}$)

or $(CH_2CH_2O)_3$-$(CH_2)_4$-$(CH_2CH_2O)_3$ polyethylene glycol ($\mathbf{47_{th}}^{2+}$ and $\mathbf{47_{photo}}^{2+}$) chains. These two last steps are described on Scheme 40. The macrocycles were prepared on a 30 mg scale.

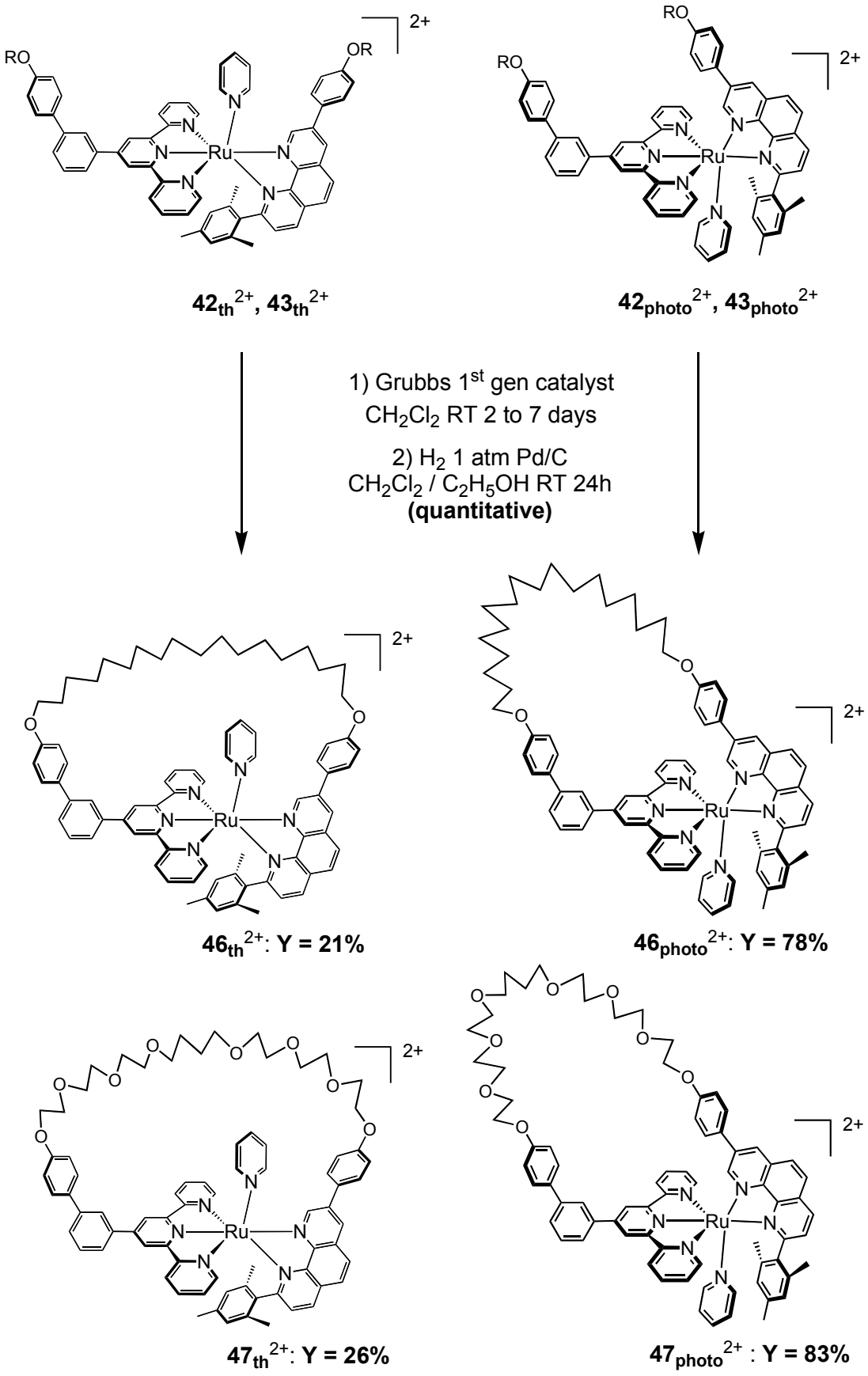

Scheme 40: last two steps and chemical structures of the four reduced ruthena-macrocycles.

III. Ligand exchange and isomerisation experiments on the macrocycles

III.1. Experimental results

Knowing the reactivity of the acyclic complexes $\mathbf{37}_{th}^{2+}$ and $\mathbf{37}_{photo}^{2+}$, we submitted their macrocyclic derivatives to the same reaction conditions than described in Chapter 3. These experiments led to the following results:

- irradiation of $\mathbf{46}_{th}^{2+}$ or $\mathbf{47}_{th}^{2+}$ with visible light at room temperature in pyridine yielded quantitatively $\mathbf{46}_{photo}^{2+}$ or $\mathbf{47}_{photo}^{2+}$, respectively;
- heating $\mathbf{46}_{photo}^{2+}$ or $\mathbf{47}_{photo}^{2+}$ two hours in DMSO at 140°C, precipitation of the supposed DMSO intermediate and heating two hours in pyridine, acetonitrile or an acetone solution of tetraethyl ammonium chloride gave with 80 to 100% yield the thermal macrocycles having respectively a C_5H_5N, CH_3CN or Cl^- monodentate ion coordinated inside the macrocyclic cavity (the analogues of $\mathbf{46}_{th}^{2+}$ with a CH_3CN, Cl^- or DMSO ligand replacing the intracyclic pyridine ligand are noted $\mathbf{48}_{th}^{2+}$, $\mathbf{49}_{th}^{2+}$, and $\mathbf{50}_{th}^{2+}$ respectively);
- back-isomerisation of $\mathbf{46}_{photo}^{2+}$ or $\mathbf{47}_{photo}^{2+}$ in 3,5-lutidine or benzonitrile was not observed in the dark at 140°C; in these conditions ligand exchange occurred to give quantitatively the photochemical macrocycles with a 3,5-lutidine or a benzonitrile ligand coordinated outside the ring cavity (the compounds with an alkane chain are noted $\mathbf{51}_{photo}^{2+}$ and $\mathbf{52}_{photo}^{2+}$, respectively);

To sum up these results, there were no observable differences in reactivity between the acyclic and the macrocyclic complexes.

III.2. Discussion

It was *a priori* difficult to predict whether the presence of the alkane or the polyether chains would change the reactivity of $\mathbf{46}^{2+}$ and $\mathbf{47}^{2+}$ complexes towards isomerisation of the phenanthroline moiety. A chain that would be too short would prevent the formation of the thermal isomer, like a short string attached to the extremities of scissors prevents the opening of it. On the contrary, a chain that would be too rigid would prevent the formation of the photochemical isomer, like the rifle in the crocodile's mouth of Tintin in Congo saved the young man from being eaten. Alkane chains are known for their tendency to prefer an "all *trans*" conformation, but the induced stabilisation may not be very high compared to other steric and electronic effects. The fact that the macrocyclic complexes behaved exactly the same way than the acyclic ones proved that the two chains that we used were neither too short, nor too stiff.

As a result, we can consider that the "inorganic part" of complexes $\mathbf{46}^{2+}$ and $\mathbf{47}^{2+}$, composed of interconnected rigid aromatic cycles coordinated to the ruthenium atom, behaved like a molecular twizer that can be photochemically opened and thermally closed. To its extremities were attached a flexible string that did not interfere with this motion and was, depending on the position of the twizer, either extended or not.

III.3. Analysis of the conformations of the flexible chains

In the crystal structure of $\mathbf{37}_{\mathbf{th}}^{2+}$ the O1-O2 distance was 17.89 Å. Chem3D molecular modelling calculations predicted that this distance could be shortened by rotation of the C8-C16 single bond. The minimum value of 15.9 Å was obtained in the conformer where the directions of the two anisyl groups were included in the plane of the phenanthroline. Unfortunately $\mathbf{37}_{\mathbf{photo}}^{2+}$ could not be crystallised, but the same molecular modelling analysis performed on this isomer gave as the shortest value 6.3 Å. Keeping in mind that molecular modelling gives only an evaluation of the distances, we could however deduce from this analysis that the O1-O2 distance in the thermal isomer was two to three times bigger than in the photochemical isomer.

In complexes $\mathbf{46}_{\mathbf{th}}^{2+}$ and $\mathbf{47}_{\mathbf{photo}}^{2+}$ where a flexible chain has been attached to these oxygen atoms, the huge variation of the O1-O2 distance may lead to a dramatic change in the conformation of the C18 alkane chain. Here again, as monocrystals of $\mathbf{46}_{\mathbf{th}}^{2+}$ and / or $\mathbf{46}_{\mathbf{photo}}^{2+}$ could not be grown, we made molecular models of these two macrocycles. Figure 29 depicts one particular conformer for each complex $\mathbf{46}_{\mathbf{th}}^{2+}$ and $\mathbf{46}_{\mathbf{photo}}^{2+}$.

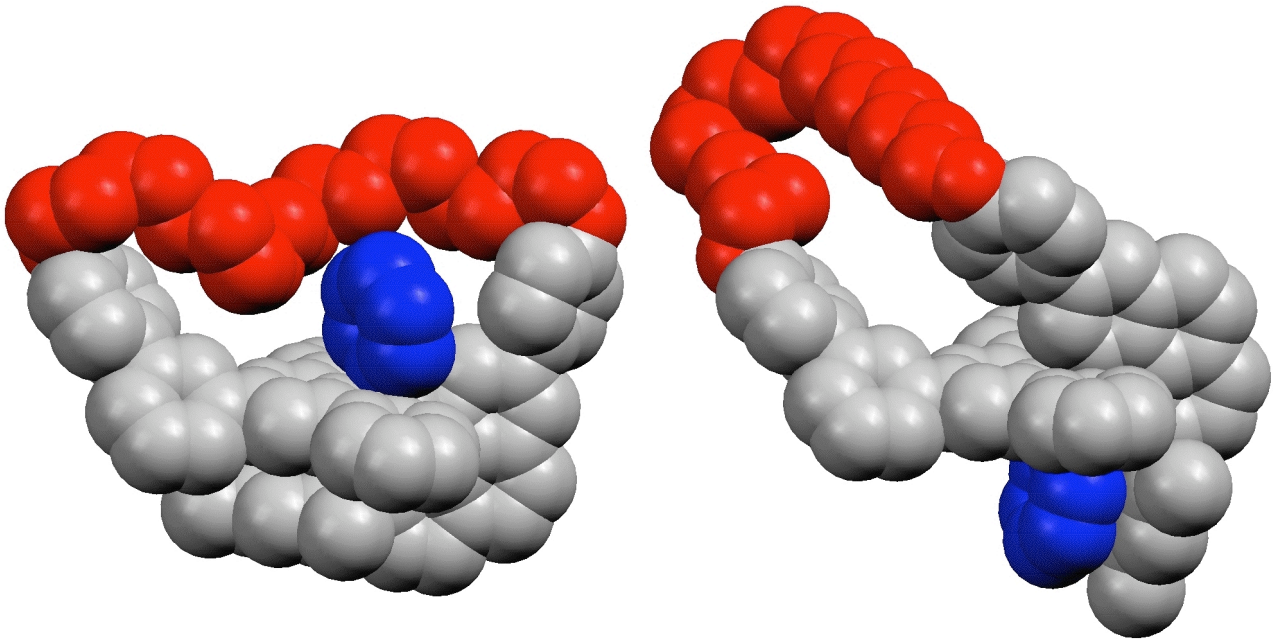

Figure 29: Chem3D models of $\mathbf{46}_{\mathbf{th}}^{2+}$ and $\mathbf{46}_{\mathbf{photo}}^{2+}$; the C18 alkane chain is in red and the pyridine ligand in blue. Hydrogen atoms have been omitted for better clarity.

One has to keep in mind that the flexibility of an alkane chain is difficult to be analysed on *one* of its conformers, but should be proved by a measure of the flatness of its conformational hypersurface. As a proof for this, the number of "*gauche*" conformations was measured in these two conformers. In $\mathbf{46}_{th}^{2+}$ seven C-C bonds in a *gauche* conformation were found whereas in $\mathbf{46}_{photo}^{2+}$ only five *gauche* single bonds could be seen. This result is counter-intuitive as one would think that in $\mathbf{46}_{th}^{2+}$ where the O1-O2 distance is longer, the alkane chain is less free to move and hence has more C-C bonds in *trans* conformation. On the contrary, in $\mathbf{46}_{photo}^{2+}$ the O1-O2 distance is shorter and for the same chain length the mobility of the chain and hence the number of bent *gauche* conformation should be higher. As appeared on the right picture of Figure 29, a lot of C-C bonds may be in *trans* conformations in the photochemical isomer. Actually, the mobility of the chain should better be expressed in terms of the number of possible conformers that have a non-zero probability to exist in solution; it is not linked to the number of *gauche* or *trans* conformations.

Such a number is a parameter that was impossible to measure experimentally. In NMR spectroscopy, the CH_2 signals that were in the middle of the chain were lost in the 1.0 to 1.5 ppm region. This lack of resolution prevented us to run variable temperature experiments that could have shown a difference in chain mobility between $\mathbf{46}_{th}^{2+}$ and $\mathbf{46}_{photo}^{2+}$. Figure 30 depicts the change of NMR spectrum of the alkane chain when going from one to the other isomer.

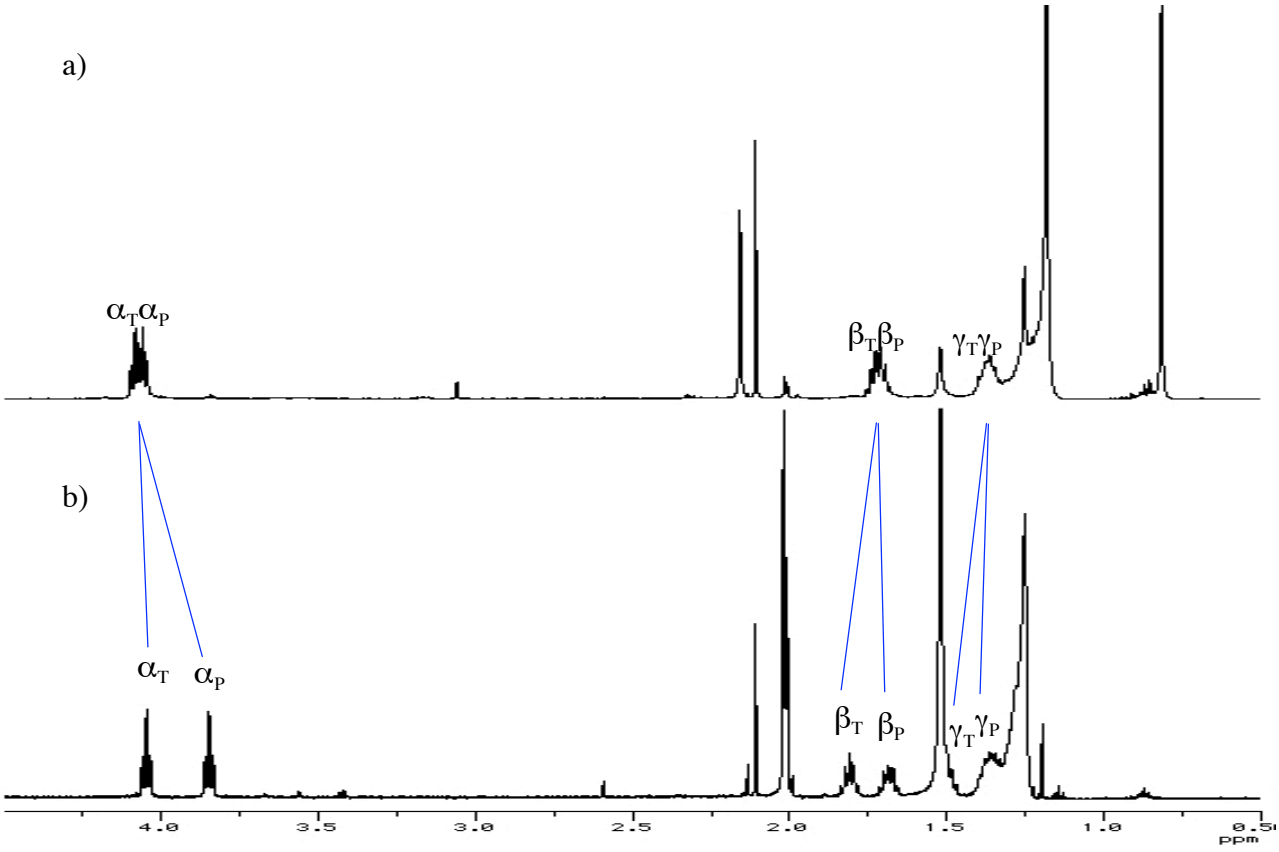

Figure 30: 500 MHz NMR spectra of the C18 alkane chains in complexes $\mathbf{46}_{th}^{2+}$ (a) and $\mathbf{46}_{photo}^{2+}$ (b); scale is 4.5-0.5 in CD_2Cl_2.

As can be seen, most inner methylene groups of the chain are hidden in the 1.4-1.2 ppm region, and only the α, β and γ signals could be clearly distinguished (see Experimental Part for complete proton assignation). The ^{3}J coupling constants for these three peaks were not conclusive about the conformation of the alkane chain. The only measurable data was the broadening of the peaks going from α_T,α_P to γ_T,γ_P.

In polyethylene glycol chains each methylene signal appears as a multiplet (instead of a quintet in alkanes), although each oxygen atom cuts the coupling scheme by isolation of the O-CH_2CH_2-O units. However, the chemical shift scale is much wider and spans from 5.0 to 3.0 ppm, which enables to assign each signal at 500MHz. Figure 31 gives the NMR spectra of $\mathbf{47}_{th}^{2+}$ and $\mathbf{47}_{photo}^{2+}$.

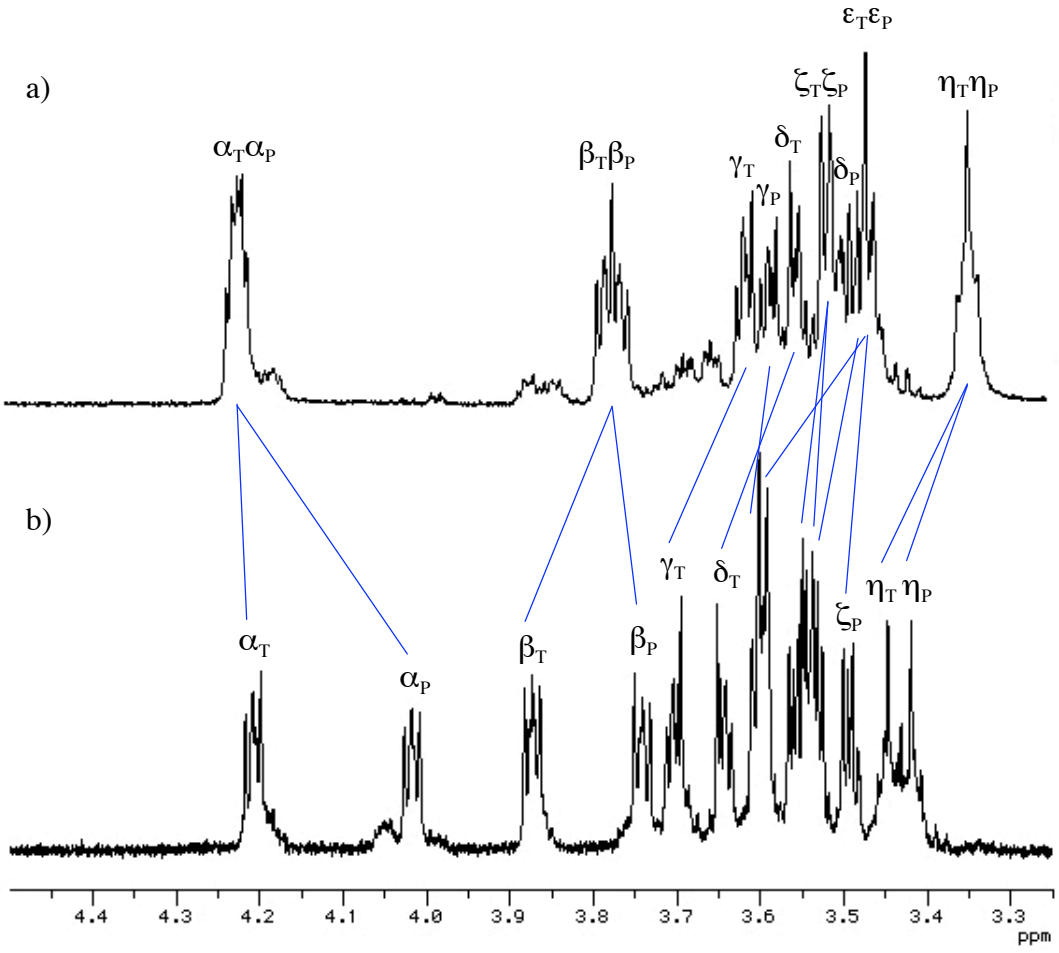

Figure 31: 500 MHz NMR spectra of the polyether chains in $\mathbf{47}_{th}^{2+}$ (a) and $\mathbf{47}_{photo}^{2+}$ (b). Scale is 4.5-3.25 ppm in CD_2Cl_2.

These two NMR spectra confirm the better resolution obtained using polyethylene glycol chain: all the individual signals could be assigned, at least on 2D experiments. However, the inherent directionality of the chain induced by the terpy → phen dissymmetry was not enough marked on the thermal isomer, and the resulting resolution was again too low to enable efficient conformational analysis based on coupling constants, even at 500MHz.

In conclusion, the NMR resolution of the spectra for macrocyclic complexes $\mathbf{46}_{\mathbf{th}}^{2+}$, $\mathbf{46}_{\mathbf{photo}}^{2+}$, $\mathbf{47}_{\mathbf{th}}^{2+}$ and $\mathbf{47}_{\mathbf{photo}}^{2+}$ were not high enough to analyse quantitatively the conformational change induced by the isomerisation of the phenanthroline. However, qualitative analysis of the spectral data and molecular modelling unambiguously demonstrated that this conformational change *was* dramatic due to the two- to three-fold change of the O1-O2 distance during the photochemically induced rotation of the phenanthroline.

IV. Conclusion: control of the conformation of a flexible chain and photochemically controlled geometry of a molecular ring

Unlike molecular elements bearing nitrogen atoms like polypyridine, poly-bipyridine and poly-phenanthroline ligands,[130, 131] flexible alkane chains do not bear any heteroatoms that would enabled them to be pre-organised. In a similar manner, polyethylene glycol chains (PEG) bear oxygen atoms that are not very prone to coordination on metals, except in macrocyclic (crown ether) or polycyclic (cavitands) species where the presence of cooperative effects enable the selective capture of some adapted spherical metal atoms.[63] For this reason, and also because they are very flexible, controlling the conformations of acyclic PEG chains is also difficult. In order to realise that, one has to use stiff elements to force the chain to adopt a given set of conformations. Such control can be realised either by managing adequate pocket-like van der Waals interactions along the chain, or by changing the positions of its extremities. Some interesting experimental results have been obtained by enclosing alkanes or PEG chains inside self-assembled pockets,[132-135] by packing them on metal surfaces like corn ears in a corn field,[136, 137] or by wrapping the chains in a helical fashion around polyalkyne wires by metal-templated.[138] However, to our knowledge switching processes controlled by an external signal and inducing a major conformational change of a flexible alkane or PEG chain has not been achieved yet.

In our work, a stiff Ru(terpy)(phen) subunit could be inscribed in a molecular ring by organic chemistry performed on the two isomers of complex Ru(**28**)(**29**)$(py)^{2+}$. The pyridine ligand was used as an inorganic protecting group for the monodentate coordination site. In order to connect the terpy unit and the phen motif, two different linkers were used: a $(CH_2)_{18}$ alkane chain and a $(CH_2CH_2O)_3$-$(CH_2)_4$-$(OCH_2CH_2)_3$ polyether chain. In both cases, the photochemically induced isomerisation of the ruthenium complex and the reverse thermal reaction were observed with no change compared to the acyclic species (see Chapter 3). This controlled rotation motion of the phenanthroline moiety around the ruthenium knee-joint induced a major change in the conformations of the flexible chains. This conformational reorganisation was due to the two- to three-fold variation of the distance between the two oxygen atoms hooking the extremities of the

molecular string to the complex. In parallel, the monodentate pyridine ligand located outside the ring in the photochemical isomer, moved to an intracavity position in the thermal isomer (see Figure 32). This macrocycle including a Ru(terpy)(phen) unit with the coordination site for a monodentate ligand inside the ring should be used for metal-templated synthesis of molecular object with non-trivial topologies like [2]-catenanes and rotaxanes.

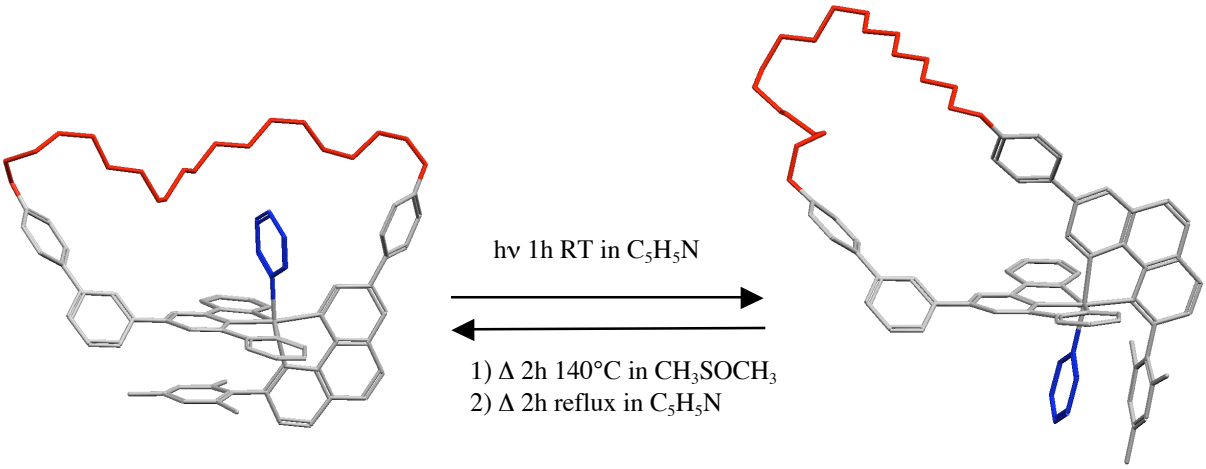

Figure 32: molecular knee-joint controlled by light. In red: the C18 alkane molecular string rearranges in order to fit its conformation to the geometry of the complex. In blue: pyridine acts like a molecular wedge by blocking the coordination sphere of the ruthenium. The structures are calculated Chem3D molecular models (for an X-ray structure of $\mathbf{46}_{\mathbf{photo}}^{2+}$, see Annex E).

ANNEX A: BROWNIAN MOTORS AND THE BROWNIAN RATCHET MODEL

I. Introduction to Brownian motion and "nanomachines"

I.1. Brownian motion

As shortly stated in Part I of the General Introduction, the Brownian nature of the world at the nanoscale cannot be ignored, as far as molecular machines are concerned. In a standard macroscopic representation, a machine is a device that continuously transforms a storable energy into another kind of energy, storable or not; during this conversion a continuous motion is produced. For example, the motor of a car transforms the chemical energy stored in alkanes into translational kinetic energy of the vehicle. Such a transformation occurs due to the rotation of an ensemble of interconnected axles attached to the wheels that are themselves in contact with the road. In such a machine, a sudden inversion of the direction of rotation of the motor is impossible because of inertia. Once a forward motion has begun, one needs to slow it down and stop it before the backward direction can be taken. A car also works because gravity forces the wheels to touch the road: the rotation of the wheels induces the translation of the car. A car floating in the see is useless: the spinning wheels will not induce motion of the vehicle, but simply heat the water.

In order to represent what Brownian motion is, one should keep in mind that a water molecule is as heavy compared to a 500 kDa protein like ATPase as a 18 g hailstone compared to a "small" 500 kg car; moreover, thermal agitation at 300K gives a mean velocity to each water molecule equal to ≈650 $m.s^{-1}$. As a mean of comparison, the radius of an 18 g hailstone is roughly 15 mm, and in a normal hail the average velocity of the hailstone touching the ground is 10 to 15$m.s^{-1}$![139] In order to imagine the impact of water molecules on natural molecular machines, one should try to imagine the force of a wind that would speed up a Ø 3 mm falling hailstone from 15 to 650 $m.s^{-1}$…

The Brownian nature of the nanoworld is one of the most important parameters to take into account when trying to understand how natural molecular machines work. In such a world, inertia is negligible compared to the Brownian torque or force applied on nanomachines: this is called the Langevin approximation.[12] In addition, gravitational forces are always negligible with respect to electromagnetic interactions. These two approximations enable a better modelling of the mechanochemistry of molecular machines.

I.2. "Hard" and "soft" machines

Another critical difference between macroscopic machines and molecular biomachines lies in their energetic behaviour. In the macroscopic world, machines are "hard". That is to say, one has to hit a paddle or a piston (= increase the pressure on it) in order to give momentum to it and induce its motion. Contact with a hard surface is needed in order to transmit mechanical energy. In addition, even in the case of chaotic systems where the time-evolution cannot be determined with accuracy, the physics involved in macroscopic systems is definitely deterministic: an equation linking cinematic coordinates (position, speed, acceleration) and forces, derived from Newton's equation, can be generally written.

By contrast, molecular biomachines are "soft". On the energetic point of view, these proteins are always in equilibrium with their environment: their potential energy hypersurface is flat, and conformational rearrangements occur continuously under the influence of thermal noise. As most of their states have the same energy, they are all populated with similar probabilities.

Let us consider a solution with ATP, ADP, inorganic phosphate (P_i) and an ATP-fuelled biomachine (ATP synthase, kinesin or myosin, for example). A chemical equilibrium is involved, characterised by its ΔG:

$$ADP + P_i \rightleftharpoons ATP + H_2O \qquad (\Delta G)$$

On the chemical point of view, ATP-fuelled biomachines are catalysts for this equilibrium. On the thermodynamical point of view, the question to know whether this equilibrium is satisfied or not does not depend on the catalyst; it only depends on the activities (≈concentrations) of ATP, ADP and P_i (H_2O is the solvent). That is too say, there is no fundamental difference between the catalyst "at rest" and the same catalyst "working". When it is "at rest", both reactions ADP + P_i → ATP + H_2O and ATP + H_2O → ADP + P_i occur randomly, with random binding / unbinding of ATP, ADP and P_i to their catalytic sites. The probabilities of both reactions are the same, they are both high due to the presence of the catalyst, and the chemical system does not change, ie the concentrations of ATP, ADP and P_i remain the same. Because of the chemo-mechanical coupling inside the protein, random motion of each catalyst molecule also takes place in both directions, with a global zero "macroscopic" displacement.

If ATP is introduced in the solution, the nature of the catalyst does not change! The same binding-unbinding events as in the equilibrated situation will occur, with a higher probability for ATP binding than for ADP binding, however. The higher probability for ATP binding is solely due to the higher concentration of ATP. All individual states involving the catalyst, between "catalyst + ATP free in solution" and "catalyst + ADP and P_i free in solution", passing through "ATP bound to

the catalyst" and "ADP and P_i bound to the catalyst", are statistically populated like in the equilibrated situation. Chemo-mechanical coupling inside the protein transforms the free chemical enthalpy flux due to the chemical reaction "ATP hydrolysis" into free mechanical enthalpy, and macroscopic motion is observed. Such "directed" motion is due to the higher probability for the "forward" motion than for the "backwards" motion. In other words, directed biological motion at the nanoscale is a statistical event produced by disequilibrium in the concentrations of ATP and ADP. It is not produced by an explosion of ATP pushing a proteic piston into a proteic cylinder…

II. The Brownian ratchet model

The fascinating efficiency of natural molecular machines is due to the high-yield transformation of free chemical enthalpy into free mechanical enthalpy. This transformation, called "chemo-mechanical coupling", is difficult to model and needs further explanation. The catalyst is involved in a chemical reaction, which consists in molecules stochastically binding, un-binding and reacting together inside different catalytic sites. These phenomena occur under the permanent solicitation of Brownian motion. It is possible to build simpler artificial systems that model this chemo-mechanical coupling. We describe in this part several of these systems.

A very important characteristic of biomachines is that the potential energy associated to the interaction between the "moving part" of the protein and its "static part" is intrinsically asymmetric. Such asymmetry is due to the homochirality of natural proteins. During its random motion and when the equilibrium between ATP and ADP is reallised, why does the protein not move more in one direction than in the other? The "Feynman ratchet" [10, 17] is a mental exercise that enables to explain it: an asymmetric potential in a single-temperature thermal bath cannot lead to directed motion, as this would be in contradiction with the 2nd Law of Thermodynamics. In chemistry, only the energy levels of the different states involved in a catalytic process have to be taken into account, not the steepness of the potential energy curve between them. Researchers have tried to understand in which conditions a spatially periodic asymmetric potential would lead to directed motion. The "Brownian ratchet" model explains how Brownian motion is needed in order to induce directed motion in a periodically modified, spatially asymmetric potential.

II.1. Asymmetric potential

In a spatially periodic potential like the interaction of F_0 and F_1 units of ATPase or the interaction between actin and myosin, asymmetry comes from the chiral nature of natural proteins. Regarding artificial systems, molecules have been synthesised, and microscopic experimental setups have been built in order to generate asymmetric potentials. For example, the interaction

between the tripticene and helicene units in Kelly's molecular ratchet (Figure 33a) has been calculated by molecular modelling studies (Figure 33b).[140] The resulting curve is asymmetric, as rotation *according to* the helicity of the helicene or *against* it lead to different spring constants. In Ajdari's microscopic sorting device, an asymmetric ladder bearing 10 µm teeth was built by photolithography (Figure 33c).[20] The asymmetric spatial disposition of the interdigitated electrodes led to a spatially periodical electric potential that was asymmetric. In Faucheux's optical thermal ratchet, a system based on rotating mirrors and neutral density filters enabled to obtain a circular laser track with asymmetric local light intensity minima along the circle (Figure 33d).[18] Whatever the details of the asymmetric potential may be, it is generally modelled by the curve on Figure 33e: a saw tooth potential with a high steepness on the first part *a* of the period L, followed by a small steepness on the second part *b* of the space-period.

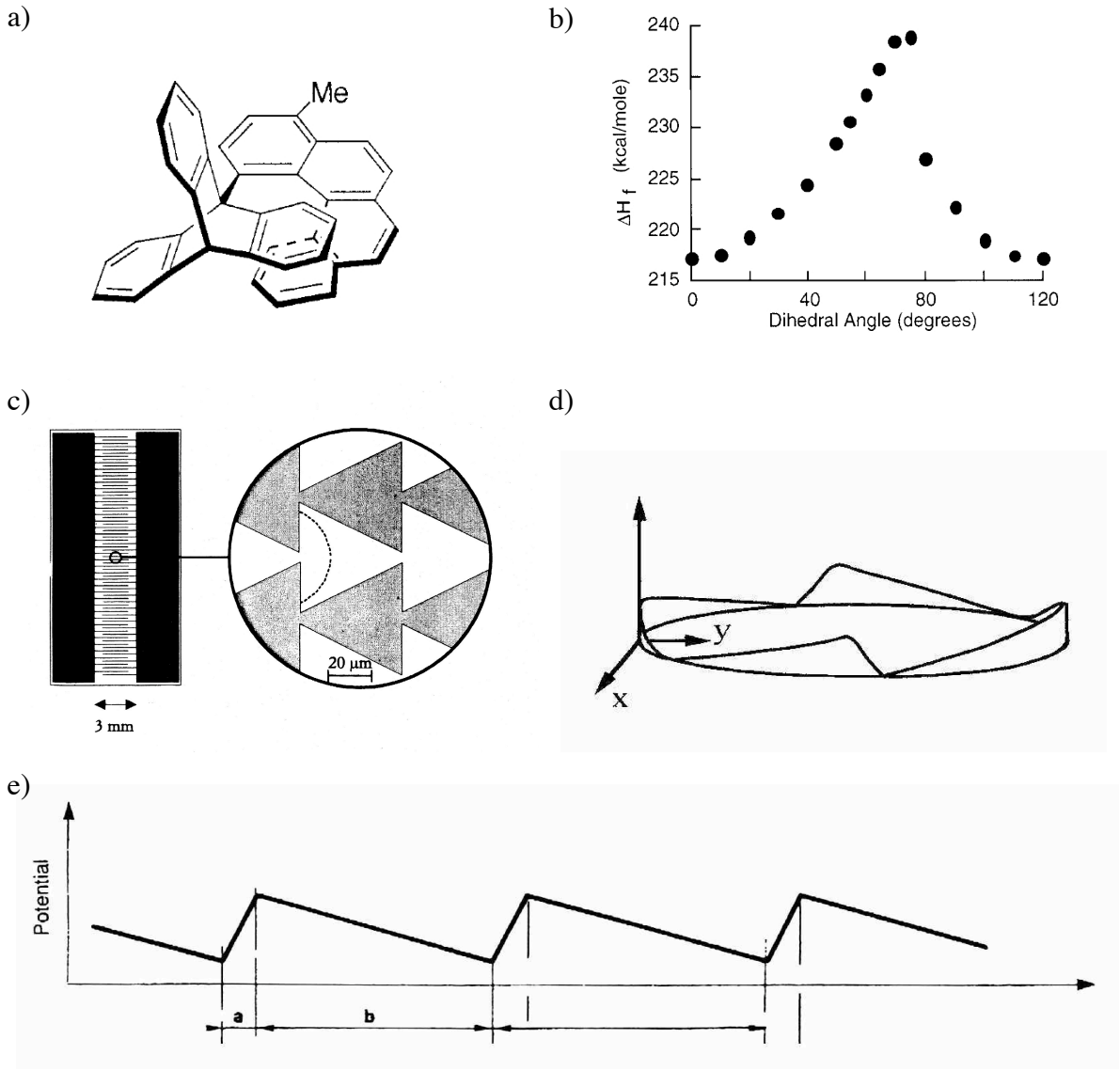

Figure 33: a) chemical formula of Kelly's molecular ratchet; b) calculated potential (ΔH_f) when the angle between tripticene and helicene evolves between 0 and 120°; c) interdigitated electrode used in Ajdari's Brownian ratchet sorting device; d) asymmetric light intensity in Faucheux's optical thermal ratchet; e) usual simple model for a spatially periodic asymmetric potential.

II.2. Modulation of the potential

Simple physical arguments are given here as an introduction. More detailed calculations can be found in the literature.[12, 19, 141, 142]

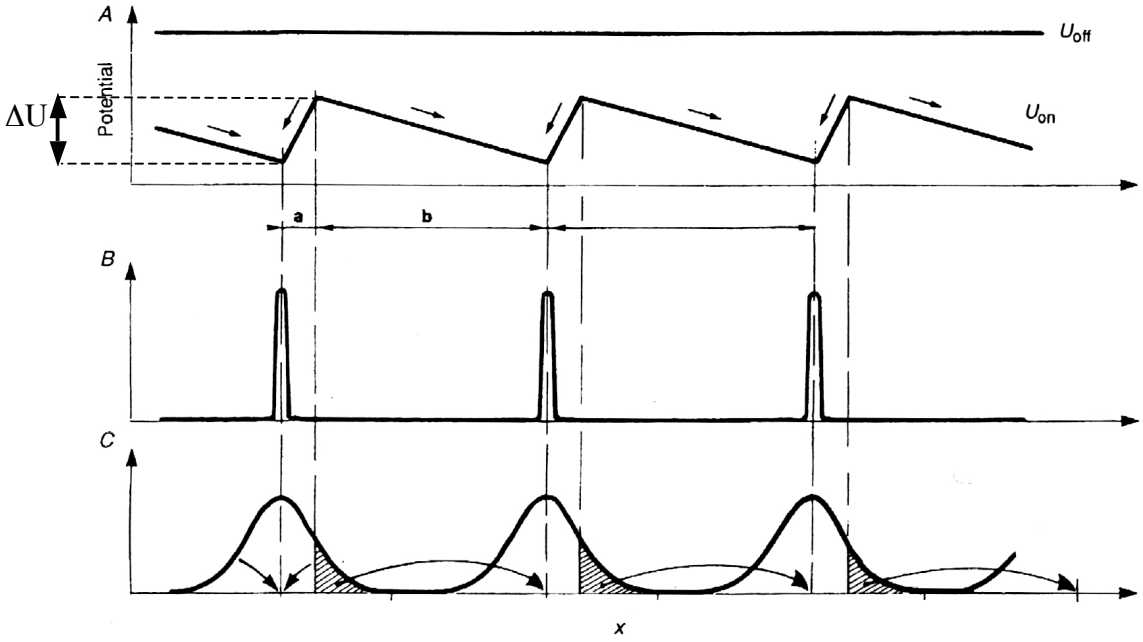

Figure 34: curve A: spatially asymmetric potential switched ON (U_{ON}) and OFF (U_{OFF}); curve B: spatial distribution of the system after the potential has been ON for a long time; curve C: spatial distribution of the system after a short time of free Brownian diffusion (potential OFF). Arrows indicate how the system moves after the potential has been switched ON again: dashed regions of curve C lead to motion towards the right; undashed regions lead to coming back to the initial position (arrows on curve A).

The following discussion refers to Figure 34, where x is an adimensional parameter representing the motion (rotation or translation). We consider that the potential energy of the system, E(x,t), is time-modulated by an external operator: it is switched ON ($E(x,t) = U_{ON}(x)$) and OFF ($E(x,t) = U_{OFF}$) regularly. Considering that the potential barrier ΔU is big at temperature T, if the potential has been ON for a long time, the spatial distribution of the system is represented curve B: all the minima have an equally high probability to be populated, with narrow Gaussian distributions depending on the ratio $kT/\Delta U$. Considering that the potential is switched off at a time t=0, diffusion will occur according to Brownian motion: after time t, the spatial distribution of the system will look like curve C: the Gaussian is all the more broadening as t evolves. If the potential is switched on again at time $t=\tau_{off}$, and if it remains ON for a long time τ, the spatial distribution of the system will evolve in order to recover the profile of curve B. In this process, the undashed region of curve C will lead back to the local minimum, which results in no global motion; but the dashed region due to the asymmetry of the potential will lead to a neat displacement towards the right of the system (arrows on curve C). If this process is repeated regularly in time, global motion

towards the right is obtained, although individual particles may sometimes go to the left or most often remain at their positions.

II.3. Critical parameters of the model

The main parameters of such a system are:

- the a/b ratio, which defines the asymmetry of the potential;
- the kT/ΔU ratio, which is linked to the intensity of the potential;
- the time τ during which the systems recovers its initial state after random diffusion;
- the time τ_{off} during which Brownian motion is taking place;
- the diffusion coefficient D of the system (or particles) in absence of the potential;
- the modulation period $\tau_{off}+\tau$;

In general, the evolution of the average global speed of the particles with respect to the time τ_{off} is bell-shaped, with an optimum value of τ_{off} for each diffusion coefficient D. Small modulation periods are needed in order to achieve many repetitions of the on/off cycle in a given time. However, it has been theoretically and experimentally proven that in many-particle systems the direction of the global motion is not only controlled by the steepness of the potential. It also depends, *both* in sign *and* amplitude, on many parameters like the diffusion coefficient D or the density of particles, for example.[143]

II.4. Controlled potential modulations

In Kelly's ratchet, the asymmetric potential could not be switched on and off or time-modulated because it was intramolecular interaction energy. As a result, directed motion was theoretically impossible and experimentally proven not to take place.[140]

In artificial systems based on electric fields or optics, the potential was switched on and off by simply manipulating the external device responsible for the potential. In the case of the interdigitated electrode of Figure 33c for example,[20] the metal electrodes were electrically linked to a generator, which enabled precise control of the values of ΔU, τ_{off} and τ. It was the first experimental setup in agreement with the Brownian ratchet model. Similar experiments have since then been developed by other teams.[144] In the optical thermal ratchet described in Part III, a neutral density filter was placed and removed periodically, leading either to the asymmetric circular pathway or to an homogenous laser track.[18]

II.5. Random potential modulations and chemical reactions

Theoretical studies showed that slight modulations of the potential, instead of "brutal" on/off switching, could also lead to directed motion.[145] In a similar way, perfect time-periodicity for the modulation of the potential is not required; under certain circumstances, randomly repeated modulations also enable directed motion to occur. As a result, chemical reactions are suitable tools for the modulation of the potential.[11] Binding or release of a molecule to / from a catalytic site is a stochastically occurring event. However, each time it may happen the potential energy hypersurface of the system evolves, going from one spatially periodic profile to another one.[146] Providing that at least one of this profile is "strong" (trapping) and another is "weak" (diffusion), directed motion may occur like in the Brownian ratchet model detailed above. Such a mechanism explains how chemical reactions may induce directed motion at the nanoscale. In such a case, the chemical free enthalpy flux released by the chemical reaction is transferred, via Brownian ratchet-type coupling, to mechanical free enthalpy, and the 2nd Law of Thermodynamics remains true!

III. Applications of the Brownian ratchet model

III.1. Experimental sorting of small-size particles

Figure 35a shows the neat displacement of 0.5 μm beads in an asymmetric ratchet similar to Ajdari's device.[144] The original interdigitated electrodes were designed in order to sort microscopic polymer beads or big molecules like DNA stands and proteins with respect to their sizes.[141] The average speed of the global displacement indeed is a function of D, τ_{off} and τ.[19] In a sample containing different particles of different sizes, for a given time-periodicity of the modulation different diffusion coefficients lead to different average speeds: after a while, separation of the particles with respect to their sizes should be achieved. Experiments with latex beads[20] followed the theoretical predictions, but aggregation phenomena and inter-particle interactions prevented the device to be really efficient. Since then, sorting machines based on 2D-Brownian ratchets were developed for DNA-analysis.[147-150] Figure 35b shows the result of one of them:[150] in a mixture of two fluorescently labelled DNA strands with two different masses, two traces can be seen after 70 minutes of electrophoresis. The performances of such a device is claimed to be 3 times better in terms of separation and 10 times better in terms of speed of fractionation than former devices.

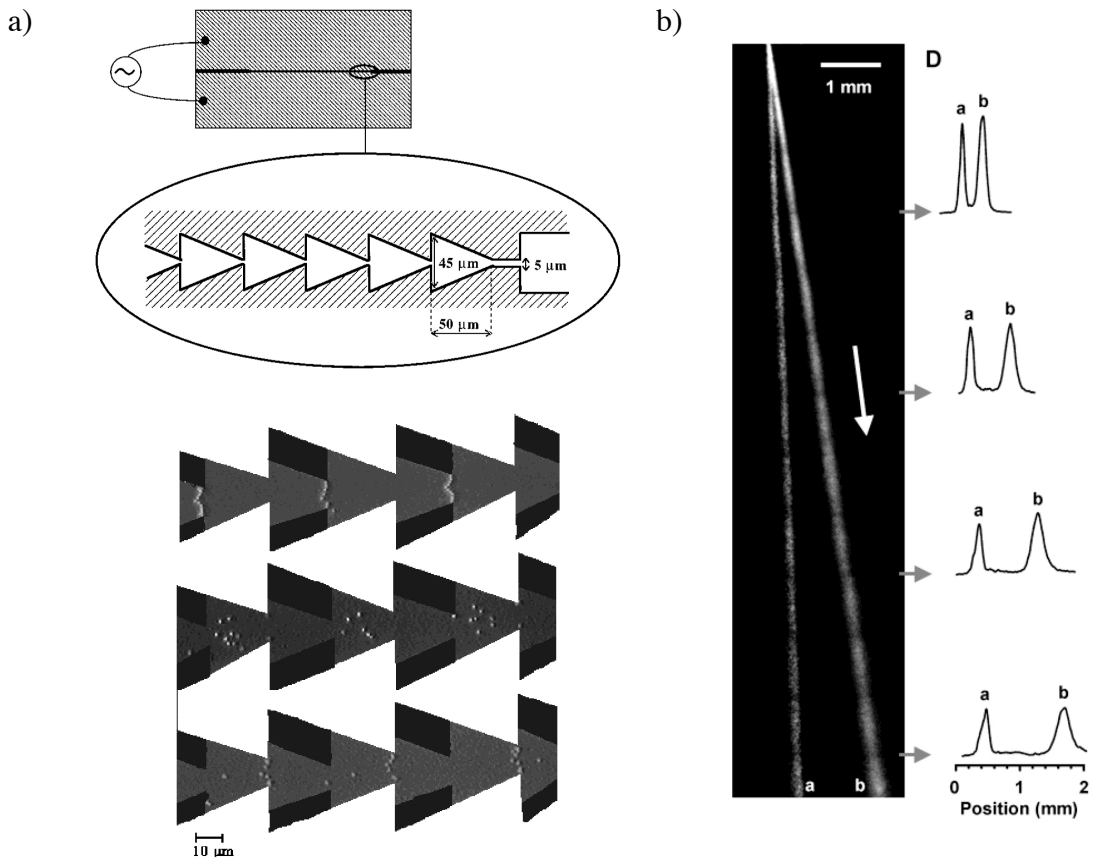

Figure 35: a) top: simple device based on asymmetric electrodes of Ajdari's type; bottom: direct observation of the migration of latex beads to the right; b) fluorescent micrograph for the separation of 48.5 and 164 kb DNA strands in Brownian 2D arrays. The mixture is injected on the top. The white arrow indicates the tilting of the flow with respect to the axis of the ratchet. Trace a: heavier DNA strand (164 kb); trace b: smaller DNA strand (48.5 kb). On the right: electrophoretograms at 3, 6, 9 and 12 mm from the injection point.

III.2. Optical thermal ratchet

This optical system described by Faucheux *et al*[18] was theoretically much more easy to understand than the electric sorting device of Ajdari *et al*[20], as single particles could be observed under the microscope. As a result, cooperative behaviours and aggregation effects were avoided. 1.5 mm diameter polystyrene beads are attracted towards regions of highest light intensity. A Ø 7 µm circular laser track was artificially created (Figure 36a) in order to confine the motion of the particles in one dimension around a circle. When the laser track was homogenous, Brownian diffusion occurred along the circumference (Figure 36b). Regularly, neutral density filters modified the light intensity along the track, so that it became spatially periodic with an asymmetric profile (Figure 36c). In this case, regions of highest intensity trapped the beads. As the asymmetric potential was periodically switched on and off, a global directed motion was observed depending on the values of τ_{off}, τ and D (see Figure 37). This systems undoubtedly proved that a single particle in a Brownian ratchet may "move forward noisily".[21]

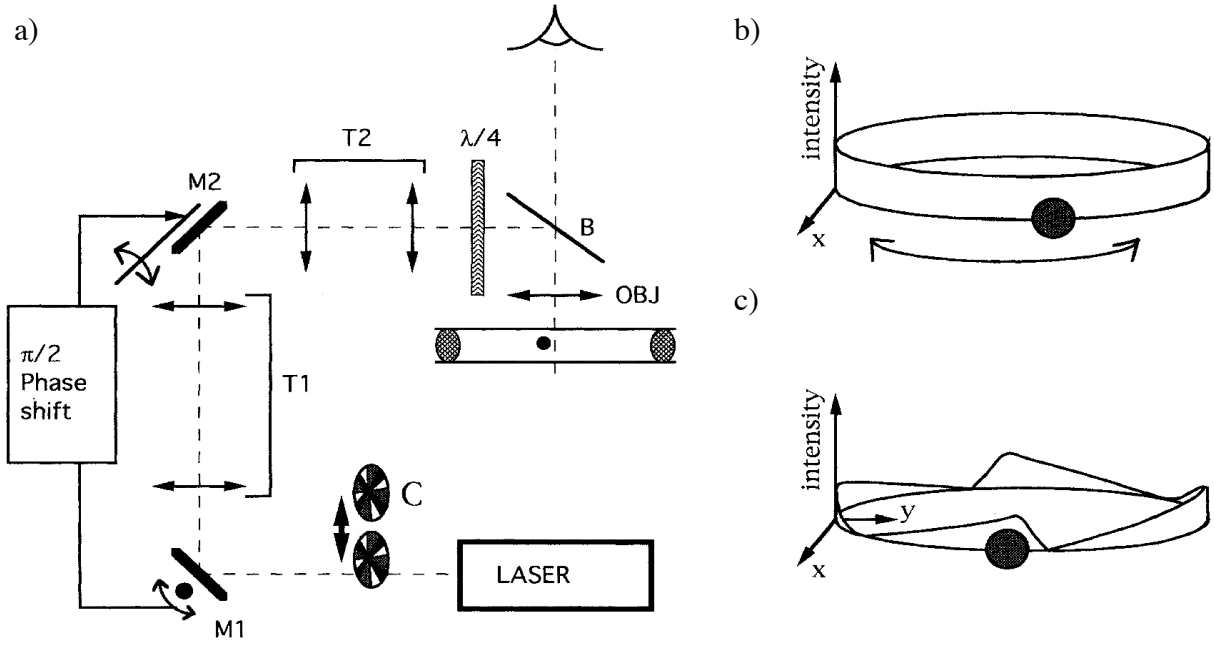

Figure 36: optical thermal ratchet a) experimental setup: the two mirrors M1 and M2 oscillate around two perpendicular axes; T1 and T2 are two telescopes; λ/4 is a quarter wave plate; B is a beam splitter; C is the chopper controlling the neutral-density filter wheel responsible for the asymmetric modulation of light intensity; the resulting optical track is a 7μm diameter circle (figure b and c). When modulation is on, the light intensity is represented on figure b; when modulation is off, the light intensity is constant along the track as represented on figure c. The highest light intensity zones attract the beads: in a constant beam they diffuse freely around the circle; in the modulated beam they concentrate at the maxima.

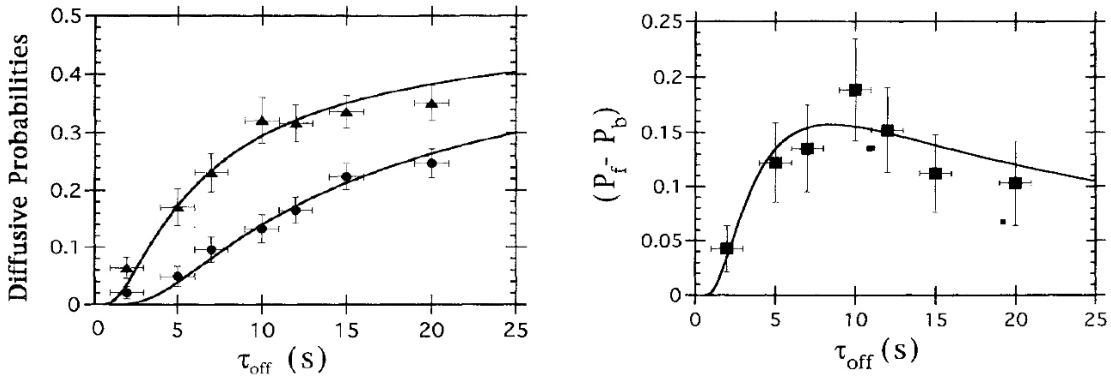

Figure 37: a) measured probabilities to go forward (triangles) or backward (circles) as a function of τ_{off}. Solid lines represent the theoretical evolution; b) measured probability current as a function of τ_{off}. Solid line is the theoretical evolution.

III.3. Coming back to ATPase

The Brownian ratchet concept has been recently used to understand how natural molecular machines work.[27, 28] In natural systems, chemical reactions like binding of ATP or small Na^+ or H^+ ions modulate the potential of the protein system. As an example, Gorge Oster *et al* proposed a model for the potential modulation in the F_0F_1 sodium-ATPase.[142, 146] This model is depicted on

Figure 38. It explains how binding/release of Na^+ ions to/from their coordination sites modifies the asymmetric potential energy of the system, so that a directed ion flux is created from the periplasm to the cytoplasm in presence of Brownian rotation of the c_{12} subunit.

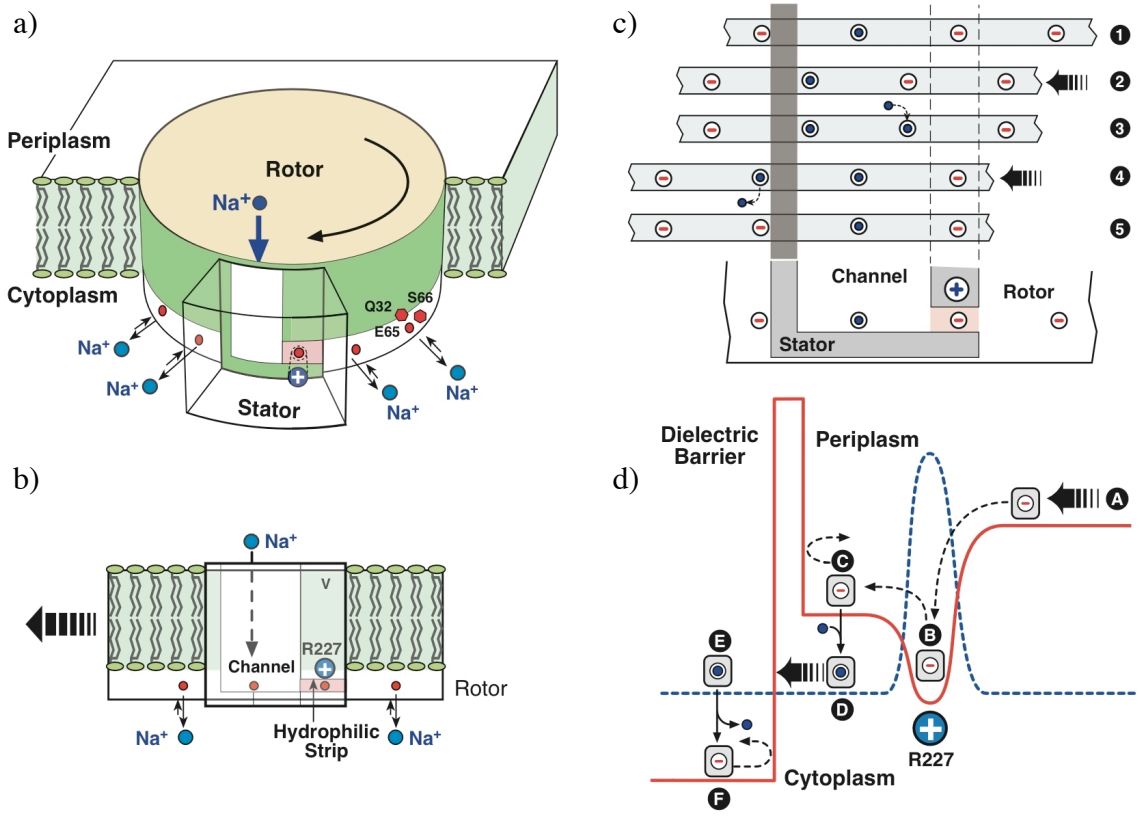

Figure 38: model for sodium ATPase a) organisation across the membrane; b) periplasmic Na^+ ions stochastically enter the stator through the channel, coordinate to the binding site on the rotor and can leave to the left if the c_{12} unit rotates in this direction; by contrast, rotation to the right leads to decomplexation of Na^+ and release in the channel because of the positively charged R227; similarly, coordination of cytoplasmic a Na^+ ion to a rotor site located on the right side of R227 preferentially leads to decomplexation without any transfer to the periplasm. The resulting average Na^+ flux goes from the periplasm to the cytoplasm, driving the rotation of the c_{12} unit; c) typical sequence of events that advance the rotor by one step of $2\pi/12$; grey circles represent neutral associations between one Na^+ ion and one negatively charged coordination site; d) coordination of Na^+ to the binding site modulate the potential of the system. State A to C: negatively charged coordination sites prefer to face the positive R227 residue; rotation of the c_{12} subunit towards the left is favourable; C→D: coordination of Na^+ inside the channel changes the potential of the system; motion towards the right becomes unfavourable due to the repulsion between Na^+ and R227; by contrast, random diffusion towards the left is possible as the association [$Na^+ \subset$ coordination site] is uncharged; E→F: release of Na^+ inside cytoplasm; back motion becomes unfavourable due to the dielectric barrier.

In this model, the R227 residue plays a central role due to its positive charge and to its asymmetric position in the a-subunit of the stator (see Figure 38a and 38b). The channel, also located inside the a-subunit, enables stochastic coordination / de-coordination of periplasmic Na^+ ions to the binding sites located on the c_{12} subunit. Random rotation to the left through the dielectric barrier is easy and leads to possible de-coordination of the bound Na^+ ion into the cytoplasm, with no back-rotation possible. Rotation to the right is also possible but leads by contrast to

decoordination of Na^+ inside the channel, resulting in no ion flux across the membrane. In a similar way, coordination of cytoplasmic Na^+ ions to the right of R227 residue is possible, but rotation to the left leads to de-complexation of Na^+ into the cytoplasm with no resulting ion flux across the membrane. Figure 38c and 38d describe the corresponding single events of this model. Coupling between such a Brownian ratchet and the $\alpha_3\beta_3$ subunits of the stator where ATP-binding / hydrolysis takes place is not described here, but a more complete study of the mechanochemistry of sodium ATPase and ATP synthase can be found elsewhere.[7, 142, 146]

III.4. Two different theoretical approaches of biological linear motors

The two main families of translational molecular machines are on the one hand the acto-myosin complex, notably responsible for the contraction of our muscles, and on the second hand the kinesin / microtubule assemblies.[151] Single molecule techniques have been recently used in order to experimentally demonstrate that these systems displayed elementary steps going both forward *and* backwards.[16, 24, 26, 31, 152] Despite the Brownian nature of single steps, the global forward direction has also been clearly demonstrated in very impressive experiments where the Brownian nature of the motion is not clearly evidenced.[153-157]

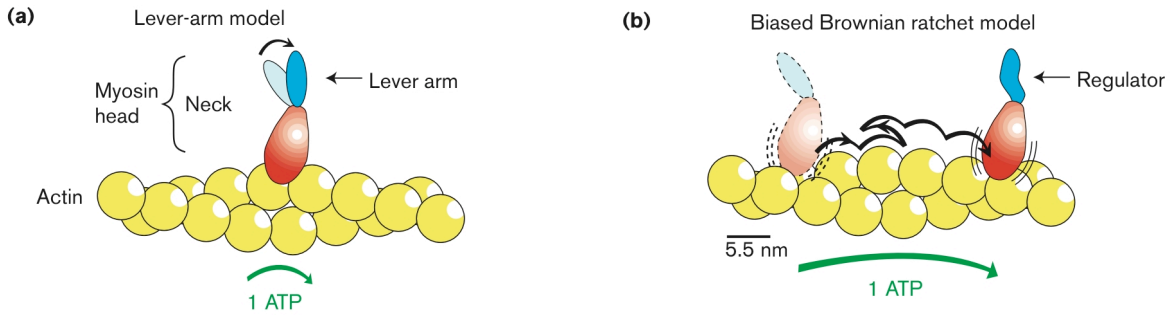

Figure 39: in the lever-arm model (a), rotation of the neck domain enables the myosin head to move one step forward on the actin filament, per ATP hydrolysed; in the biased Brownian ratchet model, hydrolysis of one ATP enables myosin to unbind, which leads to biased diffusion of the myosin head along actin. In this model, one "step" may be longer than the length of one actin molecule (5.5nm). The "lever arm" is only a regulator of the whole process.

As a consequence, the first model for linear motors was close from our macroscopic conception of machines. Its aim was to explain the gliding of myosin heads on actin filaments, and it was called "the swinging lever-arm model". In this model, the energy released by ATP hydrolysis was integrally transformed by chemomechanics of the protein into a "power stroke", which consisted in a mechanical bending of the neck domain of myosin (see Part I-4 of General Introduction and Figure 39a). This bending was transmitted, through the lever arm domain of each myosin molecule, as a force applied on the whole thick filament. This global force resulted in an

overall gliding of the thick filament along the thin filament, hence in contraction of the sarcomere. Details of the model might vary: for example, the number of heads per lever arm might be one or two,[25, 151] and two mechanisms ("inchworm" and "hand-over-hand") have been proposed to explain how two-headed myosin or kinesin might move along actin filaments or microtubules (respectively).[158, 159] However, the "power stroke" model has been by now considered as the standard model and is usually invoqued in textbooks[6], review articles[23] or in our General Introduction (Part I.4) to explain how biological linear motors work. It has also been used extensively on the Internet to build very expressive and detailed videos showing precise succession of chemical events followed by their mechanical expression;[160, 157] sometimes, exhaust pipe-like clouds have even been pictured as graphical expression of ATP-hydrolysis energy release…[157]

In the last five years however, a new theoretical approach based on the Brownian ratchet model and involving thermal diffusion, asymmetric potentials and ATP hydrolysis has been proposed (Figure 39b). It notably enabled to better understand why single-headed myosin might move more than 5.5 nm (the size of one actin element) in one step each time one ATP molecule was hydrolysed.[27, 28] Alternatively, it might explain how related proteins like kinesin and ncd may move in opposite directions along microtubules despite their almost identical structures.[161, 162] Although textbooks and classical literature do not usually refer to this model, it has been exposed recently in a very convincing way[163, 164] as it fits better to the Brownian nature of the nanoworld than the power stroke model.

ANNEXE B: ACTINOMETRY - HOW TO MEASURE THE PHOTON FLUX OF A LIGHT BEAM?

I. Principle

In photochemistry, photons have the same status than a normal chemical reagent: knowing the quantum yield of the photochemical reaction and the number of moles of the starting photoreactive species, one can calculate the number of photon needed to lead the reaction to completion. As a consequence, it can be critical to measure the photon flux in given irradiation conditions in order to be able to link the irradiation time with the number of photon "introduced" in the flask. However, the physical measurement of a photon flux is a delicate procedure that cannot be easily reproduced in a chemistry laboratory.

A more classical method for chemists is the use of a chemical actinometer: a photochemical system whose quantum yield is well known in well described experimental conditions. The ferrous oxalate actinometer developed by Parker and Hatchard[165-167] is well adapted to a chemistry laboratory: the measured number of moles of Fe^{2+} produced by the photochemical reaction is proportional to the photon flux. In this particular system, the photochemical reaction is the photoinduced decomposition of iron (III) trisoxalate complex $[Fe(C_2O_4)_3]_3^-$ into iron (II) and oxalate radical in acidic media:

$$Fe(C_2O_4)_3^{3-} \xrightarrow{h\nu} Fe^{2+} + 2\ C_2O_4^{2-} + C_2O_4^{-} \qquad (1)$$

This radical can react in the dark on the starting complex to produce one additional iron (II) ion:

$$C_2O_4^{-} + Fe(C_2O_4)_3^{3-} \longrightarrow Fe^{2+} + 3\ C_2O_4^{2-} + 2\ CO_2 \qquad (2)$$

It can also react with itself to produce carbon dioxide and ground state oxalate ion:

$$2\ C_2O_4^{-} \longrightarrow 2\ CO_2 + C_2O_4^{2-} \qquad (3)$$

As can be seen, one single photon can produce more than one iron (II) ion, because it produces also a radical that can further react. As a consequence, the quantum yield for the photoinduced production of iron (II) can be higher than unity. It is however limited because of the dark deactivation of the excited iron (III) complex, and also because of the autodestruction of the oxalate radical (reaction 3). The values of the quantum yield for this reaction are well known over a wide range of irradiation wavelengths.[168, 169] They have however not been measured at every

wavelength, so that we modelled their evolution by a third order polynomial function (see Figure 40).

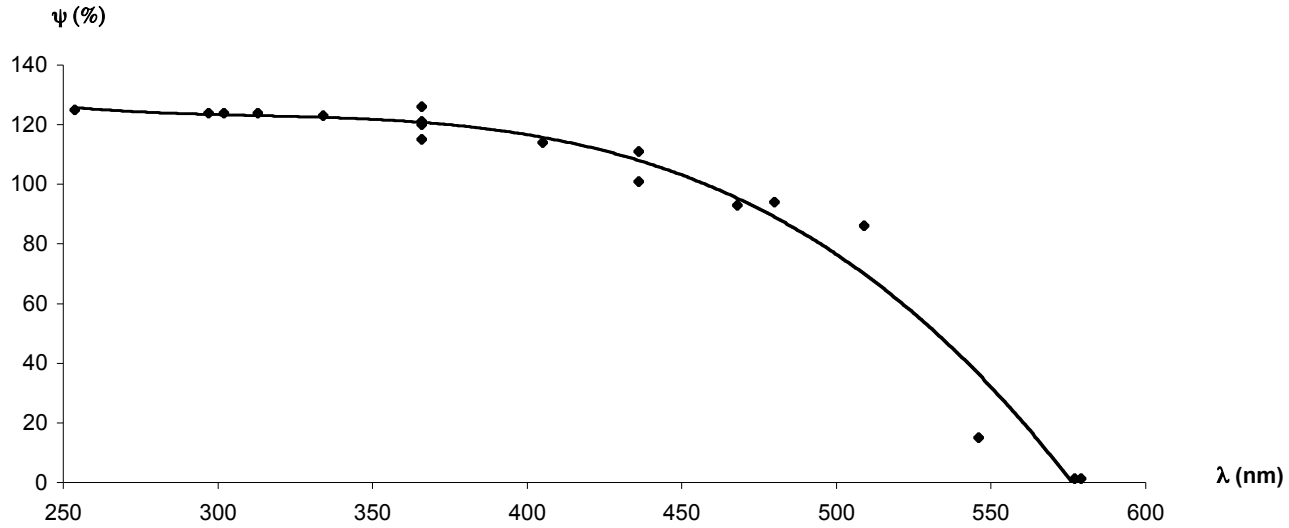

Figure 40: experimental values and model for the evolution of the quantum yield of Parker and Hatchard chemical actinometer.

II. Irradiation setup

Two different irradiation setups were used, corresponding to two different purposes and two different orders of magnitude of photon fluxes:

- a preparative irradiation apparatus: composed of a high power Müller Elektronik xenon 1000W arc lamp fitted with a water filter and an Andover interference bandpass filter. This combination enables a maximum photon flux at a controlled wavelength. The sample (UV-vis cell or NMR tube) was thermostated and continuously stirred;
- an analytic irradiation apparatus: composed of the xenon 150W arc lamp of an Aminco Bowman Luminescence Spectrophotometer Series 3 and its built-in, computer-controlled monochromator. The temperature was thermostated and the sample (UV-vis cell) was continuously stirred.

The 1000W lamp was chosen for the high power of its light beam, enabling preparative photochemical reactions or reactions followed by NMR. The light source of the fluorescence spectrophotometer was by comparison very weak, but the irradiation wavelength and dispersion were finely tenable due to the monochromator. This last setup was used for precise quantum yield measurements (see below).

III. Experimental results

In the case of the preparative irradiation setup, three different filters were used corresponding to three different wavelengths. Figure 41 shows the transmission spectra T=f(λ) for the three filters and the absorption spectra A=f(λ) of the irradiated solution.

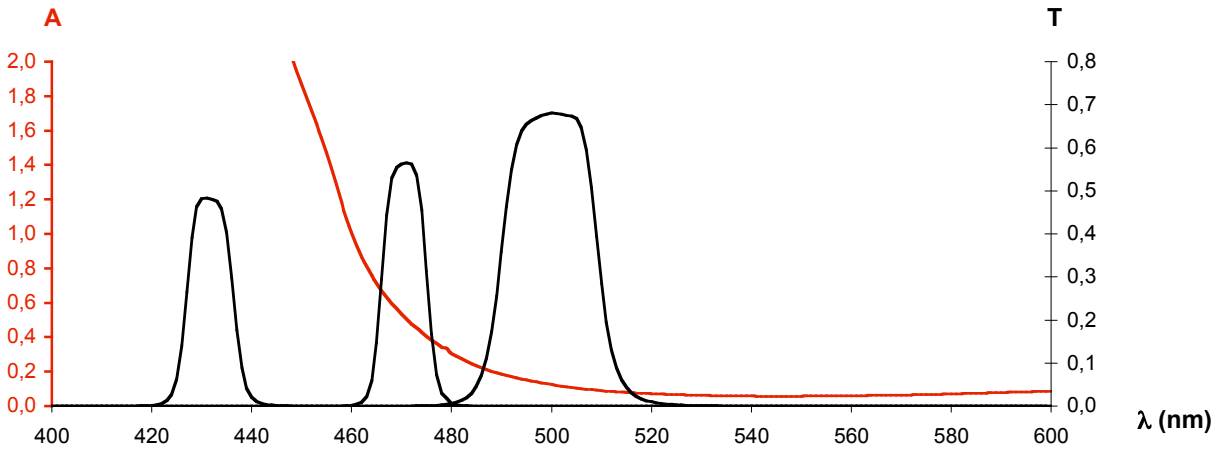

Figure 41: absorbance of the irradiated solution (in red) and transmittance of Andover filters 430FS10-50, 470FS10-50 and 500FS20-50 (centred at 430, 470 and 500 nm respectively).

The number of iron (II) ions produced was measured by UV-vis absorption spectroscopy due to the selective coordination of 1,10-phenanthroline on Fe^{2+}. Figure 42 shows a typical example of the plot of the number of Fe^{2+} ions produced in the irradiated cell versus irradiation time. The photon flux was proportional to the slope S of this curve and to the quantum yield at the irradiation wavelength (see Experimental Part).

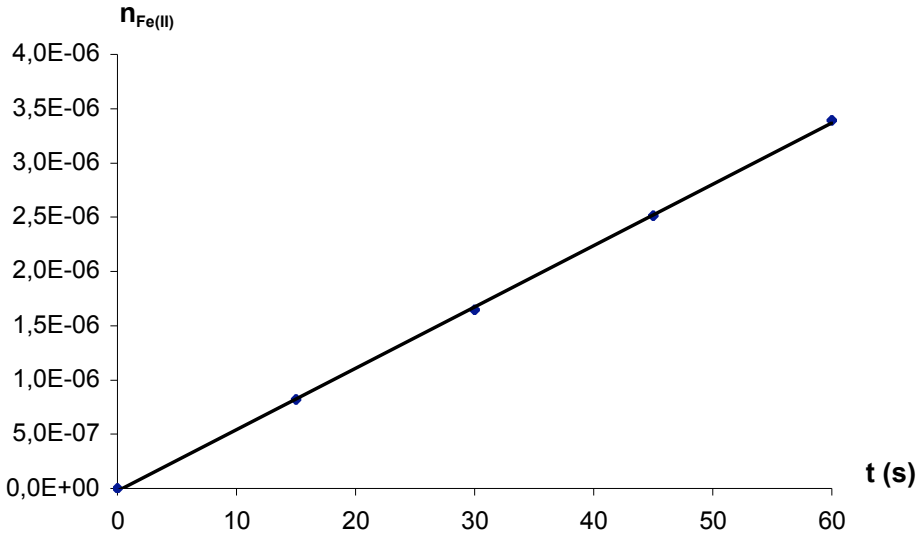

Figure 42: number of moles of iron (II) ions photochemically produced in the cell vs. time of irradiation (filter : 500FS20-50).

The results for the three different filters are summarized in Table 13.

Andover interference Filter ref.	**430FS10-50**	**470FS10-50**	**500FS20-50**
Filter transmission maximum l_{max} (nm)	430	470	500
Filter half-band width $\Delta\lambda$ (nm)	10	10	20
Temperature of the cell (°C)	22.3	20.2	22.4
Absorbance of the solution at λ_e	4.330	0.534	0.125
Photon absorption probability	1.000	0.707	0.251
Total irradiation time t (min)	1.0	1.5	1.0
Experimental slope S ($mol.s^{-1}$)	$1.32x10^{-7}$	$1.13x10^{-7}$	$5.65x10^{-8}$
Linear regression coefficient R	0.9990	0.9989	0.9997
Interpolated quantum yield	1.10	0.94	0.77
Measured flux of photons ($mol.s^{-1}$)	$1.2x10^{-7}$	$1.6x10^{-7}$	$2.2x10^{-7}$
Measured flux of photons ($mmol.min^{-1}$)	**7.0 ± 0.5**	**10 ± 0.7**	**13 ± 2.0**
Energy of a photon at $\lambda=\lambda_{max}$ (eV)	2.88	2.64	2.48
Light beam intensity ($W.m^{-2}$)	110	140	180

Table 13: experimental results for the preparative scale irradiation setup.

We observed a slight increase in the usable photon fluxes with respect to the transmission maxima of the three filters. This was consistent with the increased areas under their transmission curves (see Figure 41). In comparison, 1mL of pyridine contains 12 mmol, i.e. roughly 1 minute of irradiation with the 500FS20-50 filter.

In the case of the analytical irradiation setup, the irradiated samples were identical but the light source a lot weaker. At 513 nm the solution absorption was also small, so that irradiation times were bigger and the correlation coefficient smaller. Experimental results are summarized for three excitation wavelengths in Table 14.

Monochromator λ_{max} (nm)	**464**	**476**	**513**
Monochromator half-band width $\Delta\lambda$ (nm)	8	8	8
Temperature (°C)	25.0	26.0	25.0
Absorbance of the solution at λ_e	0.7587	0.3843	0.0827
Photon absorption probability	0.826	0.587	0.173
Total irradiation time (min)	1800	1800	5400
Experimental slope S ($mol.s^{-1}$)	$4.40x10^{-10}$	$3.32x10^{-10}$	$3.03x10^{-11}$
Linear regression coefficient R	0.998	0.9998	0.98
Interpolated quantum yield	0.97	0.91	0.67

Monochromator λ_{max} (nm)	**464**	**476**	**513**
Monochromator half-band width $\Delta\lambda$ (nm)	8	8	8
Temperature (°C)	25.0	26.0	25.0
Measured flux of photons ($mol.s^{-1}$)	$5.5x10^{-10}$	$6.2x10^{-10}$	$2.6x10^{-10}$
Measured flux of photons ($mmol.min^{-1}$)	**0.033 ± 0.004**	**0.037 ± 0.004**	**0.016 ± 0.004**
Energy of a photon at $\lambda=\lambda_{max}$ (eV)	2.84	2.60	2.42
Light beam intensity ($W.m^{-2}$)	0.47	0.52	0.20

Table 14: experimental results for the analytical irradiation setup.

In comparison, 1 minute of irradiation at 464 nm brought the same number of photons as the number of molecules contained in 25mg or Ru(terpy*)(phen)(py)$(PF_6)_2$.

As can be seen, the irradiation system based on the Müller 1000W lamp and Andover filters was roughly 500 times more powerful than the irradiation setup of the AB3 fluorescence spectrophotometer. This comes from the combined effects of the higher power of the 1 kW arc lamp and of the use of an interference filter instead of a monochromator. We measured photon fluxes of 10 and 0.02 mmol of quanta per minute, respectively, with comparable half-band widths (10 and 8 nm).

IV. Comparison with the literature

McMillin *et al* mentioned an irradiation setup based on a 1000W xenon arc lamp, a water filter and an Oriel monochromator.[84] They report a light intensity of $1\text{-}2.10^{-8}$ $mol.s^{-1}$ but don't precise the half-band width of the monochromator. This result was ten times smaller than ours, which was consistent with the replacement of a monochromator by an interference filter. The group of Peter Ford reported an irradiation setup based on a 150 W xenon arc lamp and interference filters having $\Delta\lambda$ = 10 nm.[170] They obtained light fluxes ranging from 0.022 to 0.056 $mmol.s^{-1}.cm^{-2}$ by Reinecke's ion actinometry.[171] In another paper,[172] the same group reported an irradiation setup based on a 200 W high-pressure mercury arc lamp, focused on an interference filter with $\Delta\lambda$=10 nm and followed by an infrared filter. They measured by ferrioxalate actinometry a usable intensity of 0.083 $mmol.s^{-1}.cm^{-2}$.Those results are 10 times bigger than our 150 W irradiation setup, due to the use of filters instead of a monochromator. They are also 50 times smaller than our 1000 W setup, which corroborates our measurements.

ANNEX C: QUANTUM YIELD MEASUREMENTS

I. The photochemical system

The reaction studied was the photoinduced substitution of the monodentate ligand L by pyridine. The photochemical system was an irradiated pyridine solution of the starting complex $Ru(tpy^*)(N\text{-}N)(L)^{2+}$ (N-N may be phen or dmp). Both forward and backward reactions were taken into account, and as both photosubstitution reactions seemed to follow an apparent first-order reaction rate, we defined ψ_1 and ψ_2 as the two corresponding quantum yields.

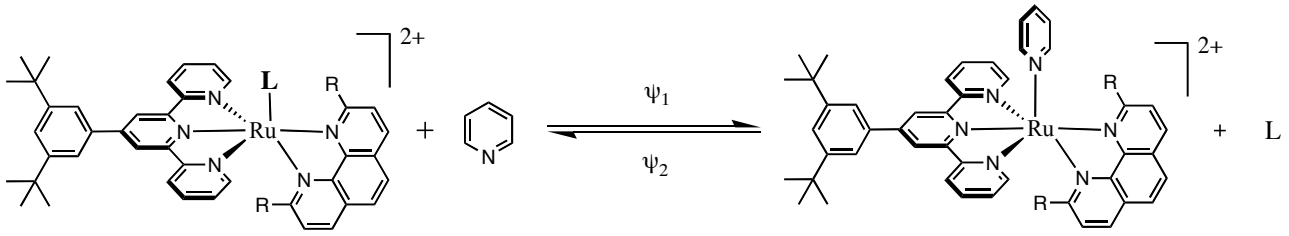

R = H or CH_3

For both the forward and the backward reactions, we supposed a rate-determining photoexpulsion step of the monodentate ligand L_1, followed by a rapid coordination of the incoming ligand L_2.

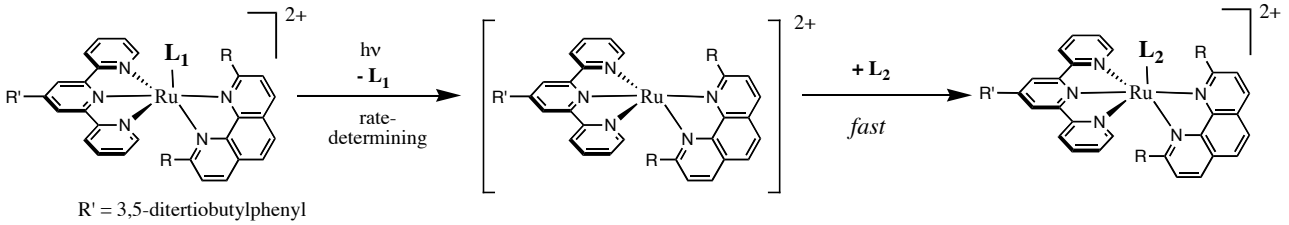

R' = 3,5-ditertiobutylphenyl

When irradiated with white light, the system was characterised by an isosbestic point at a wavelength called λ_{isosb}. To carry out a quantitative study, the light used for excitation was filtered by a monochromator set to a wavelength $\lambda_e \approx \lambda_{isosb}$. As a consequence the absorption A_e of the irradiated solution at $\lambda=\lambda_e$ was constant during the reaction, hence the number of photons absorbed by the solution, per time unit, remained constant. We called φ_0 the flux of photons with the wavelength λ_e arriving on the cell. The measured values of the two quantum yields ψ_1 and ψ_2 depend on the excitation wavelength λ_e.

II. Analytical treatment

II.1. Hypotheses

At a given time t, we considered that only the starting material Ru(terpy*)(N-N)(L)$^{2+}$ and the final product Ru(terpy*)(N-N)(py)$^{2+}$ absorbed light. We assumed that if the total absorbance of the solution was $A_{\lambda t} = l\varepsilon_{\lambda 1}C_1 + l\varepsilon_{\lambda 2}C_2$, the ratios between the numbers of photons absorbed by one species to the numbers of photons absorbed by the solution were $\frac{l\varepsilon_{\lambda 1}C_1}{A_e}$ and $\frac{l\varepsilon_{\lambda 2}C_2}{A_e}$, respectively.

II.2. Modelling the system

The aim of this section is to model the time evolution of $A_{\lambda t}$, the absorbance of the solution at a given wavelength λ. It is a generalization of the calculation done by Heinz-Helmut Perkampus.[173] In the following calculations, pyridine is written "py" and "Ru.L^{2+}" is used for Ru(tpy*)(N-N)(L),$(PF_6)_2$.

II.2.a. Notations

The initial state of the system is a pyridine solution of the complex Ru.L^{2+}, stable for several hours in the dark. We call:

– C_1 the concentration of Ru.L^{2+} at time t, $C_{1,0}$ its initial concentration and $C_{1,\infty}$ its concentration at the photostationnary state;

– C_2, $C_{2,0}$ and $C_{2,\infty}$ are similarly defined for the species Ru.py^{2+};

– x the conversion (in mol) of the reaction at time t, x_0 and x_∞ the values of x at the initial and photostationnary states, respectively;

– $A_{\lambda t}$, $A_{\lambda 0}$ and $A_{\lambda \infty}$ are the absorbances of the solution at the wavelength λ, at t, t=0 and t=∞;

– A_e is the absorbance of the solution at the irradiation wavelength λ_e, which is also the wavelength of the isosbestic point of the photochemical reaction; A_e is constant during the course of the reaction;

The absorbance of the solution at wavelength λ is given by $A_{\lambda t} = l\varepsilon_{\lambda 1}C_1 + l\varepsilon_{\lambda 2}C_2$ where $\varepsilon_{\lambda 1}$ and $\varepsilon_{\lambda 2}$ are the extinction coefficients of the starting and final complexes.

C_1 and C_2 are given by $C_1 = \frac{n_1}{V} = \frac{n_0 - x}{V}$ and $C_2 = \frac{n_2}{V} = \frac{x}{V}$, where n_1 and n_2 are the number of moles of Ru.L^{2+} and Ru.py^{2+} complexes in the solution, respectively, at time t.

Hence $A_{\lambda t} = \frac{l}{V} \times \left(\varepsilon_{\lambda 1}\left(n_0 - x\right) + \varepsilon_{\lambda 2} x\right) = \frac{l}{V}\varepsilon_{\lambda 1} n_0 + x\frac{l}{V}\left(\varepsilon_{\lambda 2} - \varepsilon_{\lambda 1}\right)$

If we call $q_\lambda = \left(\varepsilon_{\lambda 2} - \varepsilon_{\lambda 1}\right)$ then we have

$$A_{\lambda t} = A_{\lambda 0} + \frac{l q_\lambda}{V} x \qquad (1)$$

which is also

$$x = \frac{V}{l q_\lambda}\left(A_{\lambda t} - A_{\lambda 0}\right) \qquad (1')$$

x and $A_{\lambda t}$ are linearly related, thus

$$\frac{dA_{\lambda t}}{dt} = \frac{l q_\lambda}{V} \times \frac{dx}{dt} \qquad (2)$$

II.2.b. Kinetics of the reaction

The time evolution of x is given by

$$\frac{dx}{dt} = v_1 - v_2 \qquad (3)$$

where v_1 and v_2 are the rates of the forward and backward photosubstitution reactions, respectively.

We suppose that both reactions are of the first order. $\__1$ and $\__2$ being the associated quantum yields, the rates of the reactions are given by

$$v_1 = \varphi_{abs1} \times \psi_1 \text{ and } v_2 = \varphi_{abs2} \times \psi_2$$

where φ_{abs1} and φ_{abs2} are the number of photons absorbed per second by each species $Ru.L^{2+}$ and $Ru.py^{2+}$, respectively. If we call φ_0 the flux of photons arriving to the cell in the particular experimental conditions used, the number of photons absorbed by the solution in one second will be $\varphi_0 \times \left(1 - 10^{-A_e}\right)$, where A_e is the total absorbance of the solution at the irradiation wavelength.

As the ratios of the numbers of photons absorbed by each species to the numbers of photons absorbed by the solution are $\frac{l\varepsilon_{\lambda 1} C_1}{A_e}$ and $\frac{l\varepsilon_{\lambda 2} C_2}{A_e}$, respectively, it follows that $\varphi_{abs1} = \varphi_0 \times \left(1 - 10^{-A_e}\right) \times \frac{l \cdot \varepsilon_{\lambda 1} \cdot C_1}{A_e}$ and $\varphi_{abs2} = \varphi_0 \times \left(1 - 10^{-A_e}\right) \times \frac{l \cdot \varepsilon_{\lambda 2} \cdot C_2}{A_e}$.

Finally, the time evolution of x is given by the equation:

$$\frac{dx}{dt} = \varphi_0 \left(\frac{1 - 10^{-A_e}}{A_e}\right) \frac{l}{V}\left(\varepsilon_{e1} \cdot n_1 \cdot \psi_1 - \varepsilon_{e2} \cdot n_2 \cdot \psi_2\right) \qquad (4)$$

with *l* in centimetre, V in litre and φ_0 in mol of quanta per second. The factor $\frac{1-10^{-A_e}}{A_e}$ is usually called actinometry factor, and noted F_e.

II.2.c. Time-evolution of the absorbance $A_{\lambda t}$

We introduce here $\xi = \frac{\psi_2}{\psi_1}$. Replacing n_1 and n_2 by their expression as a function of x, and noticing that at the irradiation wavelength λ_e, which is also the isosbestic point of the reaction $\varepsilon_{\lambda 1} = \varepsilon_{\lambda 2}$, it is easy to deduce from equation (4) the following differential equation for x:

$$\frac{dx}{dt} = \frac{\varphi_0 \cdot F_e \cdot \varepsilon_{e1} \cdot \psi_1 \cdot l}{V}\left(n_0 - x \cdot (1+\xi)\right) \qquad (5)$$

Using equations (5) and (2) we deduce that

$$\frac{dA_{\lambda t}}{dt} = \frac{\varphi_0 \cdot F_e \cdot l^2 \cdot \varepsilon_{e1} \cdot \psi_1}{V^2}\left(q_\lambda \cdot n_0 - x \cdot q_\lambda \cdot (1+\xi)\right) \qquad (6)$$

II.2.d. Photostationnary state of the system

At t=∞ the absorbance does not evolve anymore. At the photostationnary state, equation (6) becomes $\frac{dA_{\lambda t}}{dt} = 0$, which leads to the limit of x at the photostationnary state:

$$x_\infty = \frac{n_0}{1+\xi} \qquad (7)$$

From equation (1), (7) gives $A_{\lambda\infty} = A_{\lambda 0} + \frac{l \cdot q_\lambda}{V} x_\infty$, and equation (6) turns finally into:

$$\frac{dA_{\lambda t}}{dt} = k \cdot (1+\xi) \cdot \left(A_{\lambda\infty} - A_{\lambda t}\right) \qquad (8)$$

$$\text{with } k = \varphi_0 \cdot F_e \cdot \varepsilon_{e1} \cdot \psi_1 \cdot \frac{l}{V} \qquad (8')$$

If we integrate equation (8) between t=0 and t, we get the final expression:

$$\frac{A_{\lambda t} - A_{\lambda 0}}{t} = k \cdot (1+\xi) \cdot A_{\lambda\infty} - k \cdot (1+\xi) \cdot \frac{\int_0^t A_{\lambda t'} dt'}{t} \qquad (9)$$

II.3. Analytical result

The time evolution of the total absorbance at a given wavelength λ was given by the following equation:

$$\frac{A_{\lambda t} - A_{\lambda 0}}{t} = k \cdot (1+\xi) \cdot A_{\lambda\infty} - k \cdot (1+\xi) \cdot \frac{\int_0^t A_{\lambda t'} dt'}{t}$$

where $k = \varphi_0 \cdot F_e \cdot \varepsilon_{e1} \cdot \psi_1 \cdot \frac{l}{V}$, $\xi = \frac{\psi_2}{\psi_1}$ and $F_e = \frac{1 - 10^{-A_e}}{A_e}$.

In those equations:

- φ_0 was a flux, given in mol of photon per second (mol.s^{-1})
- l was the length of the irradiation cell, in centimetre (cm)
- V was the volume of the irradiated solution, in litre (L)
- ε_{e1} was the extinction coefficient of the complex Ru.L^{2+} in pyridine, in L.mol^{-1}.cm^{-1}
- k was a first order rate constant (s^{-1})
- ξ and F_e were adimensional parameters.

II.4. Methodology

We defined $A(t) = \frac{A_{\lambda t} - A_{\lambda 0}}{t}$ and $B(t) = \frac{1}{t} \cdot \int_0^t A_{\lambda t'} dt'$. These variables were calculated from the time evolution of the absorbance of the solution, and as A(t) was plotted as a function of B(t) a straight line was obtained. Its slope $S = k(1+\xi)$ was linked to the *sum* of ψ_1 and ψ_2 by the equation $\psi_1 + \psi_2 = \frac{S \cdot V}{\varphi_0 \cdot F_e \cdot \varepsilon_{e1} \cdot l}$. Its y-intercept $Y_0 = S \cdot A_{\lambda\infty}$ enabled to calculate $A_{\lambda\infty}$ which was linked to the *ratio* between ψ_1 and ψ_2 by the relation $\xi = \frac{n_0}{x_\infty} - 1$. The individual quantum yields ψ_1 and ψ_2 were calculated by combination of their sums and ratios.

III. Experimental results

III.1. Experimental curves

Three different starting complexes were considered: **7**$^{2+}$, **12**$^{2+}$ and **13**$^{2+}$. We give Figure 43 and Figure 44 the typical curves obtained. As depicted in Figure 44, the linear correlation coefficients of the A(t) = f(B(t)) were good. One has to note that, on the point of view of kinetics, irradiation with white light led to a first order rate law (see Chapter 1 Part II-3 and III-2) whereas single-wavelength irradiation centred at the isosbestic point of the reaction did not. The final states also depended on the dispersion of the light, as the first case led to complete conversion whereas the second did not.

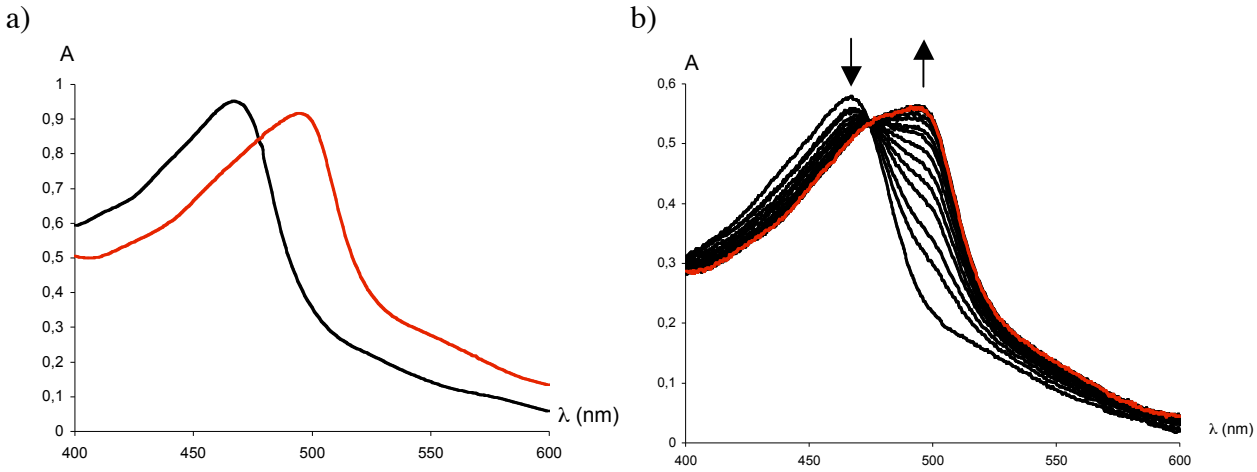

Figure 43: a) white light irradiation of $\mathbf{12}^{2+}$ showing the starting (black) and final (red) spectrum of the solution. Final state was characterised by complete conversion; b) irradiation of $\mathbf{12}^{2+}$ with a small light dispersion ($\Delta\lambda$ = 8nm) and a central wavelength centred at the isosbestic point of the reaction. The conversion at the final state was not 100% as revealed by the shoulder of the last curve (red) around 460 nm.

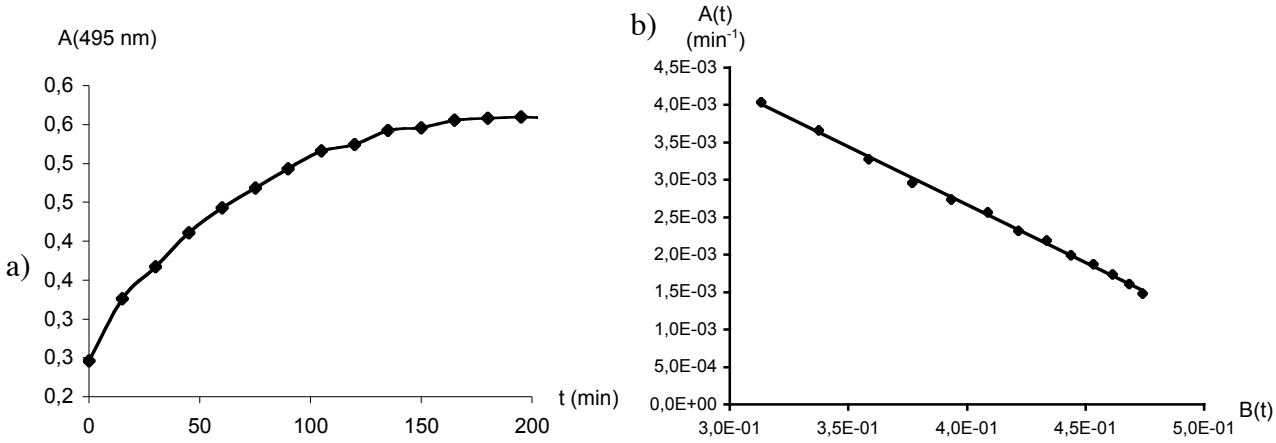

Figure 44: a) time evolution of the absorbance of the irradiated solution of $\mathbf{12}^{2+}$ at the wavelength of the appearing product Ru(terpy*)(dmp)(py)$^{2+}$ (495 nm); b) treatment A(t) = f(B(t)).

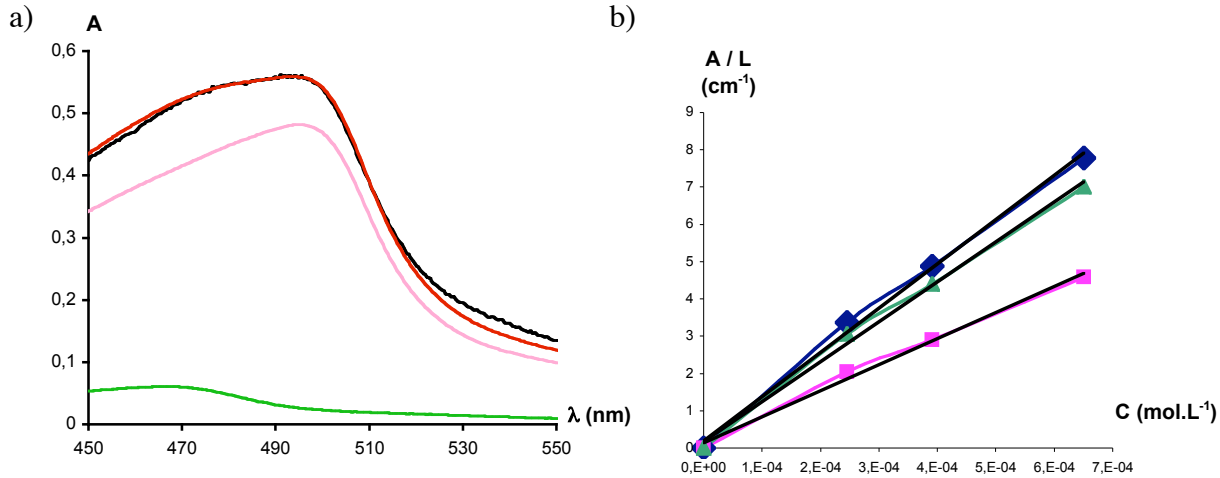

Figure 45: a) Deconvolution of the photostationnary state ($\mathbf{12}^{2+}$). Experimental curve (black), contribution of Ru.L^{2+} (green), contribution of Ru.py^{2+}(pink), theoretical spectrum (red); b) calibration curves for the determination of molar extinction coefficients of Ru(terpy*)(dmp)(py),$(PF_6)_2$ in pyridine.

III.2. Experimental numerical values

To limit experimental errors, the molar extinction coefficients of the different species were accurately determined by calibration curves. All numerical results are reported in Table 15.

Complex	**7**$^{2+}$	**12**$^{2+}$	**13**$^{2+}$
Weighed mass of solid Ru(tpy*)(N-N)(L),$(PF_6)_2$ (mg)	1.04	1.02	1.41
Volume of the solution prepared (mL)	20.0	20.0	25.0
Molar mass of the complex (g.mol^{-1})	1156	1184	1083
Concentration of the irradiated solution (mol.L^{-1})	4.50x10^{-5}	4.31x10^{-5}	5.16x10^{-5}
Volume of the irradiated sample (mL)	3.00	3.00	3.00
Number of moles of irradiated complex (mol)	1.35x10^{-7}	1.29x10^{-7}	1.55x10^{-7}
Wavelength of experimental isosbestic point (nm)	475	473.5	514
Irradiation wavelength λ_e (nm)	476	476	513
Photon flux (see Annex B) (mol.s^{-1})	6.2x10^{-10}	6.2x10^{-10}	2.6x10^{-10}
Average absorbance A_e at irradiation wavelength	0.511	0.533	0.403
Relative variation of A_e during the reaction	4.2%	4.7%	2.6%
Average probability of photon absorption	0.691	0.707	0.605
Actinometry factor F_e	1.35	1.33	1.50
Wavelength λ used for the study (nm)	487	495	495
Experimental slope S (min^{-1})	8.28x10^{-4}	1.55x10^{-2}	1.93x10^{-2}
Experimental slope S (s^{-1})	1.38x10^{-5}	2.58x10^{-4}	3.22x10^{-4}
y-intercept Y_0 (s^{-1})	7.30x10^{-6}	1.48x10^{-4}	1.83x10^{-4}
Linear regression coefficient R_	0.966	0.998	0.992
Theoretical $A_{\lambda\infty}$	0.529	0.572	0.570
Experimental $A_{\lambda\infty}$	/	0.557	0.572
Length of the irradiation cell (cm)	1.00	1.00	1.00
ε_{e2} of Ru(tpy*)(N-N)(py)$^{2+}$ in pyridine (L.mol^{-1}.cm^{-1})[a]	1.26x10^4	10.7x10^3	6.98x10^3
$\varepsilon_{\lambda 2}$ of Ru(tpy*)(N-N)(py)$^{2+}$ in pyridine (L.mol^{-1}.cm^{-1})[a]	1.32x10^4	1.19x10^4	1.19x10^4
$\psi_1 + \psi_2$	**0.0039 ± 0.0006**	**0.088 ± 0.01**	**0.36 ± 0.09**
$\varepsilon_{\lambda 1}$ of Ru(tpy*)(N-N)(L)$^{2+}$ in pyridine (L.mol^{-1}.cm^{-1})[b]	7.23x10^3	5.43x10^3	9.84x10^3
$A_{\lambda 0}$	0.285	0.246	0.502
C_0^{th} deduced from $A_{\lambda 0}$ and $\varepsilon_{\lambda 1}$ (mol.L^{-1})	3.94x10^{-5}	4.53x10^{-5}	5.10x10^{-5}
x_∞ / n_0	0.91[d]	0.90[c]	>0.95
ξ	0.099	0.11	<0.05
ψ_1	**0.0035 ± 0.0009**	**0.079 ± 0.015**	**0.36 ± 0.11**

Complex	**7^{2+}**	**12^{2+}**	**13^{2+}**
ψ_2	**0.00035 ± 0.00009**	**0.0090 ± 0.0015**	**<0.02**

Table 15: Experimental parameters for the determination of quantum yields. (a) obtained through calibration curves; (b) derived from white light irradiation experiments; (c) obtained by graphical deconvolution of photostationnary state; (d) obtained from equation (12).

IV. Validation of our results

In order to validate our procedure, we had to test it in the case of a better-known system. As there was no report of photosubstitution quantum yields on ruthenium (II) complexes in neat pyridine, we used the published experimental conditions of McMillin *et al* on the complex Ru(terpy)(bpy)(CH_3CN)(PF_6)$_2$.[84] In this article, the photosubstitution of acetonitrile by pyridine was reported with a quantum yield of 0.0013 ± 0.0001 using a 1.0 M solution of pyridine in acetonitrile as the solvent.

The phenanthroline analogue complex Ru(tpy)(phen)(CH_3CN),(PF_6)$_2$ was prepared by Emma Schoffield.[90] We determined the isosbestic point of the reaction in the white light experiment, measured the photon flux at this wavelength and performed the quantum yield measurement following exactly the experimental conditions described by McMillin (except for the dispersion $\Delta\lambda$ which was not underlined in the publication and the light intensity which was 30 times smaller in our case). The time evolution of $A_{\lambda t}$ was perfectly linear (Figures 46), so that the reverse reaction could be ignored. We calculated the quantum yield ψ_1 in this simple hypothesis according to the formula:

$$\psi_1 = \frac{S}{C_0 \cdot l \cdot \left(\varepsilon_{\lambda 2} - \varepsilon_{\lambda 1}\right)} \times \frac{V}{\varphi_0 \cdot F_e \cdot l \cdot \varepsilon_{1e}} \qquad (10)$$

In this expression S is the slope of the curve A_{483},t – $A_{483,0}$ = f(t).

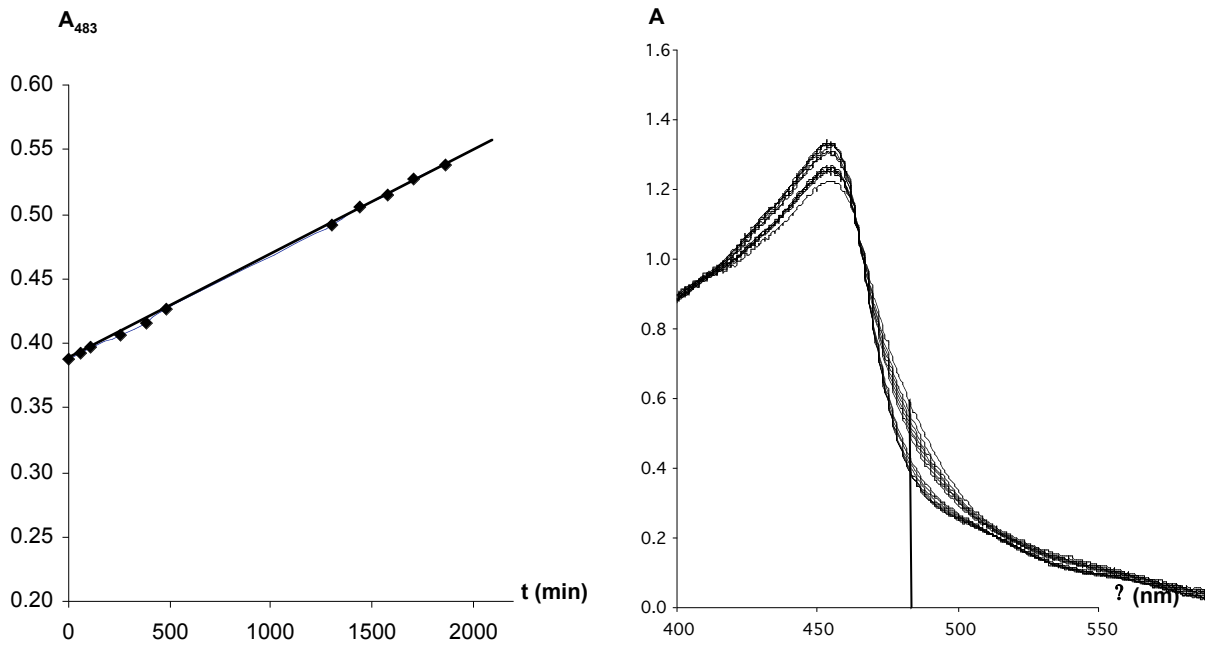

Figure 46: (a) Time evolution of the absorbance at 483 nm; (b) Superimposed absorption spectra of the solution between t = 0 and t = 2729 minutes. Straight line shows λ = 483 nm.

Experimental results are given in Table 16. Finally, the value we obtained was very close to the reported bipyridine analogue: 0.0016 ± 0.0002 against 0.0013 ± 0.0001. This experiment validates the methodology of our light intensity measurements. For the quantum yield values the conversion was a lot lower for Ru(terpy)(phen)$(CH_3CN)^{2+}$ than for **7**$^{2+}$, **12**$^{2+}$ and **13**$^{2+}$, so that the application of formula (9) to Ru(terpy)(phen)$(CH_3CN)^{2+}$ gave bad results. However the quantum yield found for **7**$^{2+}$ was very close to the one found for Ru(terpy)(phen)$(CH_3CN)^{2+}$ (0.0031 ± 0.0008 versus 0.0013 ± 0.0001). The difference can be due to the differing solvents as much as to the slight difference in coordinating properties between 2,6-dimethoxybenzonitrile and acetonitrile. As a conclusion, the ψ_1 value of Ru(terpy)(phen)$(CH_3CN)^{2+}$ validates our measurement for complex **7**$^{2+}$, which in turn validates the results for complexes **12**$^{2+}$ and **13**$^{2+}$.

Complex	**Ru(terpy)(phen)$(CH_3CN)^{2+}$**
Irradiation wavelength λ_e (nm)	464
Wavelength λ (nm)	483
$\varepsilon_{\lambda 1}$ of Ru(tpy)(phen)(CH_3CN),$(PF_6)_2$ (L.mol^{-1}.cm^{-1})	3.81x10^3
$\varepsilon_{\lambda 2}$ of Ru(tpy)(phen)(py),$(PF_6)_2$ (L.mol^{-1}.cm^{-1})	9.00x10^3
Average absorbance at the isosbestic point A_e	1.0991
Relative variation of A_e (%)	1.4
Photon absorption probability	0.920
Actinometry factor F_e	0.837

Complex	**Ru(terpy)(phen)$(CH_3CN)^{2+}$**
Concentration C_0 ($mol.L^{-1}$)	$1.03x10^{-4}$
Path length (cm)	1.00
Photon flux at λ_e ($mol.s^{-1}$)	$5.5x10^{-10}$
Volume of irradiated solution (L)	3.00
ε_{e1} of $Ru(tpy)(phen)(CH_3CN),(PF_6)_2$ ($L.mol^{-1}.cm^{-1}$)	$1.06x10^{4}$
Slope S of $A_{\lambda t}$-$A_{\lambda 0}$ = f(t) (min^{-1})	$8.09x10^{-5}$
Quantum yield ψ_1	**0.0016** ± 0.0002

Table 16: Experimental parameters for the quantum yield measurement of the photosubstitution of acetonitrile by pyridine in the complex $Ru(tpy)(phen)(CH_3CN),(PF_6)_2$. The experimental conditions were identical to the one reported by McMillin.[90]

V. Quantum yields of photosubstitution reactions on ruthenium (II) polypyridyl complexes

It is helpful to compare our results with the literature. Entries I to IX of Table 17 are listed referenced quantum yields for photosubstitution reaction on polypyridyl ruthenium (II) complexes. Entries X to XIII refer to our own work.

Entry (ref)	**Starting compound**	**Product of substitution**	**Experimental conditions**	**Quantum yields**
I[172]	$[Ru(NH_3)_5(py)],(BF_4)_2$	$[Ru(NH_3)_5(H_20)]^{2+}$	0.2 M NaCl, pH=3 aqueous solution; Δλ=10nm	0.045 ± 0.002
II[174]	$[Ru(bpy)_2(py)_2],(PF_6)_2$	$[Ru(bpy)_2(py)(X)]^{+}$	dichloromethane or acetone solutions; $X=NO_3^-$, ClO_4^-; Δλ=20 nm	0.18 ± 0.02
III[76]	$[Ru(bpy)_3],(NCS)_2$	$Ru(bpy)_2(NCS)_2$	dichloromethane solutions; Δλ=10 nm	0.068
IV[175]	$[Ru(bpy)_3],(PF6)_2$	$[Ru(bpy)_2(CH_3CN)(Cl)]^{+}$	2mM Bu_4NCl acetonitrile solutions; Δλ=10nm ;	0.029 ± 0.003
V[76]	$[Ru(phen)_3],(NCS)_2$	$Ru(phen)_2(NCS)_2$	dichloromethane solutions; Δλ=10 nm;	0.020
VI[176]	$[Ru(phen)_2(dmbp)],(PF_6)_2$	$[Ru(phen)_2(CH_3CN)_2]^{2+}$	Acetonitrile solutions;	0.020 ± 0.002
VII[176]	$[Ru(phen)_2(m36)],(PF6)_2$	$[Ru(phen)_2(CH_3CN)_2]^{2+}$	Acetonitrile solutions;	0.008 ± 0.001
VIII[177]	$[Ru(tpy)(py)_3],(PF_6)_2$	$[Ru(tpy)(py)_2(S)]^{2+}$	Acetone solutions; Δλ=10 nm	0.004
IX[84]	$[Ru(tpy)(bpy)(CH_3CN)],(PF_6)_2$	$[Ru(tpy)(bpy)(py)]^{2+}$	acetonitrile solutions with 1M pyridine;	0.0013 ± 0.0001
X	$[Ru(tpy^*)(phen)(py)],(PF_6)_2$	$[Ru(tpy^*)(phen)(Bz)]^{2+}$	Entering ligand $C=10^{-4}$ M; Pyridine solutions; Δλ=8 nm	0.00035 ± 0.00009

Entry (ref)	Starting compound	Product of substitution	Experimental conditions	Quantum yields
XI	$[Ru(tpy^*)(dmp)(py)],(PF_6)_2$	$[Ru(tpy^*)(dmp)(Bz)]^{2+}$	Entering ligand $C=10^{-4}$ M; pyridine solutions; $\Delta\lambda$=8 nm	0.0090 ± 0.0015
XII	$[Ru(tpy^*)(dmp)(dms)],(PF_6)_2$	$[Ru(tpy^*)(dmp)(py)]^{2+}$	Pyridine solutions; $\Delta\lambda$=8 nm	0.36 ± 0.11
XIII	$[Ru(tpy)(phen)(CH_3CN)],(PF_6)_2$	$[Ru(tpy)(phen)(py)]^{2+}$	acetonitrile solutions with 1M pyridine; $\Delta\lambda$=8 nm	0.0016 ± 0.0002

Table 17: Photosubstitution quantum yields of representative polypyridyl ruthenium(II) complexes.

As can be seen, the three families of polypyridyl systems $Ru(N\text{-}N\text{-}N)(py)_3^{2+}$, $Ru(N\text{-}N)_3^{2+}$ and $Ru(N\text{-}N\text{-}N)(N\text{-}N)(py)^{2+}$ (where N-N-N and N-N are terdentate and bidentate polypyridyl ligands, respectively) do not react with the same efficiency regarding the photolabilisation of a pyridine or bipyridine ligand. The quantum yields vary between 0.0004 and 0.20. Generally, the replacement of a bipyridine by a phenanthroline does not alter significantly the value of the photolabilisation quantum yield. However, hindered bipy or phen lower the ligand field and consequently increase drastically the efficiency of the reaction. Photolabilisation occurs in this case quickly and selectively, but the course of the reaction is difficult to predict, as noted by Laemmel *et al.*[80] For example $Ru(phen)_2(dmbp)^{2+}$ photolabilises the hindered ligand dmbp, whereas $Ru(terpy^*)(dmp)(py)^{2+}$ labilises the monodentate pyridine, leaving the bidentate dmp on the complex.

ANNEX D: EXPERIMENTAL DATA OF CRYSTAL STRUCTURES

Complex	**2**$^{2+}$	**5**$^{2+}$	**6**$^{2+}$	**8**$^{2+}$
Formula	$C_{97}H_{112}F_{24}N_{10}O_7P_4Ru_2$	$C_{55}H_{64}F_{12}N_6O_2P_2Ru$	$C_{50}H_{48}N_6Ru.2PF_6$ $.C_2H_6O$	$C_{172}H_{180}N_{20}Ru_4S_4.8PF_6$ $.3H_2O.6C_2H_4Cl_2$
MW	2312.03	1232.16	1170.05	4867.55
Cryst syst	hexagonal	monoclinic	monoclinic	Triclinic
Space group	P_{3221}	$C_{2/c\ 1}$	$C_{12/c1}$	P_{-1}
a (Å)	13.5432 (1)	23.7601 (2)	25.0624 (2)	11.0983 (1)
b (Å)	13.5432 (1)	13.1662 (1)	13.6912 (2)	20.9631 (3)
c (Å)	50.1170 (3)	37.2176 (4)	33.6533 (4)	23.8225 (3)
α (deg)	90	90	90	84.056 (5)
β (deg)	90	97.638 (5)	107.386 (5)	79.303 (5)
γ (deg)	120	90	90	87.692 (5)
V (Å^3)	7960.8 (1)	11539.5 (2)	11020.0 (2)	5415.6 (1)
Z	3	8	8	1
Color	red	red	orange	red
D_{calcd}(g.cm^{-3})	1.45	1.42	1.41	1.49
μ (mm^{-1})	0.443	0.411	0.425	0.615
T (K)	173	173	173	173
R[a]	0.073	0.066	0.062	0.077
R_w[b]	0.091	0.079	0.087	0.097

Complex	**12**$^{2+}$	**13**$^{2+}$	**37**$_{th}$$^{2+}$
Formula	$C_{104}H_{104}N_{12}O_4Ru_2.4PF_6.$ $4C_3H_6O.C_4H_{1O}O$	$C_{45}H_{49}N_5RuS.2PF_6.$ CH_2Cl_2	$C_{61}H_{50}F_{12}N_6O_2P_2Ru$
MW	2674.51	1167.92	1290.12
Cryst syst	triclinic	monoclinic	Tetragonal
Space group	P_{-1}	$P_{121/c\ 1}$	$I_{41/a}$
a (Å)	14.3343 (5)	12.7000 (3)	25.9568 (2)
b (Å)	15.8785 (5)	23.4037 (5)	25.9568 (2)
c (Å)	15.9528 (6)	17.3218 (4)	37.3385 (5)
α (deg)	108.482 (5)	90	90
β (deg)	102.042 (5)	103.614 (5)	90
γ (deg)	96.712 (5)	90	90
V (Å^3)	3301.7 (2)	5003.9 (2)	25157.1 (4)
Z	1	4	16
color	orange	red	red
D_{calcd}(g.cm^{-3})	1.35	1.55	1.36
μ (mm^{-1})	0.368	0.610	0.381
T (K)	173	173	173
R[a]	0.082	0.087	0.065
R_w[b]	0.096	0.102	0.087

a: $R = S\ |\ |F_o| - |F_c|\ |\ /\ |F_o|$; *b:* $R_w = [S_w\ (\ |\ F_o|\ - |F_c|\ )^2\ /\ S_w(\ |F_o|^2)]^{1/2}$

ANNEX E: X-RAY STRUCTURE OF COMPLEX $\mathbf{46}_{PHOTO}^{2+}$

Complex $\mathbf{46}_{photo}^{2+}$ was crystallised by dissolving 10 mg of $[\mathbf{46}_{photo}][PF_6]_2$ and 10 mg of potassium tetraphenylborate in 1 mL of acetone, and slowly diffusing diisopropylether vapours into it. The brown needles that were obtained were too small to be diffracted on the standard apparatus of the Service Commun de Cristallographie of the Université Louis Pasteur, but it was possible to send the crystals to Trieste and collect X-ray data at 100 K from the synchrotron that was available there. Ennio Zangrando was able to solve the collected data: he sent us recently a crystal structure of the molecule that confirmed our formulation. However, the crystal contained two independent ruthenium complexes beside four BPh_4^- anions. One complex presented the long -O-$(CH_2)_{18}$-O- chain with a rather disordered conformation, so that it had to be refined with some constraints on bond distances. The resulting resolution was unfortunately rather poor (R=22%). To date any attempt to obtain a better data set scaling the diffraction data failed. On Figure 47 (next page) are given the two geometries of complex $\mathbf{46}_{photo}^{2+}$ in the crystal structure. The O1-O2 distance is 6.23 Å and the O3-O4 distance 7.43 Å. These experimental values are very close to the calculated value given in Chapter 4, Part III.3: the shortest O-O distance in the photochemical isomer was predicted to be 6.3 Å. Moreover, the Chem3D-calculated conformation of $\mathbf{46}_{photo}^{2+}$ given in Chapter 4 (Figure 29 and Figure 32) looks very similar to the second conformation obtained in the crystal structure (complex around atom RU2, Figure 47b). As a conclusion, the X-ray structure of complex $\mathbf{46}_{photo}^{2+}$ confirmed the molecular modelling studies performed previously.

Formula: $C_{964}H_{1000}N_{48}O_{16}Ru_8B_{16}$	MW = 14495.64 $g.mol^{-1}$
Cryst syst: triclinic	Space group: $P_{21/n}$
a =13.420(4) Å	b = 24.728(5) Å
c = 63.597(7) Å	$\alpha = 90°$
$\beta = 93.08(3)°$	$\gamma = 90°$
V = 21074.2 $Å^3$	Z = 4
Color: brown	Size: 0.1x0.1x0.1 (mm)
T = 173 K	R factor = 22.4%
F(000) = 7680.0	μ = 0.44 mm-1

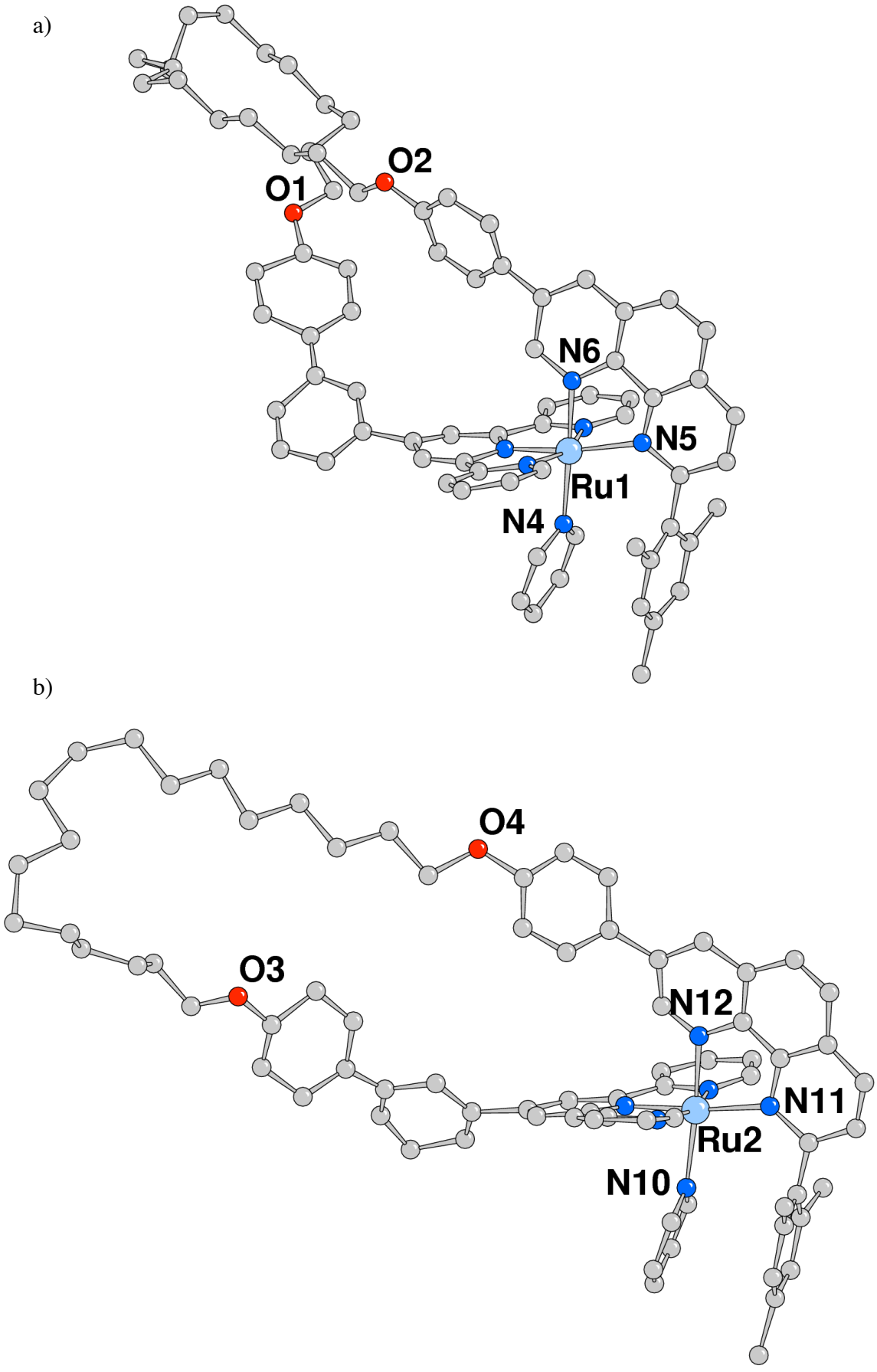

Figure 47: X-ray structure of complex $\mathbf{46}_{\mathbf{photo}}^{2+}$.

ANNEX F: CALCULATED SPECTRUM OF RU(TERPY)(PHEN)(CH_3CN)$^{2+}$

Here is shortly presented the calculations realised by Julien Bossert and Chantal Daniel (see also Chapter 1, Part IV.3).

Figure 48 gives the calculated absorption spectrum of Ru(terpy)(phen)(CH_3CN)$^{2+}$ compared to the experimental spectrum of the same complex dissolved in a 1 M acetonitrile solution of pyridine (arbitrary units). The spectrum was calculated using vertical Franck-Condon type transitions described by the Time-Dependent Density Functional Theory (TD-DFT). The ground state was minimised by DFT in order to insure the best possible results. The best fit between both spectra was obtained applying a 35 nm hypsochromic shift of the experimental spectrum. This shift can be interpreted as the difference between a solvated hexafluorophosphate dicationic complex and an isolated dication in the gas phase.

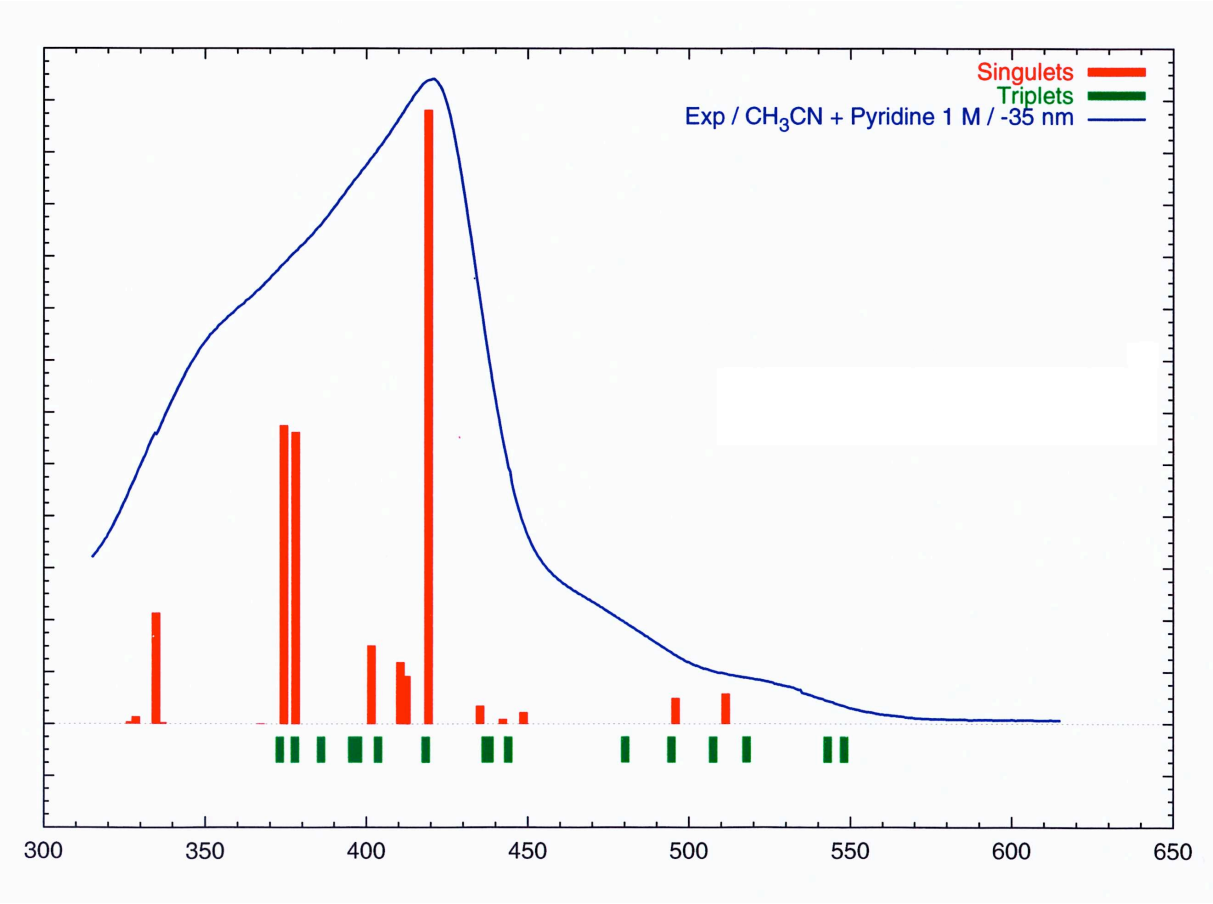

Figure 48: 35 nm hypsochromically shifted experimental spectrum (blue line) and calculated transitions (red: towards singlet excited states; green: towards triplet excited states) for Ru(terpy)(phen)(CH_3CN)$^{2+}$. Vertical scale is arbitrary; horizontal scale is in nanometer (nm).

As can be seen on Figure 48, there is a very good correlation between the theoretical and experimental spectra. The three main transitions towards singlet excited states appear on the theoretical spectrum at 419.26 nm, 377.98 nm, 374.31 nm and 334.82 nm. The maps showing the electron density difference between the excited states and the ground state are given on Figure 49 for these four states. Pink lobes correspond to a *gain* in electron density and yellow lobes to a *loss* in electron density during the transition.

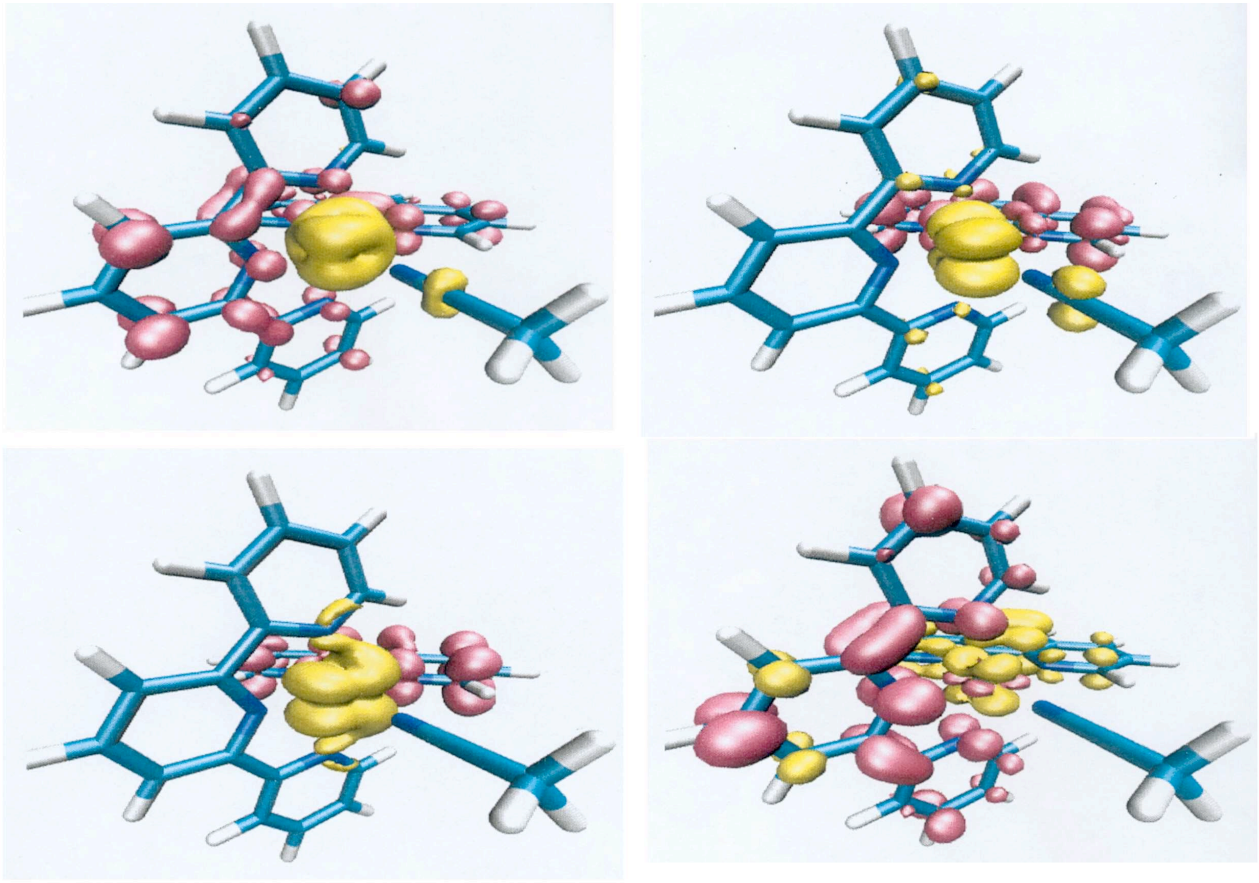

Figure 49: electron density difference maps for the four most probable calculated transitions towards singlet excited states (see Figure 1). a) 419.26 nm; b) 377.98 nm; c) 374.31 nm; d) 334.82 nm.

As can be seen on Figure 49a, the most probable transition in the visible region (419 nm) corresponds to a metal-to-ligand charge transfer state from the ruthenium to *both* the terpyridine *and* the phenanthroline chelates. The two states at 378 nm and 374 nm are ^{1}MLCT states towards the phenanthroline only. By contrast, the transition at 334 nm correspond to a ligand-to-ligand transition where the electron density moves from the phenanthroline to the terpyridine. It is important to note that there is no reliable TD-DFT method for calculating the probability of electronic transitions towards triplet excited states yet, although such transitions might exist due to the heavy-atom effect in ruthenium (II) complexes. The triplet states are noted as green sticks on Figure 48. The eleven transition with $\lambda > 400$ nm all correspond to ^{3}MLCT excited states, with the electron density going towards the phen, towards the terpy or towards both of them.

ANNEX G: PUBLICATIONS

Some of the work presented in this Ph-D thesis has been already published. The corresponding articles are:

1) Sylvestre Bonnet, Emma Schofield, Jean-Paul Collin et Jean-Pierre Sauvage, "Photochemical and thermal synthesis and characterization of polypyridine ruthénium(II) complexes containing different monodentate ligands", *Dalton Trans.* **2003**, 4654-4662;

2) Sylvestre Bonnet, Emma Schofield, Jean-Paul Collin et Jean-Pierre Sauvage, "Photochemical expulsion of the neutral monodentate ligand L in Ru(terpy*)(diimine)(L) $^{2+}$: a dramatic effect of the steric properties of the spectator diimine ligand", *Inorg. Chem.* **2004**, *43*, 8346-8354;

3) Sylvestre Bonnet, Jean-Paul Collin et Jean-Pierre Sauvage, "A Ru(terpy)(phen)-incorporating ring and its light-induced geometrical changes", *Chem. Comm.* **2005**, 3195-3197.

EXPERIMENTAL PART

Single crystal X-ray diffraction experiments were carried out using Kappa CCD and graphite-monochromated Mo-Kα radiation (λ = 0.71073 Å). For all computations, the MolEN package was used[178] and structures were drawn using ORTEP[179] and Mercury[180]. ^{1}H NMR spectra were acquired on either a Brucker AVANCE 300 (300MHz) or a Bruker AVANCE 400 (400 MHz) or a Bruker AVANCE 500 (500 MHz) spectrometer, using the deuterated solvent as the lock and residual solvent as the internal reference. Mass spectra were obtained by using a VG ZAB-HF(FAB) spectrometer, a VG-BIOQ triple quadrupole, positive mode or a Bruker MicrOTOF spectrometer (ES-MS). UV-visible spectra were recorded with a Kontron Instruments UVIKON 860 spectrometer at room temperature.

Terpy* (4'-(3,5-ditertiobutylphenyl)-2,2';6',2"-terpyridine) and aphen (4-anisyl-7-methyl-1,10-phenanthroline) were provided by Jean-Paul Collin[93] and Didier Pomeranc,[181, 182] respectively. Tetrahydropyranyl-2-(2-(2-iodoethoxy)ethoxy)ethanol[183, 184] was prepared according to literature procedure. Pyridine was distilled and kept over KOH under argon. Dimethylsulfoxide was distilled and kept under argon. Ammonium acetate and tetraethylammonium chloride were commercial product dried overnight under vacuum. 2,6-dimethylbenzonitrile, 2,6-dimethoxybenzonitrile, anhydrous 1,10-phenanthroline, monoaqua 1,10-phenanthroline, 1,10-phenanthroline hydrochloride, hemi aqua 2,9-dimethyl-1,10-phenanthroline, dimethylsulfide, phenothiazine, 3,5-lutidine, acetonitrile, 3-bromobenzaldehyde, 2-acetylpyridine, 2-(2-(2-chloroethoxy)ethoxy)ethanol, parahydroxybenzonitrile, methylthioethanol, paramethoxyphenylboronic acid, 10-bromo-dec-1-ene, Grubbs' 1st generation catalyst were commercial products. $RuCl_3.xH_2O$ was kindly provided by Johnson Matthey Incorporation. Dichloromethane was distilled under CaH_2. Tetrahydrofuran, diethylether and toluene were distilled and dried over sodium. Acetone was distilled and dried over sodium sulfate. KPF_6 was used as a 40 g/L aqueous solution. KNO_3 was used as a saturated aqueous solution.

In every synthesis of ruthenium complexes, chromatography fractions were worked up as follows: addition of an excess of KPF_6, evaporation of the organic solvent (acetone or acetonitrile) until precipitation, filtration, washing with water, recovery from the P4 frit with acetone and drying under vacuum.

I. Chapter 1: synthesis of Ru(terpy*)(N-N)(L)$^{n+}$ complexes and ligand substitution reactions

I.1. Synthesis

Ru(terpy*)Cl$_3$: 201 mg (0.479 mmol) of 4-(3,5-di-tert-butyl)phenyl-2,2';6',2"-terpyridine and

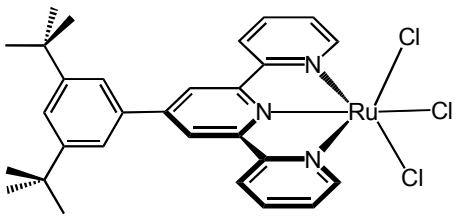

125 mg (0.478 mmol) of $RuCl_3.3H_2O$ were dissolved in ethanol (30 cm^3). The solution was heated to reflux for 1 h, cooled down and the precipitate isolated by filtration. The orange solid was washed twice with ethanol, once with water, once with diethyl ether and air dried. Yield: 299 mg (99.5%).

FAB MS *m/z (calc.):* 628.1 (628.1, [M]$^+$), 593.1 (593.1, [M – Cl]$^+$), 558.1 (558.1, [M – 2 Cl]$^+$), 523.2 (523.2, [M – 3 Cl]$^+$).

I.1.a. Phen series

1$^+$ **[Ru(terpy*)(phen)(Cl)][PF$_6$]**: 428 mg (0.68 mmol) of Ru(terpy*)Cl$_3$, 140 mg (0.708 mmol) of

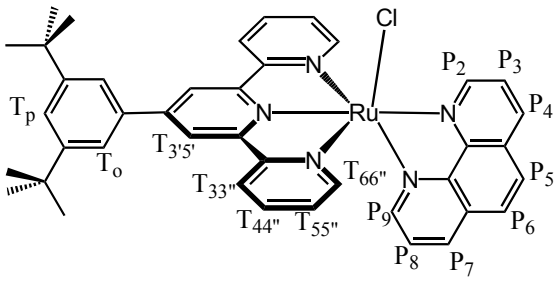

monoaqua-1,10-phenanthroline, 144 mg (3.41 mmol) of lithium chloride and 1.5 cm^3 triethylamine were heated at reflux in a degassed mixture of water (40 cm^3) and ethanol (120 cm^3) under argon for 4 h. A solution of saturated aqueous KPF_6 (40 cm^3) was added to the cooled dark reddish solution, ethanol was evaporated and the violet precipitate filtered and washed twice with water and once with ether. Column chromatography on SiO_2 (eluant acetone / water / saturated KNO_3 100:5:0.1) and vapour diffusion of diethylether into an acetone solution of the product yielded 377 mg of [**1**][PF_6] (62%).

^{1}H 400 MHz NMR: δ (ppm) in acetone-d6: 10.57 (dd, 1H, P_2, J=5.2,1.5Hz); 9.04 (2H, s, $T_{3',5'}$); 8.97 (dd, 1H, P_4, *J*=8.2,1.5Hz); 8.75 (d, 2H, $T_{33"}$, *J*=8.0Hz); 8.45 (dd, 1H, P_3, *J*=5.2,8.2Hz); 8.45 (d, 1H, P_5, *J*=8.9Hz); 8.40 (dt, 1H, P_7, *J*=8.1,1.1Hz); 8.23 (d, 1H, P_6, *J*=8.9Hz); 8.04 (d, 2H, T_o, *J*=1.7 Hz); 8.03 (dd, 1H, P_9, *J*=5.4, 1.1 Hz); 7.94 (td, 2H, $T_{44"}$, *J*=8.0,1.5Hz); 7.75 (t, 1H, T_p, *J*=1.7Hz); 7.69 (d, 2H, $T_{66"}$, *J*=5.5Hz); 7.47 (dd, 1H, P_8, *J*=5.4, 8.1Hz); 7.24 (ddd, 2H, $T_{55"}$, *J*=7.6,5.5,1.3Hz); 1.50 (s, 18H, tBu). *ES MS m/z (calc.):* 738.2 (738.2, [M – PF_6]$^+$). *UV-vis:* λ_{max} (ε in L.mol^{-1}.cm^{-1}) in dichloromethane: 266 nm (42300); 284 nm (38800); 316 nm (25500); 510 nm (11700).

2^{2+} [Ru(terpy*)(phen)(H_2O)][PF_6]$_2$: 113 mg (0.128 mmol) of [**1**][PF_6] and 248 mg (1.28 mmol) of $AgBF_4$ were dissolved in 100 cm^3 of a 3:2 acetone/water mixture. The solution was degassed and heated at reflux under argon for 3 h. AgCl was filtered over celite©, water and an aqueous solution of KPF_6 (50 cm^3) were added and acetone was evaporated. The red solid [**2**][PF_6]$_2$ was filtred, washed with water, recovered with acetone and dried. Yield: 89 mg (69%).

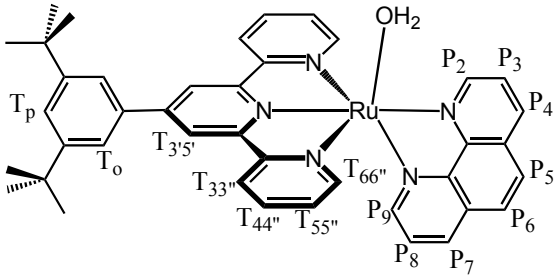

^1H 300 MHz NMR: δ (ppm) in CD_2Cl_2: 9.94 (d, 1H, P_2, J=4.9Hz); 8.82 (d, 1H, P_4, J=8.1Hz); 8.57 (s, 2H, $T_{3',5'}$); 8.41 (dd, 2H, $T_{33"}$, *J*=7.4, 0.9Hz); 8.37 (dd, 1H, P_3, *J*=8.1,4.9Hz); 8.29 (d, 1H, P_5, *J*=8.9Hz); 8.17 (d, 1H, P_7, *J*=8.1Hz); 8.06 (d, 1H, P_6, *J*=8.9Hz); 7.90 (td, 2H, $T_{44"}$, *J*=7.4Hz); 7.79 (d, 2H, T_o, *J*=1.8Hz); 7.73 (t, 1H, T_p, *J*=1.8Hz); 7.64 (d, 1H, P_9, *J*=5.0Hz); 7.53 (d, 2H, $T_{66"}$, *J*=5.3Hz); 7.42 (dd, 1H, P_8, *J*=8.1,5.0Hz); 7.25 (m, 2H, $T_{55"}$); 1.50 (s, 18H, tBu). *ES MS m/z (calc):* 722.2 (721.2, [M – 2 PF_6 + H]$^+$); 848.2 (848.2, [M – H_2O – PF_6]$^+$); 380.5 (380.6, [M – 2 PF_6 – H_2O + acetone]$^{2+}$). *UV-vis:* λ_{max} (ε in $L.mol^{-1}.cm^{-1}$) in dichloromethane: 266 nm (55100); 281 nm (37900); 314 nm (35500) ; 486 nm (13700). Recrystallisation by vapour diffusion in the dark, of diisopropyl ether into a solution of the product in acetone yielded crystals of 2(**2**)4(PF_6)5(C_3H_6O) suitable for X-ray analysis (see Annex D).

3^{2+} [Ru(terpy*)(phen)(CH_3CN)][PF_6]$_2$: 199 mg (0.226 mmol) of [**1**][PF_6] and 53.4 mg (0.259 mmol) of $AgBF_4$ were dissolved in 60 cm^3 of a 1:4 mixture of water and acetonitrile. The degassed solution was heated to reflux under argon for 4.5 h. Silver chloride was removed by filtration over celite, the volume of acetonitrile was reduced by evaporation and a solution of saturated aqueous KPF_6 (30 cm^3) was added. Evaporation of acetonitrile, filtration, washing with water, recovering with acetonitrile and vacuum drying quantitatively yielded [**3**][PF_6]$_2$.

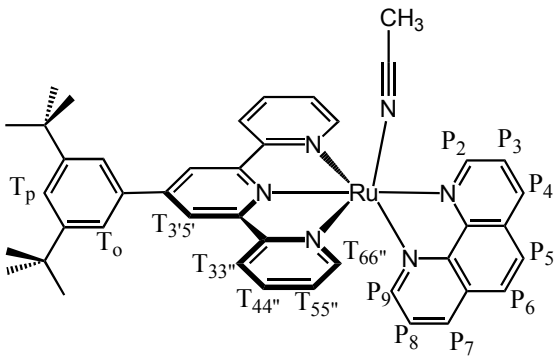

^1H 300 MHz NMR: δ (ppm) in acetone-d6: 10.28 (dd, 1H, P_2, *J*=5.2,1.5Hz); 9.20 (s, 2H, $T_{3',5'}$); 9.08 (dd, 1H, P_4, *J*=8.3,1.5Hz); 8.89 (m, 2H, $T_{33"}$, *J*=8.0Hz); 8.57 (dd, 1H, P_7, *J*=8.4,1.2Hz); 8.50 (d, 1H, P_5, *J*=8.9Hz); 8.48 (dd, 1H, P_3, *J*=8.3,5.2Hz); 8.29 (d, 1H, P_6, *J*=8.9Hz); 8.12 (td, 2H, $T_{44"}$, *J*=8.0,1.5Hz); 8.09 (dd, 1H, P_9, *J*=5.3,1.2Hz); 8.05 (d, 2H, T_o, *J*=1.7Hz); 7.87 (dm, 2H, $T_{66"}$, *J*=5.4Hz); 7.81 (t, 1H, T_p, *J*=1.7Hz); 7.60 (dd, 1H, P_8, *J*=5.3,8.4Hz); 7.38 (ddd, 2H, $T_{55"}$, *J*=5.4,8.0,1.2Hz); 2.42 (s, 3H, CH_3(AN)); 1.50 (s, 18H, tBu). *ES MS m/z (calc.):* 889.3 (889.2,

$[M–PF_6]^+$), 744.3 (744.3, $[M–2\ PF_6]^+$), 371.9 (372.1, $[M – 2\ PF_6]^{2+}$). *UV-vis:* λ_{max} (ε in $L.mol^{-1}.cm^{-1}$) in acetonitrile: 264 nm (59700); 310 nm (40000); 464 nm (17800).

4^{2+} [Ru(terpy*)(phen)(PY)][PF_6]$_2$: 35.1 mg (0.0340 mmol) of [**3**][PF_6]$_2$ were dissolved into 10 mL of neat pyridine and refluxed under argon for 2 hours. The pyridine was removed under vacuum, acetone was added and the complex was precipitated with aqueous KPF_6. The solid was filtered, washed with water, recovered with acetone and dried under vacuum to quantitatively yield [**4**][PF_6]$_2$.

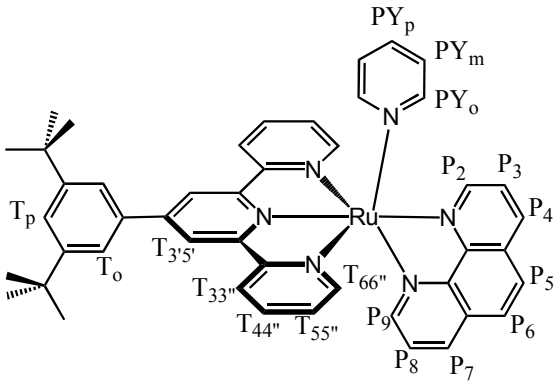

^1H 300 MHz NMR: δ (ppm) in acetone-d6: 9.42 (dd, 1H, P_2); 9.19 (s, 2H, $T_{3',5'}$); 9.07 (dd, 1H, P_4); 8.91 (dm, 2H, $T_{33"}$); 8.59 (dd, 1H, P_7); 8.52 (d, H, P_5); 8.39 (dd, 1H, P_3); 8.33 (d, 1H, P_6); 8.24 (m, 2H, PY_o); 8.14 (td, 2H, $T_{44"}$); 8.12 (dd, 1H, P_9); 8.01 (d + dm, 4H, T_o + $T_{66"}$); 7.97 (tt, 1H, PY_p); 7.77 (t, 1H, T_p); 7.61 (dd, 1H, P_8); 7.43 (m, 4H, $T_{55"}$ + PY_m); 1.47 (s, 18H, tBu). *ES MS m/z (calc.):* 391.15 (391.13, $[M – 2\ PF_6]^{2+}$). *UV-vis*: in pyridine, λ_{max} (ε in $L.mol^{-1}.cm^{-1}$): 487 nm (13200).

5^{2+} [Ru(terpy*)(phen)(LUT)][PF_6]$_2$: 24.5 mg (0.024 mmol) of [**3**][PF_6]$_2$ were dissolved in 5 cm^3 of 3,5-lutidine. The solution was degassed and heated to reflux under argon for 2 h. Lutidine was removed under vacuum, acetone (1 cm^3) and an aqueous solution of KPF_6 (10 cm^3) were added, acetone was evaporated and the solid was filtered, washed with water, Et_2O, recovered with acetone and vacuum dried. Yield: 23 mg (88%).

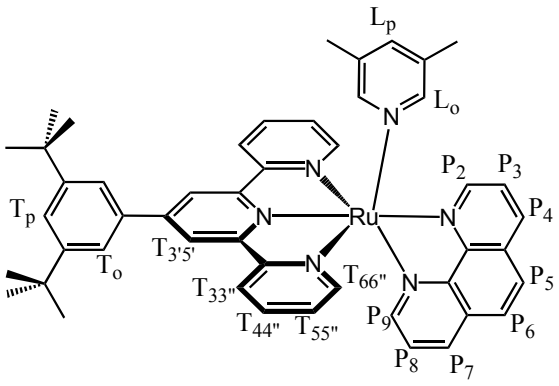

^1H 400 MHz NMR, δ (ppm) in acetone-d6: 9.39 (1H, dd, 1.2 Hz P_2, J=5.4Hz); 9.18 (2H, s, $T_{3',5'}$); 9.05 (dd, 1H, P_4, J=8.2,1.2 Hz); 8.90 (m, 2H, $T_{33"}$, J=7.8Hz); 8.57 (dd, 1H, P_7, J=8.2,1.2Hz); 8.50 (d, 1H, P_5, J=8.8Hz); 8.37 (dd, 1H, P_3, J=8.2,5.4Hz); 8.32 (d, 1H, P_6, J=8.8Hz); 8.15 (td, 2H, $T_{44"}$, J=7.8,1.5Hz); 8.08 (dd, 1H, P_9, J=5.3,1.2Hz); 8.04 (d, 2H, T_o, J=1.8Hz); 8.01 (d, 2H, $T_{66"}$, J=4.7Hz); 7.78 (3H, T_p+L_o); 7.62-7.58 (m, 2H, P_8+L_p); 7.44 (m, 2H, $T_{55"}$); 2.14 and 2.14 (2s, 6H, L_{CH3}); 1.49 (s, 18H, ^{t}Bu). *ES MS m/z (calc.):* 955.3 (955.3, $[M – PF_6]^+$), 738.2 (738.2, $[M – 2\ PF_6 – LUT + Cl]^+$), 405.0 (405.2, $[M – 2\ PF_6]^{2+}$). Crystals of (**5**)2(PF_6)(C_3H_6O)($C_4H_{10}O$) were grown by slow vapour diffusion of Et_2O in an acetone solution of the complex (see Annex D).

6^{2+},2PF_6^- **[Ru(terpy*)(phen)(MeBN)][PF_6]$_2$** : 22.5 mg (0.0217 mmol) of [**3**][PF_6]$_2$ and 28.5 mg (0.218 mmol) of 2,6-dimethylbenzonitrile were dissolved in 5 mL of acetone. The solution was degassed and refluxed under argon over night. The solution was cooled down to room temperature, the volume of acetone was reduced to 2 mL and 10 mL of KPF_6 were added. The solid was filtered, washed with water and ether and put on a silica gel column (eluent: acetone / water / KNO_3 480:20:1). To the collected fractions was added KPF_6, acetone was removed, the solid filtered, washed, recovered with acetone and dried. Yield: 16.6 mg of [**6**][PF_6]$_2$ (68%).

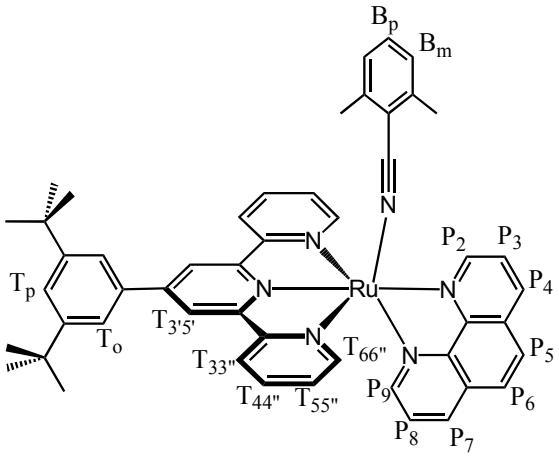

^{1}H 300 MHz NMR: δ (ppm) in acetone-d6: 10.36 (dd, 1H, P_2); 9.25 (s, 2H, $T_{3',5'}$); 9.11 (dd, 1H, P_4); 8.94 (m, 2H, $T_{33"}$); 8.64 (dd, 1H, P_7); 8.53 (d, 1H, P_5); 8.51 (dd, 1H, P_3); 8.34 (d, 1H, P_6); 8.26 (dd, 1H, P_9); 8.17 (td, 2H, $T_{44"}$); 8.04 (d, 2H, T_o); 8.02 (dm, 2H, $T_{66"}$); 7.78 (t, 1H, T_p); 7.41 (dd, 1H, P_8); 7.46-7.40 (3H, $T_{55"}$ and B_p); 7.17 (d, 2H, B_m, $^3J_{m\text{-}p}$ = 7.7 Hz); 2.13 (s, 6H, CH_3(B)); 1.48 (s, 18H, CH_3(^{t}Bu)). Monocrystals of (**6**)2(PF_6)(C_2H_6O) were grown by vapor diffusion of diisopropylether in acetone (see Annex D).

7^{2+} **[Ru(terpy*)(phen)(MeOBN)][PF_6]$_2$** : 25 mg (0.0283 mmol) of [**1**][PF_6] and 5.7 mg (0.0283 mmol) of $AgBF_4$ were dissolved in 40 mL of acetone dried over $MgSO_4$. The solution was degassed and refluxed under argon for 1 hour. The cooled solution was filtered, 3 equivalents (17 mg) of silver tetrafluoroborate were added along with 552 mg of 2,6-dimethoxybenzonitrile (120 eq) and 40 mL of n-butanol dried over $MgSO_4$. Acetone was evaporated, and the butanol solution was refluxed under argon for 4 hours. The cool solution was filtered over celite, and the butanol removed under vacuum. Acetone, 20 mL of KPF_6 and 20 mL of water were added, the acetone was evaporated, the solid was filtered, washed with water, Et_2O, recovered with acetone, dried and purified by column chromatography (SiO_2, eluent acetone / water / KNO_3 400:5:0.1). The last fraction was collected and worked up to afford 21.9 mg of [**7**][PF_6]$_2$ (67%).

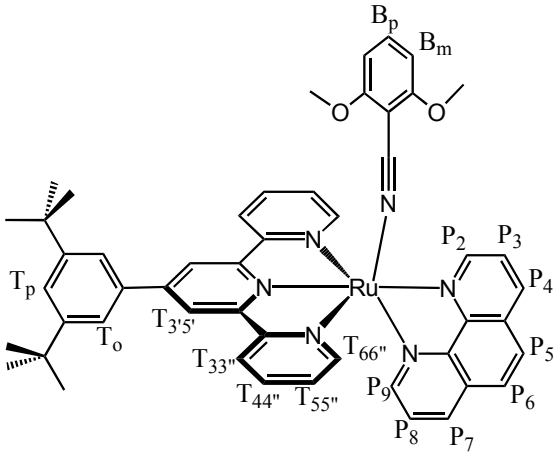

^{1}H 300 MHz NMR: δ (ppm) in acetone-d6: 10.26 (dd, 1H, P_2); 9.26 (s, 2H, $T_{3',5'}$); 9.11 (dd, 1H, P_4); 8.92 (m, 2H, $T_{33"}$); 8.63 (dd, 1H, P_7); 8.56 (dd, 1H, P_3); 8.53 (dd, 1H, P_5); 8.34 (d, 1H, P_6); 8.25

(dd, 1H, P_9); 8.15 (td, 2H, $T_{44"}$); 8.09 (d, 2H, T_o); 7.94 (dm, 2H, $T_{66"}$); 7.81 (t, 1H, T_p); 7.66 (dd, 1H, P_8); 7.57 (t, 1H, B_p, $^3J_{p\text{-}m}$ = 8.6 Hz); 7.41 (m, 2H, $T_{55"}$); 6.73 (d, 2H, B_m, $^3J_{m\text{-}p}$ = 8.6 Hz); 3.82 (s, 6H, B_{OMe}); 1.50 (s, 18H, $CH_3(^tBu)$). *ES MS m/z (calc.):* 1011.3 (1011.3, $[M - PF_6]^+$), 433.0 (433.2, $[M - 2\ PF_6]^{2+}$). *UV Vis:* in pyridine λ_{max} = 465 nm (15200).

8^{2+} [Ru(terpy*)(phen)(DMS)][PF_6]$_2$: 16.3 mg (0.0161 mmol) of [**2**][PF_6]$_2$ were dissolved in a mixture of 2 mL of dimethylsulfide and 10 mL of ethanol, the solution was degassed and refluxed under argon for 2 hours. The solvents were evaporated and the solid residue was purified by chromatography on silica gel in the dark (eluent: acetone / water / KNO_3 60:5:0.5) to quantitatively yield [**8**][PF_6]$_2$ as an orange complex.

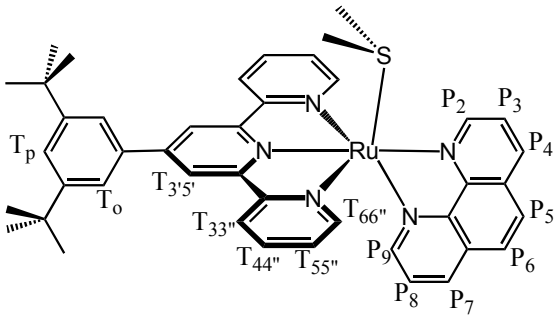

^1H 300 MHz NMR: δ (ppm) in acetone d6 : 10.30 (d, 1H, P_2); 9.29 (s, 2H, $T_{3',5'}$); 9.10 (d, 1H, P_4); 9.95 (dd, 2H, $T_{33"}$); 8.65 (dd, 1H, P_7); 8.51 (d + dd, 2H, P_3 + P_5); 8.33 (d, 1H, P_6); 8.16 (td, 2H, $T_{44"}$); 8.09 (d + d, 3H, P_9 +T_o); 7.92 (d, 2H, $T_{66"}$); 7.81 (t, 1H, T_p); 7.67 (dd, 1H, P_8); 7.40 (m, 2H, $T_{55"}$); 1.66 (s, 6H, $(CH_3)_2S$); 1.49 (s, 18H, tBu). *UV-vis*: in pyridine, λ_{max} (ε in $L.mol^{-1}.cm^{-1}$): 473 nm (11500). Monocrystals suitable for X-ray analysis were obtained by slow diffusion, in the absence of light, of iPr_2O in 1,2-dichloroethane. The positions of the solvent molecules were poorly defined because the solvents used for crystallization were very volatile, however the structure of the complex itself was determined with good accuracy; see Annex D).

9^{2+} [Ru(terpy*)(phen)(DMSO)][PF_6]$_2$: 23.9 mg (23.6 μmol) of [**2**][PF_6]$_2$ were dissolved in a mixture of 1 mL of DMSO and 10 mL of absolute ethanol, put under argon and refluxed for 2 hours. The solvents were evaporated under vacuum and the sample, still containing traces of DMSO, was chromatographed on silica gel (eluent: acetone / H_2O / KNO_3 150:40:4 to 100:10:1) to yield 19.6 mg (80% yield) of [**9**][PF_6]$_2$ as a yellow complex.

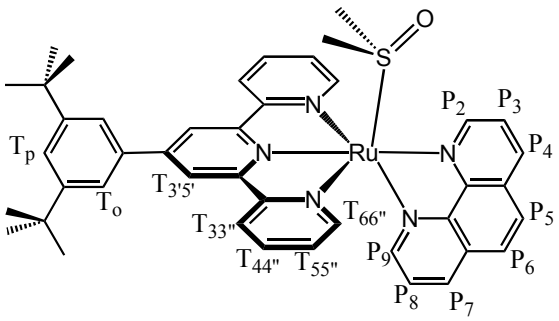

^1H 300 MHz NMR: δ (ppm) in CD_2Cl_2: 10.56 (d, 1H, P_2); 8.84 (d, 1H, P_4); 8.71 (s, 2H, $T_{3',5'}$); 8.52 (dd, 2H, $T_{33"}$); 8.48 (dd, 1H, P_7); 8.32 (dd, 1H, P_3); 8.29 (d, 1H, P_5); 8.14 (d, 1H, P_6); 8.07 (td, 2H, $T_{44"}$); 7.91 (d, 2H, T_o); 7.76 (t, 1H, T_p); 7.72-7.61 (m, 4H, P_9 + P_8 + $T_{66"}$); 7.34 (m, 2H, $T_{55"}$);

2.53 (s, 6H, $(CH_3)_2SO$); 1.50 (s, 18H, tBu). *ES MS m/z (calc.):* 926.3 (926.2, $[M - PF_6]^+$), 390.5 (390.6, $[M - 2\ PF_6]^{2+}$). *UV-vis*: in pyridine, λ_{max} (ε in $L.mol^{-1}.cm^{-1}$): 430 nm (13200).

10^{2+} [Ru(terpy*)(phen)(PTZ)][PF_6]$_2$: 25 mg (24 μmol) of [**3**][PF_6]$_2$ and 49 mg (246 μmol) of phenothiazine were dissolved in 50 mL of acetone, put under argon and irradiated with a 150 W dia-projector for 3 hours. Acetone was removed under vacuum and the crude product was purified on silica gel (eluent: acetone / water / KNO_3 500:30:5) to give 26 mg of the yellow complex [**10**][PF_6]$_2$ (yield 92 %).

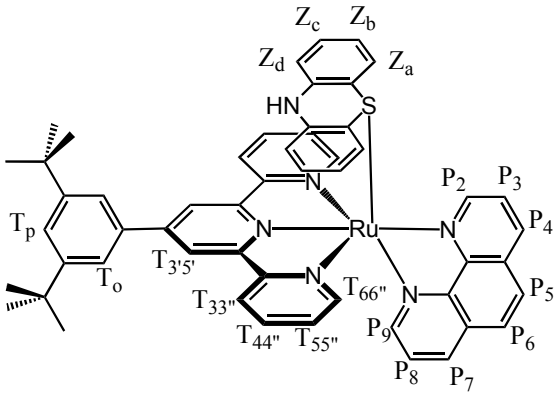

^1H 300 MHz NMR: δ (ppm) in acetone: 11.06 (dd, 1H, P_2); 9.16 (dd, 1H, P_4); 8.91 (s, 2H, $T_{3',5'}$); 8.67 (dd, 2H, P_3); 8.60 (dd, 1H, P_7); 8.52 (d, 1H, P_5); 8.47 (d, 1H, $T_{33"}$); 8.31 (d, 1H, P_6); 8.27 (s, 1H, Z_{NH}); 7.99 (d, 2H, T_o); 7.96 (dd, 1H, P_9); 7.95 (td, 2H, $T_{44"}$); 7.83 (t, 1H, T_p); 7.71 (m, 2H, $T_{66"}$); 7.60 (dd, 1H, P_8); 7.15 (m, 2H, $T_{55"}$); 7.10 (dd, 1H, Z_d); 6.85 (dd, 1H, Z_a); 6.57 (m, 2H, Z_b+Z_c); 1.52 (s, 18H, tBu). *ES MS m/z (calc.):* 451.0 (451.1, $[M - 2\ PF_6]^{2+}$), 1047.3 (1047.2, $[M - PF_6]^+$). *UV-vis*: λ_{max} (ε in $L.mol^{-1}.cm^{-1}$) in acetonitrile: 465 nm (10300).

I.1.b. Dmp series

11^{2+} [Ru(terpy*)(dmp)(CH_3CN)][PF_6]$_2$: 100 mg (0.159 mmol) of Ru(terpy*)Cl_3, 36.5 mg (0.175 mmol) of hemiaqua-2.9-dimethyl-1,10-phenanthroline, 33.7 mg (0.80 mmol) of lithium chloride were mixed with 0.5 mL of triethylamine, 10 mL of water and 30 mL of ethanol. The solution was degassed and refluxed under argon for 4 hours 15 minutes. To the cooled dark violet solution were added 20 mL of KPF_6 and 20 mL of water, ethanol was evaporated and the violet precipitate filtered and washed twice with water and once with ether. Careful column chromatography performed in the dark (SiO_2, eluent: acetone / water / KNO_3 125:5:0.1) yielded 100 mg of a mixture of the hydroxy and chloro complexes. This mixture was used without further purification. To these 100 mg (0.110 mmol) of product were added 32 mg (0.165 mmol) of $AgBF_4$, 10 mL water and 40 mL acetonitrile. The solution was degassed and refluxed under argon for 15 minutes. Silver chloride was removed by filtration over celite©, 20 mL

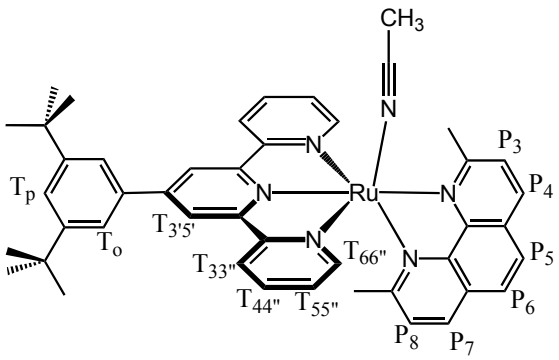

KPF_6 were added and acetonitrile was evaporated. The orange solid was washed with water and ether, recovered with acetonitrile and vacuum dried. Yield: 93 mg of [**11**][PF_6]$_2$ (80%).

^{1}H 400 MHz NMR: δ (ppm) in CD_3CN: 8.77 (s, 2H, $T_{3',5'}$); 8.75 (dd, 1H, P_4, $^3J_{3-4}$ = 8.7Hz); 8.64 (dq, 2H, $T_{33"}$, $^3J_{33"-44"}$ = 8.1Hz, $^5J_{33"-55"}$ = 0.7Hz); 8.26 (d, 1H, P_7, $^3J_{7-8}$ = 8.2Hz); 8.23 (d, 1H, P_5, $^3J_{5-6}$ = 8.7Hz); 8.13 (d, 1H, P_6, $^3J_{6-5}$ = 8.4Hz); 8.03 (d, 1H, P_3); 8.04 (td, 2H, $T_{44"}$, $^3J_{44"-33"}$ = $^3J_{44"-55"}$ = 7.9Hz, $^5J_{44"-66"}$ = 1.5Hz); 7.92 (d, 2H, T_o, $^4J_{o-p}$ = 1.8Hz); 7.77 (t, 1H, T_p, $^4J_{p-o}$ = 1.8Hz);7.64 (dq, 2H, $T_{66"}$, $^3J_{66"-55"}$ = 5.6Hz, $^5J_{66"-44"}$ = 0.7Hz); 7.30 (2dd, 2H, $T_{55"}$, $^3J_{55"-66"}$ = 5.6Hz, $^3J_{55"-44"}$ = 7.7Hz, $^5J_{55"-33"}$ = 1.3Hz); 7.29 (d, 1H, P_8, $^3J_{8-7}$ = 8.4Hz); 3.25 (s, 3H, $CH_3(P_2)$); 1.88 (s, 3H, $CH_3(P_9)$); 1.50 (s, 18H, $CH_3(^tBu)$); the methyl group of coordinated CH_3CN is lost behind the residual solvent peak. *^{1}H 300 MHz NMR:* δ (ppm) in DMSO: the three methyl peaks integrate for 3 H and are seen at 3.24 (P_2), 1.83 (P_9) and 2.21 (coordinated CH_3CN). *^{1}H 300 MHz NMR:* δ (ppm) in acetone d6 for comparison with other complexes (without coupling constants): 9.19 ($T_{3',5'}$); 8.90 (P_4 + $T_{33"}$); 8.44 (P_7); 8.36 (P_5); 8.29 (P_6); 8.18 ($T_{44"}$); 8.17 (P_3); 8.08 (T_o); 7.95 ($T_{66"}$); 7.80 (T_p); 7.47 (P_8); 7.47 ($T_{55"}$); 3.44 ($CH_3(P_2)$); 2.24 (CH_3CN); 1.49 ($CH_3(^tBu)$); the $CH_3(P_9)$ is lost behind the residual solvent peaks. *^{13}C 400 MHz NMR:* δ (ppm) in acetonitrile, assignments given by HETCORR ^{1}H-^{13}C experiments (1HMQC-HMBC): 160.1 (P_2); 159.7 (P_9); 154.8 ($T_{66"}$), 139.4 ($T_{44"}$), 138.2 (P_4), 138.2 (P_7), 128.8 ($T_{55"}$), 128.2 (P_3), 128.0 (P_5), 127.8 (P_6), 127.7 (P_8), 125.8 and 125.6 (T_p and $T_{33"}$), 123.3 and 123.3 (T_o and $T_{3',5'}$), 36.0 ($C^{IV}(^tBu)$), 31.7 ($CH_3(^tBu)$), 28.6 ($CH_3(P_2)$), 24.8 ($CH_3(P_9)$), 4.5 ($CH_3(AN)$). The 9 remaining aromatic quaternary peaks were not assigned: 167.8, 153.5, 151.5, 149.6, 148.7, 137.4, 130.5, 130.0, 127.3. *ES MS m/z (calc.):* 917.3 (917.3, $[M - PF_6]^+$), 771.3 (772.3, $[M - 2\ PF_6]^+$), 731.3 (731.3, $[M - 2\ PF_6 - CH_3CN]^+$), 386.0 (386.1, $[M - 2\ PF_6]^{2+}$), 365.5 (365.6, $[M - 2\ PF_6 - CH_3CN]^{2+}$). *UV-vis*: λ_{max} (ε in $L.mol^{-1}.cm^{-1}$) in acetone: 466 nm (12000).

12^{2+} [Ru(terpy*)(dmp)(MeOBN)][PF_6]$_2$: 26.7 mg (0.0251 mmol) of [**11**][PF_6]$_2$ and 232 mg (1.42 mmol) of 2,6-dimethoxybenzonitrile were dissolved in 15 mL acetone. The solution was degassed and refluxed under argon for 30 minutes. Acetone was evaporated, the solid was dissolved in freshly distilled dichloromethane, precipitated by adding ether, filtered and purified by column chromatography on silica gel (eluent: acetone / water / KNO_3 700:66:12). Yield: 18.1 mg of [**12**][PF_6]$_2$ as a dark orange solid (61%).

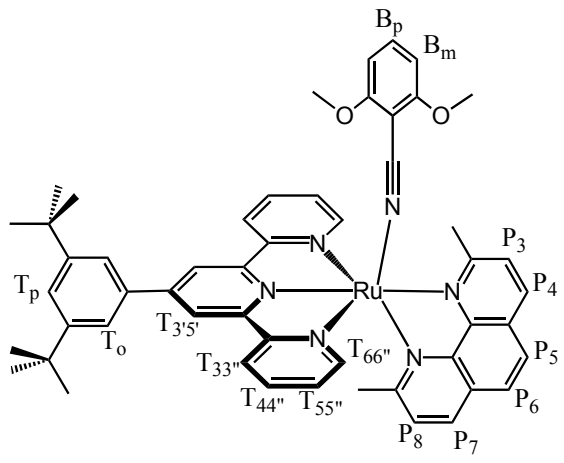

^{1}H 300 MHz NMR: δ (ppm) in acetone-d6: 9.31 (s, 2H, $T_{3',5'}$); 8.94 (d, 3H, P_4 and $T_{33"}$); 8.49 (d, 1H, P_7); 8.39 (d, 1H, P_5); 8.34 (d, 1H, P_6); 8.20 (d, 1H, P_3); 8.19 (td, 2H, $T_{44"}$); 8.11 (d, 2H, T_o); 8.03 (dm, 2H, $T_{66"}$); 7.81 (t, 1H, T_p); 7.53-7.46 (4H, P_8, $T_{55"}$ and B_p); 6.65 (d, 2H, B_m, $^3J_{m\text{-}p}$ = 8.6 Hz); 3.77 (s, 6H, OMe(B)); 1.48 (s, 18H, $CH_3(^tBu)$). *ES MS m/z (calc.):* 447.161 (447.160, $[M–2PF_6]^{2+}$). *UV-vis*: λ_{max} (ε in $L.mol^{-1}.cm^{-1}$) in dichloromethane: 467 nm (12000). Mono-crystals were grown by slow vapor diffusion of diethylether in acetone. The positions of the solvent molecules were poorly defined because the solvents used for crystallization were very volatile. However the structure of the complex itself was determined with good accuracy (see Annex D).

13^{2+} [Ru(terpy*)(dmp)(DMS)][PF_6]$_2$: 20.4 mg (19 μmol) of [**11**][PF_6]$_2$ were put under argon, a degassed mixture of 5 mL of dimethylsulfide and 1 mL acetone were added and the solution was irradiated under argon for 30 minutes. The solvents were removed under vacuum, and the complex was recrystallized overnight by slow vapor diffusion of $^iPr_2O$ in acetone in the dark. The orange crystals were isolated, washed with $^iPr_2O$ to give 10.4 mg (50%) of [**13**][PF_6]$_2$.

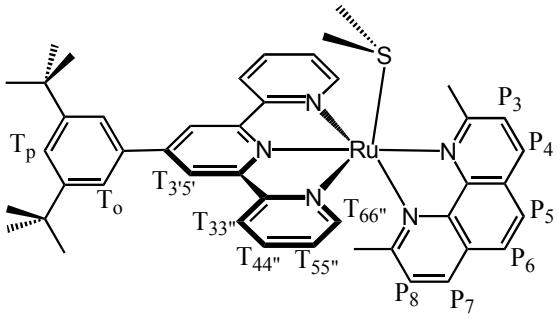

^{1}H 300 MHz NMR: δ (ppm) in CD_2Cl_2 : 8.67 (d, 1H, P_4); 8.65 (s, 2H, $T_{3',5'}$); 8.52 (d, 2H, $T_{33"}$); 8.16-8.05 (m, 5H, P_3 + P_5 + P_7 + $T_{44"}$); 7.92 (d, 1H, P_6); 7.82 (d, 2H, T_o); 7.74 (t, 1H, T_p); 7.69 (dd, 2H, $T_{66"}$); 7.41 (m, 2H, $T_{55"}$); 7.25 (d, 1H, P_8); 3.43 (s, 3H, $CH_3(P_2)$); 1.72 (s, 3H, $CH_3(P_9)$); 1.49 (s, 18H, tBu); 1.11 (s, 6H, $(CH_3)_2S$). *ES MS m/z (calc.):* 793.3 (793.3, $[M – 2\ PF_6]^+$), 396.5 (396.7, $[M – 2\ PF_6]^{2+}$), 365.5 (365.6, $[M – 2\ PF_6 – (CH_3)_2S]^{2+}$). *UV-vis*: λ_{max} (ε in $L.mol^{-1}.cm^{-1}$) in pyridine: 492 nm (9840). Mono-crystals suitable for X-ray analysis were obtained by slow diffusion of $^iPr_2O$ in CH_2Cl_2 in the dark (see Annex D).

14^{2+} [Ru(terpy*)(dmp)(PY)][PF_6]$_2$: 24 mg (23 μmol) of [**11**][PF_6]$_2$ were dissolved into 2 mL of pyridine and heated at 110°C under argon for 1 hour. To the cooled solution were added saturated aqueous KPF_6 solution and water until precipitation was complete. The solid was filtered and recovered in the absence of light with acetone. The crude product was purified on silica gel (eluent: acetone / water / sat

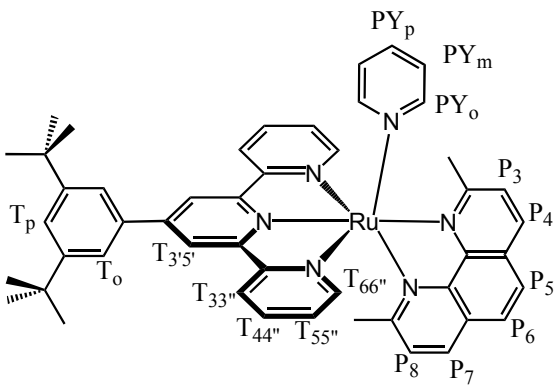

aqueous KNO_3 60:5:1) to yield 19 mg of [**14**][PF_6]$_2$ (76%).

^{1}H 300 MHz NMR: δ (ppm) in acetone-d6 : 9.15 (s, 2H, T3'5'); 8.90 (m, 3H, P_4 + $T_{33"}$); 8.44 (d, 1H, P_7); 8.39 (d, 1H, P_5); 8.22-8.11 (m, 6H, P_3 + P_6 + $T_{44"}$ + $T_{66"}$); 8.02 (d, 2H, T_o); 8.00 (m, PY_o); 7.85 (tt, 1H, PY_p); 7.76 (t, 1H, T_p); 7.53 (m, 2H, $T_{55"}$); 7.44 (d, 1H, P_8); 7.27 (m, PY_m); 2.41 (s, 3H, $CH_3(P_2)$); 1.99 (s, 3H, $CH_3(P_9)$); 1.46 (s, 18H, tBu). *ES MS m/z (calc.):* 955.277 (955.263, [M – PF_6]$^+$), 405.149 (405.149, [M – 2 PF_6]$^{2+}$), 365.627 (365.628, [M – 2 PF_6 – py]$^{2+}$). *UV-vis*: λ_{max} (ε in L.mol^{-1}.cm^{-1}) in pyridine: 495 nm (11900).

15^{2+} **[Ru(terpy*)(dmp)(LUT)][PF$_6$]$_2$** : 28 mg (26 μmol) of [**11**][PF_6]$_2$ were dissolved in 5 mL of neat 3,5-lutidine. The solution was degassed and heated to 110°C for 1 hour under argon. After cooled down to room temperature, the complex was precipitated by the addition of 50 mL of diethyl ether. The solid was filtered, washed with ether, recovered with acetone and purified over silica gel in the dark (eluent: acetonitrile / water / KNO_3) to yield 14 mg (51%) of [**15**][PF_6]$_2$.

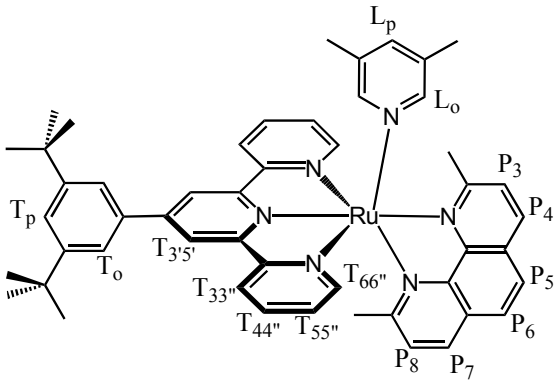

^{1}H 300 MHz NMR: δ (ppm) in acetone-d6 : 9.17 (s, 2H, T3'5'); 8.90 (m, 3H, P_4 + $T_{33"}$); 8.43 (d, 1H, P_7); 8.39 (d, 1H, P_5); 8.22-8.11 (m, 6H, P_3 + P_6 + $T_{44"}$ + $T_{66"}$); 8.04 (d, 2H, T_o); 7.77 (t, 1H, T_p); 7.58 (s, 2H, L_o); 7.53 (m, 2H, $T_{55"}$); 7.50 (t, 1H, L_p); 7.43 (d, 1H, P_8); 2.43 (s, 3H, $CH_3(P_2)$); 1.99 (s, 6H, CH_3(LUT)); 1.97 (s, 3H, $CH_3(P_9)$); 1.46 (s, 18H, tBu). *ES MS m/z (calc.):* 365.5 (365.6, [M – LUT – 2 PF_6]$^{2+}$), 419.0 (419.2, [M – 2 PF_6]$^{2+}$), 983.3 (983.3, [M – PF_6]$^+$). *UV-vis:* λ_{max} (ε in L.mol^{-1}.cm^{-1}) in nitromethane: 493 nm (12200).

I.1.c. aphen series

16$^+$ and **16'**$^+$ [Ru(terpy*)(aphen)(Cl)][PF_6]: 90 mg (143 μmol) of Ru(terpy*)Cl_3, 47 mg (157 μmol) of 4-anisyl-1,10-phenanthroline (aphen), 41 mg (858 μmol) of lithium chloride and 0.5 mL of triethylamine were dissolved with 30 mL of ethanol and 10 mL of water. The reaction flask was put under argon and heated to reflux for 4 hours. 30 mL of water and 30 mL of KPF_6 were added, which led to precipitation of the violet complex. It was filtered, washed with water and recovered with acetone to yield 42 mg of crude material. Purification over silica gel chromatography column (300 mL, eluent acetone / water / KNO_3 200:20:0.4) yielded 5.4 mg of pure isomer [**16**][PF_6] and 7.6 mg of pure isomer [**16'**][PF_6].

For both isomers: UV-vis: λ_{max} (ε in $L.mol^{-1}.cm^{-1}$) in acetone: 515 nm (15600). *ES MS m/z (calc.):* 858.257 (858.252, $[M–PF_6]^+$).

Characterization of isomer ***16***$^+$*: ^1H 300 MHz NMR:* δ (ppm) in acetone-d6: 10.45 (d, 1H, P_9, J=5.5Hz); 9.05 (s, 2H, $T_{3'5'}$); 8.77 (d, 2H, $T_{33"}$, J=8.1Hz); 8.56 (d, 1H, P_6, J=9.3Hz); 8.25 (d, 1H, P_5, J=9.5Hz); 8.05 (d, 2H, T_o, J=1.9Hz); 8.01 (d, 1H, P_2, J=5.5Hz); 7.96 (td, 2H, $T_{44"}$, J=7.9,1.4Hz); 7.75 (d, 1H, T_p, J=1.7Hz); 7.74 (d, 2H, $T_{66"}$); 7.45 (d, 2H, P_a, J=9.1Hz); 7.35 (d, 1H, P_3, J=5.7Hz); 7.29 (m, 2H, $T_{55"}$); 7.13 (d, 2H, P_b, J=9.1Hz); 3.87 (s, 3H, P_{MeO}); 3.21 (s, 3H, P_{Me}); 1.50 (s, 18H, tBu).

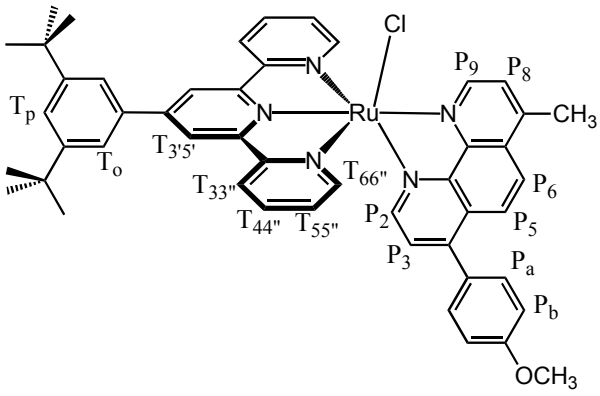

Characterization of isomer **16'**$^+$*: ^1H 300 MHz NMR:* δ (ppm) in acetone-d6: 10.60 (d, 1H, P_2, J=5.5Hz); 9.05 (s, 2H, $T_{3'5'}$); 8.76 (d, 2H, $T_{33"}$, J=8.1Hz); 8.47 (d, 1H, P_5, J=9.5Hz); 8.34 (m, 2H, P_6+P_3); 8.06 (d, 2H, T_o, J=1.9Hz); 7.95 (td, 2H, $T_{44"}$, J=7.9,1.4Hz); 7.86 (m, 3H, P_9+P_a); 7.78 (m, 3H, T_p+$T_{66"}$); 7.34 (m, 3H, P_8+P_b); 7.27 (m, 2H, $T_{55"}$); 4.01 (s, 3H, P_{MeO}); 2.77 (s, 3H, P_{Me}); 1.50 (s, 18H, tBu).

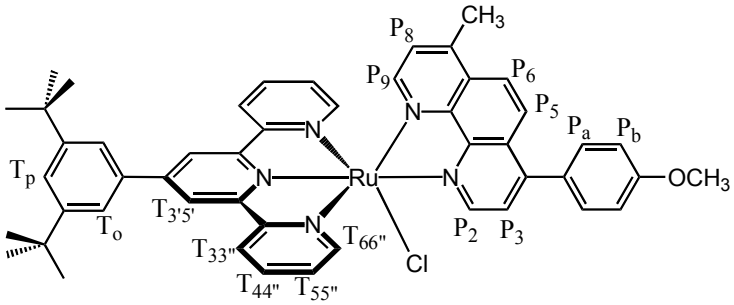

17'$^{2+}$ $[Ru(terpy^*)(aphen)(CH_3CN)][PF_6]_2$: 7.6 mg (7.6 μmol) of [**16'**][PF_6] and 16 mg (82 μmol) of silver tetrafluoroborate were dissolved in a mixture of 8 mL acetonitrile and 2 mL water. The solution was put under argon and refluxed in the dark for 4 hours. Silver chloride was filtered on celite, and the complex was precipitated by the addition of KPF_6. Purification was undertaken by preparative TLC (eluent CH_3CN / water / KNO_3 44:3:1); the yellow band was collected to afford 5.2 mg (59%) of [**17'**][PF_6]$_2$ without traces of its isomer [**17**][PF_6]$_2$.

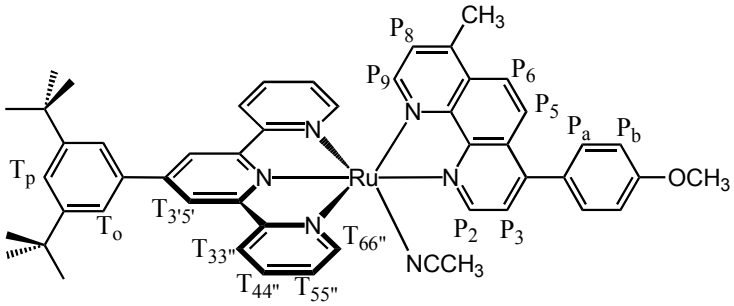

For both isomers: UV-vis: λ_{max} (ε in $L.mol^{-1}.cm^{-1}$) in acetone: 470 nm (27400). *ES MS m/z (calc.):* 432.159 (432.155, $[M – 2\ PF_6]^{2+}$).

Characterization of isomer ***17'***$^{2+}$*:* ^{1}*H 300 MHz NMR:* δ (ppm) in CD_3CN: 9.93 (d, 1H, P_2, J=5.5Hz); 8.82 (s, 2H, $T_{3'5'}$); 8.65 (d, 2H, $T_{33''}$, J=8.1Hz); 8.39 (d, 1H, P_5, J=9.5Hz); 8.22 (m, 2H, P_6+P_3); 8.00 (td, 2H, $T_{44''}$, J=7.9,1.4Hz); 7.93 (d, 2H, T_o, J=1.9Hz); 7.79 (m, 3H, T_p+P_a); 7.66 (m, 2H, $T_{66''}$); 7.56 (d, 1H, P_9, J=5.7Hz); 7.32 (d, 2H, P_b, J=9.1Hz); 7.29 (m, 3H, P_8+$T_{55''}$); 3.98 (s, 3H, P_{MeO}); 2.74 (s, 3H, P_{Me}); 1.51 (s, 18H, tBu).

Irradiation of [**17'**][PF_6]$_2$: 5 mg of [**17'**][PF_6]$_2$ were dissolved in CD_3CN in the dark; two NMR tubes were prepared out of this solution. One tube was kept in the dark at room temperature, the other was irradiated with white light (250W dia-projector filtered by a water filter). Comparison of the two NMR spectra showed that whereas in the dark the complex did not isomerize, irradiation led to a statistical 1:1 mixture of the two isomers **17**$^{2+}$:**17'**$^{2+}$.

Characterization of isomer ***17***$^{2+}$*:* ^{1}*H 300 MHz NMR:* δ (ppm) in CD_3CN : 9.81 (d, 1H, P_9, J=5.5Hz); 8.82 (s, 2H, $T_{3'5'}$); 8.65 (d, 2H, $T_{33''}$, J=8.1Hz); 8.42 (d, 1H, P_6, J=9.5Hz); 8.20 (m, 2H, P_5+P_8); 8.00 (td, 2H, $T_{44''}$, J=7.9,1.4Hz); 7.92 (d, 2H, T_o, J=1.9Hz); 7.78 (m, 2H, T_p+P_2); 7.60 (m, 2H, $T_{66''}$); 7.40 (d, 2H, P_a, J=9.1Hz); 7.29 (m, 3H, P_3+$T_{55''}$); 7.10 (d, 2H, P_b, J=9.1Hz); 3.85 (s, 3H, P_{MeO}); 3.13 (s, 3H, P_{Me}); 1.50 (s, 18H, tBu).

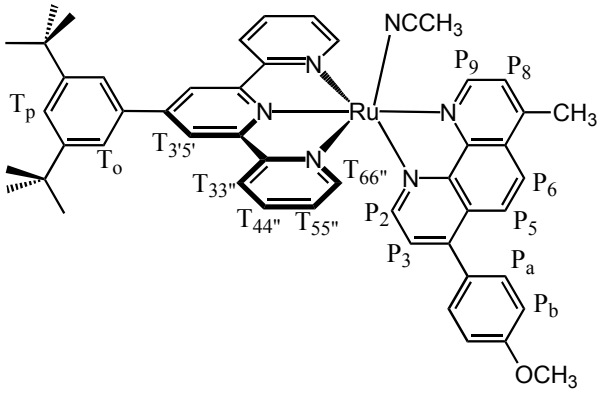

I.2. Photochemistry

I.2.a. Actinometry

Preparation of the ferrous oxalate salt: All manipulations were performed in the absence of light. A 500 mL aqueous solution containing 138.2 g of $K_2C_2O_4.H_2O$ (C=1.5M) was prepared, as well as a 200 mL aqueous solution containing 81.1 g of $FeCl_3.6H_2O$ (C=1.5M). The first solution was transferred to a 1L erlenmeyer flask, and 166 mL of the second solution were slowly added under a strong agitation. The fine precipitate was filtered and recrystallized three times in boiling water. Yield: 37.5 g of $K_3Fe(C_2O_4)_3.3H_2O$ as a green crystalline solid (25% yield).

Three solution were prepared:

- **solution a**: 7.369 g of $K_3Fe(C_2O_4)3.3H_2O$, 10.0 mL of a standard 0.5 M H_2SO_4 aqueous solution, and water up to 100 mL;

- **solution b**: 0.500 g of 1,10-phenanthroline monohydrate in 500 mL of water;
- **solution c**: 36.03 g of glacial acetic acid, 100 mL of water, 240 mL of 1.0 M aqueous sodium hydroxide and 25.57 g of anhydrous Na_2SO_4;

Calibration curve for the absorbing solution: four solutions were prepared weighing 0, 1.43, 3.16 and 4.89 of iron (II) sulfate heptahydrate, adding 2 mL of solution b and 0.5 mL of solution c and completing to 5 mL with water. 1 mL of each solution was pipette-transferred into four 5 mL volumetric flasks and completed with solution b. The absorbance A_{510} at 510 nm was recorded for each solution with a L=0.2 cm path length quartz cell, and A/L was plotted against concentration in $Fe(phen)_3^{2+}$, giving $\varepsilon_{510}=1.15x10^4$ $L.mol^{-1}.cm^{-1}$.

Measure of the photon fluxes: a volume V=3 mL of solution a was put in a glass UV-vis cell with a 1 cm pathlength. The cell was hermetically closed and put into the irradiation setup. It was stirred 2 minutes before any irradiation to insure temperature stability. The light beam was switched on for a given time t, then switched off. A volume V'=1.00 mL of the irradiated solution was pipette-transferred into a 5.00 mL volumetric flask, 2.0 mL of solution b and 0.5 mL of solution c were added, and the volume was completed to 5 mL with distilled water. A spectrum of the resulting solution in a quartz 0.200 cm UV-vis cell was measured, and the absorbance at 510 nm was recorded. The value of ε_{510} for complex $Fe(phen)_3^{2+}$ enabled to calculate $n_{Fe(II)}$ defined as the number of moles of Fe^{2+} ions produced by the photochemical reaction in the irradiated sample. $n_{Fe(II)}$ was plotted versus irradiation time t (see Annex B Figure 42). The curve was a straight line whose slope S was directly related to the flux of photons and to the interpolated quantum yield of the reaction (see numerical values in Annex B, Table 13 and Table 14).

I.2.b. Quantum yield measurements

Quantum yields were determined using the excitation system of an Aminco Bowman Series 2 Luminescence Spectrophotometer (Thermospectronic). This irradiation system consisted in a continuous wave 150W xenon lamp with a monochromator using a 1200 lines/mm, ion etched, concave, holographic gratings in a modified Seya-Namioka design with 200 mm focal length. The aperture of the monochromator was computer-set to $\Delta\lambda$ = 8 nm. The sample was immobilized in a T-Optics standardized sample chamber equipped with a SLM Aminco magnetic stirrer and thermostated to 25°C by a Bioblock Scientific Polystat 5 number 86613. The sample was made of 3 mL of the solution of the compound in a closed, UV-visible glass cell with a 1.00 cm path length under an air atmosphere. To avoid the influence of external light, the room was kept in the dark

during all experiments. Under these conditions, the light intensities were determined using ferrioxalate Actinometry (see above).

The molar extinction coefficients were determined by calibration curves and are given below. These values are those used to calculate the quantum yields in Annex C; they are by no means values for the absorption maxima of the complexes.

Complexes [(a)]	**λ_{ex} (nm) / ε_{ex} (x10^3 L.mol^{-1}.cm^{-1})**	**λ (nm) /ε_{λ} (x10^3 L.mol^{-1}.cm^{-1})**
Ru(terpy)(phen)$(CH_3CN)^{2+}$ [(b)]	464 / 10.6	483 / 3.81
Ru(terpy)(phen)$(py)^{2+}$ [(b)]	464 / 10.3	483 / 9.00
Ru(terpy*)(phen)$(MeOBN)^{2+}$ [(c)]	476 / 12.9	487 / 7.39
Ru(terpy*)(dmp)$(MeOBN)^{2+}$ [(c)]	476 / 11.4	495 / 5.43
Ru(terpy*)(dmp)$(DMS)^{2+}$ [(c)]	513 / 8.35	495 / 9.81

(a) as their PF_6^- salts; (b) solvent is pyridine 1M in acetonitrile; (c) solvent is neat pyridine

Next table shows the absorption maxima of two complexes.

Complexes	**^{1}MLCT (nm) / ε_{MLCT} (x10^3 L.mol^{-1}.cm^{-1})**
Ru(terpy)(phen)$(CH_3CN)^{2+}$ [(a)]	455 / 12.4
Ru(terpy)(phen)$(PY)^{2+}$ [(a)]	467 / 10.3 410.5 / 9.03

(a) measured in 1M acetonitrile solutions of pyridine

Manipulations: a solution of the starting complex Ru(tpy*)(N-N)(L),$(PF_6)_2$ was prepared (see numerical values in Annex C): the solid compound was accurately weighed, and distilled pyridine was added to complete to a volume V_0. An aliquot V = 3 mL of this solution was put in a 1 cm thick closed UV-vis cell made of glass. The initial absorption spectrum was measured as a reference. The sample was stirred and irradiated under temperature control, and the evolution of the absorption spectrum with irradiation time t was followed. We call Δt the time interval between two consecutive spectra. The irradiations were stopped after three consecutive identical spectra (N-N = dmp) or two days of irradiation (N-N = phen).

Numerical treatment: the absorption of the solution at the absorption maximum of the Ru(tpy*)(N-N)(py),$(PF_6)_2$ complex, called $A_{\lambda t}$, was recorded as a function of irradiation time t. B(t) represents the average value of $A_{\lambda t}$ between t = 0 and t. When Δt was kept constant between two consecutive spectra, we could numerically calculate B(t) using the discrete approximation

$\frac{1}{t}\cdot\int_0^t A_{\lambda,t'}dt' \approx \frac{1}{n+1}\sum_{k=0}^{n} A_{\lambda,t=k\Delta t}$. When Δt was not constant, we calculated the area under the curve A=f(t) by triangular approximations, and divided it by t. In any case, we plotted A = f(B) and obtained a straight line. We measured its slope S and its y-intercept Y_0. To get the ratio of the two quantum yields, we could either reach the photostationary state (N-N = dmp) or use the value of given by Y_0 (N-N = phen). With N-N = dmp, a deconvolution of the last absorption spectrum was made to get an experimental value of x_∞ (see Annex C).

I.2.c. White light irradiation experiments for the determination of rate constants

3 mL of a pyridine solution of the complex (C = 10^{-5} M) was put in a closed UV-visible glass cell. The sample was irradiated with the beam of a 250 W slide projector, filtered by a water filter and focused on the cell. The evolution of the absorption spectrum of the solution was followed with respect to irradiation time. The plots of ln [(A_0-A_∞) / (A_t-A_∞)] versus time were linear and the pseudo-first order rate constants were calculated using least-squares treatment.

II. Chapter 2: synthesis and photochemistry of a two-position Ru(terpy)(phen)(L)$^{2+}$ scorpionate complex

II.1. Synthesis of the benzonitrile chain

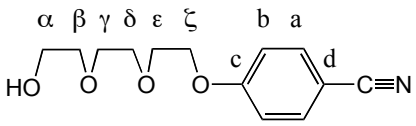

2-(2-(2-paranitrophenylethoxy)ethoxy)ethanol : a suspension of 11.3 g (34.8 mmol) of cesium carbonate in 75 mL of dimethylformamide was put under argon. 2.07 g (17.4 mmol) of parahydroxybenzonitrile in 25 mL of DMF were added dropwise without noticable colour change. The suspension was heated at 60°C and a solution 5.86 g (34.8 mmol) of 2-(2-(2-ethoxy)ethoxy)chloroethanol in 25 mL of DMF was added dropwise under argon. The reaction vessel was stirred under argon at 60°C overnight (18h) and the DMF was removed under vacuum. Water and DCM were added, and the aqueous phase was extracted three times with dichloromethane. The organic phases were combined, washed with NaOH 0.1 M, water, brine and evaporated to dryness to yield 6.56 g of crude oil. This material was put on a silica gel chromatography column using DCM / MeOH 2% as the eluent. The main fraction was collected, evaporated and weighed (5.69 g). NMR analysis revealed that the oil was a mixture of the product and the starting chlorotriethyleneglycol. TLC (silica, alumina) showed that these two compounds could not be separated by chromatography. The sample was used for the next step without further purification.

^{1}H 300 MHz NMR: δ (ppm) in $CDCl_3$: 7.54 (d, 2H, a, J=8.9Hz); 6.94 (d, 2H, b, J=9.0Hz); 4.15 (t, 2H, α, J=4.6Hz); 3.85 (t, 2H, β, J=4.8Hz); 3.75-3.56 (m, 8H, γδεζ); 2.53 (s, 1H, OH). *^{13}C 300 MHz NMR:* δ (ppm) in $CDCl_3$: 162.1 (c); 134.0 (a); 119.2 (d); 115.4 (b); 104.2 (CN); 72.6-69.4 (βγδε); 67.7 (ζ); 61.7 (α).

20: 1.01 g of the preceding mixture of alcohols were dissolved in 50 mL of dichloromethane and cooled down to 0°C under argon. 10 mL of distilled triethylamine were added. A solution containing 0.80 mL of mesylchloride into 20 mL of dry dichloromethane was added dropwise at 0°C within 20 minutes. The solution was stirred at 1°C for 4 hours and at room temperature overnight. 50 mL of water were added at 0°C under vigorous stirring. The aqueous phase was extracted with dichloromethane, the combined organic phases were washed with water and brine, dried on Na_2SO_4 and evaporated under vacuum. Yield: 1.57 g of a yellowish oil. NMR analysis showed the presence of the chloromesyltriethyleneglycol. This mesylate mixture was dissolved in 20 mL of acetone and transferred into a solution of 3.85 g (44.3 mmol) of lithium bromide in 100 mL of acetone. The solution was refluxed under argon for 4 hours. The acetone was removed under vacuum, water and DCM were added and the aqueous phase was extracted with dichloromethane. The combined organic phases were washed with water and brine and evaporated to dryness. The crude product was chromatographed on silica gel (eluent DCM / MeOH 0.5%). The bromochlorotriethyleneglycol was removed to yield 736 mg of analytically pure bromide **20** (76% from the starting alcohol).

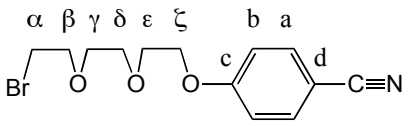

^{1}H 300 MHz NMR: δ (ppm) in $CDCl_3$: 7.51 (d, 2H, a, J=9.1Hz); 6.92 (d, 2H, b, J=8.9Hz); 4.12 (t, 2H, ζ, J=4.7Hz); 3.83 (t, 2H, ε, J=4.9Hz); 3.75 (t, 2H, β, J=6.2Hz); 3.70-3.60 (m, 4H, γδ); 3.41 (t, 2H, α, J=6.2Hz). *^{13}C 300 MHz NMR:* δ (ppm) in $CDCl_3$: 162.1 (c); 133.9 (a); 119.2 (d); 115.4 (b); 104.0 (CN); 71.2, 70.8, 70.6, 70.5, 69.4 (βγδε); 67.8 (ζ); 30.5 (α). *IE-MS m/z (calc):* 313.0 (313.0, $[M]^+$); 194.9 (195.0, $[M - OC_6H_4CN]^+$); 145.0 (146.1, $[M - Br(CH_2CH_2O)_2 + H]^+$); 106.9 (107.0, $[M - (OCH_2CH_2)_2OC_6H_4CN]^+$); 102.0 (102.0, $[M - Br(CH_2CH_2O)_3]^+$). *C,H,N for $C_{13}H_{16}BrNO_3$: calc* C, 49.70; H, 5.13; N, 4.46; *found* C, 49.96; H, 5.14; N, 4.35.

II.2. Synthesis of the sulfoxide chain

22: 2.74 g (48.9 mmol) of potassium hydroxyde were ground in a mortar and put in a 50 mL two-necked round-bottom flask. A condensor was adapted, the flask was put under argon and heated to 60°C. 4.25 mL (48.9

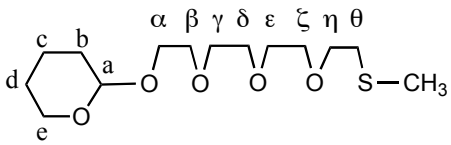

mmol) of 2-methylthioethanol were added dropwise under efficient stirring and the suspension was stirred for 15 min. 16.8 g (48.9 mmol) of tetrahydropyranyl-2-(2-(2-iodoethoxy)ethoxy)ethanol were added dropwise, so that the internal temperature did not go higher than 70°C. The reaction mixture was stirred at 60°C for 4 hours. The mixture was cooled down to RT, 80 mL of water and 80 mL of dichloromethane were added and the aqueous phase was extracted three times with dichloromethane. The combined organic phases were washed with water, brine, dried over sodium sulfate and the solvent was removed under vacuum. The crude mixture (14.4 g) was put on an alumina column and eluted with a DCM / hexane mixture (from 1:1 to 1:0). The starting alkyl iodide and the elimination product were removed to afford the substitution product **22** as a colourless oil. Yield: 5.65 g (38%).

^{1}H 300MHz NMR: δ in ppm in $CDCl_3$: 4.60 (t, 1H, a, J=3.5Hz); 3.88-3.78, 3.67-3.53 and 3.52-3.42 (m, 2H, 13H and 1H resp, α, β, γ, δ, ε, ζ, ηe); 2.66 (t, 2H, θ, J=6.9Hz); 2.11 (s, 3H, CH_3(SO)); 1.90-1.40 (m, 6H, b, c, d). *^{13}C 300MHz NMR*: δ in ppm in $CDCl_3$: 99.0 (a); 70.7-70.5 (γδεζ); 70.4 (η); 66.7 (α); 62.3 (β); 53.5 (e); 33.5 (θ); 30.7, 25.5, 19.6 (b, c, d); 16.1 (CH_3(SO)). IE-MS m/z (calc): 307.1 (308.1, $[M-H]^+$); 233.1 (233.1, $[M-CH_3SCH_2CH_2]^+$); 225.1 (225.1, $[M-THP+2H]^+$); 206.0 (206.1, $[M-THPOH]^+$); 119.1 (119.1, $[M-THPO(CH_2CH_2O)_2]^+$); 92.0 (92.1, $[M-THP(OCH_2CH_2)_3+H]^+$); 85.1 (85.1, $[M-CH_3S(CH_2CH_2O)_4]^+$); 75.1 (75.1, $[M-THPO(CH_2CH_2O)_4]^+$).

23: 752 mg (2.44 mmol) of thioether **22** were dissolved under argon in 75 mL of dichloromethane and cooled down to 0°C. 504 mg of m-chloroperbenzoic acid (75% pure with 25% of m-chlorobenzoic acid, 2.44 mmol) were dissolved in 50 mL of dichloromethane. This solution was added dropwise to the thioether at 0°C and the mixture was stirred at 0°C for 8h under argon. The solution was quenched with 50 mL of saturated aqueous sodium carbonate without letting the temperature go higher than 15°C. The mixture was extracted three times with dichloromethane, the combined organic phases were washed with brine, dried on sodium sulfate and evaporated. The crude product was put on an alumina column, the remaining starting material was removed with DCM / MeOH 0.5% and the sulfoxide was eluted with DCM / MeOH 1%. Yield: 746 mg of sulfoxide **23** (94%).

^{1}H 300MHz NMR: δ in ppm in $CDCl_3$: 4.63 (dd, 1H, a, J=2.8, 4.2 Hz); 3.95-3.80, 3.70-3.55 and 3.55-3.45 (m, 4H, 11H and 1H resp, αβγδεζ, e); 3.05-2.85 (m, 2H, θ); 2.64 (s, 3H, CH_3(SO)); 1.90-1.45 (m, 8H, b+c+d). *^{13}C 300MHz NMR*: δ in ppm in $CDCl_3$: 99.1 (a); 70.7-70.5 (γδεζ); 66.7 (α); 63.7 (η); 62.4 (β); 54.9 (θ); 53.4 (e); 39.3 (CH_3(SO)); 30.7, 25.5, 19.6 (b,c,d). *IE-MS m/z (calc):* 325.2 (325.2, $[M+H]^+$); 307.3 (307.3, $[M-OH]^+$); 295.2 (295.1, $[M-CH_3O+2H]^+$); 241.2

(241.1, [M-THP+2H]$^+$); 197.1 (197.1, [M-THPOCH$_2$CH$_2$+2H]$^+$); 153.1 (153.0, [M-THP(OCH$_2$CH$_2$)$_2$+2H]$^+$); 85.1 (85.1, [M-CH$_3$S(CH$_2$CH$_2$O)$_4$]$^+$); 63.1 (63.0, [M-THP(OCH$_2$CH$_2$)$_4$]$^+$).

24: 725 mg (2.24 mmol) of the protected alcohol **23** were dissolved in 250 mL of ethanol, a catalytic amount of p-toluenesulfonic acid was added and the solution was reflux under argon for 5 hours. The solvent was evaporated to dryness and yielded 533 mg of analytically pure **24** (99%).

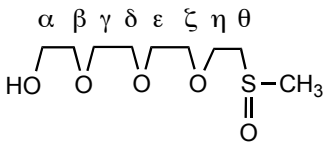

^{1}H 300MHz NMR: δ in ppm in CDCl$_3$: 3.92 (m, 2H, α); 3.71 (t, 2H, β); 3.66 (s, 8H, γδεζ); 3.59 (t, 2H, η); 3.06-2.84 (m, 2H, θ); 2.63 (s, 3H, CH$_3$(SO)); 2.50 (broad s, 1H, OH). *^{13}C 300MHz NMR*: δ in ppm in CDCl$_3$: 72.5 (α); 70.6-70.3 (γδεζ); 63.6 (η); 61.6 (β); 54.7 (θ); 39.1 (CH$_3$(SO)). *FAB-MS m/z (calc):* 241.2 (240.1, [M+H]$^+$).

25: 516 mg (2.15 mmol) of alcohol **24** and 744 mg (3.90 mmol) of p-toluenesulfonyl chloride were dissolved in 80 mL of distilled dichloromethane. The solution was put under argon and cooled down to 0°C. 4 mL of triethylamine (28.9 mmol) were added at 0°C; the solution was stirred at this temperature for 30 min and then at room temperature for 3 hours. The reaction was quenched by the addition of 408 mg of Na$_2$CO$_3$ in 30 mL of water and stirred 30 minutes at RT. 50 mL of saturated NaHCO$_3$ were added and the aqueous phase was extracted three times with dichloromethane. The organic phases were collected, evaporated and the crude material purified by chromatography on alumina (eluent DCM / MeOH 1%). Yield: 206 mg of tosylate **25** (24%).

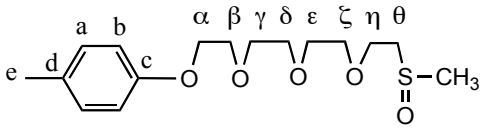

^{1}H 300MHz NMR: δ in ppm in CDCl$_3$: 7.77 (d, 2H, a, J=8.3Hz); 7.32 (d, 2H, b, J=8.0Hz); 4.13 (t, 2H, β, J=4.2, 5.4Hz); 3.88 (m, 2H, α); 3.68-3.56 (m, 10H, γδεζη); 3.05-2.93 and 2.91-2.81 (m, 2H, θ); 2.60 (s, 3H, CH$_3$(SO)); 2.42 (s, 3H, CH$_3$(Ts)). *^{13}C 300MHz NMR*: δ in ppm in CDCl$_3$: 144.9 (d); 133.0 (c); 129.9 (a); 128.0 (b); 70.8, 70.7, 70.6, 70.5 (γδεζ); 69.3 (α); 68.8 (β); 63.7 (η); 54.9 (θ); 39.3 (CH$_3$(SO)); 21.7 (CH$_3$(Ts)).

21: 179 mg (0.454 mmol) of tosylate **25** and 395 mg (4.54 mmol) of lithium bromide were dissolved in 25 mL of acetone and refluxed under argon for 4 hours. The acetone was evaporated and the crude product was purified by chromatography on silica (eluent DCM / MeOH 5%). Yield: 105 mg of bromide **21** (76%).

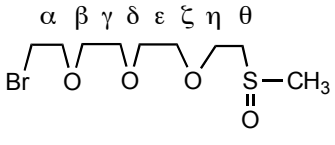

^{1}H 300MHz NMR: δ in ppm in $CDCl_3$: 3.92-3.88 (m, 2H, η); 3.80 (t, 2H, β, J=6.3Hz); 3.65 (broad s, 8H, γδεζ); 3.46 (t, 2H, α, J=6.3Hz); 3.00-2.85 (m, 2H, θ); 2.63 (s, 3H, $CH_3(SO)$). *^{13}C 300MHz NMR:* δ in ppm in $CDCl_3$: 71.3 (β); 70.8 (γ); 70.7 (δ); 70.7 (ε); 70.6 (ζ); 63.7 (η); 55.0 (θ); 39.4 ($CH_3(SO)$); 30.5 (α). *IE-MS m/z (calc):* 303.1 (303.0, $[M+H]^+$); 223.0 (223.1, $[M-Br]^+$); 196.0 (195.0, $[M-CH_3SOCH_2CH_2O]^+$); 179.1 (179.0, $[M-BrCH_2CH_2O]^+$); 151.0 (151.0, $[M-CH_3SO(CH_2CH_2O)_2]^+$); 135.1 (135.1, $[M-Br(CH_2CH_2O)_2]^+$); 107.0 (107.0, $[M-CH_3SO(CH_2CH_2O)_3]^+$); 91.1 (91.1, $[M-Br(CH_2CH_2O)_3]^+$); 63.1 (63.1, $[M-BrCH_2CH_2(OCH_2CH_2)_3]^+$).

II.3. Synthesis of phenanthroline 26

3,8-dibromo-1,10-phenanthroline: 5 g (27.8 mmol) of anhydrous 1,10-phenanthroline were dissolved into 200 mL of 1-chlorobutane. To the solution was added dropwise 7.3 mL (12.3 g, 91.1 mmol) of sulfur monochloride S_2Cl_2 at room temperature. The solution was stirred 15 minutes at room temperature. 7.3 mL (7.10 g, 89.8 mmol) of pyridine were added dropwise to the solution which was stirred an additionnal 15 minutes. 4.5 mL (14 g, 87.6 mmol) of bromine were added dropwise at room temperature, and the solution was refluxed overnight. The solution was cooled down to room temperature and the liquid phase removed by decantation. To the orange solid was added a sodium hydroxyde solution (16 g in 150 mL water) and 100 mL of chloroform, and the mixture was stirred vigorously during 3 hours to dissolve as much as possible the solid. The solution was put into a separation funnel, the organic phase was collected and filtered over Cellite©, washed with HCl 0.5 M, saturated $NaHCO_3$, evaporated and dried under vacuum to yield 7.64 g of crude material. The dibromo derivative could be easily separated from the monobromo by column chromatography on alumina (dichloromethane / hexane 1:1), but the 3,5,8-tribromoderivative was difficult to remove. We obtained three samples weighing 0.767 mg, 2.62 g and 1.09 g, the purity of which was shown to be >98%, 95% and 90% respectively in 3,8-dibromophenanthroline (measured by NMR). Total yield: 4.22 g (45%).

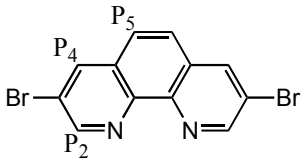

^{1}H 300MHz NMR: δ in ppm in $CDCl_3$: 9.18 (s, 2H, P_2,); 8.41 (s, 2H, P_4,); 7.77 (s, 2H, P_5).

3,8-dianisyl-1,10-phenanthroline: 1.09 g (3.22 mmol) of 3,8-dibromo-1,10-phenanthroline were dissolved in 80 mL of toluene and put under argon. 373 mg (0.324 mmol) of palladium tetrakis(triphenylphosphine) were added as a solid, followed by 25 mL of a degassed aqueous 2M solution of sodium carbonate via a cannula. A solution of 1.03 g (6.77 mmol) of 4-

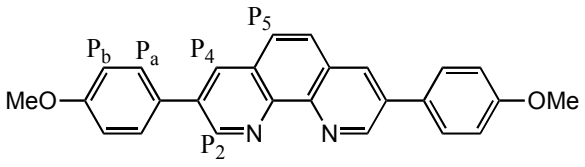

methoxyphenylboronic acid in 30 mL toluene and a few drops of ethanol was prepared and cannulated into the reaction flask under argon. The mixture was refluxed under argon overnight, allowed to cool down to R.T. and then in an ice bath, and the solid was filtered. Chloroform was added and the product was washed with water, dried over sodium sulfate, filtered and evaporated to dryness. A short alumina column was undertaken to isolate 1.07 g of the dianisylphenanthroline (yield: 84%).

^{1}H 300MHz NMR: δ in ppm in $CDCl_3$: 9.41 (d, 2H, P_2, J=2.4Hz); 8.34 (d, 2H, P_4, J=2.2Hz); 7.85 (s, 2H, P_5); 7.74 (d, 4H, P_a, 8.8Hz); 7.09 (d, 4H, P_b, J=8.8Hz); 3.90 (s, 6H, P_{OMe}).

3,8-di(parahydroxyphenyl)-1,10-phenanthroline: 44 mL of 37% hydrochloric acid were slowly added to 40 mL pyridine in a three-necked 100mL round bottom flask. A distillation apparatus was adapted and water was distilled off under argon until the internal temperature in the flask reached 220°C. The pyridinium chloride was cooled down to 140°C and 1.00 g (2.56 mmol) of 3,8-dianisylphenanthroline were added as a solid under argon. The mixture was heated at reflux (221°C) for 3 hours. The heating was stopped and when the temperature was 140°C 100 mL of water were slowly added. The reaction mixture was homogenised and transferred into a 500 mL Erlenmeyer flask with 200 mL of water and 100 mL of ethanol. The yellow suspension was neutralised with 0.1M sodium hydroxide solution until the pH of the liquid phase was stable (7.54). The solid was filtered on Millipore© and dried under vacuum using P_2O_5 as a drying agent. Yield: 933 mg (100%) of diphenolphenanthroline as a yellow solid.

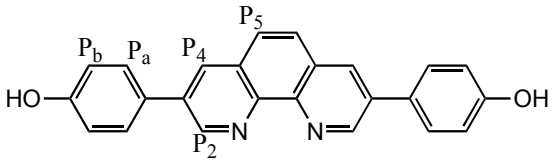

^{1}H 300MHz NMR: δ in ppm in DMSO-d6: 9.90 (s, 2H, PhOH); 9.38 (s, 2H, P_2); 8.84 (d, 2H, P_4, J=2.2Hz); 8.11 (s, 2H, P_5); 7.83 (d, 4H, P_a, 8.8Hz); 6.99 (d, 4H, P_b, J=8.8Hz). *^{13}C 500MHz NMR*: δ in ppm in DMSO-d6 (assignments were done according to HSQC and HMBC correlation experiments): 158.0 (P_c); 146.6 (P_2); 140.7 (P_6); 134.7 (P_3); 133.1 (P_4); 128.3 (P_a); 127.0 (P_5); 126.2 (P_d); 116.0 (P_b). P_7 could not be assigned. *C,H,N for $C_{24}H_{16}N_2O_2$.HCl . $2H_2O$*: *calc* C, 65.98; H, 4.84; N, 6.41; *found* C, 65.49; H, 4.82; N, 6.24.

26: 20 mg (55 μmol) of 3,8-di(parahydroxyphenyl)-1,10-phenanthroline were dissolved in 10 mL of DMF. The

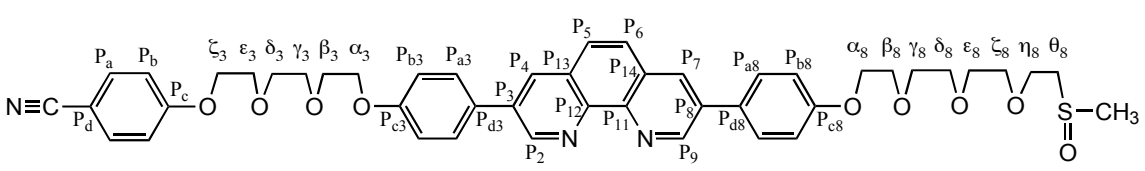

solution was put under argon and 89 mg of cesium carbonate (275 μmol) were added; in less than two minutes the yellow solution turned bright orange. A solution containing 36 mg (110 μmol) of **20** and 34 mg (110 μmol) of **21** in 12 mL of DMF was prepared and added to the phenolate solution. A condensor was adapted, the reaction mixture was degazed and heated at 60°C under argon for 24 hours. The DMF was pumped under vacuum, water and dichloromethane were added and the aqueous phase was extracted three times with DCM. The organic phases were combined, washed with water and brine, and evaporated to dryness. This crude material was put on a neutral alumina column and eluted with DCM / MeOH 1%. The positions of the three phenanthrolines in the column were followed with a UV lamp and the three compounds were collected separately. Yield: 18 mg (40%) of **26** and 9 mg of the two symmetric phenanthrolines.

*Characterization of **26**: ^{1}H 400MHz NMR*: δ in ppm in $CDCl_3$: 9.38 (s, 2H, P_2+P_9); 8.32 (d+d, 2H, P_4+P_7); 7.84 (s, 2H, P_5+P_6); 7.70 (d+d, 4H, P_{a3}+P_{a8}); 7.54 (d, 2H, P_a, J=8.9Hz); 7.08 (d+d, 4H, P_{b3}+P_{b8}); 6.95 (d, 2H, P_b, J=8.9Hz); 4.23-4.15 (m, 6H, α_3+α_8+ζ_3); 3.92-3.87 (m, 8H, β_3+β_8+ε_3+η_8); 3.76-3.66 (m, 12H, γ_3+δ_3+γ_8+δ_8+ε_8+ζ_8); 3.03-2.83 (m, 2H, θ_8); 2.61 (s, 3H, CH_3(SO)). *^{13}C 400MHz NMR*: δ in ppm in $CDCl_3$ (attribution were done according to HSQC and HMBC 2D ^{1}H-^{13}C HETCORR experiments): 162.2 (P_c); 159.34,159.30 (P_{c3},P_{c8}); 149.35 (P_2+P_9); 144.8 (P_{11}+P_{12}); 135.3 (P_{d3}+P_{d8}); 134.1 (P_a); 132.7 (P_4+P_7); 130.3 (P_3+P_8); 128.7 (P_{a3}+P_{a8}); 128.5 (P_{13}+P_{14}); 127.2,127.1 (P_5,P_6); 119.3 (P_{CN}); 115.5,115.4 (P_b,P_{b3}+P_{b8}); 104.2 (P_d); 71.1,71.0,71.0,70.8,70.6 (γ_3+γ_8+δ_3+δ_8+ε_8+ζ_8); 69.9,69.8 (β_3+β_8); 69.6 (ε_3); 67.9 (ζ_3); 67.7,67.7 (α_3+α_8); 63.7 (η_8); 54.9 (θ_8); 39.3 (CH_3(SO)). *FAB MS m/z (calc)*: 820.2 (820.3, $[M+H]^+$).

II.4. Synthesis of the scorpionates

27^+ [Ru(terpy*)(26)(Cl)][PF_6]: 17 mg (27 μmol) of Ru(terpy*)Cl_3 and 5 mg (27 μmol) of lithium chloride were weighed in a 50 mL two-necked round-bottom flask. 5 mL of water and 10 mL of ethanol were added and the suspension was put under argon. 18 mg (22 μmol) of phenanthroline **26** were dissolved in 10 mL of hot ethanol and this solution was transfered to the reaction vessel. The mixture was degazed and heated at reflux under argon for 5 hours. Aqueous KPF_6 and distilled water were added to the cooled solution, ethanol was removed under vacuum and the violet precipitate was filtered on a P4 frit and washed with water. The solid was recovered with acetone and evaporated to dryness. The mixture of chloro isomers was put on a silica gel column and eluted with a 300:15:2 acetone / water / KNO_3 mixture. The violet band was collected, precipitated with KPF_6 and water, filtered, washed with water, recovered with acetone and evaporated to dryness. Yield: 22 mg (66%) of a 1:1 mixture of the two isomers of [**27**][PF_6].

UV-visible: λ_{max} (ε) in $CHCl_3$: 367.5nm (33800); 516.5nm (11000). *ES MS m/z (calc)*: 1377.449 (1377.444, $[M - PF_6]^+$).

Preparation and characterization of isomers **27**$^+$: 3 mg of [**18**][PF_6]$_2$ (1.8 μmol) were weighed in a conical flask. 3 mg (18 μmol) of dry tetraethylammonium chloride were added and an NMR tube was prepared using CD_2Cl_2 as the solvent. The tube was irradiated 2 hours at 25°C with the Xe1000W lamp fitted with a water filter and an Andover 470FS10-50 interference filter. The colour of the solution changed from orange to violet. The solution was transferred into a flask containing 30 mL of KPF_6 and the ruthenium complex precipitated. It was filtered, washed thoroughly with water, recovered with acetone and vacuum dried. Yield: 2.8 mg (100%) of [**27**][PF_6] as a 95:5 mixture of the two isomers **27**$^+$:**27'**$^+$.

^{1}H 400MHz NMR: δ in ppm in CD_2Cl_2: 10.77 (d, 1H, P_2, J=1.9Hz); 8.89 (d, 1H, P_4, J=2.0Hz); 8.63 (s, 2H, $T_{3'5'}$); 8.49 (d, 2H, $T_{33"}$, J=8.0Hz); 8.34-8.32 (m, 2H, P_5+P_7); 8.13 (d, 1H, P_6, J=9.0Hz); 8.03 (d, 2H, P_{a3}, J=6.7Hz); 7.88 (td, 2H, $T_{44"}$, J=7.6,1.4Hz); 7.79 (d, 1H, P_9, J=1.9Hz); 7.78 (d, 2H, T_o, J=1.9Hz); 7.70 (t, 1H, T_p, J=1.7Hz); 7.62 (m, 2H, $T_{66"}$); 7.56 (d, 2H, P_a, J=9.0Hz); 7.23 (d, 2H, P_{a8}, J=8.9Hz); 7.21-7.17 (m, 4H, $T_{55"}$+P_{b3}); 6.99 (d, 2H, P_b, J=9.0Hz); 6.93 (d, 2H, P_{b8}, J=8.8Hz); 4.23 (m, 2H, α_3); 4.18 (m, ζ_3); 4.08 (m, 2H, α_8); 3.89 (m, 2H, β_3); 3.86 (m, 2H, ε_3); 3.82 (m, 2H, η_8); 3.77 (m, 2H, β_8); 3.73 (s, 4H, γ_3+δ_3); 3.64-3.62 (m, 2H, γ_8); 3.60-3.58 (m, 2H, δ_8); 3.58 (s, 4H, ε_8+ζ_8); 2.96-2.76 (m, 2H, θ_8); 2.53 (s, 3H, CH_3(SO)); 1.49 (s, 18H, tBu).

Preparation and characterization of isomer **27'**$^+$: 3 mg (1.8 μmol) of [**19**][PF_6]$_2$ were weighed in a conical flask. 3 mg (18 μmol) of dry tetraethylammonium chloride were added and an NMR tube was prepared using CD_2Cl_2 as the solvent. The tube was irradiated 2 hours at 25°C with the Xe1000W lamp fitted with a water filter and an Andover 430FS10-50 interference filter. The colour of the solution changed from yellow to violet. The solution was transferred into a

flask containing 30 mL of KPF_6 and the ruthenium complex precipitated. It was filtered, washed thoroughly with water, recovered with acetone and vacuum dried. Yield: 2.8 mg of [**27**][PF_6] as a 9:91 mixture of the two isomers **27**$^+$:**27'**$^+$.

^{1}H 400MHz NMR: δ in ppm in CD_2Cl_2: 10.78 (d, 1H, P_2, J=1.9Hz); 8.90 (d, 1H, P_4, J=2.0Hz); 8.63 (s, 2H, $T_{3'5'}$); 8.49 (d, 2H, $T_{33"}$, J=8.0Hz); 8.32 (d, 1H, P_5, J=9.0Hz); 8.31 (d, 1H, P_7, J=1.8Hz); 8.13 (d, 1H, P_6, J=9.0Hz); 8.03 (d, 2H, P_{a3}, J=6.7Hz); 7.88 (td, 2H, $T_{44"}$, J=7.6,1.4Hz); 7.79 (d, 1H, P_9, J=1.9Hz); 7.78 (d, 2H, T_o, J=1.9Hz); 7.70 (t, 1H, T_p, J=1.7Hz); 7.62 (m, 2H, $T_{66"}$); 7.51 (d, 2H, P_a, J=9.0Hz); 7.22-7.17 (m, 6H, P_{a8}+$T_{55"}$+P_{b3}); 6.95 (d, 2H, P_b, J=9.0Hz); 6.89 (d, 2H, P_{b8}, J=8.8Hz); 4.25 (m, 2H, α_3); 4.13 (m, ζ_3); 4.04 (m, 2H, α_8); 3.90 (m, 2H, β_3); 3.86 (m, 2H, ε_3); 3.82 (m, 2H, η_8); 3.77 (m, 2H, β_8); 3.65 (s, 4H, ε_8+ζ_8); 3.63 (s, 4H, γ_3+δ_3); 3.64-3.62 (m, 2H, γ_8); 3.60-3.58 (m, 2H, δ_8); 3.03-2.80 (m, 2H, θ_8); 2.57 (s, 3H, CH_3(SO)); 1.48 (s, 18H, tBu).

18^{2+} and **19**$^{2+}$ **[Ru(terpy*)(26)][PF_6]$_2$**: 18 mg (93 μmol) of silver tetrafluoroborate were dissolved in 10 mL of acetone and put under argon. A solution of 22 mg (15 μmol) of [**27**][PF_6] as an equimolar mixture of both isomers dissolved in 20 mL of acetone was transferred in the flask, the reaction mixture was degazed and refluxed under argon and in the dark for 2 hours. The silver chloride precipitate was removed by filtration on celite, the complexes were precipitated by addition of KPF_6 and water, filtered, washed with water, recovered with acetone and dried under vacuum. The crude material was put on a fine silica gel column and eluted with an acetone / water / sat. KNO_3 mixture 300:6:1. The yellow band was collected and worked up to afford 12 mg (50%) of [**19**][PF_6]$_2$. The polarity of the eluent was increased to 75:6:1 and the orange band on the column was collected and worked up to yield 12 mg (50%) of [**18**][PF_6]$_2$.

Characterization of **18**$^{2+}$: *^{1}H 500MHz NMR*: δ in ppm in acetone-d6: 10.23 (d, 1H, P_2, J=1.9Hz); 9.25 (d, 1H, P_4, J=2.0Hz); 9.24 (s, 2H, $T_{3'5'}$); 8.89 (m, 2H, J=8.9,2.5,1.3 Hz); 8.52 (d, 1H, P_5, J=8.9Hz); 8.33 (d, 1H, P_6, J=9.0Hz); 8.15-8.12 (m, 4H, $T_{66"}$+$T_{44"}$); 8.10 (d, 2H, T_o, J=1.7Hz); 8.03 (d, 1H, P_9); 8.02 (d, 2H, P_{a3}, J=6.6Hz); 7.82 (t, 1H, T_p, J=1.7Hz); 7.80 (d, 2H, BN_a, J=9.1Hz); 7.41 (m, 4H, $T_{55"}$+P_{a8}); 7.21 (d, 2H, BN_b, J=9.1Hz); 7.21 (d, 2H, P_{b3}, J=8.9Hz); 6.95 (d, 2H, P_{b8}, J=8.9Hz); 4.39 (m, 2H, ξ_3, J=4.5Hz); 4.35 (t, 2H, α_3, J=5.3Hz); 4.13 (t, 2H, α_8, J=4.7Hz); 3.83-3.79 (m, 8H,

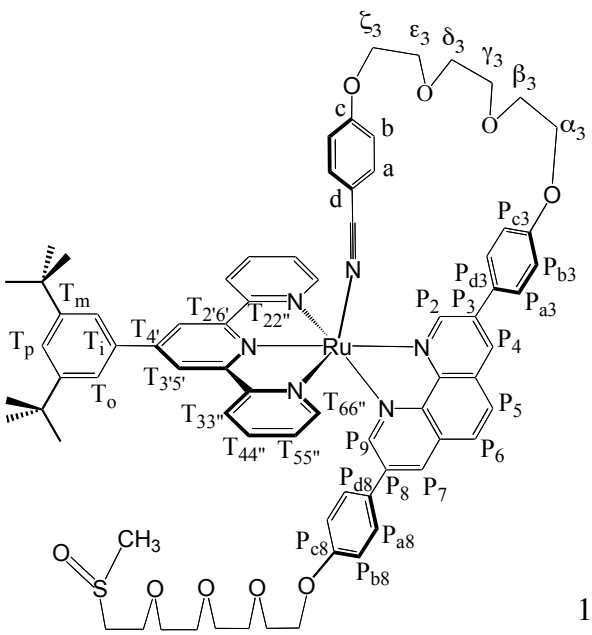

η_8+ε_3+β_3+β_8); 3.66-3.55 (m, 12H, γ_3+δ_3+γ_8+δ_8+ε_8+ξ_8); 2.97-2.90 (m, 1H, θ"$_8$); 2.82-2.74 (m, 1H, θ'$_8$); 2.50 (s, 3H, CH_3(SO)); 1.51 (s, 18H, tBu). *^{13}C NMR 500MHz NMR*: δ in ppm in acetone-d_6 (attribution were done according to HSQC and HMBC 2D ^{1}H-^{13}C HETCORR experiments): 164.0 (BN_c); 160.2 (P_{c3}); 160.0 (P_{c8}); 158.5 ($T_{22"}$); 157.7 ($T_{2'6'}$); 154.1($T_{66"}$); 151.3 (P_2); 151.1 ($T_{4'}$); 149.5 (P_9); 146.3; (P_8); 145.3 (P_3); 138.6 ($T_{44"}$); 136.6 (T_i); 135.4 (BN_a); 133.2 (P_7); 133.2 (P_{14}); 132.4 (P_{13}); 132.3 (P_4); 131 (P_{11}); 130.3 (P_{12}); 129.3 (P_{a3}); 128.8 (P_5); 128.7 (P_{d3}); 128.4 (P_{a8}); 128.4 ($T_{55"}$); 128.0 (P_6); 127.5 (P_{d8}); 126.3 (BN_d); 124.7 ($T_{33"}$); 124.5 (T_p); 122.3 (T_o); 122.2 (T_m); 122.0 ($T_{3'5'}$); 116.2 (P_{b3}); 116.2 (BN_b); 115.3 (P_{b8}); 101.2 (CN); 69 (b_3-e_3); 69 (b_8-z_8); 68.5 (z_3); 68 (a_3); 67.6 (a_8); 64.3 (h_8); 53.9 (q_8); 38.4 (CH_3(SO)); 35.0 (C(Me_3)); 30.8 (Me_3). *ES-MS m/z (calc)*: 1487.42 (1487.44, $[M\text{-}PF_6]^+$); 671.231 (671.238, $[M\text{-}2PF_6]^{2+}$). *UV-vis*: λ_{max} (ε in L.mol^{-1}.cm^{-1}) in acetone: 362 nm (23300); 468 nm (9090).

Characterization of **19**$^{2+}$: *^{1}H 500MHz NMR*: δ in ppm in acetone-d_6: 10.84 (d, 1H, P_9, J=1.9Hz); 9.37 (d, 1H, $T_{3'}$, J=1.45Hz); 9.29 (d, 1H, P_7, J=1.9Hz); 9.29 (d, 1H, $T_{5'}$, J=1.44Hz); 8.94 (d, 1H, T_3, J=7.7Hz); 8.88 (d, 1H, P_4, J=1.9Hz); 8.84 (d, 1H, $T_{3"}$, J=7.8Hz); 8.50 (d, 1H, P_6, J=8.9Hz); 8.32 (d, 1H, P_5, J=8.9Hz); 8.31 (d, 1H, $T_{6"}$, J=4.9Hz); 8.23 (td, 1H, T_4, J=7.9,1.5Hz); 8.18-8.14 (m, 2H, T_6+$T_{4"}$); 8.10 (d, 2H, P_{a8}, J=8.8Hz); 8.09 (d, 2H, T_o, J=1.7Hz); 7.84 (t, 1H, T_p, J=1.7Hz); 7.80 (d, 1H, P_2, J=1.9Hz); 7.57 (d, 2H, BN_a, J=9.0Hz); 7.52 (ddd, 1H, T_5, J=1.3,5.6,7.5Hz); 7.47 (d, 2H, P_{b8}, J=8.9Hz); 7.44 (ddd, 1H, $T_{5"}$); 7.39 (d, 2H, P_{a3}, J=8.9Hz); 7.06 (d, 2H, BN_b, J=9.0Hz); 6.89 (d, 2H, P_{b3}, J=8.8Hz); 4.49 (dddd, 2H, α_8, J=2.1,5.8,13.5,41.6Hz); 4.22 (t, 2H, ζ_3, J=4.7Hz); 4.11 (m, 1H, η_8); 4.07 (t, 2H, α_3, J=4.9Hz); 4.03 (m, 1H, $\eta_{'8}$); 3.88 (m, 2H, β_3); 3.86 (m, 1H, β_8); 3.83 (m, 2H, ε_3); 3.80 (m, 1H, $\beta_{'8}$); 3.76 (m, 1H, θ_8); 3.66 (m, 2H, γ_3); 3.61 (m, 2H, ζ_8); 3.59 (m, 2H, δ_3); 3.59 (m, 2H, γ_8); 3.57 (m, 2H, ε_8); 3.52 (m, 2H, δ_8); 2.99 (m, 1H, $\theta_{'8}$); 2.63 (s, 3H, CH_3(SO)); 1.50 (s, 18H, tBu). *^{13}C 500 MHz NMR*: δ in ppm in acetone-d_6 (attribution were done according to HSQC and HMBC 2D ^{1}H-^{13}C HETCORR experiments): 162.4 (BN_c); 161.0 (P_{c8}); 160.2 (P_{c3}); 157.9 ($T_{6'}$); 157.7 ($T_{2'}$); 157.6 ($T_{22"}$); 155.1 (P_9); 154.7 (T_6); 154.2 ($T_{6"}$); 152.5 (T_m); 147.4 (P_2); 147.1 (P_8); 144.5 (P_3); 140.1 ($T_{44"}$); 136.4 ($T_{4'}$); 134.5 (P_{13}); 134.4 (P_4); 134.0 (BN_a); 133.0 (P_7); 133.0 (P_{14}); 131.2 (P_{12}); 130.4 (P_{11}); 129.6 ($T_{5"}$); 129.5 (T_5); 129.0 (P_6); 128.8 (P_{a8}); 128.6 (P_{a3}); 128.0 (P_5); 127.9 (P_{d8}); 127.1 (P_{d3}); 126.1 ($T_{3"}$); 125.8 (T_3);

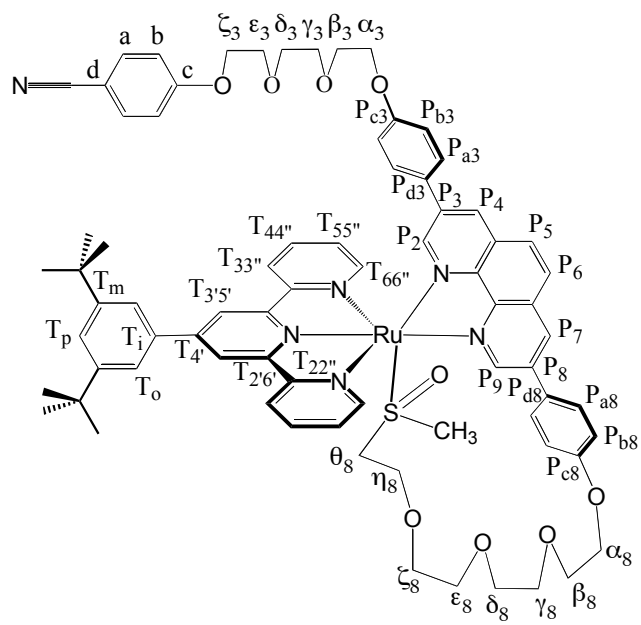

124.9 (T_i); 124.9 (T_p); 123.7 ($T_{3'}$); 123.3 ($T_{5'}$); 122.4 (T_o); 118.7 (BN_d); 117.4 (P_{b8}); 115.5 (P_{b3}); 115.5 (BN_b); 103.5 (CN); 68.7 (a_8); 68.6 (h_8); 68.1 (z_3); 67.6 (a_3); 54.8 (q_8); 69.3-71.1(b_3-e_3); 69.1-71.0 (b_8-z_8); 38.5 ($CH_3(SO)$); 34.9 ($C(Me_3)$); 31.0 (Me_3). *ES-MS m/z (calc)*: 1487.443 (1487.439, $[M-PF_6]^+$); 671.242 (671.238, $[M-2PF_6]^{2+}$). *UV-vis*: λ_{max} (ε in $L.mol^{-1}.cm^{-1}$) in acetone: 362 nm (23400); shoulder at 428 nm (8330).

II.5. Irradiation experiments

In a typical experiment, 3 mg of [**18**][PF_6]$_2$ or [**19**][PF_6]$_2$ (1.8 μmol) were weighed in a vial, the deuterated solvent was added (CD_3CN, C_4D_8O or an acetone-d_6 / D_2O mixture 9:1) and an NMR tube was prepared in the dark. A reference spectrum was taken at t=0 and the course of the reaction was followed by NMR. Irradiations were performed in the following conditions: the NMR tubes were fitted to a glass cell thermostated at T = 25°C. The lamp was a high pressure 1000 W xenon arc lamp providing a parallel beam of white light. The beam was filtered by a 10 cm thick water filter filled with running water at 5°C and secondly by an Andover interference filter with $\Delta\lambda$ = 10 nm, centered either at 430 nm (for **19**$^{2+}$) or 470 nm (for **18**$^{2+}$) (reference of the filters: 430FS10-50 and 470FS10-50, respectively).

Characterization of Ru(terpy*)(**26**)$(D_2O)^{2+}$,$2PF_6^-$: *^{1}H 300MHz NMR*: δ in ppm in acetone-d6 / D_2O 20%: 10.26 (d, 1H, $P_{2,9}$); 9.17 (d, 1H, P_4); 9.06 (s, 2H, $T_{3',5'}$); 8.77 (d, 2H, $T_{33"}$); 8.51 (m, 1H, P_7); 8.45 (d, 1H, P_5); 8.23 (d, 1H, P_6); 8.14 (d, 2H, P_{a3}); 8.01 (td, 2H, $T_{44"}$); 7.99 (d, 2H, T_o); 7.94 (m, 2H, $T_{66"}$); 7.80 (d, 1H, P_9); 7.71 (t, 1H, T_p); 7.62 (d, 2H, P_a); 7.36-7.19 (m, 6H, P_{a8}+ $T_{55"}$+P_{b3}); 7.09 (d, 2H, P_b); 6.89 (d, 2H, P_{b8}); 4.31-3.52 (m, 12H, α_3-ζ_3+α_8-η_8); 3.13-2.88 (m, 2H, θ_8); 2.63 (s, 3H, $CH_3(SO)$ on the side of D_2O) or 2.59 (s, 3H, $CH_3(SO)$ opposite to D_2O); 1.43 (s, 18H, tBu).*UV-visible:* λ_{max} (ε in $L.mol^{-1}.cm^{-1}$) in acetone / water: 505 nm (7900). *MS ES m/z (calc):* 671.26 (671.24, $[M - 2\ PF_6 - D_2O]^{2+}$); 680.8 (681.2, $[M - 2\ PF_6]^{2+}$); 700.24 (700.26, $[M - 2\ PF_6 - D_2O + CH_3COCH_3]^{2+}$); 1423.3 (1423.5, $[M - PF_6 - D_2O + CH_3COCH_3 + Na]^+$).

III. Chapter 3: Ru(terpy)(phen)$(L)^{n+}$ complexes with a dissymmetric 2-anisyl-8-mesityl-1,10-phenanthroline

III.1. Synthesis of APterpy

30: In a 500 mL two-necked round-bottom flask 29.6 g (160 mmol) of 3-bromobenzaldehyde were dissolved in 250 mL of methanol. To the well-stirred solution were successively added 18 mL (160 mmol) of 2-acetylpyridine and a solution of 6.4 g of sodium hydroxide in 50 mL of water. The solution was stirred

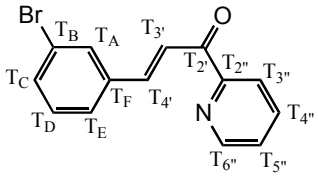

at room temperature for 15 minutes. The white precipitate was filtered, washed with water and dissolved in dichloromethane. The organic phase was still washed once with water and evaporated to dryness to yield 28.2 g of chalcone **30** (61%).

^{1}H 500 MHz NMR: δ in ppm in $CDCl_3$: 8.75 (dq, 1H, $T_{6''}$, J=4.8,0.9Hz); 8.29 (d, 1H, $T_{4'}$, J=16.1Hz); 8.19 (dt, 1H, $T_{3''}$, J=7.7,1.2Hz); 7.88 (td, 1H, $T_{4''}$, J=7.7,1.8Hz); 7.88 (s, 1H, T_A); 7.84 (d, 1H, $T_{3'}$, J=16.1Hz); 7.62 (d, 1H, T_C, J=7.7Hz); 7.51 (m, 2H, T_E+$T_{5''}$); 7.28 (t, 1H, T_D, J=7.9Hz). *^{13}C 500 MHz NMR*: δ in ppm in $CDCl_3$ (attribution were done according to HSQC and HMBC 2D ^{1}H-^{13}C HETCORR experiments): 189.0 ($T_{2'}$); 153.8 ($T_{2''}$); 148.8 ($T_{6''}$); 142.7 ($T_{3'}$); 137.2 (T_B); 136.9 ($T_{4''}$); 133.1 (T_E); 131.0 (T_A); 130.2 (T_D); 127.4 (T_C); 126.9 ($T_{5''}$); 122.9 (T_F); 122.8 ($T_{3''}$); 122.0 ($T_{4'}$). *C,H,N for $C_{14}H_{10}BrNO$*: calc C, 58.36; H, 3.50; N, 4.86; found C, 58.48; H, 3.72; N, 4.77.

31: 40.6 g (160 mmol) of iodine, 18 mL (160 mmol) of 2-acetylpyridine and 40 mL (248 mmol) of pyridine were added in a two-necked 100 mL round-bottom flask equipped with a big size stirring bar. The flask was put under argon and plunged into an oil bath previously heated at 120°C. The reaction was refluxed 5 minutes and removed from the hot bath as soon as the mixture crystallized. The flask was let cool down to room temperature overnight. The solid was transferred in a 1L flask, 90 mL of silica gel and 200 mL of acetonitrile were added, well stirred and the solvent was removed on a büchi. The solid phase was put on top of a silica gel column (500 mL) and eluted with a 85:15 acetonitrile / water mixture. The main fraction was collected before the black color arrived on the bottom of the column. The solvents were evaporated and the product was recrystallised in 200 mL of methanol. Yield: 40.2 g (77%) of **31** as yellowish crystals.

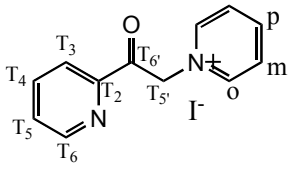

^{1}H 500 MHz NMR: δ in ppm in CD_3CN: 8.81 (m, 1H, T_6); 8.75 (d, 2H, o, J=5.5Hz); 8.64 (tt, 1H, p, J=7.9,1.3Hz); 8.15 (t, 2H, m, J=6.9Hz); 8.09-8.03 (m, 2H, T_4+T_3); 7.74 (m, 1H, T_5); 6.43 (s, 2H, $T_{5'}$). *^{13}C 500 MHz NMR*: δ in ppm in CD_3CN (assignments were done according to HSQC 2D ^{1}H-^{13}C HETCORR experiments): 192.0 ($T_{6'}$); 150.6 (T_6); 147.7 (p); 147.0 (o); 138.9 (T_4); 130.2 (T_5); 129.0 (m); 123.2 (T_3); 67.6 ($T_{5'}$). *C,H,N for $C_{12}H_{11}IN_2O$*: calc C, 44.19; H, 3.40; N, 8.59; found C, 44.29; H, 3.67; N, 8.32.

32: 79.0 g (1.03 mol) of dry ammonium acetate, 24.7 g (85.5 mmol) of chalcone **30** and 42.0 g (128 mmol) of acetylpyridinium iodide **31** were mixed in a three-necked 1 L round-bottom flask and dissolved in 400 mL of methanol. The clear solution was refluxed under air for 24 hours. The suspension was cooled down to 0°C for 15 minutes and the pure terpyridine was filtered, washed with methanol and dried. Yield: 20.9 g of terpyridine **32** (63%).

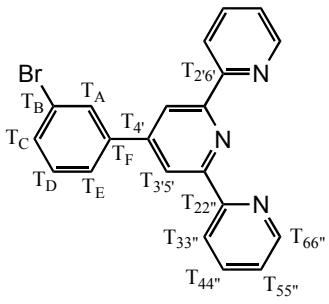

^{1}H 500 MHz NMR: δ in ppm in $CDCl_3$: 8.72 (dq, 2H, $T_{66"}$, J=4.5,0.5Hz); 8.68 (s, 2H, $T_{3',5'}$); 8.66 (dt, 2H, $T_{33"}$, J=8.0,0.9Hz); 8.03 (t, 1H, T_A, J=1.8Hz); 7.87 (td, 2H, $T_{44"}$, J=7.7,1.8Hz); 7.81 (dq, 1H, T_C, J=8.0,1.0Hz); 7.58 (dq, 1H, T_E, J=8.0,1.0Hz); 7.37 (t, 1H, T_D, J=8.0Hz); 7.35 (m, 2H, $T_{55"}$). *^{13}C 500 MHz NMR*: δ in ppm in $CDCl_3$ (attribution were done according to HSQC and HMBC 2D ^{1}H-^{13}C HETCORR experiments): 156.0 ($T_{22"}$); 155.9 ($T_{2',6'}$); 149.0 ($T_{66"}$); 148.7 (T_B); 140.6 (T_F); 136.8 ($T_{44"}$); 131.8 (T_E); 130.3 (T_D); 130.1 (T_A); 125.9 (T_C); 123.8 ($T_{55"}$); 123.0 ($T_{4'}$); 121.2 ($T_{33"}$); 118.7 ($T_{3',5'}$). *FAB MS m/z (calc)*: 388.0 (388.0, $[M+H]^+$). *C,H,N for $C_{21}H_{14}BrN_3$*: calc C, 64.96; H, 3.63; N, 10.82; found C, 64.93; H, 3.79; 10.93.

28: 1.16 g (3.0 mmol) of terpyridine **32** were dissolved in 100 mL of toluene in a three-necked 250 mL round-bottom flask. The flask was put under argon, 173 mg (150 µmol, 5 mol%) of palladium tetrakis(triphenylphosphine) were added under argon. 20 mL of a degassed 2 M sodium carbonate aqueous solution were cannulated in the reaction mixture, followed by 502 mg (3.30 mmol) of paramethoxyphenylboronic acid dissolved in 50 mL toluene and 8 mL of ethanol. The reaction mixture was degassed and refluxed under argon overnight. The solvents were evaporated, water was added and extracted with dichloromethane. The organic phase was washed once with water and evaporated. The product was purified on neutral alumina (200 mL) using a 3:7 to 35:15 diethylether / pentane mixture as the eluent. Yield: 879 mg of terpyridine **28** (71%).

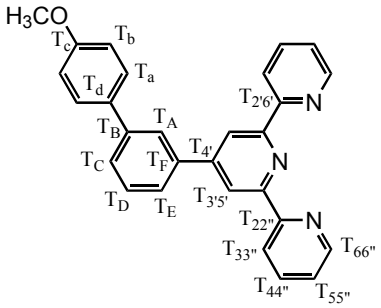

^{1}H 500 MHz NMR: δ in ppm in $CDCl_3$: 8.79 (s, 2H, T3'5'); 8.73 (m, 2H, T66"); 8.68 (dt, 2H, T33", J=7.9,1.1Hz); 8.05 (t, 1H, TA, J=1.8Hz); 7.88 (td, 2H, T44", J=7.7,1.8Hz); 7.82 (m, 1H, TE); 7.64-7.61 (m, 3H, TC+Ta); 7.56 (t, 1H, TD, J=7.7Hz); 7.35 (m, 2H, T55"); 7.02 (d, 2H, Tb, J=8.8Hz); 3.87 (s, 3H, OMe). *^{13}C 500 MHz NMR*: δ in ppm in $CDCl_3$ (attribution were done according to HSQC and HMBC 2D ^{1}H-^{13}C HETCORR experiments): 159.3 (T_c); 156.2 ($T_{22"}$); 155.9 ($T_{2',6'}$); 150.5 (T_F); 149.1 ($T_{66"}$); 141.6 (T_B); 139.1 ($T_{4'}$); 136.8 ($T_{44"}$); 133.4 (T_d); 129.3 (T_D); 128.4

(T_a); 127.4 (T_C); 125.7,125.7 (T_A+T_E); 123.8 ($T_{55"}$); 121.4 ($T_{33"}$); 119.0 ($T_{3',5'}$); 114.2 (T_b); 55.4 (T_{OMe}). *HR FAB MS m/z (calc)*: 416.1769 (416.1762, $[M+H]^+$). *C,H,N for* $C_{28}H_{21}N_3O$: *calc* C, 80.94; H, 5.09; N, 10.11; *found* C, 80.69; H, 5.17; N, 10.03.

III.2. Synthesis of AMphen

3-bromo-1,10-phenanthroline: a suspension of 20.0 g (92 mmol) of 1,10-phenanthroline hydrochloride in 40 mL of nitrobenzene was prepared in a two-necked 500 mL round-bottom flask and heated at 145°C. A solution of 6.6 mL (129 mmol) of bromine in 25 mL of nitrobenzene was added drop by drop within 2 hours at 145°C and the reaction mixture was stirred at 145°C an additional 3 hours. After cooling down to room temperature, 200 mL of concentrated ammonium hydroxide were added and well stirred. The solution was extracted with dichloromethane, the organic phase was washed thoroughly with water and evaporated to dryness. The crude material was put on silica gel (450mL) and eluted with a 100:0 to 98:2 dichloromethane / methanol mixture to remove nitrobenzene, unreacted 1,10-phenanthroline and 3,5,8-tribromo-1,10-phenanthroline. The main fraction contained 6.1 g (26%) of 3-bromo-1,10-phenanthroline contaminated with 8% of 3,5-dibromo-1,10-phenanthroline that could not be removed by chromatography.

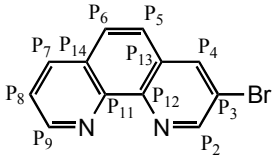

Purification by selective precipitation of the HCl adduct: in a typical experiment, an impure sample containing 6.37 g (24.6 mmol) of 3-bromo-1,10-phenanthroline and 0.72 g (2.1 mmol, 8%) of 3,5-dibromo-1,10-phenanthroline was dissolved in 100 mL of dichloromethane and cooled to –15°C. 11.7 mL (23.4 mmol, 0.95 eq) of a 2.0M ether solution of hydrochloric acid were slowly added with a syringe. At –15°C the resulting well stirred solution remained clear, but upon removing of the cooling bath a white precipitate slowly appeared. Once warmed up to room temperature, the precipitate was filtered, recovered with water and reacted with 75 mL of 1 M aqueous solution of sodium hydroxide. The aqueous phase was thogoughly extracted with dichloromethane and the organic phases were evaporated. Yield: 6.51 g of 3-bromo-1,10-phenanthroline containing less than 5% of 3,5-dibromo-1,10-phenanthroline (94%).

^{1}H 300 MHz NMR: δ in ppm in $CDCl_3$: 9.19 (d, 1H, P_2, J=1.8Hz); 9.17 (m, 1H, P_9); 8.39 (d, 1H, P_4, J=2.4Hz); 8.24 (dd, 1H, P_7, J=8.1,1.8Hz); 7.82 (d, 1H, P_5, J=8.9Hz); 7.70 (d, 1H, P_6, J=8.9Hz); 7.65 (dd, 1H, P_8). *^{13}C 300 MHz NMR*: δ in ppm in $CDCl_3$ (attribution were done according to HSQC and HMBC 2D ^{1}H-^{13}C HETCORR experiments): 151.4 (P_2); 150.7 (P_9); 146.0 (P_{12}); 144.4 (P_{11}); 137.4 (P_4); 136.1 (P_7); 129.6 (P_{13}); 128.6 (P_{14}); 127.9 (P_5); 125.4 (P_6); 123.3 (P_8); 119.9 (P_3). *C,H,N for* $C_{12}H_7BrN_2$: *calc* C, 55.63; H, 2.72; N, 10.81; *found* C, 55.24;H, 3.07;N, 10.70.

33: In a 500 mL two-necked round-bottom flask add 3.00 g (11.6 mmol) of 3-bromophenanthroline, 150 mL of toluene and a stirring bar. The flask was put under argon, 669 mg (580 µmol, 5 mol%) of palladium tetrakis(triphenylphosphine) were added under argon, 60 mL (120 mmol) of a degassed 2M aqueous sodium carbonate solution and a degassed solution containing 2.12 g (13.9 mmol) of paramethoxyphenyl boronic acid in 100 mL of toluene and 15 mL of ethanol were successively cannulated into the reaction flask. The solution was degassed and refluxed under argon overnight. The solvents were evaporated, water was added and the aqueous phase was extracted with dichloromethane. The collected organic phases were washed with water and evaporated to dryness. The crude product (5.05 g) was purified by chromatography on silica gel using dichloromethane / methanol mixtures to yield 3.01 g (91%) of phenanthroline **33**.

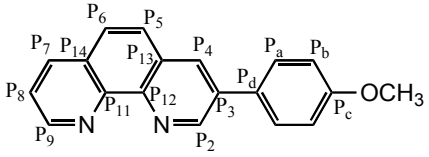

^{1}H 300 MHz NMR: δ in ppm in $CDCl_3$: 9.33 (d, 1H, P_2, J=2.4Hz); 9.10 (dd, 1H, P_9, J=4.4,1.8Hz); 8.16 (d, 1H, P_4, J=2.3Hz); 8.08 (dd, 1H, P_7, J=8.1,1.8Hz); 7.63 (d, 2H, P_a, J=3.3Hz); 7.61-7.58 (m, 2H, P_5+P_6); 7.49 (dd, 1H, P_8); 6.96 (d, 2H, P_b, J=8.8Hz); 3.77 (s, 3H, P_{OMe}). *^{13}C 300 MHz NMR*: δ in ppm in $CDCl_3$ (attribution were done according to HSQC and HMBC 2D ^{1}H-^{13}C HETCORR experiments): 160.2 (P_c); 150.3 (P_9); 149.4 (P_2); 146.4 (P_{11}); 144.8 (P_{12}); 136.1 (P_7); 135.6 (P_3); 132.7 (P_4); 130.1 (P_d); 128.8 (P_a); 128.7 (P_{13}); 128.6 (P_{14}); 127.0 (P_6); 126.8 (P_5); 123.0 (P_8); 114.9 (P_b); 55.6 (P_{MeO}). *FAB MS m/z (calc)*: 287.1 (287.1, $[M + H]^+$). *C,H,N for $C_{19}H_{14}N_2O$*: *calc* C, 79.70; H, 4.93; N, 9.78; *found* C, 78.65; H, 5.25; N, 7.63.

29: 434 mg (2.18 mmol) of mesitylbromide were put under argon in a 100 mL round-bottom flask. 50 mL of dry diethylether were cannulated, 1.57 mL of n-buthyllithium (1.37 M, 2.15 mmol) were added and the mixture was stirred under argon for 5 hours. In a three-necked 250 mL round-bottom flask, 513 mg (1.79 mmol) of phenanthroline **33** were weighed and dissolved in 150 mL of dry diethylether or toluene under argon. The ether solution of aryllithium was dropwise cannulated at room temperature into the reaction flask, leading to a fast colour change from colourless to deep violet. The solution was stirred under argon at room temperature for 20 hours and quenched with 25 mL of water. The solvents were evaporated, water was added and the aqueous phase was extracted with dichloromethane. To the combined yellow dichloromethane extracts were added 10 eq (1.6 g) of manganese dioxide. The solution was stirred at room temperature for 5 minutes, and this procedure was repeated twice again. The manganese oxide was filtered on celite and the clear solution evaporated to dryness, yielding 728 mg of re-

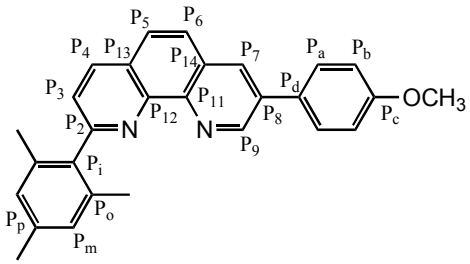

aromatised crude product. The two phenanthroline regioisomers were separated on acidic alumina (200 mL) using a 20:2:2 pentane / dichloromethane / ethylacetate mixture as the eluent. Yield: 188 mg (26%) of **29** (isomer 2,8) and 143 mg (19%) of **29'** (isomer 2,3).

Characterization for **29**: *^{1}H 500 MHz NMR*: δ in ppm in $CDCl_3$: 9.42 (d, 1H, P_9, J=2.5Hz); 8.34 (d, 1H, P_7, J=2.5Hz); 8.28 (d, 1H, P_4, J=8.2Hz); 7.85 (s, 2H, $T_{3',5'}$); 7.71 (d, 2H, P_a, J=8.8Hz); 7.55 (d, 1H, P_3, J=8.2Hz); 7.07 (d, 2H, P_b, J=8.8Hz); 6.95 (s, 2H, P_m); 3.89 (s, 3H, P_{OMe}); 2.35 (s, 3H, Me^p); 2.09 (s, 6H, Me^o). *^{13}C 500 MHz NMR*: δ in ppm in $CDCl_3$ (attribution were done according to HSQC and HMBC 2D ^{1}H-^{13}C HETCORR experiments): 160.9 (P_2); 160.0 (P_c); 149.4 (P_9); 146.3 (P_{12}); 145.0 (P_{11}); 138.5 (P_o); 137.4 (P_p); 136.1, 136.0 (P_i+P_4); 135.2 (P_8); 132.5 (P_7); 130.1 (P_d); 128.8 (P_{14}); 128.6 (P_a); 128.2 (P_m); 126.9 (P_{13}); 126.8 (P_5); 126.4 (P_6); 124.6 (P_3); 114.7 (P_b); 55.4 (P_{OMe}); 21.1 (Me^p); 20.4 (Me^o). *HR FAB MS m/z (calc)*: 405.1971 (405.1967, $[M+H]^+$). *C,H,N for $C_{28}H_{24}N_2O$*: *calc* C, 83.14; H, 5.98; N, 6.93; *found* C, 88.77; H, 6.04; N, 6.57.

Characterization for **29'**: *^{1}H 300 MHz NMR*: δ in ppm in $CDCl_3$: 9.19 (dd, 1H, P_9, J=4.3,1.7Hz); 8.23 (dd, 1H, P_7, J=8.1,1.9Hz); 8.23 (s, 1H, P_4); 7.85 (d, 1H, P_5, J=8.8Hz); 7.79 (d, 1H, P_6, J=8.8Hz); 7.58 (dd, 1H, P_8, J=8.1,4.3Hz); 7.15 (d, 2H, P_a, J=9.1Hz); 6.78 (s, 2H, P_m); 6.77 (d, 2H, P_b, J=9.1Hz); 3.77 (s, 3H, P_{OMe}); 2.26 (s, 3H, Me^p); 1.93 (s, 6H, Me^o).

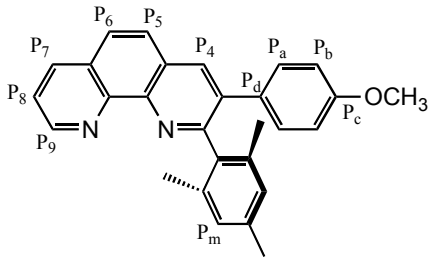

III.3. Synthesis of ruthenium complexes

34: 4.10 g (9.87 mmol) of terpyridine **28** and 2.59 g (9.9 mmol) of triaqua ruthenium trichloride were mixed in 500 mL of ethanol and refluxed under air for one hour. The mixture was cooled down to room temperature and filtered. The solid was washed twice with ethanol and dried to yield 5.84 g of **34** as a brown solid (95%).

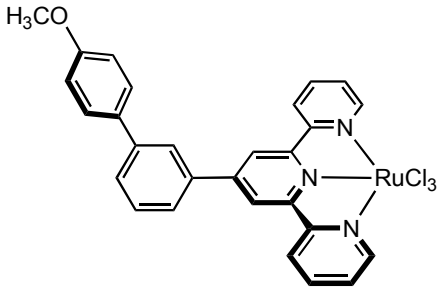

FAB MS m/z (calc): 621.9 (622.0, $[M]^+$); 586.9 (587.0, $[M - Cl]^+$); 552.0 (552.0, $[M – 2 Cl]^+$); 517.0 (517.1, $[M – 3 Cl + H]^+$). *C,H,N for $C_{28}H_{21}C_{l3}N_3ORu$*: *calc* C, 53.99; H, 3.40; N, 6.75; *found* C, 49.34; H, 3.70; N, 6.44.

35_{th}^{+} [Ru(APterpy)(AMphen)(Cl)][PF_6]: 185 mg (297 µmol) of **34**, 40 mL of ethanol and 53 mg (1.24 mmol) of lithium chloride were mixed in a two-necked 250 mL round-bottom flask. 100 mg (248 µmol) of phenanthroline **29** were dissolved in 40 mL of hot ethanol and added to the reaction mixture. 20 mL of water and 2 mL of triethylamine were added, the reaction flask was put under argon and refluxed for 4 hours. The violet complex was precipitated by the addition at room temperature of 50 mL of KPF_6 and 30 mL of water, the precipitate was filtered, washed with water, recovered with acetone and dried. The minimum amount of acetone was added to dissolve the crude material, toluene was added until complete precipitation of the complex and the remaining free phenanthroline, soluble in toluene, was removed by filtration. The violet solid was recovered with acetone, dried and purified by chromatography on silica gel using a 500:5:0.5 mixture of acetone, water and KNO_3. Yield: 147 mg (54%) of analytically pure [$\mathbf{35_{th}}$][PF_6].

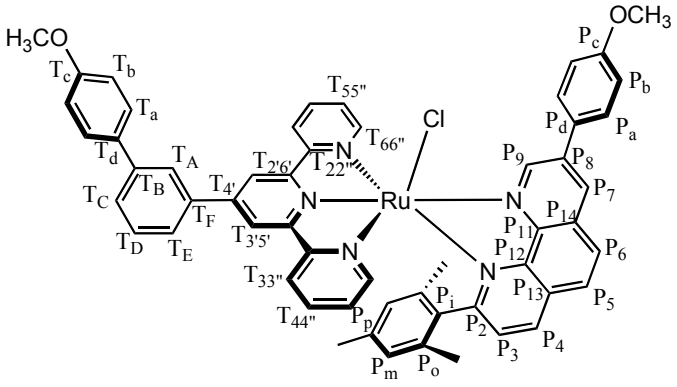

^{1}H 500 MHz NMR: δ in ppm in $CDCl_3$: 10.88 (d, 1H, P_9); 8.83 (d, 1H, P_7); 8.32 (d, 1H, P_6, J=8.9Hz); 8.23 (d, 1H, P_4); 8.22 (d, 2H, $T_{33"}$); 8.11 (d, 1H, P_5, J=8.9Hz); 8.07 (s, 2H, $T_{3'5'}$); 7.97 (d, 2H, P_a, J=8.0Hz); 7.90 (s, 1H, T_A); 7.72 (m, 1H, T_E); 7.68 (d, 2H, T_a); 7.68 (td, 2H, $T_{44"}$); 7.67 (m, 1H, T_C); 7.57 (m, 1H, T_D); 7.44 (d, 2H, $T_{66"}$, J=5.5Hz); 7.10 (d, 2H, P_b, J=8.0Hz); 7.07 (m, 2H, $T_{55"}$); 7.02 (d, 2H, T_b, J=8.0Hz); 6.94 (d, 1H, P_3, J=8.2Hz); 6.37 (s, 2H, P_m); 3.87 (s, 3H, T_{MeO}); 3.85 (s, 3H, P_{MeO}); 1.86 (s, 3H, Me^p); 0.74 (s, 6H, Me^o). *^{13}C 500 MHz NMR*: δ in ppm in $CDCl_3$ (attribution were done according to HSQC and HMBC 2D ^{1}H-^{13}C HETCORR experiments): 167.9 (P_2); 160.9 (P_c); 160.1 ($T_{22"}$); 159.7 (T_c); 158.3 ($T_{2'6'}$); 152.6 (P_9); 152.0 ($T_{66"}$); 149.7 (P_{12}); 146.0 (P_{11}); 145.4 ($T_{4'}$); 142.1 (T_F); 139.7 (P_p); 137.6 (P_8); 137.3 (P_{14}); 137.0 (T_B); 136.6 ($T_{44"}$); 136.2 (P_4); 136.0 (P_{13}); 134.8 (P_o); 132.5 (T_d); 131.5 (P_7); 130.1 (T_D); 129.7 (T_C); 129.3 (P_a); 128.5 (T_a); 128.2 (P_5); 1282 (P_d); 128.0 (P_6); 128.0 (P_m); 126.8 (P_3); 126.8 ($T_{55"}$); 125.6 (T_E); 125.0 (T_A); 123.5 ($T_{33"}$); 119.1 ($T_{3'5'}$); 115.2 (P_b); 114.6 (T_b); 55.5 (P_{MeO}); 55.5 (T_{MeO}); 21.4 (Me^p); 20.4 (Me^o). P_i could not be assigned. *UV-vis*: λ_{max} (ε in $L.mol^{-1}.cm^{-1}$) in acetone: 515 nm (17100). *ES MS m/z (calc)*: 956.2305 (956.2305, $[M - PF_6]^+$).

36_{th}^{2+} [Ru(APterpy)(AMphen)(CH_3CN)][PF_6]$_2$: 131 mg (119 µmol) of [**35_{th}**][PF_6] were dissolved in a mixture of 80 mL acetonitrile and 20 mL water. The solution was degassed and refluxed under argon for two days. Complete precipitation of the complex was obtained by adding enough KPF_6 at room temperature. The orange precipitate was filtered, washed with water, recovered with acetone, dried and purified on silica gel using a 80:5:0.5 acetonitrile / water / KNO_3 mixture as eluent. Yield: 112 mg (75%) of [**36_{th}**][PF_6]$_2$.

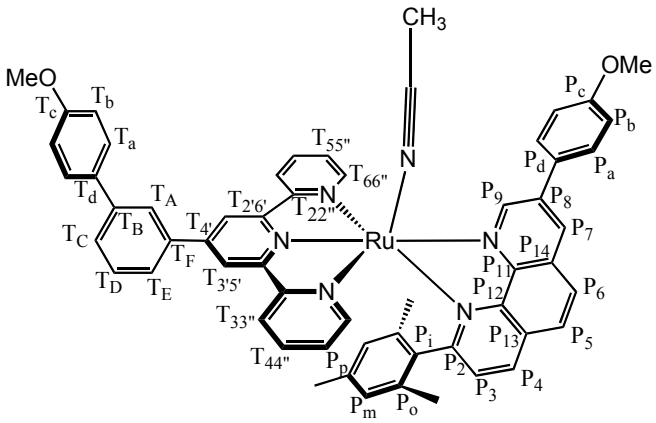

^{1}H 300 MHz NMR: δ in ppm in CD_3CN: 9.94 (d, 1H, P_9); 9.11 (d, 1H, P_7); 8.54 (s, 2H, $T_{3',5'}$); 8.52 (m, 2H, $T_{33"}$); 8.49 (d, 1H, P_4); 8.44 (d, 1H, P_6, J=8.9Hz); 8.33 (s, 1H, T_A); 8.27 (d, 1H, P_5, J=8.9Hz); 8.06 (m, 5H, P_a+$T_{44"}$+T_E); 7.86 (m, 3H, T_a+T_C); 7.81 (m, 1H, T_D); 7.61 (m, 2H, $T_{66"}$); 7.24 (m, 5H, P_3+T_b+$T_{55"}$); 7.16 (d, 2H, P_b, J=8.0Hz); 6.53 (s, 2H, P_m); 3.91 (s, 3H, T_{MeO}); 3.90 (s, 3H, P_{MeO}); 2.08 (s, 3H, AN_{CH3}); 1.98 (s, 3H, Me^p); 0.86 (s, 6H, Me^o). *ES MS m/z (calc)*: 481.136 (481.144, [M – 2 PF_6]$^{2+}$); 460.62 (460.63, [M - CH_3CN – 2 PF_6]$^{2+}$).

36_{photo}^{2+} [Ru(APterpy)(AMphen)(CH_3CN)][PF_6]$_2$: 50 mg (45 µmol) of [**3 5_{th}**][PF_6] were dissolved in 4 mL of acetonitrile and 2 mL of water, put under argon and white-light irradiated for 1 hour at room temperature with a 1000W xenon arc lamp filtered by a water filter. The resulting orange solution was transferred into 20 mL of KPF_6, upon which precipitation occurred. The solid was filtered, washed with water, recovered with acetone and dried to yield 52 mg (100%) of the photochemical isomer [**36_{photo}**][PF_6]$_2$.

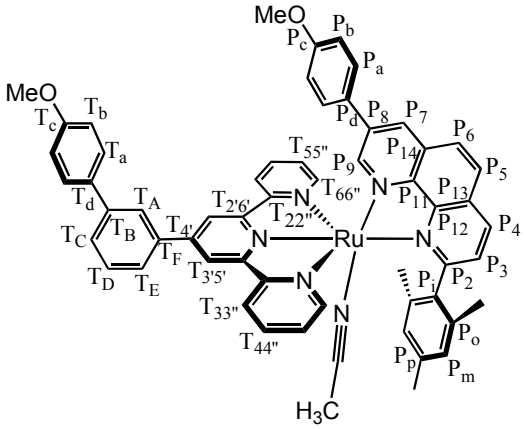

^{1}H 300 MHz NMR: δ in ppm in CD_3CN: 8.92 (d, 1H, P_4, J=8.3Hz); 8.83 (s, 2H, $T_{3',5'}$); 8.58-8.55 (m, 3H, P_7+$T_{33"}$); 8.41 (d, 1H, P_5, J=8.8Hz); 8.32 (t, 1H, T_A, J=1.9Hz); 8.21 (d, 1H, P_6, J=8.8Hz); 8.09-7.99 (m, 4H, T_E+P_3+$T_{44"}$); 7.93-7.82 (m, 4H, T_C+P_9+T_a); 7.80 (t, 1H, T_D, J=7.9Hz); 7.71-7.69 (m, 2H, $T_{66"}$); 7.31 (d, 2H, P_a, J=8.9Hz); 7.23 (m, 2H, $T_{55"}$); 7.12 (d, 2H, T_b, J=8.8Hz); 6.94 (s, 2H, P_m); 6.90 (d, 2H, P_b, J=8.9Hz); 3.88 (s, 3H, T_{MeO}); 3.74 (s, 3H, P_{MeO}); 2.24 (s, 3H, Me^p); 2.09 (s, 6H, Me^o). *^{13}C 300 MHz NMR*: δ in ppm in CD_3CN (attribution were done according to HSQC and HMBC 2D ^{1}H-^{13}C HETCORR experiments): 167.9 (P_2); 160.8 (P_c); 160.1 (T_c); 158.5 ($T_{22"}$); 154.4 ($T_{66"}$); 149.3 (P_9); 147.5 (P_{12}); 149.3 (T_4); 146.7 (P_{11}); 137.0 (T_F); 139.3 (P_p); 138.9

($T_{44"}$); 138.0 (P_4); 137.6 (P_8); 142.0 (T_B); 137.2 (P_i); 136.4 (P_o); 133.4 (P_7); 132.5 (T_d); 130.7 (P_{14}); 130.8 (P_{13}); 130.2 (T_D); 129.2 (P_3); 127.7 (P_6); 127.7 ($T_{55"}$); 129.2 (P_a); 128.4 (T_C); 128.4 (P_m); 128.4 (T_a); 128.8 (P_5); 127.1 (P_d); 126.0 (T_E); 124.7 ($T_{33"}$); 126.0 (T_A); 121.8 ($T_{3'5'}$); 117.2 (AN_{CN}); 114.7 (P_b); 114.3 (T_b); 55.0 (P_{OMe}); 55.4 (T_{OMe}); 20.7 ($ANCH_3$); 20.7 (Me^o); 20.1 (Me^p). $T_{2'6'}$ could not be assigned. *ES MS m/z (calc)*: 460.6316 (460.6311, $[M - 2\ PF_6 - CH_3CN]^{2+}$); 1107.2534 (1107.2534, $[M - PF_6]^+$). *UV-vis*: λ_{max} (ε in $L.mol^{-1}.cm^{-1}$) in acetone: 461 nm (12500).

37_{th}^{2+} [Ru(APterpy)(AMphen)(PY)][PF_6]$_2$: 64 mg (51 μmol) of [$\mathbf{36_{th}}$][PF_6]$_2$were dissolved in 5 mL of pyridine. The solution was degassed and refluxed under argon for 2 hours. Precipitation was obtained by addition of KPF_6 at room temperature; the solid was filtered, washed with water and recovered with acetone. Yield: 66 mg (100%) of [$\mathbf{37_{th}}$][PF_6]$_2$.

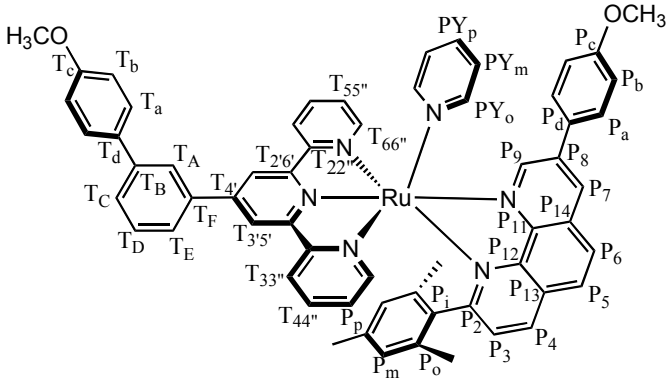

^{1}H 500 MHz NMR: δ in ppm in acetone-d6: 9.28 (d, 1H, P_7, J=1.8Hz); 9.01 (d, 1H, P_9, J=1.8Hz); 8.94 (s, 2H, $T_{3'5'}$); 8.92 (d, 2H, $T_{33"}$, J=8.1Hz); 8.76 (d, 1H, P_4, J=8.1Hz); 8.62 (d, 1H, P_6, J=8.8Hz); 8.47 (d, 1H, P_5, J=8.8Hz); 8.37 (t, 1H, T_A, J=1.8Hz); 8.22 (td, 2H, $T_{44"}$, J=7.7,1.5Hz); 8.18 (m, 1H, T_E); 8.11 (m, 2H, $T_{66"}$); 7.90-7.86 (m, 2H, T_C+PY_p); 7.81-7.75 (m, 7H, PY_o+T_a+P_a+T_D); 7.51 (m, 2H, $T_{55"}$); 7.43 (d, 1H, P_3, J=8.1Hz); 7.32 (dd, 2H, PY_m); 7.12 (d, 2H, T_b, J=8.8Hz); 7.10 (d, 2H, P_b, J=8.8Hz); 6.63 (s, 2H, P_m); 3.90 (s, 3H, T_{MeO}); 3.86 (s, 3H, P_{MeO}); 2.03 (s, 3H, Me^p); 0.98 (s, 6H, Me^o). *^{13}C 500 MHz NMR*: δ in ppm in $CDCl_3$ (attribution were done according to HSQC and HMBC 2D ^{1}H-^{13}C HETCORR experiments): 167.4 (P_2); 160.9 (P_c); 159.9 (T_c); 159.7 ($T_{22"}$); 157.4 ($T_{2'6'}$); 153.3 ($T_{66"}$); 151.9 (PY_o); 150.9 (P_9); 148.4 (P_{12}); 147.2 (T_F); 145.0 (P_{11}); 141.9 (T_d); 141.8 (P_d); 139.6 (P_p); 138.4 (T_D); 138.4 (PY_p); 138.4 ($T_{44"}$); 138.0 (P_8); 137.8 (P_4); 137.0 ($T_{4'}$); 135.3 (P_i); 134.9 (P_o); 132.7 (P_7); 132.3 (T_B); 131.7 (P_{14}); 129.6 (P_{13}); 128.8 (P_a); 128.4 (P_5); 128.4 ($T_{55"}$); 128.2 (T_C); 128.2 (T_a); 128.2 (P_m); 128.0 (P_6); 127.6 (P_3); 126.2 (PY_m); 125.5 (T_E); 125.3 ($T_{33"}$); 125.1 (T_A); 121.0 ($T_{3'5'}$); 114.7 (P_b); 114.1 (T_b); 54.6 (T_{MeO}); 54.5 (P_{MeO}); 20.3 (Me^p); 18.5 (Me^o). *UV-vis*: λ_{max} (ε in $L.mol^{-1}.cm^{-1}$) in acetone: 485nm (17900). *ES MS m/z (calc)*: 500.157 (500.152, $[M - 2\ PF_6]^{2+}$); 1145.280 (1145.268, $[M - PF_6]^+$).

37_{photo}^{2+} [Ru(APterpy)(AMphen)(PY)][PF_6]$_2$: *Thermal preparation*: 64 mg (51 µmol) of [$\mathbf{36}_{photo}$][PF_6]$_2$ were dissolved in 5 mL of pyridine. The solution was degassed and refluxed under argon for 2 hours. Precipitation was obtained by addition of KPF_6 at room temperature; the solid was filtered, washed with water and recovered with acetone. Yield: 65 mg (100%) of [$\mathbf{37}_{photo}$][PF_6]$_2$. *Photochemical preparation*: 64 mg (51 µmol) of [**36**][PF_6]$_2$ (either thermal or photochemical isomer) were dissolved in 3 mL of pyridine. The solution was degassed and white-light irradiated for 1 hour at room temperature with a 1000W xenon arc lamp filtered by a water filter. Precipitation was obtained by addition of KPF_6; the solid was filtered, washed with water and recovered with acetone. Yield: 66 mg (100%) of [$\mathbf{37}_{photo}$][PF_6]$_2$.

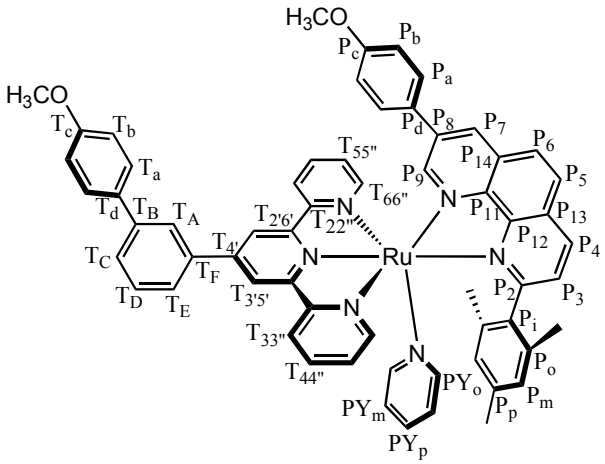

^{1}H 500 MHz NMR: δ in ppm in acetone-d6: 9.14 (s, 2H, $T_{3'5'}$); 9.13 (d, 1H, P_4, J=7.8Hz); 8.90 (d, 2H, $T_{33"}$, J=7.8Hz); 8.78 (d, 1H, P_7, J=2.0Hz); 8.57 (d, 1H, P_5, J=9.0Hz); 8.38 (d, 1H, P_6, J=8.4Hz); 8.30 (m, 3H, T_A+$T_{66"}$); 8.19 (td, 2H, $T_{44"}$, J=7.8,1.5Hz); 8.07 (d, 1H, P_3, J=8.4Hz); 8.05 (m, 1H, T_E); 8.04 (d, 2H, P_9, J=2.0Hz); 7.84 (d, 1H, T_C, J=8.5Hz); 7.74 (d, 2H, T_a, J=9.0Hz); 7.70 (t, 1H, T_D, J=7.8Hz); 7.59 (t, 1H, PY_p, J=7.8Hz); 7.55 (m, 2H, $T_{55"}$); 7.31 (d, 2H, P_a, J=8.4Hz); 7.27 (d, 2H, PY_o, J=5.4Hz); 7.08 (d, 2H, T_b, J=8.4Hz); 6.87 (d, 2H, P_b, J=8.4Hz); 6.85 (t, 2H, PY_m, J=7.2Hz); 6.43 (s, 2H, P_m); 3.87 (s, 3H, T_{MeO}); 3.73 (s, 3H, P_{MeO}); 2.16 (s, 6H, Me^o); 2.03 (s, 3H, Me^p). *^{13}C 500 MHz NMR*: δ in ppm in $CDCl_3$ (attribution were done according to HSQC and HMBC 2D ^{1}H-^{13}C HETCORR experiments): 168.7 (P_2); 160.7 (P_c); 159.9 (T_c); 158.4 ($T_{22"}$); 154.3($T_{2'6'}$); 153.9 ($T_{66"}$); 151.3 (PY_o); 149.0 (P_9); 148.0 (P_{12}); 146.6 ($T_{4'}$); 146.4 (P_{11}); 141.9 (T_F); 139.0 (P_p); 138.6 ($T_{44"}$); 138.4 (P_4); 137.2 (P_8); 136.6 (T_B); 136.2 (P_i); 135.3 (PY_p); 134.9 (P_o); 132.9 (P_7); 132.1 (T_d); 130.8 (P_{14}); 130.4 (P_{13}); 129.8 (T_D); 129.6 (P_3); 129.0 (P_6); 128.6 ($T_{55"}$); 128.4 (P_a); 128.4 (T_C); 128.2 (P_m); 128.0 (T_a); 127.8 (P_5); 126.8 (P_d); 125.3 (T_E); 125.1 (PY_m); 125.1 ($T_{33"}$); 125.1 (T_A); 121.5 ($T_{3'5'}$); 114.5 (P_b); 114.1 (T_b); 54.6 (P_{OMe}); 54.6 (T_{OMe}); 20.3 (Me^o); 19.7 (Me^p). *ES MS m/z (calc)*: 500.146 (500.152, [M – 2 PF_6]$^{2+}$); 1145.266 (1145.268, [M - PF_6]$^+$). *UV-vis*: λ_{max} (ε in L.mol^{-1}.cm^{-1}) in acetone: 482nm (13700).

35_{photo}^{+} [Ru(APterpy)(AMphen)(Cl)][PF_6]: A sample containing 5.0 mg (3.8 µmol) of [$\mathbf{37}_{photo}$][PF_6]$_2$ and 5.1 mg (31 µ mol) of tetraethylammonium chloride in $C_2D_2Cl_4$ was prepared. The closed NMR tube tube was heated at 140°C for 2 hours in the dark and directly analysed in the NMR spectrometer. Yield: 87% of [$\mathbf{35}_{photo}$][PF_6] and 13% of [$\mathbf{35}_{th}$][PF_6].

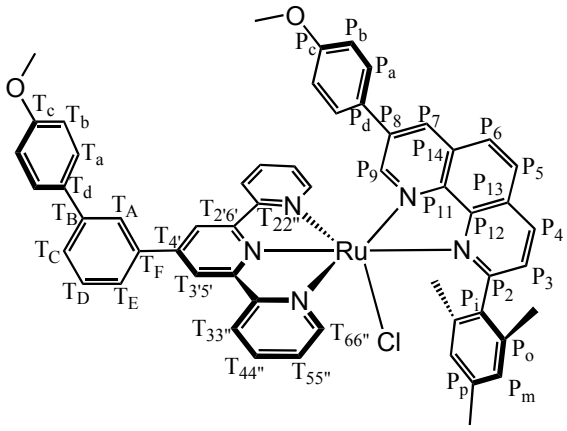

^{1}H 500 MHz NMR: δ in ppm in $CDCl_3$: 8.70 (P_4); 8.34 ($T_{3',5'}$); 8.22 ($T_{33"}$); 8.22 (P_5); 8.20 (P_7); 8.09 (P_6); 7.93 (P_3); 7.93 (T_A); 7.72 (T_C); 7.70 (T_E); 7.65 ($T_{66"}$); 7.65 (T_D); 7.63 (P_9); 7.60 ($T_{44"}$); 7.13 (P_a); 7.08 ($T_{55"}$); 6.96 (T_a); 6.95 (T_a); 6.87 (P_b); 6.84 (P_m); 3.87 (T_{OMe}); 3.70 (P_{OMe}); 2.21 (Me^p); 2.16 (Me^o). *^{13}C 500 MHz NMR*: δ in ppm in $CDCl_3$ (assignments according to HSQC and HMBC 2D ^{1}H-^{13}C HETCORR experiments): 169.8 (P_2); 160.7 (P_c); 159.5 (T_c); 152.7 ($T_{66"}$); 151.1 ($T_{2',6'}$); 149.3 (P_9); 147.6 (P_{12}); 147.5 ($T_{22"}$); 147.3 (P_{11}); 146.6 (T_F); 138.2 (P_p); 137.6 (P_o); 137.4 (P_d); 136.8 ($T_{4'}$); 136.6 ($T_{44"}$); 136.6 (P_4); 135.2 (P_i); 132.2 (T_d); 131.3 (P_{13}); 131.1 (P_7); 130.6 (P_{14}); 129.9 (T_E); 129.4 (P_3); 128.4 (P_a); 128.4 (P_5); 128.2 (T_a); 128.2 (T_C); 127.8 (P_m); 127.6 (P_6); 127.0 (P_8); 126.4 ($T_{55"}$); 125.5 (T_D); 125.2 (T_A); 123.7 ($T_{33"}$); 119.8 ($T_{3',5'}$); 114.7 (P_b); 114.3 (T_b); 55.3 (T_{OMe}); 55.3 (P_{OMe}); 21.3 (Me^o); 20.9 (Me^p). *UV-vis*: λ_{max} (ε in $L.mol^{-1}.cm^{-1}$) in acetone: 517 nm (11000). *ES MS m/z (calc)*: 956.25 (956.23, [M - PF_6]$^+$).

38_{photo}^{2+} [Ru(APterpy)(AMphen)(LUT)][PF_6]$_2$: 5 mg (3.8 µmol) of [$\mathbf{37}_{photo}$][PF_6]$_2$ were dissolved in 4 mL of 3,5-lutidine and heated under argon at 140°C for 2 hours. The complex was precipitated with heptane, washed with heptane and recovered with acetone to quantitatively yield [$\mathbf{38}_{photo}$][PF_6]$_2$.

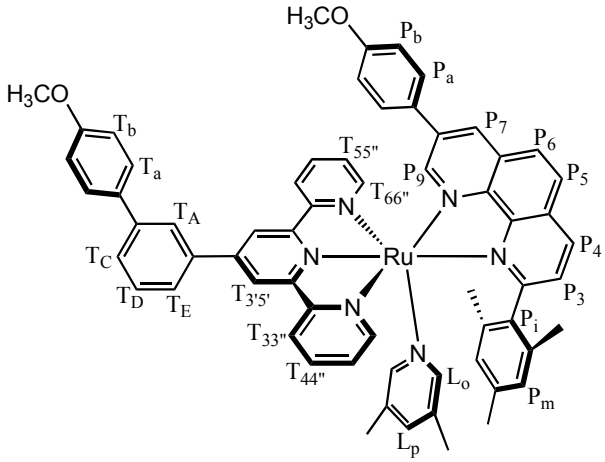

^{1}H 300 MHz NMR: δ in ppm in acetone-d_6: 9.14 (s, 2H, $T_{3',5'}$); 9.13 (d, 1H, P_4, J=7.8Hz); 8.92 (d, 2H, $T_{33"}$, J=7.8Hz); 8.79 (d, 1H, P_7, J=2.0Hz); 8.59 (d, 1H, P_5, J=9.0Hz); 8.39 (d, 1H, P_6, J=8.4Hz); 8.30 (m, 3H, $T_{66"}$+T_A); 8.21 (m, 2H, $T_{44"}$); 8.05 (m, 3H, P_3+P_9+T_E); 7.85 (m, 1H, T_C); 7.75 (d, 2H, T_a, J=9.0Hz); 7.70 (m, 1H, T_D); 7.56 (m, 2H, $T_{55"}$); 7.32 (d, 2H, P_a, J=8.4Hz); 7.21 (s, 1H, L_p); 7.09 (d, 2H, T_b); 6.87 (d, 2H, P_b, J=8.4Hz); 6.74 (s, 2H, L_o); 6.53 (s, 2H, P_m); 3.88 (s, 3H, T_{MeO}); 3.73 (s, 3H, P_{MeO}); 2.18 (s, 6H, Me^o); 2.01 (s, 3H, Me^p)1.84 (s, 6H, L_{Me}). *ES MS m/z (calc)*: 1173.307

(1173.301, [M - PF_6]$^+$); 2491.589 (2491.568, [[M – 2 PF_6]$_2$ + 3 PF_6]$^+$, [[M – 2 PF_6]$_2$ + 3 PF_6]$_2^{2+}$ and [[M – 2 PF_6]$_2$ + 3 PF_6]$_3^{3+}$).

39_{photo}^{2+} [Ru(APterpy)(AMphen)(C_6H_5CN)][PF_6]$_2$: 5 mg (3.8 μmol) of [$\mathbf{37}_{photo}$][PF_6]$_2$ were dissolved in 4 mL of benzonitrile and heated under argon at 140°C for 2 hours. The complex was precipitated with heptane, washed with heptane and recovered with acetone to quantitatively yield [$\mathbf{39}_{photo}$][PF_6]$_2$.

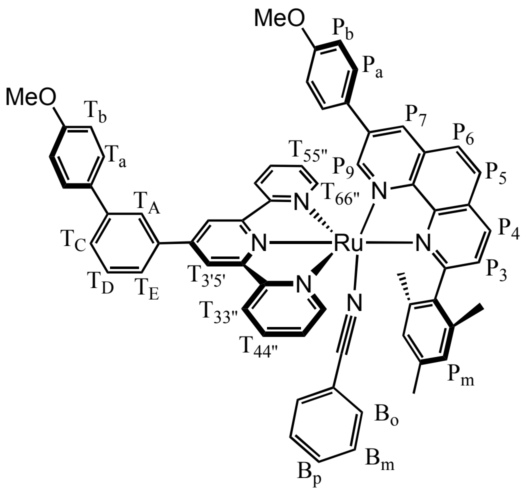

^1H 300 MHz NMR: δ in ppm in acetone-d6: 9.25 (s, 2H, $T_{3'5'}$); 9.15 (d, 1H, P_4, J=7.8Hz); 8.93 (d, 2H, $T_{33''}$, J=7.8Hz); 8.84 (d, 1H, P_7, J=2.0Hz); 8.59 (d, 1H, P_5, J=9.0Hz); 8.41 (d, 1H, P_6, J=8.4Hz); 8.32 (m, 2H, P_9+T_A); 8.19-8.16 (m, 5H, P_3+$T_{66''}$+$T_{44''}$); 8.09 (m, 1H, T_E); 7.86 (m, 1H, T_C); 7.74 (d, 2H, T_a, J=9.0Hz); 7.72 (m, 1H, T_D); 7.59 (t, 1H, B_p, J=7.5Hz); 7.49 (m, 2H, $T_{55''}$); 7.42 (m, 2H, B_o); 7.36 (d, 2H, P_a, J=8.4Hz); 7.09 (m, 4H, B_m+T_b); 6.88 (d, 2H, P_b, J=8.4Hz); 6.80 (s, 2H, P_m); 3.88 (s, 3H, T_{MeO}); 3.74 (s, 3H, P_{MeO}); 2.27 (s, 6H, Me^o); 1.60 (s, 3H, Me^p). *ES MS m/z (calc)*: 1169.274 (1169.269, [M-PF_6]$^+$).

40_{th}^{2+} [Ru(APterpy)(AMphen)(DMSO)][PF_6]$_2$: A sample containing 5.0 mg (3.8 μmol) of [$\mathbf{37}_{photo}$][PF_6]$_2$ in CD_3SOCD_3 was prepared. The closed NMR tube was heated at 140°C for 2 hours in the dark, yielding a mixture of O-bonded and S-bonded thermal complexes. After waiting at room temperature for 8 hours in the dark, the mixture evolved and the major product (S-bonded) remained almost alone. This complex was precipitated with KPF_6, washed with water, recovered with acetone, dried, but purification on silica gel was impossible as it led to decomposition. Yield in [$\mathbf{40}_{th}$][PF_6]$_2$ >95%. When [$\mathbf{40}_{th}$][PF_6]$_2$ was dissolved in acetonitrile, pyridine or in a dichloromethane solution of tetraethylammonium chloride and refluxed for 2 hours under argon and in the dark, it afforded after precipitation with KPF_6 complexes [$\mathbf{36}_{th}$][PF_6]$_2$,

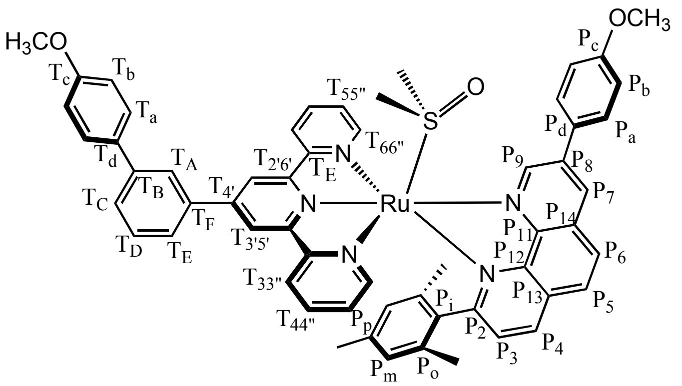

[$\mathbf{37_{th}}$][PF_6]$_2$ or [$\mathbf{35_{th}}$][PF_6], respectively. These complexes were purified on silica gel (acetone / water / KNO_3 80:5:0.5) with an overall yield (from the photochemical isomer) of ≈ 85%.

Characterization of [$\mathbf{40_{th}}$][PF_6]$_2$: *^1H 500 MHz NMR*: δ in ppm in acetone-d6: 11.04 (d, 1H, P_9, J=2.1Hz); 9.37 (d, 1H, P_7, J=1.9Hz); 9.06 (s, 2H, $T_{3'5'}$); 8.96 (d, 2H, $T_{33''}$, J=7.6Hz); 8.81 (d, 1H, P_4, J=8.3Hz); 8.60 (d, 1H, P_6, J=8.8Hz); 8.45-8.42 (m, 2H, P_5+T_A); 8.33-8.23 (m, 3H, $T_{44''}$+T_E); 8.18 (m, 2H, $T_{66''}$); 8.10 (d, 2H, T_a, J=9.1Hz); 7.96 (m, 1H, T_C); 7.85-7.81 (m, 3H, T_D+P_a); 7.55 (m, 2H, $T_{55''}$); 7.46 (d, 1H, P_3, J=8.1Hz); 7.26 (d, 2H, T_b, J=9.1Hz); 7.14 (d, 2H, P_b, J=9.1Hz); 6.62 (s, 2H, P_m); 3.94 (s, 3H, T_{MeO}); 3.90 (s, 3H, P_{MeO}); 1.17 (s, 6H, Me^o). Me^p is hidden behind the residual solvent peak. *ES MS m/z (calc)*: 460.633 (460.631, [M – CH_3SOCH_3 - $2PF_6$]$^{2+}$); 499.643 (499.638, [M – 2 PF_6]$^{2+}$); 1144.244 (1144.241, [M - PF_6]$^+$). *UV-vis*: λ_{max} in DMSO: ~437 nm (S-bonded); ~490 nm (O-bonded).

IV. Chapter 4: inclusion of a Ru(terpy)(phen)(L)$^{2+}$ complex in molecular macrocycles with a photoswitchable shape

In order to avoid any interference with light, all the following manipulations were done in the dark.

IV.1. Synthesis of RCM precursors

IV.1.a. Deprotection of the methoxy groups

51 mg (39 μmol) of [**37**][PF_6]$_2$ were weighed in a Schlenk flask, put under argon, dissolved with 3 mL of dry dichloromethane and cooled to –78°C. 1.40 mL (1.40 mmol) of 1M boron tribromide in DCM were added via a syringe at –78°C. The mixture was stirred for 1.5 hour at –78°C and 1 hour at 15°C. 2 mL of water and 2 mL of acetone were added, the solution was stirred at RT for 5 minutes, the organic solvents were evaporated, acetone was added and the complex was precipitated with KPF_6. The solid was filtered, washed with water and recovered with acetone. Yield in [**41**][PF_6]$_2$: 50 mg (100%).

Characterization of $\mathbf{41_{th}}^{2+}$: *^1H NMR 500MHz :* δ (ppm) in acetone-d6*:* 9.26 (d, 1H, P_7, J=1.8Hz); 9.00 (d, 1H, P_9, J=1.8Hz); 8.96 (s, 2H, $T_{3'5'}$); 8.95 (d, 2H, $T_{33''}$, J=8.1Hz); 8.77 (d, 1H, P_4, J=8.1Hz); 8.62 (d, 1H, P_6, J=8.8Hz); 8.48 (d, 1H, P_5, J=8.8Hz); 8.33 (s, 1H, T_A); 8.24 (td, 2H, $T_{44''}$, J=7.7,1.5Hz); 8.15-8.13 (m, 3H, T_E+$T_{66''}$); 7.90 (td, 1H, PY_p); 7.85 (m, 1H, T_C); 7.79 (d, 2H, PY_o, J=5.1Hz); 7.75 (t, 1H, T_D); 7.70

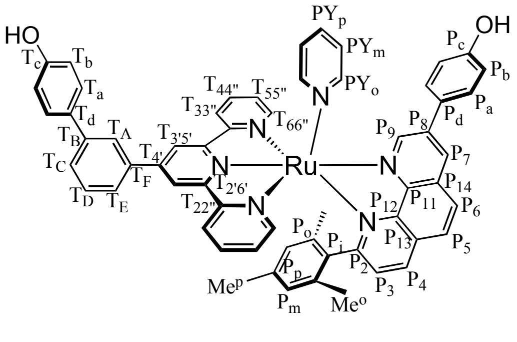

(d, 2H, T_a, J=8.8Hz); 7.66 (d, 2H, P_a, J=8.4Hz); 7.52 (m, 2H, $T_{55"}$); 7.44 (d, 1H, P_3, J=8.1Hz); 7.33 (dd, 2H, PY_m); 7.03 (d, 2H, T_b, J=8.8Hz); 7.01 (d, 2H, P_b, J=8.8Hz); 6.63 (s, 2H, P_m); 2.03 (s, 3H, Me^p); 0.99 (s, 6H, Me^o). *^{13}C NMR 500MHz :* δ (ppm) in acetone-d6*:* 168.4 (P_2); 160.8 ($T_{22"}$); 159.8 (P_c); 158.8 ($T_{2'6'}$); 158.4 (T_c); 154.3 ($T_{66"}$); 153.1 (PY_o); 151.8 (P_7); 149.6 (P_{12}); 146.7 (P_{11}); 143.2 (T_F); 139.4 ($T_{44"}$); 139.4 (PY_p); 138.8 (P_4); 137.8 ($T_{4'}$); 137.8 (T_B); 133.4 (P_9); 132.8 (P_{13}); 132.2 (T_d); 130.7 (T_D); 130.6 (P_{14}); 129.8 (P_a); 129.5 ($T_{55"}$); 129.4 (P_5); 129.2 (T_C); 129.2 (T_a); 128.9 (P_6); 128.9 (P_8); 128.3 (P_3); 127.5 (P_d); 127.3 (PY_m); 126.3 (T_E); 126.1 ($T_{33"}$); 125.9 (T_A); 122.0 ($T_{3'5'}$); 117.1 (P_b); 116.5 (T_b); 21.4 (Me^p); 19.3 (Me^o). *UV-visible*: λ_{max} (ε in L.mol^{-1}.cm^{-1}) in acetone: 485.5 nm (7390). *ES MS m/z (calc)*: 486.137 (486.136, $[M - 2\ PF_6]^{2+}$).

Characterization of **41**$_{photo}^{2+}$: *^{1}H NMR 500MHz :* δ (ppm) in CD_2Cl_2: 8.84 (d, 1H, P_4, J=7.8Hz); 8.55 (s, 2H, $T_{3',5'}$); 8.51 (d, 2H, $T_{33"}$, J=7.8Hz); 8.36 (d, 1H, P_7, J=2.0Hz); 8.35 (d, 1H, P_5, J=9.0Hz); 8.17 (d, 1H, P_6, J=8.4Hz); 8.07 (td, 2H, $T_{44"}$, J=7.8,1.5Hz); 8.02 (m, 1H, T_A, J=1.5Hz); 7.88 (d, 1H, P_3, J=8.4Hz); 7.84 (m, 3H, T_E+$T_{66"}$); 7.72 (m, 1H, T_C); 7.65-7.63 (m, 2H, T_D+P_9); 7.61 (d, 2H, T_a, J=9.0Hz); 7.42-7.38 (m, 3H, $T_{55"}$+PY_p); 7.09 (d, 2H, P_a, J=8.4Hz); 6.94 (d, 2H, T_b, J=8.4Hz); 6.92 (d, 2H, PY_o, J=5.4Hz); 6.81 (d, 2H, P_b, J=8.4Hz); 6.68 (dd, 2H, PY_m); 6.38 (s, 2H, P_m); 6.09 (s, 1H, OH_T); 5.63 (s, 1H, OH_P); 2.02 (s, 6H, Me^o); 2.01 (s, 3H, Me^p). *^{13}C NMR 500MHz* : δ (ppm) in CD_2Cl_2 (assignments according to HSQC and HMBC 2D ^{1}H-^{13}C HETCORR experiments): 168.8 (P_2); 157.9 ($T_{22"}$); 157.7 (P_c); 156.3 (T_c); 153.5 ($T_{66"}$); 150.6 (PY_o); 149.8 ($T_{4'}$); 149.0 (P_9); 148.9 (P_{11}); 147.9 (P_{12}); 142.4 (T_B); 139.8 ($T_{44"}$); 138.7 (P_4); 138.5 (P_8); 136.3 (T_F); 135.7 (PY_p); 133.4 (P_7); 132.2 (T_d); 131.2 (P_{14}); 130.2 (P_{13}); 130.2 (T_D); 129.8 (P_3); 129.1 (P_5); 128.9 ($T_{55"}$); 128.9 (T_C); 128.7 (P_a); 128.5 (T_a); 128.1 (P_6); 126.7 (P_d); 125.7 (T_E); 125.7 (PY_m); 125.7 ($T_{33"}$); 125.5 (T_A); 121.6 ($T_{3'5'}$); 116.7 (P_b); 116.1 (T_b); 30.6 (Me^o); 21.0 (Me^p). $T_{2',6'}$ could not be found. *ES MS m/z (calc)*: 486.16 (486.14, $[M - 2\ PF_6]^{2+}$). *UV-vis*: λ_{max} (ε in L.mol^{-1}.cm^{-1}) in acetone: 481 nm (11000).

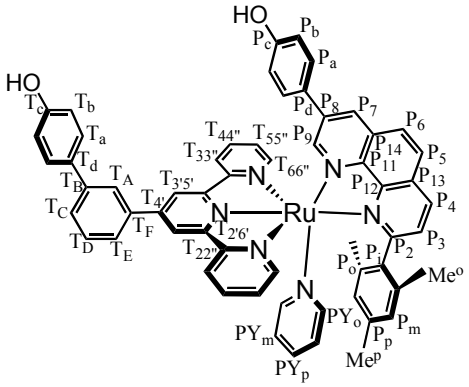

IV.1.b. Williamson reaction with the allyl alkane chain

53 mg (42 µmol) of [**41**][PF_6]$_2$ were weighed in a 50 mL flask. 79 mg (570 µmol) of potassium carbonate, 174 mg (794 µmol) of 10-bromodec-1-ene and 10mL of dimethylformamide were added, the reaction flask was put under argon and stirred at 60°C for 8 hours. DMF was removed under vacuum, acetone was added and the complex was precipitated by the addition of KPF_6. The complex was filtered, washed with water, recovered with acetone, precipitated with

diethylether, filtered and washed with diethylether in order to remove the excess of the chain. The complex was recovered with acetone and dried. Yield in [**42**][PF_6]$_2$: 65 mg (>99%).

Characterization of **42$_{th}$**$^{2+}$: *^{1}H NMR 500MHz* : δ (ppm) in acetone-d6: 9.27 (d, 1H, P_7, J=1.8Hz); 9.00 (d, 1H, P_9, J=1.8Hz); 8.93 (s, 2H, $T_{3',5'}$); 8.92 (d, 2H, $T_{33"}$, J=8.1Hz); 8.75 (d, 1H, P_4, J=8.1Hz); 8.61 (d, 1H, P_6, J=8.8Hz); 8.47 (d, 1H, P_5, J=8.8Hz); 8.37 (s, 1H, T_A); 8.22 (td, 2H, $T_{44"}$, J=7.7,1.5Hz); 8.17 (m, 1H, T_E); 8.11 (m, 2H, $T_{66"}$); 7.90-7.86 (m, 2H, T_C+PY_p); 7.80-7.74 (m, 7H, PY_o+T_a+P_a+T_D); 7.51 (m, 2H, $T_{55"}$); 7.42 (d, 1H, P_3, J=8.1Hz); 7.32 (dd, 2H, PY_m); 7.12 (d, 2H, T_b, J=8.8Hz); 7.10 (d, 2H, P_b, J=8.8Hz); 6.63 (s, 2H, P_m); 5.87-5.76 (m, 2H, ι_T+ι_P); 5.02-4.89 (m, 4H, κ_T+κ_P); 4.11 (t, 2H, α_T, J=6.6Hz); 4.07 (t, 2H, α_P, J=6.6Hz); 2.05-2.03 (m, 4H, θ_T+θ_P); 2.03 (s, 3H, Me^p); 1.85-1.78 (m, 4H, β_T+β_P); 1.54-1.47 (m, 4H, γ_T+γ_P); 1.45-1.28 (m, $\delta_T\delta_P\varepsilon_T\varepsilon_P\zeta_T\zeta_P\eta_T\eta_P$); 0.98 (s, 6H, Me^o). *^{13}C NMR 500MHz* : δ (ppm) in acetone-d6 (assignments according to HSQC and HMBC 2D ^{1}H-^{13}C HETCORR experiments): 172.0 (P_2); 164.7 (P_c); 164.1 ($T_{22"}$); 163.7 (T_c); 162.0 ($T_{2'6'}$); 157.8 ($T_{66"}$); 156.5 (PY_o); 155.3 (P_7); 152.9 (P_{12}); 151.6 (T_F); 150.4 (P_{11}); 143.3 (ι_T+ι_P); 143.1 ($T_{44"}$); 142.9 (PY_p); 142.3 (P_4); 141.4 ($T_{4'}$); 137.2 (P_9); 136.7 (T_B); 136.5 (T_d); 134.3 (T_D); 134.1 (P_{13}); 133.3 (P_a); 132.9 ($T_{55"}$); 132.8 (P_5); 132.7 (T_C); 132.7 (T_a); 132.6 (P_d); 132.5 (P_6); 132.0 (P_8); 131.8 (P_3); 131.6 (P_{14}); 130.8 (PY_m); 130.2 (T_E); 129.8 ($T_{33"}$); 129.6 (T_A); 125.5 ($T_{3'5'}$); 119.8 (P_b); 119.2 (T_b); 117.9 (κ_T+κ_P); 72.2 (α_T+α_P); 37.8 (θ_T+θ_P); 33.5 (δ_T+δ_P); 33.5 (ε_T+ε_P); 33.5 (ζ_T+ζ_P); 33.5 (η_T+η_P); 33.4 (β_T+β_P); 30.0 (γ_T+γ_P); 25.0 (Mẽ); 22.9 (s, 6H, Mẽ). *ES MS m/z (calc)*: 624.29 (624.28, [M – 2 PF_6]$^{2+}$). *UV-visible*: λ_{max} (ε in L.mol^{-1}.cm^{-1}) in acetone: 486 nm (15900).

Characterization of **42$_{photo}$**$^{2+}$: *^{1}H NMR 500MHz* : δ (ppm) in acetone-d6: 9.13 (s, 2H, $T_{3',5'}$); 9.12 (d, 1H, P_4, J=7.8Hz); 8.90 (d, 2H, $T_{33"}$, J=7.8Hz); 8.77 (d, 1H, P_7, J=2.0Hz); 8.57 (d, 1H, P_5, J=9.0Hz); 8.37 (d, 1H, P_6, J=8.4Hz); 8.30-8.28 (m, 3H, T_A+$T_{66"}$); 8.19 (td, 2H, $T_{44"}$, J=7.8,1.5Hz); 8.07 (d, 1H, P_3, J=8.4Hz); 8.03 (m, 1H, T_E); 8.02 (d, 2H, P_9, J=2.0Hz); 7.84 (d, 1H, T_C, J=8.5Hz); 7.73 (d, 2H, T_a, J=9.0Hz); 7.70 (t, 1T, T_D, J=7.8Hz); 7.59 (t, 1H, PY_p, J=7.8Hz); 7.55 (m, 2H, $T_{55"}$); 7.29 (d, 2H, P_a, J=8.4Hz); 7.27 (d, 2H, PY_o, J=5.4Hz); 7.08 (d, 2H, T_b, J=8.4Hz); 6.86 (d, 2H, P_b, J=8.4Hz); 6.85 (t, 2H, PY_m, J=7.2Hz); 6.43 (s,

2H, P_m); 5.86-5.74 (m, 2H, $\iota_P+\iota_T$); 5.02-4.87 (m, 4H, $\kappa_P+\kappa_T$); 4.08 (t, 2H, α_T, J=6.6Hz); 3.92 (t, 2H, α_P, J=6.4Hz); 2.16 (s, 6H, Me^o); 2.03 (s, 3H, Me^p); 2.03-1.95 (m, 4H, $\theta_T+\theta_P$); 1.82 (q, 2H, β_T, J=6.6Hz); 1.69 (q, 2H, β_P, J=6.6Hz); 1.52 (q, 2H, γ_T, J=7.3Hz); 1.44-1.26 (m, 18H, $\gamma_P\varepsilon_T\varepsilon_P\delta_T\delta_P\zeta_T\zeta_P\eta_T\eta_P$). *^{13}C NMR 500MHz* : δ (ppm) in acetone-d6 (assignments according to HSQC and HMBC 2D ^{1}H-^{13}C HETCORR experiments): 169.5 (P_2); 161.3 (P_c); 160.3 (T_c); 159.3 ($T_{2'6'}$); 159.2 ($T_{22''}$); 155.2 ($T_{66''}$); 152.1 (PY_o); 149.9 (P_9); 149.7 ($T_{4'}$); 149.0 (P_{12}); 147.6 (P_{11}); 142.7 (T_F); 139.9 ($T_{44''}$); 139.9 ($\iota_P+\iota_T$); 139.4 (P_4); 138.4 (P_8); 137.6 (T_B); 136.4 (PY_p); 133.9 (P_7); 132.9 (T_d); 131.9 (P_{14}); 131.5 (P_{13}); 130.9 (T_D); 130.7 (P_3); 129.8 (P_5); 129.6 ($T_{55''}$); 129.4 (P_a); 129.2 (T_C); 129.0 (T_a); 128.8 (P_6); 127.6 (P_d); 126.8 (T_E); 126.6 (PY_m); 126.6 ($T_{33''}$); 126.4 (T_A); 122.7 ($T_{3'5'}$); 116.1 (P_b); 115.7 (T_b); 114.7 ($\kappa_P+\kappa_T$); 68.7 (α_P); 68.7 (α_T); 29.5 -30.5 (δ_P-η_P + δ_T-η_T); 34.4 ($\theta_P+\theta_T$); 30.1 (β_T); 29.7 (β_P); 26.9 (γ_P); 26.4 (γ_T); 21.3 (Me^o); 20.7 (Me^p). *ES MS m/z (calc)*: 624.2772 (624.2772, $[M - 2\ PF_6]^{2+}$). *UV-visible*: λ_{max} (ε in $L.mol^{-1}.cm^{-1}$) in acetone: 482 nm (10800).

IV.1.c. Preparation of 8-bromo-3,6-dioxaoctyl allyl ether

8-allyloxy-3,6-dioxaoctanol: 11.2 g (200 mmol) of potassium hydroxyide were ground in a mortar and put in a 100 mL reaction flask. 26.7 mL (30 g, 200 mmol) of triethylene glycol were slowly added to the solid base under stirring at 60°C. 17.4 mL (200 mmol) of allyl bromide were then added dropwise to the reddish suspension. Leave at 60°C for 3h after the end of the addition. Add 100 mL water and 100 mL toluene, extract three times the water phase with toluene in order to remove the bis-allyl product. Extract the aqueous phase with dichloromethane to isolate the analytically pure mono-allyl alcohol. Yield: 15.0 g (40%).

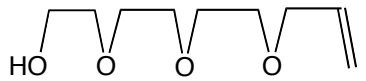

8-allyloxy-3,6-dioxa-1-mesyloctanol: 15.0 g (79.1 mmol) of the alcohol were dissolved in 200 mL distilled dichloromethane and 65 mL of distilled triethylamine. The mixture was cooled to 0°C and 8.0 mL (103 mmol) of mesyl chloride were added dropwise to the reaction flask under argon. The solution was stirred at 0°C for 8h and quenched at 0°C with 50 mL water. It is important that during quenching the internal temperature did not exceed 5°C. The solution was transferred to a separating funnel and washed successively with 10% hydrochloric acid, sodium hydrogenocarbonate, and brine. The dichloromethane phase was dried under sodium sulfate and evaporated to dryness to yield 19.0 g of the mesylate. Yield: 89%.

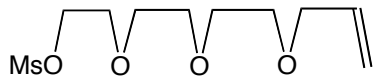

8-bromo-3,6-dioxaoctyl allyl ether: 19.0 g (71 mmol) of the mesylate were dissolved with

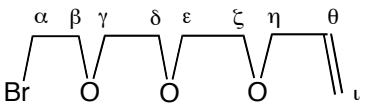

61 g (708 mmol) of lithium bromide in 300 mL acetone. The solution was refluxed under argon for 3h and evaporated. Water was added and extracted with dichloromethane. The organic phases were assembled and washed with water and brine. Evaporation yielded 15.3 g of analytically pure product (85%).

^{1}H NMR 300MHz : δ (ppm) in $CDCl_3$: 5.96-5.85 (m, 1H, θ); 5.30-5.16 (m, 2H, I); 4.04-4.01 (m, 2H, η); 3.81 (t, 2H, α); 3.69-3.60 (m, 8H, γ+δ+ε+ζ); 3.47 (t, 2H, β).

IV.1.d. Williamson reaction with 8-bromo-3,6-dioxaoctyl allyl ether

43$_{th}^{2+}$: 35 mg (28 μmol) of [**41$_{th}$**][PF_6]$_2$ were weighed in a 50 mL flask. 38 mg (280 μmol) of potassium carbonate, 140 mg (560 μmol) of 8-bromo-3,6-dioxaoctyl allyl ether and 10 mL of dimethylformamide were added, the reaction flask was put under argon and stirred at 60°C for 8 hours. DMF was removed under vacuum, acetone was added and the complex was precipitated by the addition of KPF_6. The complex was filtered, washed with water, recovered with acetone and purified over 200 mL of fine silica gel (eluent acetone / water / KNO_3 100:5:0.1). Yield: 39 mg of complex [**43$_{th}$**][PF_6]$_2$ (87%).

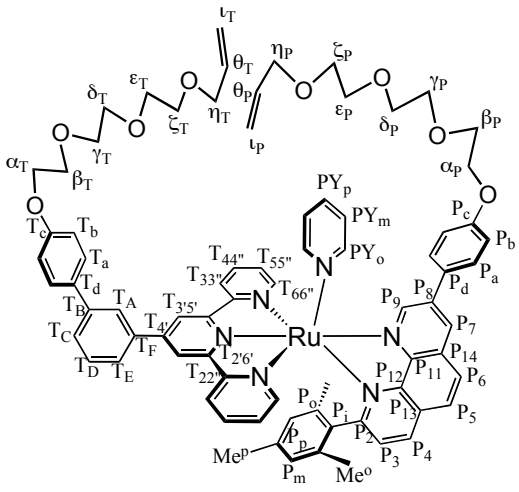

^{1}H NMR 500MHz : δ (ppm) in acetone-d6: 9.30 (d, 1H, P_7, J=1.8Hz); 9.07 (d, 1H, P_9, J=1.8Hz); 8.96 (s, 2H, $T_{3'5'}$); 8.94 (d, 2H, $T_{33"}$, J=8.1Hz); 8.77 (d, 1H, P_4, J=8.1Hz); 8.62 (d, 1H, P_6, J=8.8Hz); 8.48 (d, 1H, P_5, J=8.8Hz); 8.37 (s, 1H, T_A); 8.24 (td, 2H, $T_{44"}$, J=7.7,1.5Hz); 8.17 (m, 1H, T_E); 8.13 (m, 2H, $T_{66"}$); 7.90-7.87 (m, 2H, T_D+PY_p); 7.83 (m, 1H, T_C); 7.80-7.74 (m, 6H, PY_o+T_a+P_a); 7.51 (m, 2H, $T_{55"}$); 7.44 (d, 1H, P_3, J=8.1Hz); 7.32 (dd, 2H, PY_m); 7.14 (d, 2H, T_b, J=8.8Hz); 7.12 (d, 2H, P_b, J=8.8Hz); 6.63 (s, 2H, P_m); 5.94-5.84 (m, 2H, θ_T+θ_P); 5.28-5.22 (m, 2H, *cis*- ι_T+ι_P); 5.12-5.08 (m, 2H, *trans*- ι_T+ι_P); 4.25-4.20 (m, 4H, α_T+α_P); 4.00-3.96 (m, 4H, η_T+η_P); 3.89-3.83 (m, 4H, β_T+β_P); 3.71-3.55 (m, 16H, $\gamma_T\gamma_P\delta_T\delta_P\varepsilon_T\varepsilon_P\zeta_T\zeta_P$); 2.04 (s, 3H, Me^p); 0.99 (s, 6H, Me^o). *^{13}C NMR 500MHz* : δ (ppm) in acetone-d6 (assignments according to HSQC and HMBC 2D ^{1}H-^{13}C HETCORR experiments): 168.5 (P_2); 161.4 (P_c); 160.7 ($T_{22"}$); 160.1 (T_c); 158.7 ($T_{2'6'}$); 154.4 ($T_{66"}$); 153.0 (PY_o); 151.9 (P_9); 149.6 (P_{12}); 148.4 ($T_{4'}$); 147.1 (P_{11}); 140.6 (P_p); 139.6 (PY_p); 139.6 ($T_{44"}$); 139.5 (T_B); 139.0 (P_8); 138.9 (P_4); 138.1 (T_F); 136.5 (θ_P); 136.5 (θ_T); 135.9 (P_i); 133.8 (P_{14}); 133.7 (P_7); 133.6 (T_d); 132.9 (P_{13}); 130.9 (T_D); 129.7 (P_a); 129.4 (P_6); 129.4 ($T_{55"}$); 129.3 (T_C); 129.2 (P_5); 129.2 (P_m); 129.2 (T_a); 129.0 (P_d); 128.7 (P_3); 127.3 (PY_m); 126.6 (T_E); 126.2 ($T_{33"}$); 126.2 (T_A);

122.1 ($T_{3'5'}$); 116.3 (P_b); 116.3 (ι_P); 116.3 (ι_T); 115.9 (T_b); 72.6 (η_P); 72.6 (η_T); 70.5-71.3 (γ_P-ζ_P+ γ_T-ζ_T); 70.5 (β_P); 70.5 (β_T); 68.5 (α_P); 68.5 (α_T); 21.4 (Me^p); P_o and Me^o were not measured. *ES MS m/z (calc)*: 658.246 (658.247, $[M\text{-}2PF_6]^{2+}$). *UV-visible*: λ_{max} (ε in $L.mol^{-1}.cm^{-1}$) in acetone: 486 nm (12000).

43$_{photo}^{2+}$: 50.4 mg (40 μmol) of [**41**$_{photo}$][PF_6]$_2$, 63 mg (456 μmol) of K_2CO_3 and 107 mg (422 mmol) of 3,6-dioxa-8-bromooctyl allyl ether were weighed in a flask. 8 mL of dimethylformamide were added, the reaction mixture was put under argon and stirred at 60°C for 8 hours. DMF was removed by high vacuum, acetone was added followed by KPF_6 until precipitation occurred. The complex was filtered, washed with water, recovered with acetone, dried and purified over silica gel (eluent acetone / water / KNO_3 100:5:0.1). The main fraction was precipitated by KPF_6, washed with water, recovered with acetone and dried to afford 58.3 mg of precursor [**43**$_{photo}$][PF_6]$_2$ (91%).

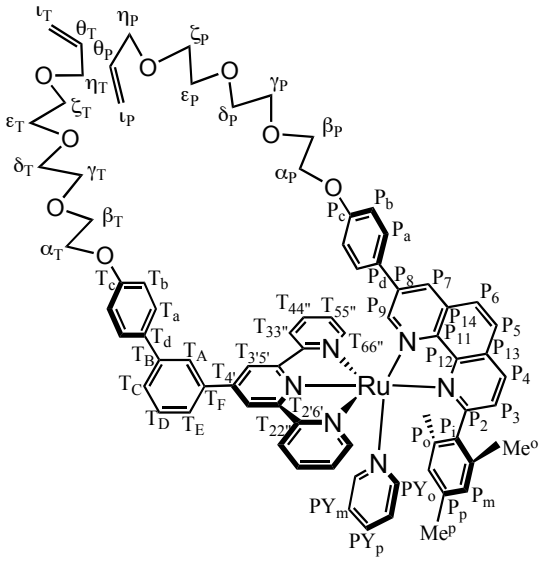

^{1}H NMR 500MHz : δ (ppm) in acetone-d6: 9.15 (s, 2H, $T_{3',5'}$); 9.13 (d, 1H, P_4, J=8.0Hz); 8.91 (d, 2H, $T_{33''}$, J=8.1Hz); 8.79 (d, 1H, P_9, J=1.8Hz); 8.58 (d, 1H, P_5, J=8.8Hz); 8.39 (d, 1H, P_6, J=8.8Hz); 8.31 (m, 2H, $T_{66''}$); 8.29 (t, 1H, T_A, J=1.8Hz); 8.20 (td, 2H, $T_{44''}$, J=7.7,1.5Hz); 8.09 (d, 1H, P_3, J=8.1Hz); 8.04 (d, 1H, P_9, J=2.0Hz); 8.03 (m, 1H, T_E); 7.86 (m, 1H, T_C); 7.74 (d, 2H, T_a, J=8.9Hz); 7.71 (m, 1H, T_D); 7.59 (tt, 1H, PY_p, J=7.7,1.5Hz); 7.55 (m, 2H, $T_{55''}$); 7.31 (d, 2H, P_a, J=8.9Hz); 7.28 (m, 2H, PY_o); 7.11 (d, 2H, T_b, J=8.9Hz); 6.89 (d, 2H, P_b, J=8.8Hz); 6.85 (m, 2H, PY_m); 6.43 (s, 2H, P_m); 5.93-5.80 (m, 2H, θ_T+θ_P); 5.26 (ddd, 1H, *trans*-ι_T, J=17.3,3.8,1.7Hz); 5.20 (ddd, 1H, *trans*-ι_P, J=17.3,3.8,1.7Hz); 5.10 (ddd, 1H, *cis*-ι_T, J=10.5,2.1,1.5Hz); 5.05 (ddd, 1H, *cis*-ι_P, J=10.5,2.1,1.5Hz); 4.22 (m, 2H, α_T); 4.06 (m, 2H, α_P); 3.99 (m, 2H, η_T); 3.93 (m, 2H, η_P); 3.87 (m, 2H, β_T); 3.75 (m, 2H, β_P); 3.69 (m, 2H, γ_T); 3.64 (m, 2H, δ_T); 3.62 (m, 2H, ε_T); 3.59 (m, 2H, γ_P); 3.57 (m, 2H, ζ_T); 3.56 (m, 2H, δ_P); 3.54 (m, 2H, ε_P); 3.51 (m, 2H, ζ_P); 2.16 (s, 6H, Me^o); 2.03 (s, 3H, Me^p). *^{13}C NMR 500MHz* : δ (ppm) in acetone: 169.5 (P_2); 161.3 (P_c); 160.3 ($T_{2'6'}$); 160.2 (T_c); 159.4 ($T_{22''}$); 155.1 ($T_{66''}$); 152.3 (PY_o); 150.0 (P_9); 149.8 ($T_{4'}$); 149.0 (P_{12}); 147.4 (P_{11}); 142.9 (T_B); 140.1 ($T_{44''}$); 139.4 (P_4); 138.4 (P_8); 137.6 (T_F); 136.4 (PY_p); 136.2 (θ_P+θ_T); 134.1 (P_7); 133.2 (T_d); 131.8 (P_{14}); 131.6 (P_{13}); 130.9 (T_D); 130.7 (P_3); 129.9 (P_5); 129.6 ($T_{55''}$); 129.5 (P_a); 129.5 (PY_m); 129.4 (T_C); 129.1 (T_a); 128.9 (P_6); 127.8 (P_d); 126.8 (T_E); 126.5 ($T_{33''}$); 126.5 (T_A); 122.7 ($T_{3'5'}$); 116.2 (P_b);

116.2 (ι_P+ι_T); 115.9 (T_b); 72.3 (η_P+η_T); 71.3-71.1 (γ_T-ε_T + γ_P-ε_T); 70.3 (β_T); 70.3 (ζ_T+ζ_P); 70.1 (β_P); 68.5 (α_P+α_T); 21.4 (Me^o); 20.8 (Me^p). *ES MS m/z (calc)*: 658.2470 (658.2468, $[M - 2\ PF_6]^{2+}$); 1461.451 (1461.458, $[M - PF_6]^+$). *UV-visible*: λ_{max} (ε in $L.mol^{-1}.cm^{-1}$) in acetone: 481.5 nm (12800).

IV.2. Grubbs olefin metathesis reactions

IV.2.a. On thermal isomers

44_{th}^{2+}: 17 mg of [**42_{th}**][PF_6]$_2$ and 13 mg (16 μmol) of Grubbs' 1st generation catalyst were

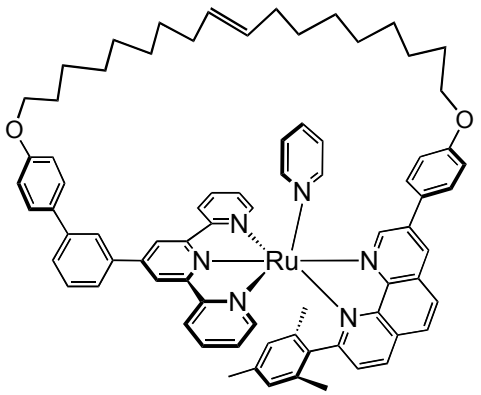

dissolved in dichloromethane and stirred under argon in the dark for 7 days. Acetone was added along with aqueous potassium hexafluorophosphate, and removal of the organic solvents led to precipitation of the complex. The solid was filtered, washed with water and recovered with acetone. Chromatography over silica gel (acetone / water / KNO_3 100:5:0.1 to 60:5:1) was undertaken in order to separate, in this order, traces of the remaining starting material, the monomer [**44_{th}**][PF_6]$_2$ (3.6 mg, 21% yield) and the corresponding dimer (4.3 mg, 25% yield).

ES MS m/z (calc): for the monomer 610.31 (610.26, $[M - 2\ PF_6]^{2+}$); for the dimer 610.31 (610.26, $[M - 4\ PF_6]^{4+}$); 862.06 (862.00, $[M - 3\ PF_6]^{3+}$); 1365.6 (1365.5, $[M - 2\ PF_6]^{2+}$).

45_{th}^{2+}: 31 mg (19 μmol) of [**43_{th}**][PF_6]$_2$, 13 mg (16 μmol) of Grubbs' 1st generation catalyst were

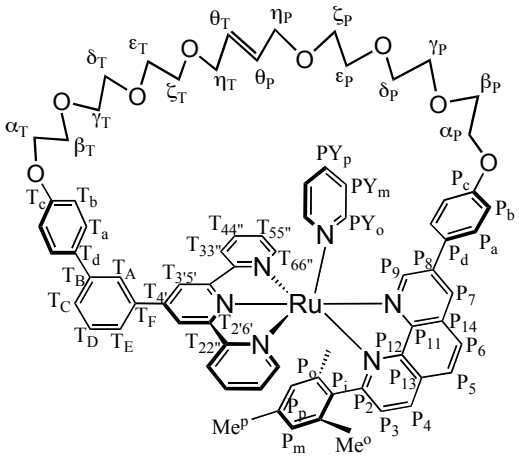

weighed in a flask and put under argon. 100 mL of dry dichloromethane were added in the dark and the solution was stirred for 5 days and flushed with argon regularly. The DCM was removed under vacuum, acetone was added, the complex was precipitated with KPF_6, filtered, washed with water, recovered with acetone and put on 200 mL fine silica gel for purification (eluent: acetone / water / KNO_3 80:5:0.3). The monomer was the less polar fraction and the dimer the most polar. Yield: 8.1 mg for the monomer [**45_{th}**][PF_6]$_2$ (26%) and 8.7 mg for the corresponding dimer (28%).

^{1}H NMR 500MHz : δ (ppm) in acetone-d6: 9.26 (d, 1H, P_7, J=1.8Hz); 8.91 (d, 2H, $T_{33"}$, J=8.1Hz); 8.84 (s, 2H, $T_{3'5'}$); 8.81 (d, 1H, P_9, J=1.8Hz); 8.80 (d, 1H, P_4, J=8.1Hz); 8.63 (d, 1H, P_6, J=8.8Hz); 8.50 (d, 1H, P_5, J=8.8Hz); 8.24 (td, 2H, $T_{44"}$, J=7.7,1.5Hz); 8.19 (m, 1H, T_E); 8.08 (m, 2H, $T_{66"}$); 7.95 (s, 1H, T_A); 7.89-7.85 (m, 2H, T_C+PY_p); 7.78 (m, 1H, T_D); 7.73 (d, 2H, PY_o, J=5.5Hz); 7.68 (d, 2H, T_a, J=9.0Hz); 7.66 (d, 2H, P_a, J=9.0Hz); 7.53-7.49 (m, 3H, P_3+$T_{55"}$); 7.29 (dd, 2H, PY_m); 7.14 (d, 2H, T_b, J=8.8Hz); 7.13 (d, 2H, P_b, J=8.8Hz); 6.67 (s, 2H, P_m); 5.66 (m, 2H, θ_T+θ_P); 4.28 (m, 4H, α_T+α_P); 3.87 (m, 4H, η_T+η_P); 3.80,3.76 (m, 2×2H, β_T and β_P); 3.62 (m, 2H, γ_T); 3.56 (m, 2H, γ_P); 3.55 (m, 2H, δ_T); 3.50 (m, 2H, δ_P); 3.49 (m, 2H, ε_T); 3.46 (m, 2H, ε_P); 3.46 (m, 2H, ζ_T); 3.43 (m, 2H, ζ_P); 2.14 (s, 3H, Me^p); 0.95 (s, 6H, Me^o). *^{13}C NMR 500MHz* : δ (ppm) in acetone-d6 (assignments according to HSQC and HMBC 2D ^{1}H-^{13}C HETCORR experiments): 168.3 (P_2); 161.2 (P_c); 160.4 ($T_{22"}$); 160.2 (T_c); 158.7 ($T_{2'6'}$); 154.5 ($T_{66"}$); 153.1 (PY_o); 152.1 (P_9);149.7 (P_{12}); 148.8 ($T_{4'}$); 146.9 (P_{11}); 142.8 (T_B); 140.6 (P_p); 139.6 (PY_p); 139.6 ($T_{44"}$); 138.9 (P_8); 138.8 (P_4); 138.8 (T_F); 136.0 (P_o); 133.6 (T_d); 133.0 (P_7); 132.8 (P_{14}); 130.8 (P_i); 130.7 (T_D); 130.6 (P_{13}); 130.0 (θ_P); 130.0 (θ_T); 129.6 (P_a); 129.5 (P_5); 129.4 ($T_{55"}$); 129.0 (P_6); 129.0 (P_d); 129.0 (P_m); 129.0 (T_a); 128.3 (T_C); 128.1 (P_3); 127.9 (T_A); 127.3 (PY_m); 126.3 (T_E); 126.1 ($T_{33"}$); 122.8 ($T_{3'5'}$); 116.9 (P_b); 116.5 (T_b); 71.5 (η_P); 71.5 (η_T); 71.3 (γ_P); 71.3 (γ_T); 70.9 (δ_P+ε_P); 70.9 (δ_T+ε_T); 70.5 (β_T); 70.3 (β_P); 69.9 (ζ_P); 69.0 (ζ_T); 68.9 (α_P); 68.9 (α_T); 21.5 (Me^p); 19.2 (Me^o). *ES MS m/z (calc)*: 644.2317 (644.2311, $[M - 2\ PF_6]^{2+}$); 1433.44 (1433.43, $[M - PF_6]^+$).

IV.2.b. On photochemical isomers

44$_{photo}$ $^{2+}$: 157 mg (102 μmol) of [**42$_{photo}$**][PF_6]$_2$ and 35 mg (42 μmol) of Grubbs' 1st generation catalyst were weighed in a 100 mL flask and put under argon. 150 mL of dry dichloromethane were cannulated and the solution was stirred in the dark at room temperature for 60 hours. During the course of the reaction, the solution was flushed three times with argon in order to remove ethylene. The DCM was evaporated, acetone was added, the complex was precipitated with KPF_6, filtered, washed with water, recovered with acetone and purified over 300 mL of fine silica gel (eluent : acetone / water / KNO_3 80:5:0.5). Yield: 126 mg of [**44$_{photo}$**][PF_6]$_2$ (78%).

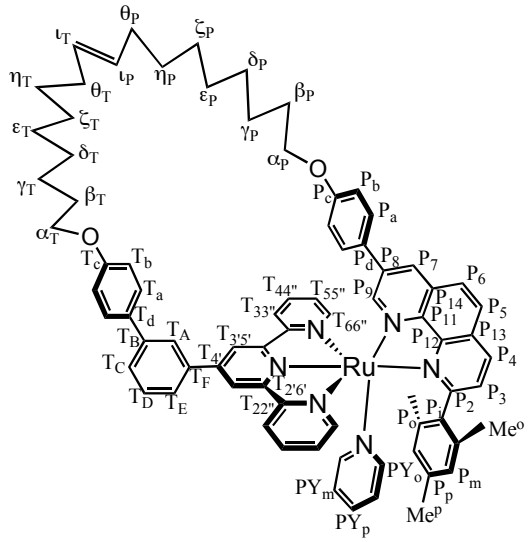

8.03 (m, 1H, T_E); 8.02 (d, 2H, P_9, J=2.0Hz); 7.84 (d, 1H, T_C, J=8.5Hz); 7.73 (d, 2H, T_a, J=9.0Hz); 7.70 (t, 1H, T_D, J=7.8Hz); 7.59 (t, 1H, PY_p, J=7.8Hz); 7.55 (m, 2H, $T_{55"}$); 7.29 (d, 2H, P_a, J=8.4Hz); 7.27 (d, 2H, PY_o, J=5.4Hz); 7.08 (d, 2H, T_b, J=8.4Hz); 6.86 (d, 2H, P_b, J=8.4Hz); 6.85 (t, 2H, PY_m, J=7.2Hz); 6.43 (s, 2H, P_m); 5.86-5.74 (m, 2H, $\iota_P+\iota_T$); 5.02-4.87 (m, 4H, $\kappa_P+\kappa_T$); 4.08 (t, 2H, α_T, J=6.6Hz); 3.92 (t, 2H, α_P, J=6.4Hz); 2.16 (s, 6H, Me^o); 2.03 (s, 3H, Me^p). *^{13}C NMR 500MHz* : δ (ppm) in acetone-d6 (assignments according to HSQC and HMBC 2D ^1H-^{13}C HETCORR experiments): 168.9 (P_2); 160.7 (P_c); 159.7 (T_c); 159.1 ($T_{22"}$); 158.5 ($T_{2'6'}$); 154.4 ($T_{66"}$); 151.5 (PY_o); 149.3 (P_9); 148.2 (P_{12}); 146.8 (P_{11}); 141.9 (T_B); 139.5 (P_p); 139.3 ($T_{44"}$); 139.3 ($T_{4'}$); 138.6 (P_4); 137.6 (P_8); 137.4 (T_F); 136.4 (P_i); 135.6 (PY_p); 135.4 (P_o); 133.1 (P_7); 132.3 (T_d); 131.1 (P_{14}); 130.8 (P_{13}); 130.7 ($\iota_P+\iota_T$); 130.1 (P_3); 130.1 (T_D); 129.2 (P_5); 129.0 ($T_{55"}$); 128.6 (P_a); 128.6 (P_m); 128.6 (T_C); 128.4 (T_a); 128.2 (P_6); 126.8 (P_d); 126.0 (T_A); 126.0 (T_E); 125.8 (PY_m); 125.8 ($T_{33"}$); 122.3 ($T_{3'5'}$); 115.4 (P_b); 115.1 (T_b); 68.1 (α_P); 67.7 (α_T); 32.3 ($\theta_P+\theta_T$); 28.9-29.7 (δ_P-$\eta_P+\delta_T$-η_T); 29.1 ($\beta_P+\beta_T$); 25.6 ($\gamma_P+\gamma_T$); 21.0 (Me^o); 20.1 (Me^p). *UV-visible*: λ_{max} (ε in $L.mol^{-1}.cm^{-1}$) in acetone: 482 nm (10900). *ES MS m/z (calc)*: 610.27 (610.26, $[M - 2\ PF_6]^{2+}$); 1365.51 (1365.49, $[M - PF_6]^+$).

45_{photo}^{2+}: 50 mg (31 µmol) of [**43_{photo}**][PF_6]$_2$ and 10 mg (12 µmol) of Grubbs' 1st generation catalyst were weighed in a 100 mL flask and put under argon. 50 mL of dry dichloromethane were cannulated and the solution was stirred in the dark at room temperature for 60 hours. During the course of the reaction, the solution was flushed three times with argon in order to remove ethylene. The DCM was evaporated, acetone was added, the complex was precipitated with KPF_6, filtered, washed with water, recovered with acetone and purified over 180 mL of silica gel (eluent : acetone / water / KNO_3 100:5:0.1 to 80 :5 :0.5). Yield : 41 mg of [**45_{photo}**][PF_6]$_2$ (83%).

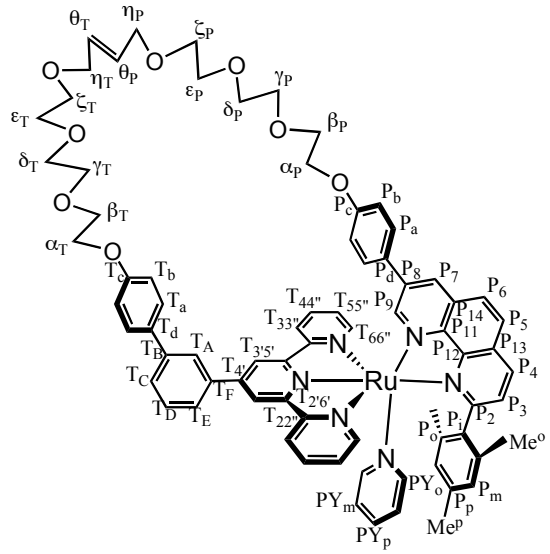

^1H NMR 500MHz : δ (ppm) in acetone-d6: 9.15 (s, 2H, $T_{3',5'}$); 9.13 (d, 1H, P_4, J=7.8Hz); 8.91 (d, 2H, $T_{33"}$, J=7.8Hz); 8.78 (d, 1H, P_7, J=2.0Hz); 8.58 (d, 1H, P_5, J=9.0Hz); 8.38 (m, 2H, T_A+P_6); 8.31 (d, 2H, $T_{66"}$, J=5.5Hz); 8.20 (td, 2H, $T_{44"}$, J=7.8,1.5Hz); 8.09 (d, 1H, P_3, J=8.4Hz); 7.98 (d, 2H, P_9, J=2.0Hz); 7.97 (m, 1H, T_E); 7.85 (d, 1H, T_C, J=8.5Hz); 7.77 (d, 2H, T_a, J=9.0Hz); 7.69 (m, 1H, T_D); 7.60 (t, 1H, PY_p); 7.55 (m, 2H, $T_{55"}$); 7.30 (d, 2H, P_a, J=8.4Hz); 7.28 (d, 2H, PY_o, J=5.4Hz); 7.13 (d, 2H, T_b, J=8.4Hz); 6.87 (d, 2H, P_b, J=8.4Hz); 6.86 (m, 2H, PY_m); 6.44 (s, 2H, P_m); 5.76 (m, 69% of 2H, $\theta_P+\theta_T$); 5.62 (m, 31% of 2H, $\theta_P+\theta_T$); 4.23 (m, 2H, α_T); 4.03 (m, 2H, α_P); 3.99 (m, 2H,

η_T); 3.93 (m, 2H, η_P); 3.88 (m, 2H, β_T); 3.72 (m, 2H, β_P); 3.69 (m, 2H, γ_T); 3.63 (m, 2H, δ_T); 3.62 (m, 2H, γ_P); 3.57 (m, 2H, δ_P); 3.56-3.52 (m, 6H, ε_T+ζ_T+ε_P); 3.49 (m, 2H, ζ_P); 2.17 (s, 6H, Me^o); 2.03 (s, 3H, Me^p). *^{13}C NMR 500MHz* : δ (ppm) in acetone: 169.5 (P_2); 161.1 (P_c); 160.1 (T_c); 159.3 ($T_{22"}$); 155.1 ($T_{66"}$); 152.3 (PY_o); 150.0 (P_9); 149.6 ($T_{4'}$); 149.0 (P_{12}); 147.4 (P_{11}); 142.9 (T_B); 139.9 (P_p); 139.8 ($T_{44"}$); 139.5 (P_4); 138.2 (P_8); 137.7 (T_F); 137.0 (P_i); 136.4 (PY_p); 135.9 (P_o); 134.0 (P_7); 133.2 (T_d); 131.8 (P_{14}); 131.3 (P_{13}); 130.8 (T_D); 130.7 (P_3); 129.9 (P_5); 129.9 (θ_P+θ_T); 129.7 ($T_{55"}$); 129.4 (P_a); 129.3 (P_m); 129.3 (T_C); 129.0 (T_a); 128.9 (P_6); 127.8 (P_d); 126.6 ($T_{33"}$); 126.6 (T_E); 126.5 (PY_m); 126.5 (T_A); 122.7 ($T_{3'5'}$); 116.2 (P_b); 116.1 (T_b); 71.5 (γ_T); 71.4 (δ_T); 71.3 (γ_P); 71.3 (η_P); 71.2 (δ_P); 71.2 (ε_T+ζ_T); 71.2 (η_T); 70.4 (β_T); 70.3 (ε_P); 70.2 (ζ_P); 70.1 (β_P); 68.6 (α_P); 68.6 (α_T); 21.4 (Me^o); 21.0 (Me^p); ($T_{2'6'}$) could not be assigned. *ES MS m/z (calc)*: 644.22 (644.23, $[M - 2\ PF_6]^{2+}$); 1433.39 (1433.43, $[M - PF_6]^+$). *UV-visible*: λ_{max} (ε in $L.mol^{-1}.cm^{-1}$) in acetone: 479.5 nm (13200).

IV.3. Reduced macrocycles

IV.3.a. Thermal isomers

46$_{th}$ $^{2+}$: 16 mg (11 μmol) of [**46$_{photo}$**][PF_6]$_2$ were dissolved in 4 mL of distilled DMSO, put under argon and heated in the dark at 140°C for 2 hours. The complex was precipitated with KPF_6, filtered, washed with water, recovered with acetone and dried. 4 mL of pyridine were added, the solution was flushed with argon and refluxed for 2 hours under argon. KP_6 was added until complete precipitation, the solid was filtered, washed with water, recovered with acetone and dried. Column chromatography on 80 mL of silica gel (eluent: acetone / water / KNO_3 80:5:0.5) yielded 13 mg of [**46$_{th}$**][PF_6]$_2$ (85%).

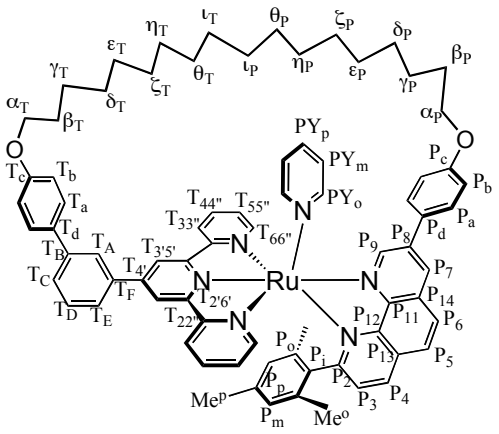

^{1}H NMR 500MHz: δ (ppm) in CD_2Cl_2 : 8.90 (d, 1H, P_7, J=1.8Hz); 8.49 (d, 1H, P_4, J=8.1Hz); 8.44 (d, 3H, P_6+$T_{33"}$); 8.40 (d, 1H, P_9, J=1.8Hz); 8.28 (d, 1H, P_5, J=8.8Hz); 8.21 (s, 2H, $T_{3',5'}$); 8.10 (td, 2H, $T_{44"}$, J=7.7,1.5Hz); 7.88 (m, 1H, T_E); 7.79 (m, 1H, T_C); 7.74 (m, 1H, T_D); 7.67-7.63 (m, 6H, T_a+$T_{66"}$+T_A+PY_p); 7.50 (d, 2H, P_a, J=8.8Hz); 7.42 (m, 2H, $T_{55"}$); 7.32 (d, 2H, PY_o, J=5Hz); 7.29 (d, 1H, P_3, J=8.1Hz); 7.18 (m, 2H, PY_m); 7.01 (d, 2H, T_b, J=8.8Hz); 6.99 (d, 2H, P_b, J=8.8Hz); 6.59 (s, 2H, P_m); 4.09 (t, 2H, α_T, J=6.6Hz); 4.07 (t, 2H, α_P, J=7.0Hz); 2.17 (s, 3H, Me^p); 1.73 (m, 4H, β_T+β_P); 1.37 (4H, γ_T+γ_P); 1.34-1.18 (m, 24H, δ_T-ι_T+δ_P-ι_P); 0.83 (s, 6H, Me^o). *^{13}C NMR 500MHz* : δ (ppm) in CD_2Cl_2 (assignments according to HSQC and HMBC 2D ^{1}H-^{13}C HETCORR experiments): 167.7 (P_2); 160.4 (P_c); 159.3 ($T_{22"}$); 159.2 (T_c); 157.6 ($T_{2'6'}$); 153.0 ($T_{66"}$); 151.2 (P_9); 149.0 ($T_{4'}$);

148.6 (P_{12}); 145.7 (P_{11}); 142.5 (T_B); 140.5 (P_p); 139.3 (P_8); 139.1 ($T_{44"}$); 138.1 (P_4); 137.7 (T_F); 135.6 (P_i); 134.6 (P_o); 132.8 (P_7); 132.7 (P_{13}); 132.3 (T_d); 132.2 (P_{14}); 130.1 (T_D); 129.1 (P_a); 129.1 ($T_{55"}$); 128.7 (P_5); 128.5 (T_a); 128.3 (P_6); 128.3 (P_m); 127.9 (T_C); 127.7 (T_A); 127.5 (P_d); 127.3 (P_3); 125.2 ($T_{33"}$); 124.9 (T_E); 121.6 ($T_{3'5'}$); 115.8 (P_b); 115.4 (T_b); 68.0 (α_P); 68.0 (α_T); 29.8 ($\delta_P\delta_T$); 28.4 ($\beta_P\beta_T$); 25.7 ($\gamma_P\gamma_T$); 21.2 (Me^p); 18.8 (Me^o); 29.8-30.6 ($\varepsilon_P\varepsilon_T..\iota_P\iota_T$). *HR ES MS m/z (calc)*: 611.2676 (611.2688, $[M\text{-}2PF_6]^{2+}$).

47$_{th}^{2+}$: 8 mg (5 μmol) of [**45**$_{th}$][PF_6]$_2$ were mixed with 7 mg of 10% palladium black on carbon. 2 mL of ethanol and 4 mL of dichloromethane were added, the mixture was saturated with dihydrogen by bubbling H_2 for 5 minutes, and the reaction flask was stirred for 24 hours at room temperature in the dark under a 1 atm dihydrogen pressure. The catalyst was removed by filtration of the reaction mixture on celite©, the solvents were evaporated and the product purified by chromatography on 90 mL of fine silica gel (eluent: acetone / water / KNO_3 80:5:0.5). The main fraction contained 7 mg (87%) of the reduced macrocycle [**47**$_{th}$][PF_6]$_2$.

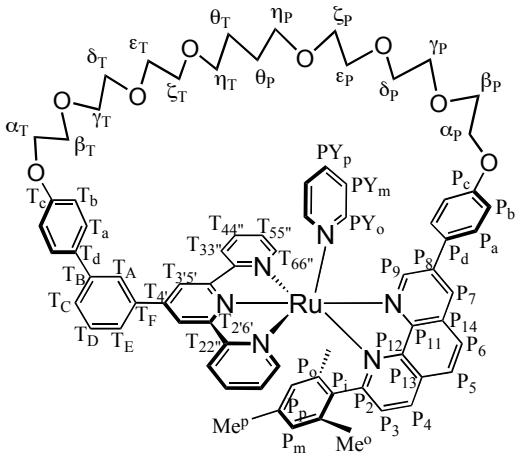

^{1}H NMR 500MHz : δ (ppm) in CD_2Cl_2: 8.91 (d, 1H, P_7, J=1.8Hz); 8.49 (d, 1H, , J=8.1Hz); 8.46-8.43 (m, 4H, $T_{33"}$+P_6+P_4); 8.37 (d, 1H, P_9, J=1.8Hz); 8.28 (d, 1H, P_5, J=8.8Hz); 8.23 (s, 2H, $T_{3',5'}$); 8.11 (t, 2H, $T_{44"}$, J=7.7Hz); 7.92 (m, 1H, T_E); 7.80 (m, 1H, T_C); 7.76 (m, 1H, T_D); 7.72 (s, 1H, T_A); 7.70 (m, 1H, PY_p); 7.65 (m, 4H, T_a+$T_{66"}$); 7.51 (d, 2H, P_a, J=9.0Hz); 7.43 (m, 2H, $T_{55"}$); 7.28 (m, 3H, P_3+PY_o); 7.17 (m, 2H, PY_m); 7.08 (d, 2H, T_b, J=8.8Hz); 7.07 (d, 2H, P_b, J=8.8Hz); 6.59 (s, 2H, P_m); 4.23 (m, 4H, α_T+α_P); 3.78 (m, 4H, β_T+β_P); 3.63-3.46 (m, 20H, γ_T+γ_P+δ_T+δ_P+ε_T+ε_P+ζ_T+ζ_P); 3.36 (m, 4H, η_T+η_P); 2.16 (s, 3H, Me^p); 1.53 (m, 4H, θ_T+θ_P); 0.84 (s, 6H, Me^o). *^{13}C NMR 500MHz* : δ (ppm) in CD_2Cl_2 (assignments according to HSQC and HMBC 2D ^{1}H-^{13}C HETCORR experiments: 167.8 (P_2); 160.7 (T_c); 159.5 ($T_{22"}$); 159.4 (P_c); 157.8 ($T_{2'6'}$); 153.0 ($T_{66"}$); 151.4 (P_9); 149.1 ($T_{4'}$); 148.8 (P_{12}); 145.8 (P_{11}); 142.7 (T_B); 140.6 (P_p); 139.3 ($T_{44"}$); 138.3 (P_4); 137.6 (T_F); 135.6 (P_o); 134.9 (P_i); 133.2 (P_7); 133.0 (P_d); 133.0 (T_d); 132.1 (P_{14}); 130.5 (T_D); 129.9 (P_{13}); 129.5 ($T_{55"}$); 129.3 (T_a); 128.9 (P_5); 128.7 (P_6); 128.7 (P_a); 128.7 (P_m); 128.6 (P_8); 128.3 (T_C); 127.7 (P_3); 127.4 (T_A); 125.2 ($T_{33"}$); 125.2 (T_E); 121.7 ($T_{3'5'}$); 116.4 (T_b); 115.8 (P_b); 71.3 ($\eta_P\eta_T$); 70.9 ($\gamma_P\gamma_T$); 70.6 ($\delta_P\delta_T$); 70.0 ($\varepsilon_P\varepsilon_T$); 70.0 ($\zeta_P\zeta_T$); 69.8 ($\beta_P\beta_T$); 68.2 ($\alpha_P$); 68.2 ($\alpha_T$); 26.4 ($\theta_P\theta_T$); 21.4 ($Me^p$); 19.3 ($Me^o$). *HD ES MS m/z (calc)*: 645.236 (645.238, $[M - 2\ PF_6]^{2+}$).

IV.3.b. Photochemical isomers

46$_{photo}^{2+}$: 50 mg (33 µmol) of the unsaturated macrocycle [**44**$_{photo}$][PF_6]$_2$ and 14 mg of 10% palladium black on carbon were weighed in a flask and dissolved with 8 mL of dichloromethane and 5 mL of ethanol. The mixture was saturated with dihydrogen by bubbling H_2 for 5 minutes, and the reaction flask was stirred for 24 hours at room temperature in the dark under a 1 atm dihydrogen pressure. The catalyst was removed by filtration of the reaction mixture on celite© and the solvents were evaporated. Yield: 50 mg of [**46**$_{photo}$][PF_6]$_2$ (100%).

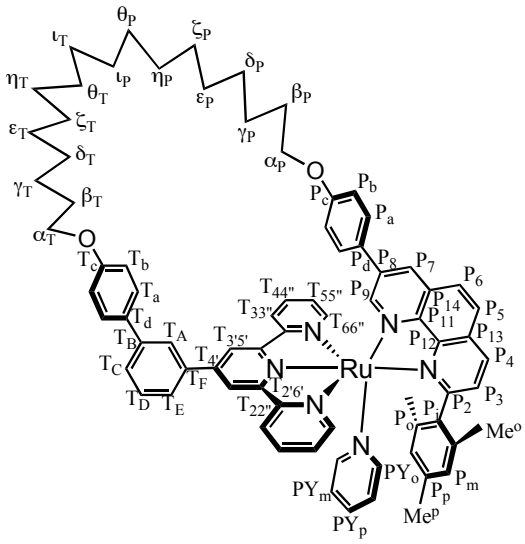

^{1}H NMR 500MHz: δ (ppm) in CD_2Cl_2: 8.85 (d, 1H, P_4, J=7.8Hz); 8.57 (s, 2H, $T_{3'5'}$); 8.52 (d, 2H, $T_{33"}$, J=7.8Hz); 8.41 (d, 1H, P_7, J=2.0Hz); 8.37 (d, 1H, P_5, J=9.0Hz); 8.19 (d, 1H, P_6, J=8.4Hz); 8.14 (s, 1H, T_A); 8.10 (td, 2H, $T_{44"}$, J=7.8,1.5Hz); 7.89 (d, 1H, P_3, J=8.4Hz); 7.85 (m, 2H, $T_{66"}$); 7.81-7.79 (m, 2H, T_C+T_E); 7.73 (d, 2H, T_a, J=9.0Hz); 7.67 (t, 1H, T_D, J=7.8Hz); 7.65 (d, 2H, P_9, J=2.0Hz); 7.43 (m, 2H, $T_{55"}$); 7.40 (t, 1H, PY_p, J=7.8Hz); 7.16 (d, 2H, P_a, J=8.4Hz); 7.06 (d, 2H, T_b, J=8.4Hz); 6.92 (d, 2H, PY_o, J=5.4Hz); 6.88 (d, 2H, P_b, J=8.4Hz); 6.69 (t, 2H, PY_m, J=7.2Hz); 6.39 (s, 2H, P_m); 4.06 (t, 2H, α_T, J=6.6Hz); 3.86 (t, 2H, α_P, J=6.4Hz); 2.03 (s, 6H, Me^o); 2.02 (s, 3H, Me^p); 1.82 (q, 2H, β_T, J=6.6Hz); 1.70 (q, 2H, β_P, J=6.6Hz); 1.55-1.47 (m, 2H, γ_T); 1.42-1.23 (m, 26H, γ_P-ι_P+δ_T-ι_T). *^{13}C NMR 500MHz* : δ (ppm) in CD_2Cl_2 (assignments according to HSQC and HMBC 2D ^{1}H-^{13}C HETCORR experiments): 169.1 (P_2); 160.9 (P_c); 159.8 (T_c); 158.5 ($T_{2'6'}$); 158.1 ($T_{22"}$); 153.5 ($T_{66"}$); 150.7 (PY_o); 148.8 (P_9); 148.0 (P_{12}); 146.4 (P_{11}); 139.7 ($T_{44"}$); 138.8 (P_4); 138.6 (P_8); 136.4 ($T_{4'}$); 135.6 (PY_p); 133.7 (T_F); 133.5 (P_7); 132.2 (T_d); 131.4 (P_{14}); 130.5 (P_{13}); 130.5 (T_D); 129.8 (P_3); 129.4 (T_C); 129.2 (P_5); 129.0 ($T_{55"}$); 128.6 (P_a); 128.6 (T_B); 128.4 (T_a); 128.2 (P_6); 126.6 (P_d); 126.0 (T_E); 125.8 ($T_{33"}$); 125.8 (PY_m); 125.3 (T_A); 121.7 ($T_{3'5'}$); 115.7 (P_b); 115.1 (T_b); 68.6 (α_P); 68.2 (α_T); 29.4 (β_P); 29.1 (β_T); 28.7 (δ_P); 28.7 (δ_T); 26.1 (γ_P); 25.7 (γ_T); 29.0-29.6 ($\varepsilon_P\varepsilon_T\zeta_P\zeta_T\eta_P\eta_T\theta_P\theta_T\iota_P\iota_T$); 21.4 ($Me^o$); 20.6 ($Me^p$). *ES MS m/z (calc)*: 1367.3 (1367.5, [M - PF_6]$^+$). *UV-visible*: λ_{max} (ε in L.mol^{-1}.cm^{-1}) in acetone: 481 nm (10700).

47$_{photo}^{2+}$: *Thermal preparation*: 37 mg (23 μmol) of the unsaturated macrocycle [**45**$_{photo}$][PF_6]$_2$ and 10 mg of 10% palladium black on carbon were weighed in a flask and dissolved with 30 mL of dichloromethane and 10 mL of ethanol. The mixture was saturated with dihydrogen by bubbling H_2 for 5 minutes, and the reaction flask was stirred for 20 hours at room temperature in the dark under a 1 atm dihydrogen pressure. The catalyst was removed by filtration of the reaction mixture on celite© and the solvents were evaporated. Yield: 38 mg of [**47**$_{photo}$][PF_6]$_2$ (100%). *Photochemical preparation*: 6 mg (3.8 μmol) of [**47**$_{th}$][PF_6]$_2$ were dissolved in 2 mL of pyridine and irradiated for 1 hour at room temperature with a xenon 1000 W arc lamp filtered by a water filter. The complex was precipitated by the addition of KPF_6, filtered, washed with water, recovered with acetone and dried. Yield in [**47**$_{photo}$][PF_6]$_2$: 6 mg (100%).

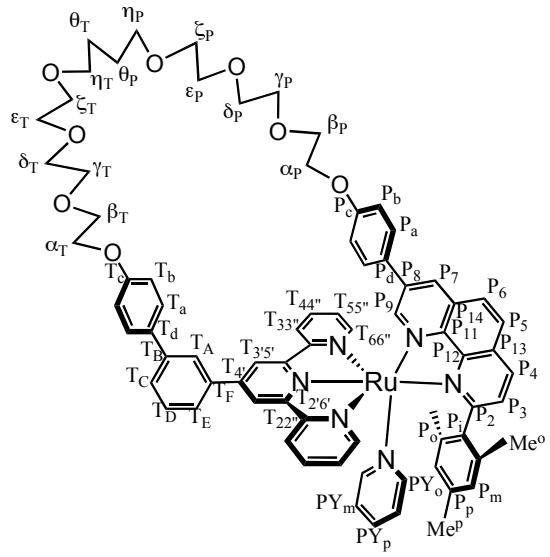

^{1}H NMR 500MHz: δ (ppm) in CD_2Cl_2: 8.85 (d, 1H, P_4, J=7.8Hz); 8.57 (s, 2H, $T_{3',5'}$); 8.51 (d, 2H, $T_{33"}$, J=7.8Hz); 8.42 (d, 1H, P_7, J=2.0Hz); 8.37 (d, 1H, P_5, J=9.0Hz); 8.19 (d, 1H, P_6, J=8.4Hz); 8.10 (td, 3H, $T_{44"}$+T_A); 7.90 (d, 1H, P_3, J=8.4Hz); 7.86 (m, 2H, $T_{66"}$); 7.82-7.79 (m, 2H, T_C+T_E); 7.71 (d, 2H, T_a, J=9.0Hz); 7.68 (t, 1H, T_D, J=7.8Hz); 7.63 (d, 2H, P_9, J=2.0Hz); 7.45-7.41 (m, 3H, $T_{55"}$+PY_p); 7.16 (d, 2H, P_a, J=8.4Hz); 7.09 (d, 2H, T_b, J=8.4Hz); 6.93-6.90 (d, 4H, PY_o+P_b); 6.70 (t, 2H, PY_m, J=7.2Hz); 6.39 (s, 2H, P_m); 4.21 (m, 2H, α_T); 4.02 (m, 2H, α_P); 3.87 (m, 2H, β_T); 3.74 (m, 2H, β_P); 3.71-3.69 (m, 2H, γ_T); 3.65-3.63 (m, 2H, δ_T); 3.61-3.58 (m, 4H, γ_P+ε_T); 3.57-3.52 (m, 6H, δ_P+ζ_T+ε_P); 3.50 (m, 2H, ζ_P); 3.43 (m, 2H, η_T); 3.42 (m, 2H, η_P); 2.03 (s, 6H, Me^o); 2.02 (s, 3H, Me^p); 1.60 (m, 4H, θ_T+θ_P). *^{13}C NMR 500MHz*: δ (ppm) in CD_2Cl_2 (assignments according to HSQC and HMBC 2D ^{1}H-^{13}C HETCORR experiments): 169.4 (P_2); 160.8 (P_c); 159.6 (T_c); 158.7 ($T_{2'6'}$); 158.2 ($T_{22"}$); 153.8 ($T_{66"}$); 150.3 ($T_{4'}$); 149.1 (P_9); 148.3 (P_{12}); 146.7 (P_{11}); 142.9 (T_B); 140.4 (P_p); 139.9 ($T_{44"}$); 139.1 (P_4); 138.8 (P_8); 136.5 (T_F); 136.1 (P_i); 135.2 (P_o); 133.8 (P_7); 132.9 (T_d); 131.6 (P_{14}); 130.7 (P_{13}); 130.7 (T_D); 130.1 (P_3); 129.7 (P_5); 129.7 (T_C); 129.5 ($T_{55"}$); 129.3 (P_m); 128.9 (P_a); 128.7 (P_6); 128.7 (T_a); 127.3 (P_d); 126.2 (T_E); 126.0 ($T_{33"}$); 125.8 (T_A); 121.9 ($T_{3'5'}$); 116.2 (P_b); 115.6 (T_b); 71.3 (γ_T); 71.3 (η_P); 71.1 (δ_T); 71.1 (ε_T); 71.1 (γ_P); 70.6 (ζ_T); 70.6 (δ_P); 70.6 (ε_P); 70.4 (η_T); 70.4 (ζ_P); 70.0 (β_T); 69.8 (β_P); 68.2 (α_P); 68.2 (α_T); 26.7 (θ_T); 26.7 (θ_P); 21.2 (Me^p); 21.2 (Me^o); . *UV-vis*: λ_{max} (ε in L.mol^{-1}.cm^{-1}) in acetone: 479.5 nm (11600). *HD ES MS m/z (calc)*: 645.2391 (645.2389, [M – 2 PF_6]$^{2+}$).

IV.4. Changing the monodentate ligand

48$_{th}^{2+}$: 21 mg (14 µmol) of [**46**$_{photo}$][PF_6]$_2$ were dissolved in 2 mL of distilled DMSO, put under argon and heated in the dark at 140°C for 2 hours. The complex was precipitated with KPF_6, filtered, washed with water, recovered with acetone and dried. 5 mL of acetonitrile were added, the solution was flushed with argon and refluxed for 2 hours under argon and in the dark. KP_6 was added until complete precipitation, the solid was filtered, washed with water, recovered with acetone and dried. Column chromatography on 150 mL of silica gel (eluent: acetone / water / KNO_3 80:5:0.5) yielded 17 mg of [**48**$_{th}$][PF_6]$_2$ (84%).

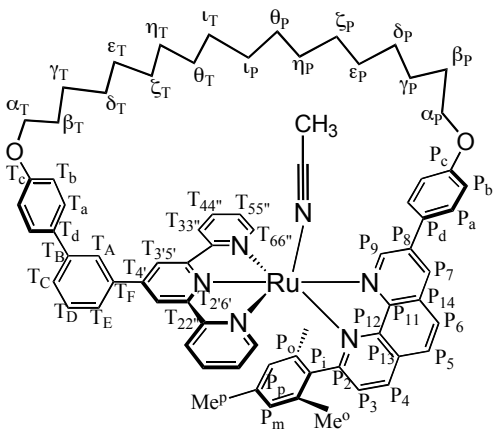

^{1}H NMR 500MHz: δ (ppm) in CD_2Cl_2 : 9.81 (d, 1H, P_9, J=1.8Hz); 8.93 (d, 1H, P_7, J=1.8Hz); 8.48 (d, 1H, P_4, J=8.1Hz); 8.43 (d, 1H, P_6); 8.37 (d, 2H, $T_{33"}$); 8.26 (s, 2H, $T_{3'5'}$); 8.23 (d, 1H, P_5, J=8.8Hz); 8.03 (td, 2H, $T_{44"}$, J=7.7,1.5Hz); 7.94 (d, 2H, P_a, J=8.8Hz); 7.90 (m, 1H, T_E); 7.84 (m, 2H, T_A+T_C); 7.78 (m, 1H, T_D); 7.69 (d, 2H, T_a); 7.48 (d, 2H, $T_{66"}$); 7.30 (m, 3H, P_3+$T_{55"}$); 7.17 (d, 2H, P_b, J=8.8Hz); 7.02 (d, 2H, T_b, J=8.8Hz); 6.58 (s, 2H, P_m); 4.14 (t, 2H, α_P, J=7.0Hz); 4.09 (t, 2H, α_T, J=6.6Hz); 2.20 (s, 3H, Me^p); 2.07 (s, 3H, AN_{Me}); 1.75 (m, 4H, β_T+β_P); 1.39 (4H, γ_T+γ_P); 1.30-1.10 (m, 24H, δ_T-ι_T+δ_P-ι_P); 0.85 (s, 6H, Me^o). *^{13}C NMR 500MHz*: δ (ppm) in CD_2Cl_2 (assignments according to HSQC and HMBC 2D ^{1}H-^{13}C HETCORR experiments): 167.6 (P_2); 160.7 (P_c); 159.5 ($T_{22"}$); 159.1 (T_c); 158.1 ($T_{2'6'}$); 153.2 ($T_{66"}$); 152.2 (P_9); 148.9 ($T_{4'}$); 148.9 (P_{12}); 145.3 (P_{11}); 142.5 (T_B); 140.2 (P_p); 139.2 (P_8); 138.9 ($T_{44"}$); 138.0 (P_4); 138.0 (T_F); 135.6 (P_o); 134.8 (P_i); 132.8 (P_7); 132.3 (T_d); 131.9 (P_{14}); 130.1 (T_D); 129.6 (P_{13}); 129.5 (P_a); 128.7 (P_5); 128.6 (T_a); 128.5 (P_m); 128.4 (P_6); 128.3 ($T_{55"}$); 127.9 (T_C); 127.9 (T_A); 127.7 (P_d); 127.2 (P_3); 125.7 (AN_{CN}); 125.1 (T_E); 124.7 ($T_{33"}$); 121.7 ($T_{3'5'}$); 116.3 (P_b); 115.5 (T_b); 68.1, 68.0 (α_P, α_T); 30.2-30.4 ($\varepsilon_P\varepsilon_T$..$\iota_P\iota_T$); 29.8 ($\delta_P$+$\delta_T$); 28.6 ($\beta_P$+$\beta_T$); 25.8 ($\gamma_P$+$\gamma_T$); 21.3 ($Me^p$); 19.1 ($Me^o$); 4.3 ($AN_{CH3}$). *HR ES MS m/z (calc)*: 1329.490 (1329.488, [M - PF_6]$^+$). *UV-visible*: λ_{max} (ε in L.mol^{-1}.cm^{-1}) in acetone: 462 nm (14700).

49$_{th}^{+}$: 25 mg (17 µmol) of [**46**$_{photo}$][PF_6]$_2$ were dissolved in 4 mL of distilled DMSO, put under argon and heated in the dark at 140°C for 2 hours. The complex was precipitated with KPF_6, filtered, washed with water, recovered with acetone and dried. 50 mg of tetraethylammonium chloride and 10 mL of acetone were added, the solution was put under argon, refluxed for 3 hours and let cool down to room temperature overnight. KP_6 was added until complete precipitation, the solid was filtered, washed with water, recovered with acetone and dried. Column chromatography on 160 mL of silica gel (eluent: acetone / water / KNO_3 80:5:0.5) yielded 23 mg of [**49**$_{th}$][PF_6] (Y=100%).

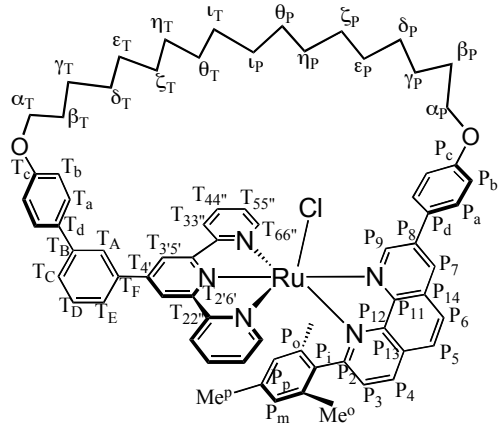

^{1}H NMR 500MHz: δ (ppm) in acetone-d6 : 10.94 (d, 1H, P_9, J=1.8Hz); 9.18 (d, 1H, P_7, J=1.8Hz); 8.71 (d, 2H, $T_{33"}$); 8.66 (s, 2H, $T_{3'5'}$); 8.62 (d, 1H, P_4, J=8.1Hz); 8.57 (d, 1H, P_6); 8.40 (d, 1H, P_5, J=8.8Hz); 8.13 (m, 1H, T_E); 8.02-7.95 (m, 5H, $T_{44"}$+P_a+T_A); 7.83 (m, 1H, T_C); 7.78 (m, 1H, T_D); 7.73 (m, 4H, T_a+$T_{66"}$); 7.37 (d, 1H, P_3); 7.25 (m, 2H, $T_{55"}$); 7.22 (d, 2H, P_b, J=8.8Hz); 7.06 (d, 2H, T_b, J=8.8Hz); 6.64 (s, 2H, P_m); 4.21 (t, 2H, α_P, J=7.0Hz); 4.16 (t, 2H, α_T, J=6.6Hz); 2.20 (s, 3H, Me^p); 1.76 (m, 4H, β_T+β_P); 1.42 (4H, γ_T+γ_P); 1.30 (m, 4H, δ_T+δ_P); 1.25-1.13 (m, 20H, ε_T-ι_T+ε_P-ι_P); 0.90 (s, 6H, Me^o). *^{13}C NMR 500MHz*: δ (ppm) in acetone-d6 (assignments according to HSQC and HMBC 2D ^{1}H-^{13}C HETCORR experiments): 168.0 (P_2); 161.7 ($T_{2'6'}$); 160.9 (P_c); 160.9 ($T_{22"}$); 159.6 (T_c); 153.7 (P_9); 153.1 ($T_{66"}$); 150.7 (P_{12}); 147.2 (P_{11}); 142.7 (T_B); 140.0 (P_p); 139.9 (T_F); 138.1 (P_8); 137.6 ($T_{44"}$); 137.0 (P_4); 136.3 (P_o); 135.7 (P_i); 133.5 (T_d); 132.4 (P_{13}); 131.6 (P_7); 130.6 (T_D); 130.3 (P_{14}); 129.8 (P_a); 129.2 (T_a); 128.9 (P_5); 128.9 (P_m); 128.8 (P_6); 128.0 (T_A); 127.6 ($T_{55"}$); 127.6 (T_C); 127.3 (P_3); 126.1 (T_E); 124.5 ($T_{33"}$); 121.0 ($T_{3'5'}$); 116.9 (P_b); 116.1 (T_b); 68.5 (α_P); 68.3 (α_T); 31.1-30.5 ($\varepsilon_P\varepsilon_T..\iota_P\iota_T$); 29.9 ($\delta_P$+$\delta_T$); 28.9 ($\beta_P$+$\beta_T$); 26.2 ($\gamma_P$+$\gamma_T$); 21.7 ($Me^p$); 19.3 ($Me^o$). P_d and $T_{4'}$ could not be assigned. *ES-MS m/z (calc):* 1178.462 (1178.465, [M - PF_6]$^{+}$). *UV-visible*: λ_{max} (ε in $L.mol^{-1}.cm^{-1}$) in acetone: 512 nm (11600).

50$_{th}^{2+}$: 6 mg (4 µmol) of [**46**$_{photo}$][PF_6]$_2$ were put in an NMR tube and dissolved in deuterated DMSO. The tube was closed with a normal stopper and a reference spectrum was taken. The tube was heated in the dark at 140°C for 2 hours. After cooling down to room temperature, a spectrum was taken showing complete isomerization of the macrocycle and removal of pyridine, giving a 66:33 mixture of products analyzed as S-bonded:O-bonded [**50**$_{th}$][PF_6]$_2$, respectively. After one night at room temperature in the dark the mixture evolved to a 87:13 ratio, which enabled analysis of the main product (S-bonded [**50**$_{th}$][PF_6]$_2$).

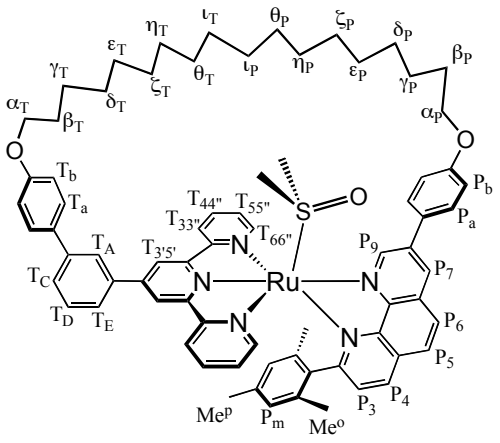

^{1}H NMR 300MHz: δ (ppm) in DMSO-d6 : 10.67 (d, 1H, P_9); 9.42 (d, 1H, P_7); 8.88 (d, 2H, $T_{33"}$); 8.85 (s, 2H, $T_{3',5'}$); 8.83 (d, 1H, P_4); 8.59 (d, 1H, P_6); 8.45 (d, 1H, P_5); 8.23 (td, 2H, $T_{44"}$); 8.21 (m, 1H, T_E); 8.01 (m, 3H, P_a+T_A); 7.92-7.76 (m, 6H, T_C+T_D+T_a+$T_{66"}$); 7.46 (m, 3H, P_3+$T_{55"}$); 7.26 (d, 2H, P_b); 7.10 (d, 2H, T_b); 6.53 (s, 2H, P_m); 4.18 (m, 4H, α_P+α_T); 2.13 (s, 3H, Me^p); 2.10 (s, 6H, $DMSO_{CH3}$); 1.68 (m, 4H, β_T+β_P); 1.42-1.10 (m, 28H, γ_T-ι_T+γ_P-ι_P); 0.94 (s, 6H, Me^o). *ES-MS m/z (calc):* 571.745 (571.748, [M – DMSO – 2 PF_6]$^{2+}$); 609.74 (610.755, [M – H_2 – 2 PF_6]$^{2+}$); 1222.4 (1221.5, [M + H - PF_6]$^+$). *UV-visible*: λ_{max} in acetone: ~438 nm (S-bonded) and ~496 nm (O-bonded).

51$_{photo}^{2+}$: 3.6 mg (2.4 µmol) of [**46**$_{photo}$][PF_6]$_2$ were dissolved in 1 mL of 3,5-dimethylpyridine, put under argon and heated in the dark at 140°C for 2 hours. The complex was precipitated with heptane, filtered, washed with heptane, recovered with acetone and dried to quantitatively give [**51**$_{photo}$][PF_6]$_2$.

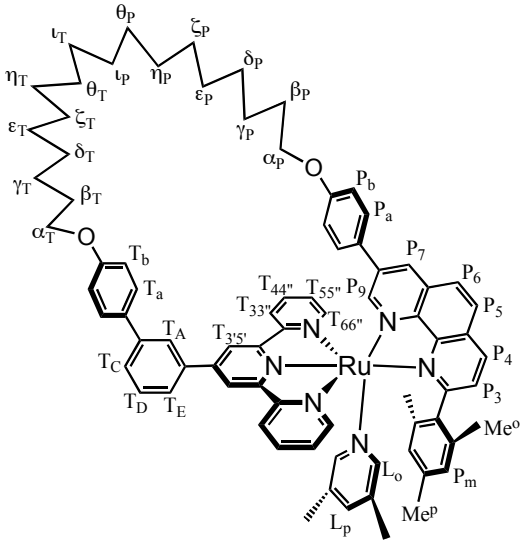

^{1}H NMR 300MHz: δ (ppm) in acetone-d6: 9.15 (s, 2H, $T_{3',5'}$); 9.13 (d, 1H, P_4); 8.92 (d, 2H, $T_{33"}$); 8.79 (d, 1H, P_7); 8.59 (d, 1H, P_5); 8.39 (d, 1H, P_6); 8.37 (s, 1H, T_A); 8.31 (m, 2H, $T_{66"}$); 8.22 (td, 2H, $T_{44"}$); 8.07 (d, 1H, P_3); 8.03 (d, 2H, P_9); 7.97 (m, 1H, T_C); 7.86 (m, 1H, T_E); 7.78 (d, 2H, T_a); 7.69 (m, 1H, T_D); 7.56 (m, 2H, $T_{55"}$); 7.31 (d, 2H, P_a); 7.22 (s, 1H, L_p); 7.10 (d, 2H, T_b); 6.85

(d, 2H, P_b); 6.74 (s, 2H, L_o); 6.53 (s, 2H, P_m); 4.11 (t, 2H, α_T); 3.89 (t, 2H, α_P); 2.18 (s, 6H, Me^o); 2.02 (s, 3H, Me^p); 1.84 (s, 6H, L_{CH3}); 1.68 (m, 2H, β_T); 1.52 (m, 2H, β_P); 1.45-1.23 (m, 28H, γ_P-ι_P+γ_T-ι_T).

52$_{photo}^{2+}$: 3.6 mg (2.4 µmol) of [**46**$_{photo}$][PF_6]$_2$ were dissolved in 1 mL of benzonitrile, put under argon and heated in the dark at 140°C for 2 hours. The complex was precipitated with heptane, filtered, washed with heptane, recovered with acetone and dried to give quantitatively [**52**$_{photo}$][PF_6]$_2$.

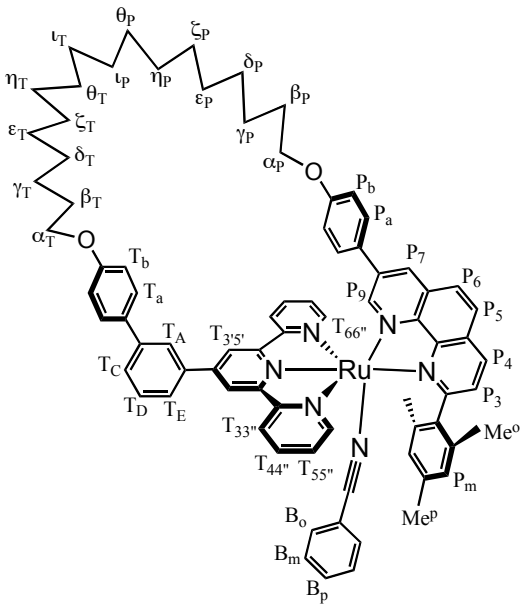

^{1}H NMR 300MHz: δ (ppm) in CD_2Cl_2: 8.86 (d, 1H, P_4); 8.71 (s, 2H, $T_{3'5'}$); 8.58 (d, 2H, $T_{33"}$); 8.45 (d, 1H, P_7); 8.37 (d, 1H, P_5); 8.20 (d, 1H, P_6); 8.18 (s, 1H, T_A); 8.09 (td, 2H, $T_{44"}$); 7.99 (d, 1H, P_3); 7.89 (m, 1H, T_C); 7.83 (d, 2H, P_9); 7.81 (m, 1H, T_E); 7.74 (m, 4H, $T_{66"}$+T_a); 7.68 (m, 1H, T_D); 7.50 (m, 2H, P_3+B_p); 7.34 (m, 4H, B_o+$T_{55"}$); 7.21 (d, 2H, P_a); 7.05 (d, 2H, T_b); 6.90 (m, 4H, P_b+B_m); 6.71 (s, 2H, P_m); 4.05 (t, 2H, α_T); 3.86 (t, 2H, α_P); 2.14 (s, 6H, Me^o); 1.59 (s, 3H, Me^p); 1.81 (m, 2H, β_T); 1.69 (m, 2H, β_P); 1.53-1.17 (m, 28H, γ_P-ι_P+γ_T-ι_T). *ES-MS m/z (calc):* 623.28 (623.27, [M – 2 PF_6]$^{2+}$); 1391.53 (1391.50, [M - PF_6]$^+$).

BIBLIOGRAPHY

1. Robertus, J. Biochemistry I CH339K. http://courses.cm.utexas.edu/jrobertus/ch339k/overheads-1/ch7_mus-contract.jpg

2. Hinohara, T.; Block, B. E. Ribosome. http://sun.menloschool.org/~birchler/cells/animals/ribosome/

3. Chou, K. C.; Carlacci, L.; Maggiora, G. M.; Parodi, L. A.; Schulz, M. W. bacteriorhodopsin structure. http://www.imb-jena.de/cgi-bin/ImgLib.pl?CODE=1bad

4. Macer, D. R. J. Human sperm picture. http://www.biol.tsukuba.ac.jp/~macer/BetCD/Bet8sp.jpg

5. Balzani, V.; Venturi, M.; Credi, A., *Molecular Devices and Machines*. Wiley-VCH: Weinheim, 2003; p 494.

6. Voet, D.; Voet, J. G., *Biochemistry*. Second ed.; John Wiley & Sons: New York, 1995; p 1361.

7. Wang, H.; Oster, G., Energy transduction in the F1 motor of ATP synthase. *Nature* **1998,** 396, (19), 279-282.

8. Oster, G.; Wang, H., Reverse engineering a protein: the mechanochemistry of ATP synthase. *Biochimica et Biophysica Acta* **2000,** 1458, 482-510.

9. Noji, H.; Yasuda, R.; Yoshida, M.; Jr, K. K., Direct observation of the rotation of F1-ATPase. *Nature* **1997,** 386, 299-302.

10. Astumian, D., Les moteurs moleculaires. *Pour la Science* **2001,** 290, 67-73.

11. Astumian, D., Thermodynamics and kinetics of a Brownian motor. *Science* **1997,** 276, 917-922.

12. Reimann, P.; Hänggi, P., Introduction to the physics of Brownian motors. *Applied Physics A* **2002,** 75, 169-178.

13. Oster, G., Darwin's motor. *Nature* **2002,** 417, 25.

14. Yasuda, R.; Noji, H.; Kinosita, K.; Yoshida, M., F1-ATPase is a higly efficient molecular motor that rotates with discrete 120 degrees steps. *Cell* **1998,** 93, (7), 1117-1124.

15. Mehta, A. D.; Rief, M.; Spudich, J. A.; Smith, D. A.; Simmons, R. M., Single-molecule biomechanics with optical methods. *Science* **1999,** 283, 1689-1695.

16. Visscher, K.; Schnitzer, M. J.; Block, S. M., Single kinesin molecules studied with a molecular force clamp. *Nature* **1999,** 400, 184-189.

17. Feynman, R. P.; Leighton, R. B.; Sands, M., The Feynman lectures on physics. In Addison-Wesley: Reading, MA, 1966; Vol. 1.

18. Faucheux, L. P.; Bourdieu, L. S.; Kaplan, P. D.; Libchaber, A. J., Optical thermal ratchet. *Physical Review Letters* **1995,** 74, (9), 1504-1507.

19. Adjari, A.; Prost, J., Mouvement induit par un potentiel périodique de basse symétrie: diélectrophorèse pulsée. *Comptes Rendus de l'Académide des Sciences de Paris* **1992,** 315, 1635-1639.

20. Rousselet, J.; Salome, L.; Adjari, A.; Prost, J., Directional motion of brownian particles induced by a periodic asymmetric potential. *Nature* **1994,** 370, 446-448.

21. Leibler, S., Moving forward noisily. *Nature* **1994,** 370, 412-413.

22. Mietkiewski, K.; Domka, F.; Malendowicz, L.; Malendowicz, J., ATP hydrolysis in medium for histochemical demonstration of ATPase activity. *Histochemie* **1970,** 24, (4), 343-353.

23. Spudich, J. A., How molecular motors work. *Nature* **1994,** 372, (8), 515-518.

24. Kitamura, K.; Tokunaga, M.; Iwane, A. H.; Yanagida, T., A single myosin head moves along an actin filament with regular steps of 5.3 nanometers. *Nature* **1999,** 397, 129-134.

25. Tyska, M. J.; Dupuis, D. E.; Guilford, W. H.; Patlak, J. B.; Waller, G. S.; Trybus, K. M.; Warshaw, D. M.; Lowey, S., Two heads of myosin are better than one for generating force and motion. *Proceedings of the National Academia of Sciences of USA* **1999,** 96, (April 1999), 4402-4407.

26. Ishijima, A.; Kojima, H.; Funatsu, T.; Tokunaga, M.; Higuchi, H.; Tanaka, H.; Yanagida, T., Simultaneous observation of indivual ATPase and mechanical events by a single myosin molecule during interaction with actin. *Cell* **1998,** 92, 161-171.

27. Yanagida, T.; Iwane, A. H., A large step for myosin. *Proceedings of the National Academia of Sciences of USA* **2000,** 97, (17), 9357-9359.

28. Yanagida, T.; Kitamura, K.; Tanaka, H.; Iwane, A. H.; Esaki, S., Single molecule analysis of the actomyosin motor. *Current opinion in Cell Biology* **2000,** 12, 20-25.

29. Mallery, C., Mechanism of myosin / actin interaction. **2003**.

30. Dominguez, R. Actin / myosin power stroke. http://www.bbri.org/faculty/dominguez/Movies/ActoMyosin_PowerStroke_Movie.gif

31. Ishii, Y.; Esaki, S.; Yanagida, T., Experimental studies of the myosin-actin motor. *Applied Physics A* **2002,** 75, 325-330.

32. Amendola, V.; Fabbrizzi, L.; Mangano, C.; Pallavicini, P., Molecular machines based on metal ion translocation. *Accounts of Chemical Research* **2001,** 34, 488-493.

33. Leigh, D. A.; Wong, J. K.; Dehez, F.; Zerbetto, F., Unidirectional rotation in a mechanically interlocked molecular rotor. *Nature* **2003,** 424, 174-179.

34. Tian, Y.; Mao, C., Molecular gears: a pair of DNA circles continuously rolls against each other. *Journal of the American Chemical Society* **2004,** 126, 11410-11411.

35. Kottas, G. S.; Clarke, L. I.; Horinek, D.; Michl, J., Artificial molecular rotors. *Chemical Review* **2005,** 105, (1281-1376).

36. Livoreil, A.; Sauvage, J.-P.; Armaroli, N.; Balzani, V.; Flamigni, L.; Ventura, B., Electrochemically and photochemically driven ring motions in a disymmetrical copper (2)-catenate. *Journal of the American Chemical Society* **1997,** 119, 12114-12124.

37. Ashton, P. R.; Ballardini, R.; Balzani, V.; Baxter, I.; Credi, A.; Fyfe, M. C. T.; Gandolfi, M.-T.; Gomez-Lopez, M.; Martinez-Diaz, M.-V.; Piersanti, A.; Spencer, N.; Stoddart, F. J.; Venturi, M.; White, A. J. P.; Williams, D. J., Acid-base controllable molecular shuttles. *Journal of the American Chemical Society* **1998,** 120, 11932-11942.

38. Badjic, J. D.; Balzani, V.; Credi, A.; Silvi, S.; Stoddart, F. J., A molecular elevator. *Science* **2004,** 303, 1845-1849.

39. Jimenez-Molero, M. C.; Dietrich-Buchecker, C.; Sauvage, J.-P., Chemically induced contraction and stretching of a linear rotaxane dimer. *Chemistry a European journal* **2002,** 8, (6), 1456-1466.

40. Tseng, H.-R.; Vignon, S. A.; Stoddart, F. J., toward chemically controlled nanoscale molecular machinery. *Angewandte Chemie International Edition* **2003,** 42, 1491-1495.

41. Brouwer, A. M.; Frochot, C.; Gatti, F. G.; Leigh, D. A.; Mottier, L.; Paolucci, F.; Roffia, S.; Wurpel, G. W. H., Photoinduction of fast, reversible translational motion in a hydrogen-bonded molecular shuttle. *Science* **2001,** 291, (5511), 2124-2128.

42. Mobian, P.; Kern, J.-M.; Sauvage, J.-P., Light-driven machine prototypes based on dissociative excited states: photoinduced decoordination and thermal recoordination of a ring in a ruthenium(II)-containing 2-catenane. *Angewandte Chemie International Edition* **2004,** 43, 2392-2395.

43. Saha, S.; Johansson, L. E.; Flood, A. H.; Tseng, H.-R.; Zink, J. I.; Stoddart, F. J., powering a supramolecular machine with a photoreactive molecular triad. *Small*
2005, 1, (1), 87-90.

44. Delden, R. A. v.; Koumura, N.; Schoevaars, A.-M.; Meetsma, A.; Feringa, B. L., A donor-acceptor substituted molecular motor: unidirectional rotation driven by visible light. *Organic Biomolecular Chemistry* **2003,** 1, (1), 33-35.

45. Wiel, M. K. J. t.; Delden, R. A. v.; Meetsma, A.; Feringa, B. L., increased speed of rotation for the smallest light-driven molecular motor. *Journal of the American Chemical Society* **2003,** 125, 15076-15086.

46. Pomeranc, D.; Jouvenot, D.; Chambron, J.-C.; Collin, J.-P.; Sauvage, J.-P.; Heitz, V., Templated synthesis of a rotaxane with a $(Ru(diimine)_3)^{2+}$ core. *Chemistry a European journal* **2003,** 9, (17), 4247-4254.

47. Sauvage, J.-P.; Dietrich-Buchecker, C., *Molecular catenanes, rotaxanes and knots*. Wiley-VCH: Weinheim, 1999; p 368.

48. Dietrich-Buchecker, C.; Sauvage, J.-P.; Kintzinger, J.-P., Une nouvelle famille de molécules: les métallo-caténanes. *Tetrahedron Letters*
1983, 24, (46), 5095-5098.

49. Fujita, M.; F., I.; Hagihara, H.; Ogura, K., *Nature* **1994,** 367, 720.

50. Ogino, H., Relatively high-yield syntheses of rotaxanes. Syntheses and properties of compounds consisting of cyclodextrins threaded by alpha, omega-diaminoalkanes coordinated to cobalt(III) complexes. *Journal of the American Chemical Society* **1981,** 103, 1303-1304.

51. Ashton, P. R.; Fyfe, M. C. T.; Hickingbottom, S. K.; Menzer, S.; Stoddart, F. J.; White, A. J. P.; Williams, D. J., combining different hydrogen-bonding motifs to self-assemble interwoven superstructures. *Chemistry a European journal* **1998,** 4, (4), 577-589.

52. Gatti, F. G.; Leigh, D. A.; Nepogodiev, S. A.; Slawin, A. M. Z.; Teat, S. J.; Wong, J. K. Y., Stiff, and sticky in the right places: the dramatic influence of preorganizing guest binding sites on the hydrogen bond-directed assembly of rotaxanes. *Journal of the American Chemical Society* **2001,** 123, (5983-5989).

53. Voegtle, F.; Duennwald, T.; Schmidt, T., Catenanes and rotaxanes of the amide type. *Accounts of Chemical Research* **1996,** 29, 451-460.

54. Anelli, P. L.; Ashton, P. R.; Ballardini, R.; Balzani, V.; Delgado, M.; Gandolfi, M.-T.; Goodnow, T. T.; Kaifer, A. E.; Philp, D.; Pietraszkiewicz, M.; Prodi, L.; Reddington, M. V.; Slawin, A. M. Z.; Spencer, N.; Stoddart, F. J.; Vicent, C.; Williams, D. J., Molecular mecano 2-rotaxanes and 2-catenane made to order. *Journal of the American Chemical Society* **1992,** 114, 193-218.

55. Hamilton, D. G.; Feeder, N.; Prodi, L.; Teat, S. J.; Clegg, W.; Sanders, J. K. M., Tandem Hetero-catenation: templating and self-assembly in the mutual closure of two different interlocking rings. *Journal of the American Chemical Society* **1998,** 120, 1096-1097.

56. Schill, G., *Catenanes, rotaxanes, and knots.* Academic Press: New York, 1971.

57. Hiratani, K.; Suga, J.-i.; Nagawa, Y.; Houjou, H.; Tokuhisa, H.; Numata, M.; Watanabe, K., A new synthetic method for rotaxanes via tandem Claisen rearrangement, diesterification, and aminolysis. *Tetrahedron Letters* **2002,** 43, 5747-5750.

58. Heitz, V. Elaboration et étude de systèmes multiporphyriniques à géométrie contrôlée: sépération photoinduite intramoléculaire des charges. Louis Pasteur, Strasbourg, 1992.

59. Sauvage, J.-P., Transition metal-containing rotaxanes and catenanes in motion: towards molecular machines and motors. *Accounts of Chemical Research* **1998,** 31, 611-619.

60. Chambron, J.-C.; Collin, J.-P.; Heitz, V.; Jouvenot, D.; Kern, J.-M.; Mobian, P.; Pomeranc, D.; Sauvage, J.-P., Rotaxanes and catenanes built around octahedral transition metals. *European Journal of Organic Chemistry* **2004,** 8, 1627-1638.

61. Rogers, C. W.; Zhang, Y.; Patrick, B. O.; Jr, W. E. J.; Wolf, M. O., Photophysical effect of the coordination of water by ruthenium(II) bipyridyl complexes containing hemilabile phosphine-ether ligands. *Inorganic Chemistry* **2002,** 41, (5), 1162-1169.

62. Trofimenko, S., Recent advances in poly(pyrazolyl)borate (scorpionate) chemistry. *Chemical Review* **1993,** 93, 843-980.

63. Lehn, J.-M., *La Chimie Supramoléculaire - concepts et perspectives*. De Boeck Université: 1997; p 273.

64. Bissell, R. A.; Cordova, E.; Kaifer, A. E.; Stoddart, F. J., A chemically and electrochemically switchable molecular shuttle. *Nature* **1994,** 369, 133-137.

65. Anelli, P. L.; Spencer, N.; Stoddart, F. J., A molecular shuttle. *Journal of the American Chemical Society* **1991,** 113, 5131-5133.

66. Shinkai, S.; Ogawa, T.; Nakaji, T.; Kusano, Y.; Nanabe, O., Photocontrolled extraction ability of azobenzene-bridged azacrown ether. *Tetrahedron Letters* **1979,** 20, (47), 4569-4572.

67. Shinkai, S.; Nakaji, T.; Nishida, Y.; Ogawa, T.; Manabe, O., Photoresponsive crown ethers. 1. Cis-trans isomerism of azobenzene as a tool to enforce conformational changes of crown ethers and polymers. *Journal of the American Chemical Society* **1980,** 102, 5860-5865.

68. Norikane, Y.; Tamaoki, N., light-driven molecular hinge: a new molecular machine showing a light-intensity-dependent photoresponse that utilizes the trans-cis isomerization of azobenzene. *Organic Letters* **2004,** 6, (15), 2595-2598.

69. Muraoka, T.; Kinbara, K.; Kobayashi, Y.; Aida, T., Light-driven open-close motion of chiral molecular scissors. *Journal of the American Chemical Society* **2003,** 125, (19), 5612-5613.

70. Heberle, J.; Fitter, J.; Sass, H.-J.; Büldt, G., Bacteriorhodopsin: the functional details of a molecular machine are being resolved. *Biophysical Chemistry* **2000,** 85, 229-248.

71. Hernandez, J. V.; Kay, E. R.; Leigh, D. A., A reversible synthetic rotary molecular motor. *Science* **2004,** 306, 1532-1537.

72. Altieri, A.; Bottari, G.; Dehez, F.; Leigh, D. A.; Wong, J. K.; Zerbetto, F., Remarkable positional discrimination in bistable light- and heat-switchable hydrogen-bonded molecular shuttles. *Angewandte Chemie International Edition* **2003,** 42, 2296-2300.

73. Koumura, N.; Geertsema, E. M.; Gelder, M. B. v.; Meetsma, A.; Feringa, B. L., Second generation light-driven molecular motors. Unidirectional rotation controlled by a single stereogenic

center with near-perfect photoequilibria and acceleration of the speed of rotation by structural modification. *Journal of the American Chemical Society* **2002,** 124, 5037-5051.

74. Koumura, N.; Zijlstra, R. W. J.; Delden, R. A. v.; Harada, N.; Feringa, B. L., Light-driven monodirectional molecular rotor. *Nature* **1999,** 401, 152-155.

75. Poleschak, I.; Kern, J.-M.; Sauvage, J.-P., A copper-complexed rotaxane in motion: pirouetting of the ring on the millisecond timescale. *Chemical Communication* **2004,** 4, 474-476.

76. Durham, B.; Caspar, J. V.; Nagle, J. K.; Meyer, T. J., Photochemistry of Ru(bpy)32+. *Journal of the American Chemical Society* **1982,** 104, 4803-4810.

77. Baranoff, E.; Collin, J.-P.; Furusho, J.; Furusho, Y.; Laemmel, A.-C.; Sauvage, J.-P., Photochemical or thermal chelate exchange in the ruthenium coordination sphere of complexes of the $Ru(phen)_2L$ family (L=diimine or dinitrile ligands). *Inorganic Chemistry* **2002,** 41, 1215-1222.

78. Mobian, P.; Kern, J.-M.; Sauvage, J.-P., A 2catenane constructed around a $Ru(diimine)_3^{2+}$ complex used as a template. *Journal of the American Chemical Society* **2003,** 125, (8), 2016-2017.

79. Mobian, P.; Kern, J.-M.; Sauvage, J.-P., Building 2catenanes around a tris(diimine)ruthenium(2+) complex core used as template. *Helvetica Chimica Acta* **2003,** 86, 4195-4213.

80. Laemmel, A.-C. Vers des mouvements moléculaires photoinduits dans des complexes de ruthenium(II) de type rotaxane. Louis Pasteur, Strasbourg, 2000.

81. Sauvage, J.-P., Transition metal-complexed catenanes and rotaxanes as molecular machine prototypes. *Chemical Communication* **2005**, 1507-1510.

82. Jouvenot, D. Rotaxanes fondés sur des complexes de ruthenium(II): vers des machines moléculaires photoactives. Louis Pasteur, Strasbourg, 2004.

83. Sauvage, J.-P.; Collin, J.-P.; Chambron, J.-C.; Guillerez, S.; Coudret, C., Ruthenium(II) and osmium(II) bis(terpyridine) complexes in covalently-linked multicomponent systems: synthesis, electrochemical behavior, absorption spectra, and photochemical and photophysical properties. *Chemical Review* **1994,** 94, (993-1019).

84. Hecker, C. R.; Fanwick, P. E.; McMillin, D. R., Evidence for dissociative photosubstitution reactions of $Ru(trpy)(bpy)(NCCH_3)^{2+}$. Crystal and molecular structure of $Ru(trpy)(bpy)(py)(PF_6)_2.(CH_3)_2CO$. *Inorganic Chemistry* **1991,** 30, 659-666.

85. Berger, R. M.; McMillin, D. R., Localized states in reduced and excited-states ruthenium(II) terpyridyls. *Inorganic Chemistry* **1988,** 27, 4245-4249.

86. Laemmel, A.-C.; Collin, J.-P.; Sauvage, J.-P., Photosubstitution of ancillary ligands in octahedral mono-terpyridine ruthenium(II) complexes. *Comptes Rendus de l'Académie des Sciences de Paris* **2000,** 3, 43-49.

87. Gerli, A.; Reedijk, J.; Lakin, M. T.; Spek, A. L., Redox properties and electrocatalytic activity of the oxo/aqua system Ru(terpy)(bpz)O^{2+}/Ru(terpy)(bpz)$(H_2O)^{2+}$. X-ray crystal structure of Ru(terpy)(bpz)Cl,PF_6.MeCN (terpy=2,2',2"-terpyridine;bpz=2,2'-bipyrazine). *Inorganic Chemistry* **1995,** 34, 1836-1843.

88. Adcock, P. A.; Keene, F. R.; Smythe, R. S.; Snow, M. R., Oxidation of isopropylamine and related amines coordinated to ruthenium. Formation of monodentate imine and alkylideneamido complexes of ruthenium. *Inorganic Chemistry* **1984,** 23, 2336-2343.

89. Takeuchi, K. J.; Thompson, M. S.; Pipes, D. W.; Meyer, T. J., Redox and spectral properties of monooxo polypyridyl complexes of ruthenium and osmium in aqueous media. *Inorganic Chemistry* **1984,** 23, (1845-1851).

90. Bonnet, S.; Collin, J.-P.; Gruber, N.; Sauvage, J.-P.; Schofield, E. R., Photochemical and thermal synthesis and characterization of polypyridine ruthenium(II) complexes containing different monodentate ligands. *Dalton Transactions* **2003**, 4654-4662.

91. Schofield, E. R.; Collin, J.-P.; Gruber, N.; Sauvage, J.-P., Photochemical and thermal ligand exchange in a ruthenium(II) complex based on a scorpionate terpyridine ligand. *Chemical Communication* **2003**, 188-189.

92. Bonnet, S.; Schofield, E. R.; Collin, J.-P.; Sauvage, J.-P., Photochemical expulsion of the neutral monodentate ligand L in Ru(terpy)(diimine)$(L)^{2+}$: a dramatic effect of the steric properties of the spectator diimine ligand. *Inorganic Chemistry* **2004,** 43, (26), 8346-8354.

93. Collin, J.-P.; Dixon, I. M.; Sauvage, J.-P.; Williams, J. A. G.; Barigelletti, F.; Flamigni, L., Synthesis and photophysical properties of iridium(III) bisterpyridine and its homologues: a family of complexes with a long-lived excited state. *Journal of the American Chemical Society* **1999,** 121, 5009-5016.

94. Calvert, J. M.; Schmehl, R. H.; Sullivan, B. P.; Facci, J. S.; Meyer, T. J.; Murray, R. W., Synthetic and mechanistic investigations of the reductive electrochemical polymerization of vinyl-containing complexes of iron(II), ruthenium(II), and osmium(III). *Inorganic Chemistry* **1983,** 22, 2151-2162.

95. Rasmussen, S. C.; Ronco, S. E.; Mlsna, D. A.; Billadeau, M. A.; Pennington, W. T.; Lolis, J. K.; Petersen, J. D., Ground- and excited-state properties of ruthenium(II) complexes containing tridentate azine ligands, Ru(tpy)(bpy)L^{2+}, where L is a polymerizable acetylene
. *Inorganic Chemistry* **1995,** 34, 821-829.

96. Kalyanasundaram, K., Photophysics, photochemistry and solar energy conversion with tris(bipyridyl)ruthenium(II) and its analogues. *Coordination Chemistry Reviews* **1982,** 46, 159-244.

97. Adamson, A. W.; Feischauer, P. D., *Concepts of inorganic photochemistry.* Wiley: New York, 1975.

98. Bossert, J. Spectroscopie électronique et photochimie de complexes à transfert de charge du rhénium et du ruthenium. Louis Pasteur, Strasbourg, 2004.

99. Kroener, R.; Heeg, M. J.; Deutsch, E., Synthesis and characterization of polypyridine ruthenium(II) complexes containing S-bonded thioether ligands. X-ray crystal structures of cis- and trans-bis(2,2'-bipyridine)bis(phenothiazine-S)ruthenium(II) hexafluorophosphates. *Inorganic Chemistry* **1988,** 27, 558-566.

100. Rack, J. J.; Winkler, J. R.; Gray, H. B., Phototriggered Ru(II)-dimethylsulfoxide linkage isomerization in crystals and films. *Journal of the American Chemical Society* **2001,** 123, 2432-2433.

101. Yeh, A.; Scott, N.; Taube, H., S to O and O to S linkage isomerization in sulfoxide complexes of pentaammineruthenium. *Inorganic Chemistry* **1982,** 21, 2542-2545.

102. Sano, M.; Taube, H., "Molecular hysteresis". *Journal of the American Chemical Society* **1991,** 113, (2327-2328).

103. Sano, M.; Taube, H., "Molecular hysteresis" in an electrochemical system revisited. *Inorganic Chemistry* **1994,** 33, (705-709).

104. Tomita, A.; Sano, M., Linkage isomerization of (sulfoxide)ammineruthenium complexes induced by electrochemical processes. *Inorganic Chemistry* **1994,** 33, 5825-5830.

105. Rack, J. J.; Rachford, A. A.; Shelker, A. M., Turning off phototriggered linkage isomerizations in ruthenium dimethyl sulfoxide complexes. *Inorganic Chemistry* **2003,** 42, 7357-7359.

106. Rack, J. J.; Mockus, N. V., Room-temperature photochromism in cis- and trans-(Ru(bpy)2(dmso)2)2+. *Inorganic Chemistry* **2003,** 42, 5792-5794.

107. Smith, M. K.; Gibson, J. A.; Young, C. G.; Broomhead, J. A.; Junk, P. C.; Keene, F. R., Photoinduced ligand isomerization in dimethylsulfoxide complexes of ruthenium(II). *European Journal of Inorganic Chemistry* **2000**, 1365-1370.

108. Bessel, C. A.; Margarucci, J. A.; Acquaye, J. H.; Rubino, R. S.; Crandall, J.; Jircitano, A. J.; Takeuchi, K. J., Steric ligand effects of six bidentate bipyridyl ligands. *Inorganic Chemistry* **1993,** 32, 5779-5784.

109. Huynh, M. H. V.; Smyth, J.; Wetzler, M.; Mort, B.; Gong, P. K.; Witham, L. M.; Jameson, D. L.; Geiger, D. K.; Lasker, J. M.; Charepoo, M.; Gornikiewicz, M.; Cintron, J. M.; Imahori, G.; Sanchez, R. R.; Marschilok, A. C.; Krajkowski, L. M.; Churchill, D. G.; Churchill, M. R.; Takeuchi, K. J., Remarkable rate enhancement of ligand substitution promoted by geometrical arrangement of tridentate "spectator" ligands. *Angewandte Chemie International Edition* 40, (23), 4469-4473.

110. Ross, H. B.; Boldaji, M.; Rillema, D. P.; Blanton, C. B.; White, R. P., Photosubstitution in tris chelate complexes of ruthenium(II) containing the ligands 2,2'-bipyrazine, 2,2'-bipyrimidine, 2,2'-bipyridine, and 4,4'-dimethyl-2,2'-bipyridine: energy gap control. *Inorganic Chemistry* **1989,** 28, 1013-1021.

111. Zelewsky, A. v.; Gremaud, G., Ruthenium(II) complexes with three different diimine ligands. *Helvetica Chimica Acta* **1988,** 71, (5), 1108-1115.

112. Mobian, P. Caténanes construits sur un métal octaédrique: mise en mouvement sous l'action de la lumière. Louis Pasteur, Strasbourg, 2003.

113. Jamorski, C.; Casida, M. E.; Salahub, D. R., Dynamic polarizabilities and excitation spectra from a molecular implementation of time-dependent density-functional response theory: N_2 as a case study. *Journal of Chemical Physics* **1996,** 104, 5134-5147.

114. Saitoh, Y.; Koizumi, T.-a.; Osakada, K.; Yamamoto, T., Preparation of symmetric dibromides of 1,10-phenanthroline. *Canadian Journal of Chemistry* **1997,** 75, 1336-1339.

115. Dietrich-Buchecker, C.; Jimenez, M. C.; Sauvage, J.-P., Selective and efficient synthesis of di-, tri- and tetrasubstituted 1,10-phenanthrolines. *Tetrahedron Letters* **1999,** 40, 3395-3396.

116. Moyer, B. A.; Thompson, M. S.; Meyer, T. J., Chemically catalyzed net electrochemical oxidation of alcohols, aldehydes, and unsaturated hydrocarbons using the system (tpy)(bpy)Ru$(OH_2)^{2+}$ / (tpy)(bpy)RuO^{2+}. *Journal of the American Chemical Society* **1980,** 102, (7), 2310-2312.

117. Thompson, M. S.; Meyer, T. J., Mechanisms of oxidation of 2-propanol by polypyridyl complexes of ruthenium(III) and ruthenium(IV). *Journal of the American Chemical Society* **1982,** 104, 4106-4115.

118. Thompson, M. S.; Meyer, T. J., Kinetics and mechanism of oxidation of aromatic hydrocarbons by Ru(trpy)(bpy)O^{2+}. *Journal of the American Chemical Society* **1982,** 104, (19), 5070-5074.

119. Heller, M.; Schubert, U. S., Syntheses of functionalized 2,2':6',2"-terpyridines. *European Journal of Organic Chemistry* **2003**, 947-961.

120. Thompson, A. M. W. C., Synthesis of 2,2':6',2"-terpyridine ligands - versatile building blocks for supramolecular chemistry. *Coordination Chemistry Reviews* **1997,** 160, 1-52.

121. Miyaura, N.; Suzuki, A., Palladium-catalyzed cross-coupling reactions of organoboron compounds. *Chemical Review* **1995,** 95, 2457-2483.

122. Tzalis, D.; Tor, Y.; Failla, S.; Siegel, J. S., Simple one-step synthesis of 3-bromo- and 3,8-dibromo-1,10-phenanthroline: fundamental buidling blocks in the design of metal chelates. *Tetrahedron Letters* **1995,** 36, (20), 3489-3490.

123. Dietrich-Buchecker, C.; Sauvage, J.-P., Direct synthesis of disubstituted aromatic polyimine chelates. *Tetrahedron Letters* **1982,** 23, (50), 5291-5294.

124. Lüning, U.; Müller, M., Bimacrocyclic 1,10-phenanthroline cyclophanes. *Chemische Berichte* **1990,** 123, 643-645.

125. Liu, S.-X.; Michel, C.; Schmittel, M., A highly regioselective Sonogashira coupling as a key step in the preparation of the first phenanthroline with two diverse reactive groups in 3,8-position. *Organic Letters* **2000,** 2, (25), 3959-3962.

126. Boldron, C.; Pitié, M.; Meunier, B., Simple and efficient syntheses of 1,10-phenanthrolines substituted at C3 or C3 and C8 by bromo, methoxy or hydroxy groups. *Synlett* **2001,** 10, 1629-1631.

127. Durham, B.; Wilson, S. W.; Hodgson, D. J.; Meyer, T. J., Cis-trans photoisomerization in (Ru(bpy)2(OH2)2)2+. Crystal structure of trans-$(Ru(bpy)_2(OH_2)(OH))(ClO_4)_2$. *Journal of the American Chemical Society* **1980,** 102, (2), 600-607.

128. Arico, F.; Mobian, P.; Kern, J.-M.; Sauvage, J.-P., Synthesis of a 2catenane around a $Ru(diimine)_3^{2+}$ scaffold by ring-closing metathesis of olefins. *Organic Letters* **2003,** 5, (11), 1887-1890.

129. Belfrekh, N.; Dietrich-Buchecker, C.; Sauvage, J.-P., Unexpected synthesis of an 8-shaped macrocycle instead of an interlocking-ring system. *Inorganic Chemistry* **2000,** 39, (22), 5169-5172.

130. Piguet, C.; Borkovec, M.; Hamacek, J.; Zeckert, K., Strict self-assembly of polymetallic helicates: the concept behind the semantics. *Coordination Chemistry Reviews* **2005,** 249, 705-726.

131. Swiegers, G. F.; Malefetse, T. J., New self-assembled structural motifs in coordination chemistry. *Chemical Review* **2000,** 100, 3483-3537.

132. Trembleau, L.; Jr., J. R., Helical conformation of alkanes in a hydrophobic cavitand. *Science* **2003,** 301, 1219-1220.

133. Scarso, A.; Trembleau, L.; Jr., J. R., Helical folding of alkanes in a self-assembled, cylindrical capsule. *Journal of the American Chemical Society* **2004,** 126, 13512-13518.

134. Purse, B. W.; Jr., J. R., Encapsulation of oligoethylene glycols and perfluoro-n-alkanes in a cylindrical host molecule. *Chemical Communication* **2004**, 722-724.

135. Scarso, A.; Trembleau, L.; Jr., J. R., Encapsulation induces helical folding of alkanes. *Angewandte Chemie International Edition* **2003,** 42, 5499-5502.

136. Love, J. C.; Wolfe, D. B.; Haasch, R.; Chabinyc, M. L.; Paul, K. E.; Whitesides, G. M.; Nuzzo, R. G., Formation and structure of self-assembled monolayers of alkanethiolates on palladium. *Journal of the American Chemical Society* **2003,** 125, 2597-2609.

137. Love, J. C.; Estroff, L. A.; Kriebel, J. K.; Nuzzo, R. G.; Whitesides, G. M., Self-assembled monolayers of thiolates on metals as a form of nanotechnology. *Chemical Review* **2005,** 105, 1103-1169.

138. Stahl, J.; Bohling, J. C.; Bauer, E. B.; Peters, T. B.; Mohr, W.; Martin-Alvarez, J. M.; Hampel, F.; Gladysz, J. A., sp carbon chains surrounded by sp3 carbon double helices: a class of molecules that are accessible by self-assembly and models for "insulated" molecular-scale devices. *Angewandte Chemie International Edition* **2002,** 41, (11), 1871-1876.

139. Flüeler, P., The hail resistance of plastic components of the building Shell. In *3rd International Symposium on Roofs and Roofing*, J. O. May, British Board of Agreement: Bournemouth, England, 1988.

140. Sestelo, J. P.; Kelly, T. R., a prototype of a rationally designed chemically powered Brownian motor. *Applied Physics A* **2002,** 75, 337-343.

141. Ajdari, A.; Prost, J., Free-flow electrophoresis with trapping by a transverse inhomogeneous field. *Proceedings of the National Academia of Sciences of USA* **1991,** 88, 4468-4471.

142. Wang, H.; Oster, G., Ratchets, power strokes, and molecular motors. *Applied Physics A* **2002,** 75, 315-323.

143. Derenyi, I.; Ajdari, A., Collective transport of particles in a "flashing" periodic potential. *Physical Review E* **1996,** 54, (1), R5-R8.

144. Gorre-Talini, L.; Spatz, J. P.; Silberman, P., Dielectrophoretic ratchets. *Chaos* **1998,** 8, (3), 650-656.

145. Astumian, D.; Chock, P. B.; Tsong, T. Y.; Chen, Y.-d.; Westerhoff, H. V., Can free energy be transduced from electric noise? *Proceedings of the National Academia of Sciences of USA* **1987,** 84, 434-438.

146. Dimroth, P.; Wang, H.; Grabe, M.; Oster, G., Energy transduction in the sodium-ATPase of propionigenium modestum. *Proceedings of the National Academia of Sciences of USA* **1999,** 96, 4924-4929.

147. Oudenaarden, A. v.; Boxer, S. G., Brownian ratchets: molecular separation in lipid bilayers supported on patterned arrays. *Science* **1999,** 285, 1046-1048.

148. Ashton, R.; Padala, C.; Kane, R. S., Microfluidic separation of DNA. *Current opinion in biotechnology* **2003,** 14, 497-504.

149. Bader, J. S.; Hammond, R. W.; Henck, S. A.; Deem, M. W.; McDermott, G. A.; Bustillo, J. M.; Simpson, J. W.; Mulhern, G. T.; Rothberg, J. M., DNA transport by a micromachined Brownian ratchet device. *Proceedings of the National Academia of Sciences of USA* **1999,** 96, (23), 13165-13169.

150. Huang, L. R.; Cox, E. C.; Austin, R. H.; Sturm, J. C., Tilted Brownian ratchet for DNA analysis. *Analytical Chemistry* **2003,** 75, (6963-6967).

151. Kinbara, K.; Aida, T., Toward intelligent molecular machines: directed motions of biological and artificial molecules and assemblies. *Chemical Review* **2005,** 105, 1377-1400.

152. Coy, D. L.; Wagenbach, M.; Howard, J., Kinesin takes one 8-nm step for each ATP that it hydrolyzes. *The Journal of Biological Chemistry* **1999,** 274, (6), 3667-3671.

153. Ott, A., Actin-myosin mobility viewed with epifluorescence microscopy. In 2005.

154. Riveline, D.; Ott, A.; Jülicher, F.; Cardoso, O.; Magnusdottir, S.; Viovy, J. L.; Prost, J., Actin on actin: the electric mobility assay. *European Biophysical Journal* **1998,** 27, 403-408.

155. Winkelmann, D. A.; Bourdieu, L.; Ott, A.; Kinose, F.; Libchaber, A., Flexibility of myosin attachement to surfaces influences F-actin motion. *Biophysical Journal* **1995,** 68, 2444-2453.

156. Waterman-Storer, C.; Duey, D. Y.; Weber, K. L.; Keech, J.; Cheney, R. E.; Salmon, E. D.; Bement, W. M., Microtubules remodel actomyosin networks in Xenopus egg extracts via two mechanisms of F-actin transport. *Journal of Cell Biology* **2000,** 150, 361-376.

157. Vale, R. Movies of the Vale Lab. http://valelab.ucsf.edu/movies/movies.html#anchor149123640

158. Hua, W.; Chung, J.; Gelles, J., Distinguishing inchworm and hand-over-hand processive kinesin movement by neck rotation measurements. *Science* **2002,** 295, 844-848.

159. Yildiz, A.; Selvin, P. R., Fluorescence imaging with one nanometer accuracy: application to molecular motors. *Accounts of Chemical Research* **2005,** 38, 574-582.

160. Sabbadini, R. 3D animation of actin-myosin crossbridge using QuickTime. http://www.sci.sdsu.edu/movies/actin_myosin.html

161. Hasson, T.; Cheney, R. E., Mechanisms of motor protein reversal. *Current opinion in Cell Biology* **2001,** 13, 29-35.

162. Endow, S. A.; Higuchi, H., A mutant of the motor protein kinesin that moves in both directions on microtubules. *Nature* **2000,** 406, 913-916.

163. Astumian, D., Protein molecular motors: not different, just better. In Institut de Science et d'Ingénierie Supramoléculaire, 2005.

164. Astumian, D., Making molecules into motors. *Scientific American* **2001,** 285, (1), 56-64.

165. Hatchard, C. G.; Parker, C. A., *Proceedings of the Royal Society (London) A* **1956,** 235, 518.

166. Parker, C. A., *Proceedings of the Royal Society (London) A* **1953,** 220, 104.

167. Parker, C. A.; Hatchard, C. G., Photodecomposition of complex oxalates. Some preliminary experiments by flash photolysis. *Proceedings of the Royal Society (London) A* **1959,** 63, 22-26.

168. Calvert, J. G.; Pitts, J. N., Chemical actinometer for the determination of ultraviolet light intensities. In *Photochemistry*, Sons, W. a., Ed. New York, 1967; pp 780-786.

169. Lee, J.; Seliger, H. H., Quantum yield of the ferrioxalate actinometer. *The Journal of Chemical Physics* **1964**

, 40, (2), 519-523.

170. Malouf, G.; Ford, P. C., Photochemistry of the ruthenium(II) ammine complexes, $Ru(NH_3)_5(py\text{-}X)^{2+}$. Variation of systemic parameters to modify photochemical reactivities. *Journal of the American Chemical Society* **1977,** 99, (22), 7213-7221.

171. Wegner, E. E.; Adamson, A. W., Photochemistry of complex ions. III. Absolute quantum yields for the photolysis of some aqueous chromium(III) complexes. Chemical actinometry in the long wavelength visible region. *Journal of the American Chemical Society* **1966,** 88, (3), 394-404.

172. Chaisson, D. A.; Hintze, R. E.; Stuermer, D. H.; Petersen, J. D.; McDonald, D. P.; Ford, P. C., Photochemical reaction pathways of ruthenium(II) complexes. III. Metal-to-ligand charge-transfer excitation of the pentaamminepyridineruthenium(II) cation and related species. *Journal of the American Chemical Society* **1972,** 94, (19), 6665-6673.

173. Perkampus, H. H., Evaluation of kinetic measurements. In *UV-VIS spectroscopy and its applications*, Springer-Verlag, Ed. Berlin Heidelberg, 1992; pp 179-190.

174. Durham, B.; Walsh, J. L.; Carter, C. L.; Meyer, T. J., Synthetic applications of photosubstitution reactions of poly(pyridyl) complexes of ruthenium(II). *Inorganic Chemistry* **1980,** 19, 860-865.

175. Allen, G. H.; White, R. P.; Rillema, D. P.; Meyer, T. J., Synthetic control of excited-state properties. Tris-chelate complexes containing the ligand 2,2'-bipyrazine, 2,2'-bipyridine, and 2,2'-bipyrimidine. *Journal of the American Chemical Society* **1984,** 106, 2613-2620.

176. Laemmel, A.-C.; Collin, J.-P.; Sauvage, J.-P.; Accorsi, G.; Armaroli, N., Macrocyclic complexes of $(Ru(N\text{-}N)_2)^{2+}$ units (N-N=1,10 phenanthrolines of 4-(p-anisyl)-1,10-phenanthroline): synthesis and photochemical expulsion studies. *European Journal of Inorganic Chemistry* **2003**, 467-474.

177. Suen, H.-F.; Wilson, S. W.; Pomerantz, M.; Walsh, J. L., Photosubstitution reactions of terpyridine complexes of ruthenium(II). *Inorganic Chemistry* **1989,** 28, 786-791.

178. Fair, C. K., *MolEN, An interactive intelligent system for crystal structure analysis.* Delft, The Netherlands, 1990.

179. Johnson, C. K.; Burnett, M. N. *ORTEP-III: Oak Ridge Thermal Ellipsoid Plot Program for Crystal Structure Illustrations*; ORNL-6895; Oak Ridge National Laboratory: Oak Ridge, USA, 1996.

180. Bruno, I. J.; Cole, J. C.; Edgington, P. R.; Kessler, M. K.; Macrae, C. F.; McCabe, P.; Pearson, J.; Taylor, R., New software for searching the Cambridge Structural Database and visualising crystal structures. *Acta Crystallographica* **2002,** B58, 389-397.

181. Pomeranc, D.; Chambron, J.-C.; Heitz, V.; Sauvage, J.-P., A bis 1,10-phenanthroline ligand leading to octahedral Ru(II) complexes containing a well-defined axis. *Comptes Rendus de l'Académide des Sciences de Paris, Serie IIc: Chimie* **2001,** 4, (3), 197-200.

182. Pomeranc, D.; Heitz, V.; Chambron, J.-C.; Sauvage, J.-P., Octahedral Fe(II) and Ru(II) complexes based on a new bis 1,10-phenanthroline ligand that imposes a well defined axis. *Journal of the American Chemical Society* **2001,** 123, (49), 12215-12221.

183. Slama, J. S.; Rando, R. R., Lectin-mediated aggregation of liposomes containing glycolipids with variable hydrophilic spacer arms. *Biochemistry* **1980,** 19, 4595-4600.

184. Koizumi, M.; Dietrich-Buchecker, C.; Sauvage, J.-P., A (2)catenane containing 1,1'-binaphtyl units and 1,10-phenanthroline fragments: synthesis and intermolecular energy transfer processes. *European Journal of Organic Chemistry* **2004**, 770-775.

RESUME ETENDU EN FRANÇAIS

I. Introduction et synopsis

Une « machine moléculaire » est une molécule composée de deux sous-parties distinctes dont le mouvement de l'une relativement à l'autre peut être contrôlé. En pratique, ce « contrôle » du mouvement à l'échelle moléculaire est réalisé grâce à des signaux externes macroscopiques imposés par l'opérateur, tels qu'un signal électrochimique à une électrode, l'ajout d'un réactif chimique dans le milieu ou l'utilisation de lumière (signal photonique). Dans ce dernier cas, le milieu réactionnel n'est pas altéré par l'introduction de matière étrangère puisque ce sont les photons seuls qui déclenchent le mouvement. Dans le cas idéal, le mouvement aller *et* le retour à la position de départ pourraient être réalisés grâce à l'utilisation de lumières de longueurs d'onde différentes : ainsi un mouvement de va-et-vient contrôlé par l'extérieur pourrait voir le jour sans que le milieu dans lequel est plongée la « machine moléculaire » ne soit altéré.

Dans cette optique, le groupe de Jean-Pierre Sauvage a cherché à développer des prototypes de machines moléculaires activées par la lumière. Les complexes polypyridyl de ruthénium (II) ont une réactivité photochimique intéressante qui en font les candidats idéals pour ce type de réalisations. Excités dans leur bande de transfert de charge grâce à de la lumière visible, ils photoéjectent un des ligands de la sphère de coordination pour donner un complexe insaturé ; celui-ci capte un ligand présent à proximité de l'atome métallique pour donner une nouvelle espèce saturée et stable. La proximité spatiale entre le ligand « rentrant » et le métal peut être assurée par la construction de molécules à topologie non triviale comme des caténanes et des rotaxanes. Grâce au lien mécanique non covalent inhérent à leur structure, ceux-ci peuvent maintenir un ou des ligand(s) à proximité immédiate de l'atome métallique, de telle façon que les échanges de ligands photoinduits puissent se passer de façon *intra*moléculaire. Appliqué au noyau $Ru(phen)_2(L)^{2+}$ où L est un chélate encombré de type 6,6'-dimethyl-2,2'-bipyridine, ce concept a permis de réaliser des prototypes de pistons moléculaires photo-contrôlés (thèses de Pierre Mobian et Damien Jouvenot).

Dans le double but de 1) pouvoir diversifier les ligands pouvant être échangés et 2) faciliter la réaction thermique de retour, notre groupe s'est penché sur le noyau $Ru(N\text{-}N\text{-}N)(N\text{-}N)(L)^{2+}$ où N-N-N est une terpyridine, N-N un chélate bidenté de type phénanthroline et L un ligand monodenté. Un travail préliminaire d'Emma Schofield, réalisé au sein du laboratoire en 2001-2002, a permis de démontrer que ce nouveau noyau pouvait conduire au même type de comportement que le noyau

$Ru(phen)_2(L)^{2+}$. Dans notre travail de thèse, nous complétons ce travail et tentons d'utiliser le noyau $Ru(terpy)(phen)(L)^{n+}$ pour la synthèse de machines moléculaires photoactivées.

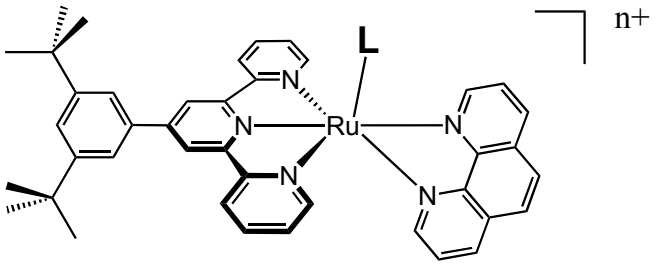

Pour cela, nous avons synthétisé (Chapitre 1) des complexes modèles de formule $Ru(terpy^*)(phen)(L)^{n+}$ (n = 1 ou 2) avec une grande variété de ligands monodentés. Nous montrons que l'irradiation de ces complexes donne lieu à une substitution sélective du ligand monodenté par une molécule de solvant. Par ailleurs, nous montrons que l'utilisation de la 2,9-dimethyl-1,10-phénanthroline (dmp) au lieu de la phénanthroline (phen) conduit à une distorsion importante des structures à l'état solide, distorsion qualitativement corrélée à l'augmentation des rendements quantiques de photosubstitution du ligand monodenté.

Dans le Chapitre 2, nous décrivons la synthèse d'un complexe de type scorpionate à deux positions construit à partir d'une phénanthroline dissymétrique substituée en positions 3 et 8. Nous avons séparé les deux isomères de ce produit et nous montrons que ce sont deux isomères de coordination, différents l'un de l'autre par la nature du ligand monodenté coordiné sur le ruthénium. Nous expliquons comment nous pouvons passer de l'un à l'autre par irradiation : lors de la photoexpulsion du ligand monodenté, la phénanthroline effectue un mouvement de rotation de 90° autour du ruthénium, à la façon d'une rotule. Nous expliquons pourquoi la nature localement symétrique et non encombrée de la phénanthroline utilisée limite notre système à une composition statistique des deux isomères.

Dans le Chapitre 3, nous montrons la synthèse d'une phénanthroline dissymétrique substituée sur le noyau aromatique en positions 2 et 8 (AMphen). Ce chélate, lorsqu'il est coordiné à un Ru(APterpy), se comporte de façon originale : nous montrons que sa rotation au sein de complexes $Ru(APterpy)(AMphen)(L)^{n+}$ est quantitative et qu'elle peut être contrôlée dans un sens par la lumière, dans l'autre par chauffage dans le DMSO.

Enfin, dans le travail exposé au Chapitre 4 nous avons intégré le complexe $Ru(APterpy)(AMphen)(L)^{n+}$ au sein de macrocycles qui incluent l'atome de ruthénium. Nous montrons que la réactivité de l'espèce cyclique est identique à celle de l'espèce acyclique. Ainsi, nous pouvons contrôler la conformation des chaînes souples du macrocycle grâce au mouvement photoinduit d'isomérisation de la phénanthroline.

II. Chapitre 1 : synthèse de complexes modèles de type Ru(terpy)(N-N)(L)$^{n+}$ et réactions d'échanges de ligands

Nous avons synthétisé par des réactions thermiques d'échanges de ligands la série de complexes Ru(terpy*)(phen)(L)$^{n+}$ avec L = Cl^-, H_2O, CH_3CN, C_5H_5N, 3,5-dimethylpyridine (LUT), 2,6-dimethylbenzonitrile (MeBN), 2,6-dimethoxybenzonitrile (MeOBN), diméthylsulfure (DMS), phénothiazine (PTZ) et diméthylsulfoxyde (DMSO). Nous avons obtenu quatre structures cristallographiques qui montrent le caractère non encombré de ces complexes (voir Figure 50).

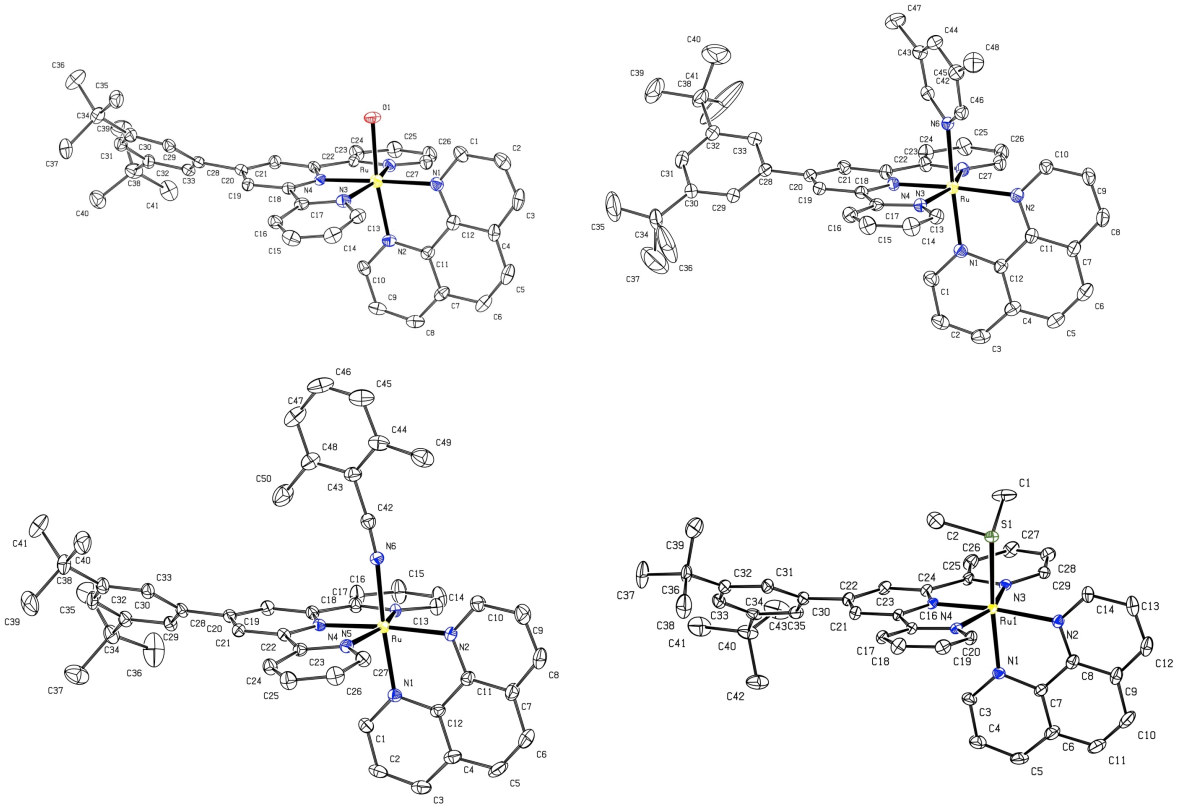

Figure 50: structures cristallographiques de quatre complexes de type Ru(terpy*)(phen)(L)$^{2+}$ avec L = H_2O, LUT, MeBN et DMS.

Nous avons montré la généralité des réactions photoinduites d'échanges de ligands (voir Schéma 1). Des études par spectroscopies UV-visible et RMN ont confirmé que la polydenticité des ligands terpyridine et phénanthroline permettait une réaction extrêmement sélective de photosubstitution sur le ligand monodenté. Nous avons mesuré les cinétiques de ces réactions dans des conditions comparables, et nous montrons comment des constantes de vitesse obtenues sont compatibles avec l'hypothèse d'un mécanisme dissociatif.

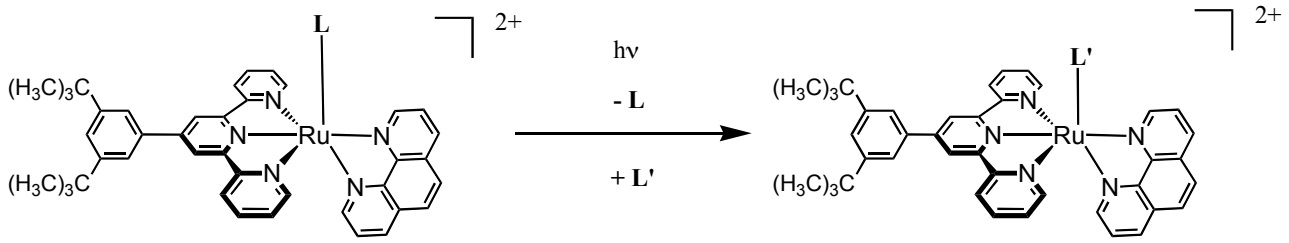

Schéma 1: photosubstitution du ligand monodenté dans les complexes Ru(terpy*)(phen)(L)$^{2+}$.

L'utilisation de la 2,9-dimethyl-1,10-phenanthroline (dmp) a conduit à une autre série de complexes de formule Ru(terpy*)(dmp)(L)$^{2+}$ avec L = CH_3CN, C_5H_5N, 3,5-lutidine (LUT), 2,6-dimethoxybenzonitrile (MeOBN) et dimethylsulfide (DMS). Deux structures cristallographiques ont été obtenues (voir Figure 51) et montrent par la distorsion de la dmp le caractère fortement encombré de ces complexes.

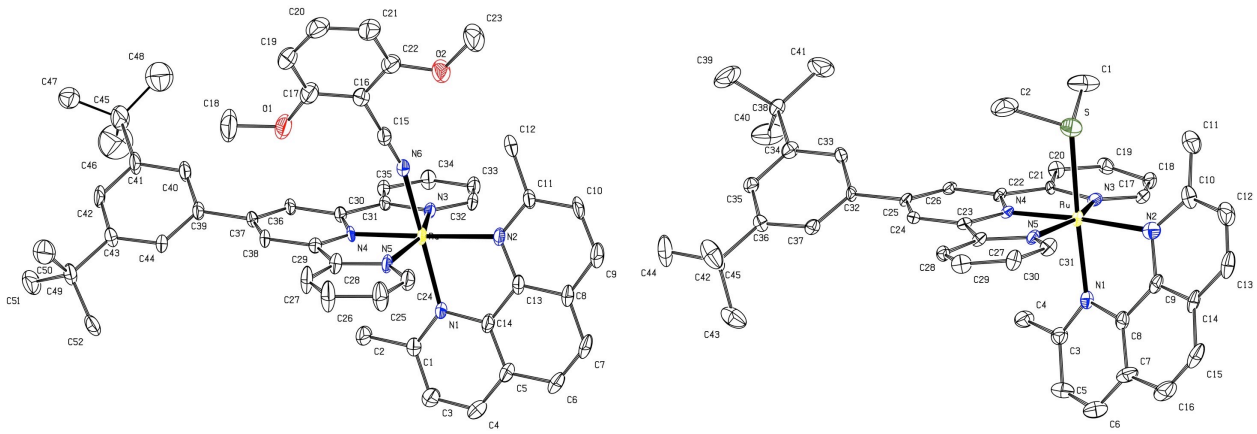

Figure 51: structures cristallographiques des complexes Ru(terpy*)(dmp)(L)$^{2+}$ avec L = MeOBN et DMS.

Le groupement méthyle en position 2 de la dmp provoque une gêne stérique importante avec le ligand monodenté. Les réactions photoinduites d'échange de ligands ont été étudiées sur cette nouvelle série de complexes et nous avons montré qu'elles étaient de un à deux ordres de grandeur plus rapides que dans le cas de la série phen. Des mesures précises de rendements quantiques ont été réalisées sur trois complexes et confirment quantitativement cette augmentation de réactivité (voir valeurs ci-dessous).

Les distorsions observées sur les structures cristallographiques des complexes Ru(terpy*)(N-N)(L)$^{2+}$ peuvent être qualitativement corrélées à leur photoréactivité (voir vues de face ci-dessus) : les structures les plus distordues correspondent aux photosensibilités les plus élevées. Dans le cas de la structure du complexe Ru(terpy*)(dmp)(DMS)$^{2+}$ par exemple, le rendement quantique obtenu ϕ = 0.36 pour la réaction de photosubstitution du ligand DMS par la pyridine dans la pyridine est particulièrement élevé pour un complexe polypyridine de ruthénium (II).

Complexes	ϕ
$Ru(terpy)(bpy)(CH_3CN)^{2+}$ (a)	0.0013 ±0.0001
$Ru(terpy)(phen)(CH_3CN)^{2+}$	0.0016 ±0.0002
$Ru(terpy^*)(phen)(MeOBN)^{2+}$	0.0035 ±0.0009
$Ru(terpy^*)(dmp)(MeOBN)^{2+}$	0.079 ±0.015
$Ru(terpy^*)(dmp)(DMS)^{2+}$	0.36 ±0.11

(a) *Mesuré par Meyer et al.*

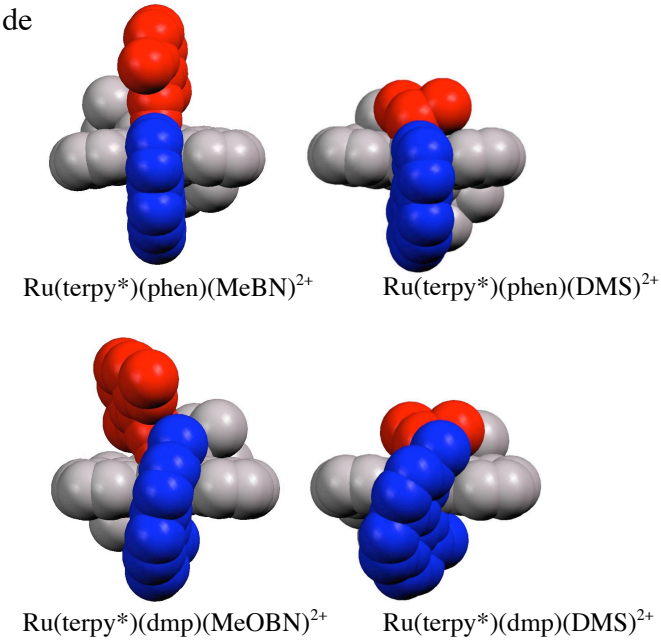

Enfin, quelques investigations mécanistiques ont été entreprises et valident expérimentalement l'hypothèse généralement admise d'un mécanisme dissociatif. Cette hypothèse est également confirmée par quelques-uns des résultats théoriques obtenus en collaboration avec Julien Bossert et Chantal Daniel.

III Chapitre 2: synthèse et photochimie d'un complexe $Ru(terpy)(phen)(L)^{2+}$ à deux positions de type scorpionate

Ce projet est une extension du travail d'Emma Schofield *et al.* Il consiste à synthétiser un complexe de type scorpionate intégrant le noyau $Ru(terpy)(phen)^{2+}$ dans lequel la phénanthroline possède deux ligands monodentés différents, un de type benzonitrile et un de type diméthylsulfoxyde, attachés tous deux au centre aromatique du chélate par des bras covalents longs et flexibles (composé **26**). La sixième position sur la sphère de coordination du ruthénium peut être occupée soit par l'un, soit par l'autre de ces ligands monodentés, en fonction de la position du chélate bidenté. Aux deux positions de la phénanthroline correspondent deux isomères de coordination différents, $\mathbf{18}^{2+}$ et $\mathbf{19}^{2+}$, représentés Figure 52.

Nous avons synthétisé ces deux isomères et montré à quel point leur polarité, leur spectre UV-visible et leur spectre de RMN sont différents. La nature du ligand coordiné, et donc la position correspondante du chélate bidenté est prouvée à la fois par spectroscopie UV-vis et par expériences 2D-ROESY de RMN du proton.

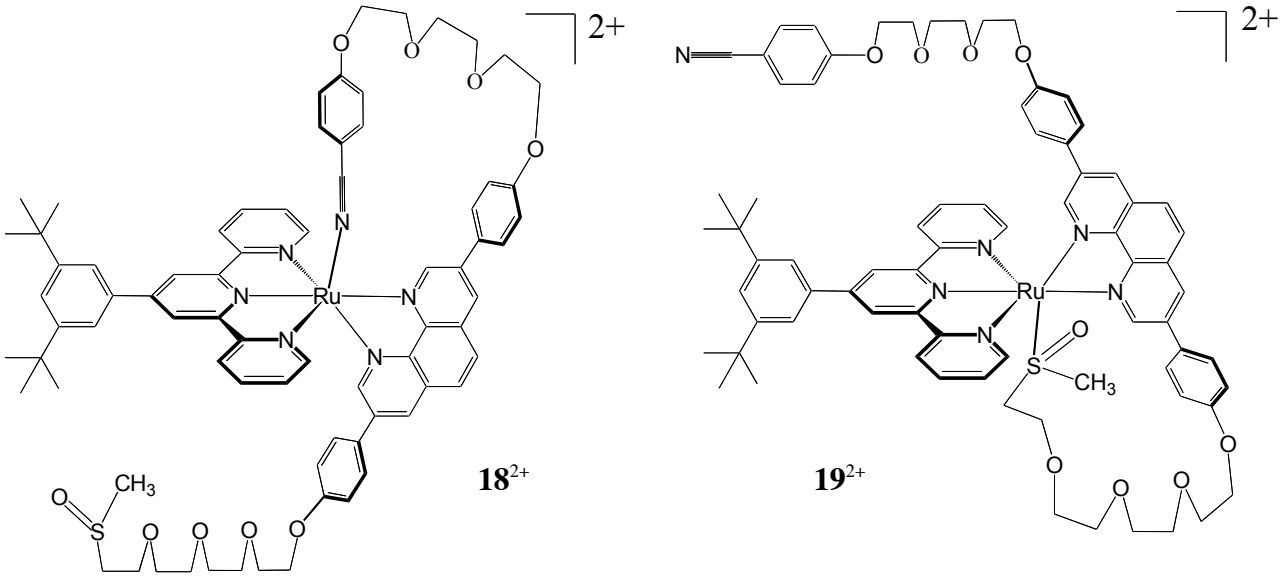

Figure 52: isomères de coordination d'un scorpionate construit à partir de la phénanthroline **26**.

Nous avons étudié la réaction photochimique d'expulsion de la « queue » du scorpion (benzonitrile ou diméthylsulfoxyde). Nous avons notamment observé que cette photoexpulsion était accompagnée d'un phénomène d'isomérisation partiel de la phénanthroline correspondant à une rotation de 90° autour de l'atome de ruthénium.D'après les calculs TD-DFT menés par Julien Bossert dans le cadre de sa thèse, cette isomérisation pourrait avoir lieu sur l'espèce pentacoordinée du mécanisme dissociatif de la réaction de photosubstitution du ligand monodenté par une molécule de solvant. Le caractère *localement symétrique* et *non encombré* de la phénanthroline **26** induit une distribution statistique des deux produits « ouverts » Ru(terpy*)(**26**)(S)$^{n+}$, pourvu que la durée d'irradiation soit suffisamment longue.

Dans certaines conditions, les produits ouverts peuvent être « refermés » par une réaction thermique, en l'absence de lumière. Une telle réaction conduit à un mélange du produit initialement irradié et de son isomère de coordination. Lors du processus thermique de fermeture du ruthéna-macrocycle, la phénanthroline ne s'isomérise pas ; nous soupçonnons une contribution majoritaire du mécanisme associatif dans ces réactions intramoléculaires. Ainsi, un cycle « ouverture photoinduite » – « fermeture thermique » peut conduire à une rotation de la phénanthroline pour au maximum 50% des molécules de l'échantillon (voir Schéma 2).

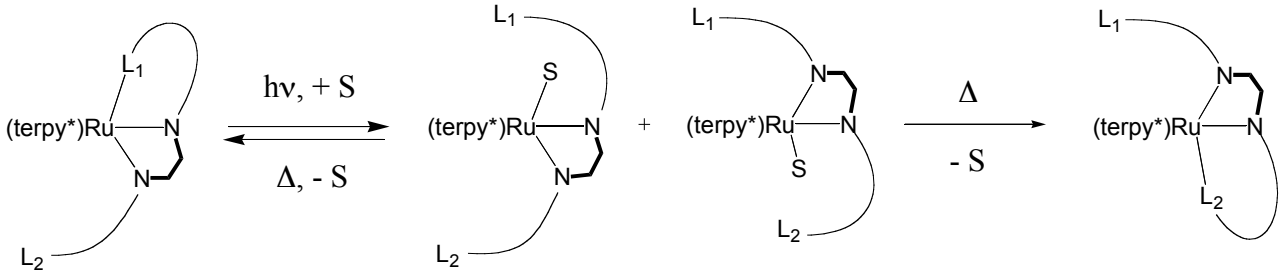

Schéma 2: ouverture-fermeture des scorpionates (S : solvant).

Enfin, l'irradiation sélective de $\mathbf{18}^{2+}$ au sein d'un mélange de $\mathbf{18}^{2+}$ et $\mathbf{19}^{2+}$ est possible grâce à l'utilisation d'un filtre interférentiel de type « passe-bande » centré sur 470 nm. Cette irradiation sélective conduit, après re-fermeture du produit d'irradiation dans des conditions thermiques, à un enrichissement progressif en l'isomère $\mathbf{19}^{2+}$. Un tel processus répété deux fois sur le même échantillon a permis de dépasser la composition statistique et d'atteindre un ratio $\mathbf{18}^{2+}$:$\mathbf{19}^{2+}$ = 44 :56 à partir d'un échantillon pur de $\mathbf{18}^{2+}$.

La nature non encombrée et localement symétrique de la phénanthroline utilisée, ainsi que la longueur et la flexibilité des chaînes polyéther qui permettent d'attacher les deux ligands monodentés au chélate limitent fortement ce type de système du point de vue des applications : le mouvement d'isomérisation est trop lent, et l'état photostationaire est caractérisé par une distribution statistique des deux isomères. Néanmoins, de tels systèmes pourraient être améliorés afin d'utiliser l'ambidenticité du ligand L_1-phen-L_2 dans des interrupteurs moléculaires photoactivés.

IV. Chapitre 3 : complexes Ru(terpy)(phen)(L)$^{n+}$ avec un chélate bidenté 2,8-dissymmétriquement substitué

Dans ce chapitre, un groupement mésityle encombrant en α d'un des deux atomes d'azote sur la phénanthroline est utilisé dans l'espoir de bloquer un des deux isomères de rotation du chélate bidenté. Les deux ligands APterpy (4'-(3-anisylphényl)-2,2';6',2''-terpyridine) et AMphen (8-anisyl-2-mésityl-1,10-phénanthroline) ont été synthétisés. La série de complexes de ruthénium(II) Ru(APterpy)(AMphen)(L)$^{n+}$ avec L = Cl^-, CH_3CN ou C_5H_5N a été synthétisée par échanges thermiques classiques de ligand (voir Schéma 3). La géométrie de ces complexes est prouvée par étude RMN ainsi que par une structure cristallographique : le groupement anisyle de la phen est situé du même côté que le ligand L, et le groupement mésityle se place juste sous le ligand terpyridine (voir Figure 53).

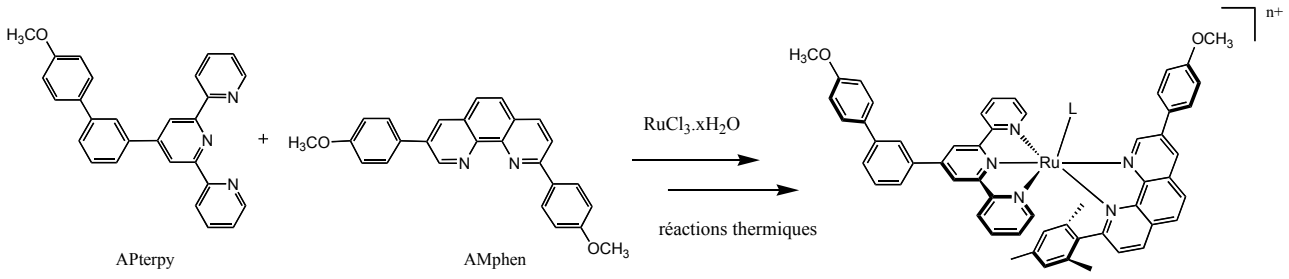

Schéma 3 : structure des ligands APterpy et AMphen et coordination au ruthénium (II) par voie thermique.

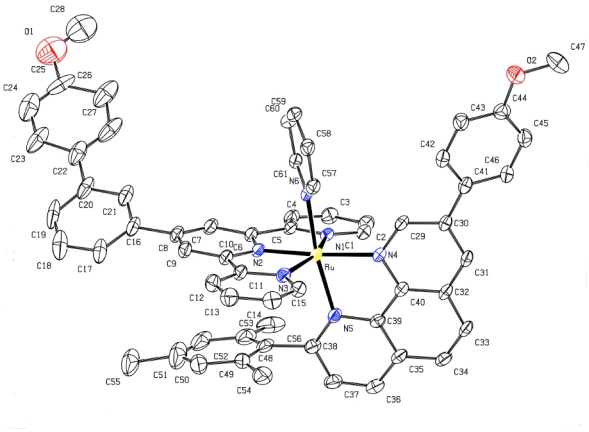

Figure 53 : structure cristallographique du complexe $\mathbf{37}_{\mathbf{th}}^{2+}$ ($Ru(APterpy)(AMphen)(PY)^{2+}$).

Cependant, l'irradiation de ces complexes « thermiques » dans l'acétonitrile ou dans la pyridine produit une rotation *quantitative* de 90° de la phénanthroline. La série correspondante de complexes isomères est appelée série « photochimique ». Dans ces nouveaux complexes, les spectres de corrélation ROESY en solution prouvent que c'est le groupement mésityle qui se trouve du côté du ligand L (voir Schéma 4).

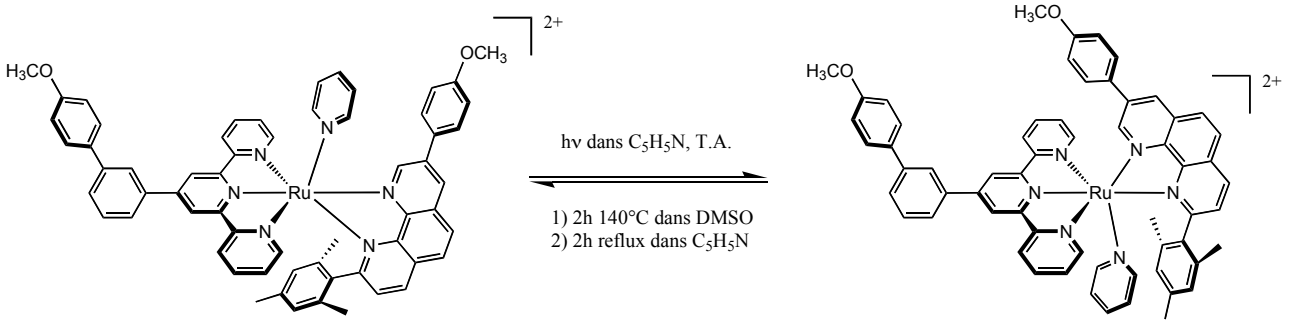

Schéma 4: isomérisation photoinduite des complexes de la série « thermique » et isomérisation retour, dans des conditions thermiques particulières (DMSO 140°C 2h), de la série « photochimique ».

Nous avons étudié le processus d'isomérisation retour de la phénanthroline afin de voir s'il était possible de revenir à la série « thermique » de complexes de départ. Nous avons montré que cette isomérisation retour n'avait lieu efficacement que dans le diméthylsulfoxyde à 140°C pendant au moins 2h et en l'absence de lumière. D'autres types de solvants moins encombrants comme le benzonitrile ou la 3,5-diméthylpyridine (LUT) mènent à une substitution du ligand L *sans isomérisation* de la phénanthroline.

Pour conclure, nous disposons d'un système bistable caractérisé par la position de la phénanthroline par rapport au ligand monodenté : le groupe anisyle du ligand AMphen se trouve soit du même côté que L (série « thermique »), soit de l'autre côté (série « photochimique »). La rotation du ligand AMphen autour de l'atome de ruthénium est parfaitement contrôlée grâce, dans un sens à une irradiation, dans l'autre sens à un chauffage dans le DMSO. À la fin de ce chapitre,

nous proposons un modèle cinétique des réactions de substitution de ligand qui rende compte de l'ensemble des résultats d'isomérisation obtenus au cours de nos travaux.

V. Chapitre 4 : inclusion d'un complexe Ru(terpy)(phen)(L)$^{2+}$ dans un macrocycle moléculaire à géométrie photocontrôlée.

La stabilité des liaisons ruthénium-azote dans les complexes Ru(APterpy)(AMphen)(PY)$^{2+}$ nous a permis de réaliser à la périphérie des ligands polydentés quatre étapes de synthèse organique sans modification du centre inorganique. Cette stratégie de « chimie sur le complexe » a conduit à une synthèse efficace de macrocycles à 39 et 43 atomes qui comprennent l'unité Ru(APterpy)(AMphen)(PY)$^{2+}$. L'étape clé de ces synthèses, une métathèse d'oléfine catalysée par le catalyseur de Grubbs, est très sensible à la géométrie des précurseurs. Dans notre cas, les isomères photochimiques ont donné de bien meilleurs rendements de macrocyclisation que les isomères thermiques car ils placent les extrémités réactives du précurseur à proximité l'une de l'autre. Les rendements obtenus sont très bons, jusqu'à 83% pour le passage de $\mathbf{37}_{\mathbf{photo}}{}^{2+}$ à $\mathbf{46}_{\mathbf{photo}}{}^{2+}$ (4 étapes).

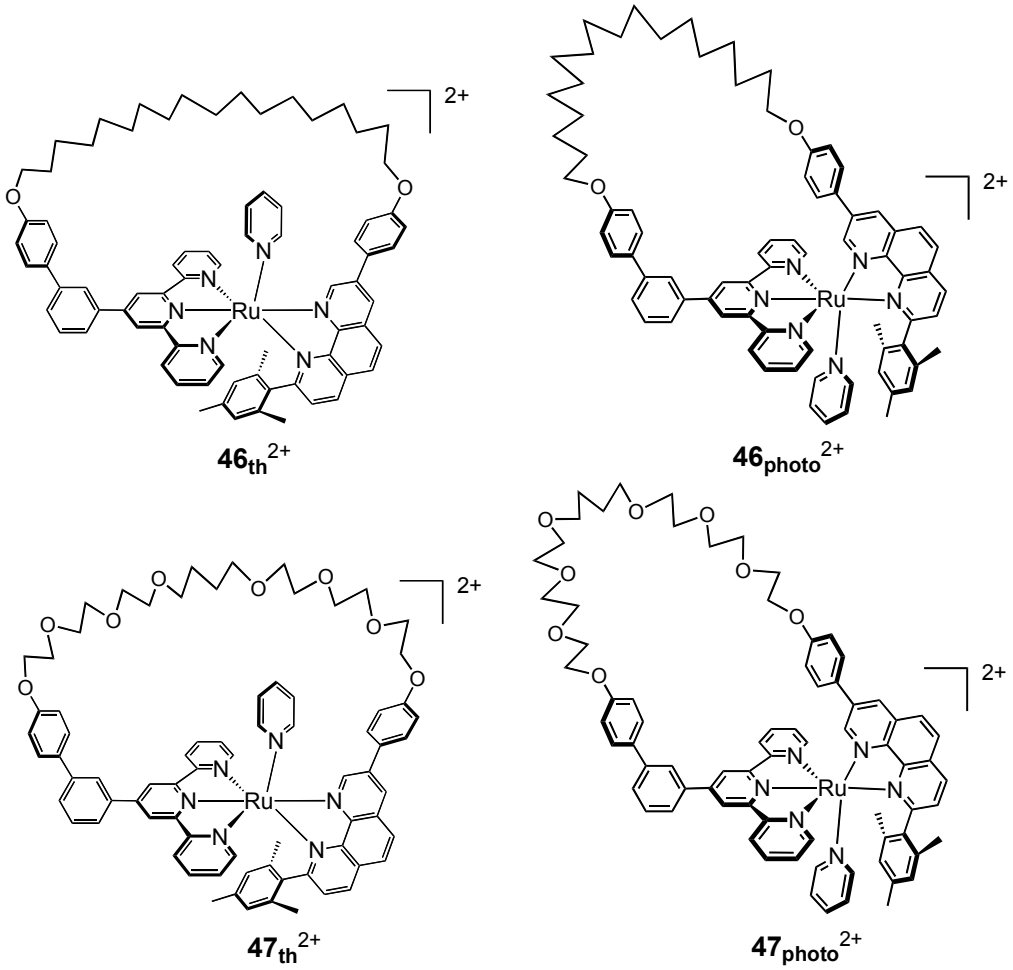

Schéma 5: formules de quatre ruthéno-macrocycles comprenant l'unité Ru(terpy)(phen).

Deux chaînes flexibles de nature différente ont été utilisées : une chaîne de type alcane à 18 atomes de carbone (composé **46**$^{2+}$) et une chaîne de type polyéther de glycol (composé **47**$^{2+}$). De même que pour les espèces acycliques décrites au Chapitre 3, ces deux macrocycles existent chacun soit dans une géométrie « thermique », soit dans une géométrie « photochimique ». Les quatre composés correspondants sont représentés Schéma 5.

Une fois la double liaison réduite, la chimie de coordination étudiée au Chapitre 3 a pu être reproduite sur ces espèces macrocycliques sans différence notable de réactivité avec les complexes acycliques. Ceci signifie que la partie aromatique des complexes **46**$^{2+}$ et **47**$^{2+}$ impose sa géométrie à la chaîne flexible de type alcane ou polyethylène glycol. Ainsi, la rotation photoinduite de la phénanthroline AMphen au sein du complexe conduit à une réorganisation majeure de la conformation des chaînes flexibles. Bien que le manque de résolution rende toute étude quantitative de la conformation des chaînes impossible, cette modification de l'agencement conformationnel des chaînes a pu être qualitativement démontré par RMN. Une modélisation Chem3D de cette réorganisation est proposée Figure 54.

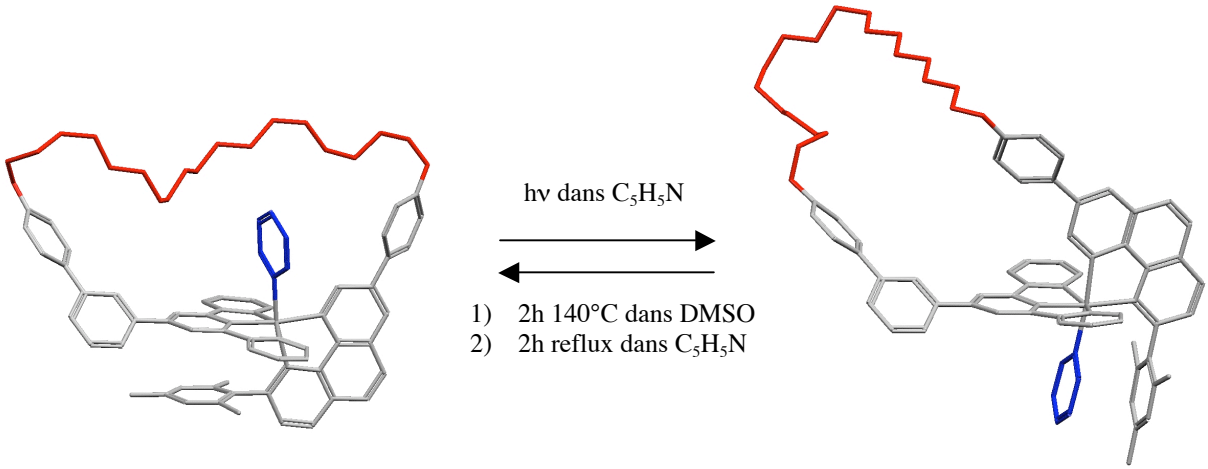

Figure 54 : contrôle de la conformation d'une chaîne flexible de type alcane par une isomérisation photoinduite de la phénanthroline 2,8-disubstituée. Structures calculées par modélisation moléculaire (Chem3D ; pour la structure RX de **46**$_{photo}^{2+}$, voir Annexe E).

En conclusion, nous avons réalisé la synthèse de macrocycles **46**$^{2+}$ et **47**$^{2+}$ comprenant l'unité Ru(terpy)(phen)(L)$^{2+}$. Chacun de ces macrocycles existe sous les deux formes « thermique » et « photochimique » étudiées au Chapitre 3 qui imposent à la chaîne flexible une conformation « tendue » ou « relâchée » (respectivement). On peut passer de la forme thermique à la forme photochimique par irradiation, et la réaction retour est réalisée par chauffage dans le DMSO.

Remarque : dans l'isomère thermique, le ligand monodenté PY se trouve *à l'intérieur* de la cavité macrocyclique (voir Figure 5). Au contraire dans l'isomère photochimique le ligand

monodenté se trouve *à l'extérieur* de la cavité macrocyclique. Seul le premier pourra être utilisé pour une synthèse par effet template de caténanes ou rotaxanes.

VI. Publications

Ce travail de thèse a donné lieu à la publication des articles suivants:

4) Sylvestre Bonnet, Emma Schofield, Jean-Paul Collin et Jean-Pierre Sauvage, "Photochemical and thermal synthesis and characterization of polypyridine ruthénium(II) complexes containing different monodentate ligands", *Dalton Trans.* **2003**, 4654-4662 ;

5) Sylvestre Bonnet, Emma Schofield, Jean-Paul Collin et Jean-Pierre Sauvage, "Photochemical expulsion of the neutral monodentate ligand L in Ru(terpy*)(diimine)(L) $^{2+}$: a dramatic effect of the steric properties of the spectator diimine ligand", *Inorg. Chem.* **2004**, *43*, 8346-8354.

6) Sylvestre Bonnet, Jean-Paul Collin et Jean-Pierre Sauvage, "A Ru(terpy)(phen)-incorporating ring and its light-induced geometrical changes", *Chem. Comm.* **2005**, 3195-3197.

RESUME

Ce travail de thèse s'inscrit dans le domaine des machines moléculaires activées par la lumière. Il consiste en l'étude des complexes de ruthenium (II) de formule générale Ru(N-N-N)(N-N)(L)$^{n+}$, où N-N-N est un ligand terdenté de type terpyridine, N-N est un ligand bidenté de type 1,10-phénanthroline, et L est un ligand monodenté de type chlorure, acéto- ou benzonitrile, pyridine, éther de soufre ou dialkylsulfoxyde. Irradiés par de la lumière visible, ces complexes photosubstituent sélectivement et quantitativement le ligand monodenté L par une molécule de solvant. Trois rendements quantiques de photosubstitution ont été mesurés et montrent que l'efficacité de ce processus peut être régulée par la nature du substituant (H ou CH_3) en a des atomes d'azote de la phénanthroline. Par ailleurs, un processus d'isomérisation de la phénanthroline a lieu pendant cette phosubstitution, ce qui corrobore l'hypothèse d'un mécanisme dissociatif. Cette photoisomérisation correspond à une rotation de 90° du chélate bidenté par rapport à la terpyridine.

Dans l'espoir de tirer parti de ce phénomène, les deux isomères de coordination d'un complexe de type scorpionate ont été synthétisés et caractérisés. La phénanthroline utilisée porte deux long bras flexibles terminés par deux ligands monodentés différents qui viennent, l'un ou l'autre, se coordiner sur le ruthénium. La plus grande lenteur du processus de photoisomérisation par rapport à la réaction de photoéjection de la « queue » du scorpion limite l'efficacité de cette molécule en tant qu'interrupteur moléculaire.

Afin de dissymétriser plus efficacement l'environnement de coordination du ruthénium, un groupement encombrant de type mésityle a été introduit en position 2 sur la phénanthroline. Basée sur une nouvelle phénanthroline dissymétrique AMphen, une famille de complexes acycliques de formule Ru(APterpy)(AMphen)(L)$^{n+}$ a été synthétisée et caractérisée. La rotation du chélate bidenté au sein de ces complexes est contrôlée dans un sens par irradiation, dans l'autre par chauffage dans le diméthylsulfoxyde. Le rendement de l'étape de photoisomérisation devenu quantitatif, ce système est un des rares exemples où la sphère de coordination d'un métal de transition se réarrange sous contrôle photonique.

La réorganisation géométrique résultant de la photoisomérisation de AMphen a été utilisée dans la synthèse efficace de deux macrocycles moléculaires comportant l'unité Ru(terpy)(phen)(py)$^{2+}$. La géométrie de l'isomère photochimique est la plus adéquate pour l'étape de macrocyclisation par métathèse d'oléfines. Une fois réduite, la chaîne flexible reliant l'unité phénanthroline à l'unité terpyridine est stable, ce qui permet à nouveau les réactions d'échange de ligands et d'isomérisation étudiée sur les espèces acycliques. La forme de ces macrocycles, et donc la conformation des chaînes flexibles, est ainsi contrôlée dans un sens par la lumière, dans l'autre par chauffage dans le diméthylsulfoxyde.

MOTS-CLEFS

Synthèse organique, synthèse de complexes, photochimie, machine moléculaire, photosubstitution, photoisomérisation, phénanthroline, terpyridine, macrocycle, ruthénium (II), scorpionate, métathèse d'oléfines, mécanisme dissociatif, conformation de chaînes alcane.

DISCIPLINES

Chimie organique, chimie de coordination, photochimie.

LABORATOIRE

Laboratoire de Chimie Organo-Minérale
UMR 7513 CNRS / Université Louis Pasteur
Institut Le Bel 6ème étage Sud
4 rue Blaise Pascal 67070 STRASBOURG Cedex